Universitat Politècnica de Catalunya

Doctoral Thesis

Stochastic and complex dynamics in mesoscopic brain networks

Author:
Daniel Malagarriga i Guasch

Supervisors:
Prof. Dr. Antonio J. Pons Rivero
Prof. Dr. Jordi García-Ojalvo
Prof. Dr. Alessandro E.P. Villa

A thesis submitted in fulfillment of the requirements
for the degree of Doctor in Physics
in the

Nonlinear Dynamics, Nonlinear Optics and Lasers group (DONLL)
Departament de Física

"The task is...not so much to see what no one has yet seen; but to think what nobody has yet thought, about that which everybody sees."

Erwin Schrödinger

Agraïments

No és fàcil enumerar totes les persones que han contribuït en aquesta tesi i han fet que sigui realitat. De ben segur que no m'hagués fixat en la biofísica si en David J no m'hagués mostrat tota la seva bellesa. Tanmateix, però, probablement tot va començar fa uns cinc anys, en un laboratori de biologia perdut a la facultat de Física de la Universitat de Barcelona: allà en Jordi S, la Sara i el Javier em van fer despertar l'interès per la recerca en neurociència. Afortunadament, aquest interès encara no s'ha adormit! Gràcies al meu pas per la UB vaig poder conèixer als qui de ben segur han estat els majors contribuents en aquesta tesi, en Toni i en JGO. Gràcies Toni per les hores que em vas dedicar, colze a colze, programant davant de l'ordinador! Tot el què he après ha estat gràcies a tu. I gràcies JGO pel teu mentoratge, per la teva vitalitat i, sobretot, per la teva clarividència. Res del que hi ha en aquesta tesi hagués estat possible sense tu! Us asseguro que en aquest espai no hi cap tot el meu agraïment cap a vosaltres!

Però bé, també tinc un especial record de tots aquells amb els quals he compartit el plaer de treballar a Terrassa: Belén, Marta, Pau, Elena, Lorena, Jordi T, Jordi Z, Andrés, Lina, Ignacio, Giulio, Auro, Carlos, Bingxia, Shubham, Jose María, Sandro, Yu-Chieh, Waqhas, Mohammed, John, Dario! I Crina, Cristina, Carme, Ramon, Muriel, Kestas, Josep Lluís, Simone, Carles! També per aquells amb els quals he treballat i coincidit a Barcelona: Maciek, Alessandro B, Marçal, Letícia, Lara, Rosa, Carlos! I, per descomptat, per aquells que he conegut a Lausanne: Alessandra, Sarah, Céline, Jérémie, Natalí, Paolo! De Lausanne també m'emporto el plaer d'haver pogut conèixer i treballar amb l'Alessandro Villa. Mil gracias Alessandro por darme la oportunidad de aprender tanto contigo! Finalment, agraeixo als meus nous companys que em facin el dia a dia tant agradable i divertit al CRG: thanks Matthieu, Elena, Elie, David, Andy, Mariana, Avinash, Daeyeon, Ximena, Eva, Iris, Nico, Ajinkya!

Els amics i família mereixen una menció apart. Gràcies, encara que estiguem tots lluny, a tots aquells físics, matemàtics i d'altres espècimens que van fer dels anys de carrera els més divertits i productius de la meva vida d'estudiant: Masu, Faixedas, Helens, Fageda, Peter, Aina, Walker, Johnny G, Juli, Edu, Antón, Tximet, Sergi! I també als biofísics del màster: Maria, Marc, David, Marina, Carles, Iago, Agustí, Gabriel, Christopher!

Gràcies a aquells músics bojos que m'ajuden a escapar d'atractors estranys i diagrames d'estabilitat: Xuri, Piuri, Yanka, Miquel, Oscar, Jordi C, Violeta! Sense Múrgula tampoc existiria aquesta tesi! Gràcies també als Miaús, als "copetins" i a tota la fauna sadurninenca amb qui he passat tants bons moments aquests anys. Gràcies també als cosins i tiets, al meu avi, i a tots aquells que ja no hi són. Gràcies Carmen, gràcies Ramon. Però sobretot gràcies a vosaltres, Papa i Mama. Heu estat, sou i sempre ho sereu tot per mi. Dono gràcies a la vida per haver-nos fet coincidir en l'espai-temps aquell dia calorós de Juny.

I gràcies a tu, Mònica. T'he deixat pel final però tu saps que sempre has estat el principi, de tot.

Resum de la tesi

Estocasticitat i dinàmica complexa en xarxes cerebrals mesoscòpiques

L'objectiu d'aquesta tesi és aprofundir en la comprensió dels mecanismes responsables de la generació de dinàmica complexa i estocàstica, així com de fenòmens emergents, en el cervell humà. Des d'un punt de vista microscòpic, les neurones són les responsables de processar la informació, sensorial o provinent d'altres fonts, i transmetre-la elèctricament a través d'extenses xarxes cel·lulars que conformen el sistema nerviós. La informació es processa mitjançant l'anomenat *codi neuronal*, que es basa en l'activació elèctrica de les neurones exclusivament quan el seu potencial de membrana supera el llindar d'activació. D'aquesta manera, els *potencials d'acció*, o descàrregues elèctriques, actuen com a unitat d'informació en un sistema binari de codificació. Aquest sistema gaudeix d'una precisió temporal excepcional que permet codificar la informació en seqüències de descàrregues i així emmagatzemar memòria, processar informació o donar resposta a diversos estímuls.

Una qüestió cabdal en neurociència és la relació entre l'activitat neuronal i la fenomenologia emergent característica del comportament humà i animal: Quins són els mecanismes de la consciència? Com s'emmagatzema memòria en el cervell? Generalment s'intenta desgranar cadascuna de les característiques per després associar-les a l'activitat neuronal a diferents escales espai-temporals del cervell. D'aquesta manera es creu que la capacitat d'emmagatzemar memòria és una característica de l'activitat microscòpica del cervell, mentre que a escales més grans la coordinació de l'activitat d'àrees distants del cervell està relacionada amb la cognició i la percepció. La visió que prenem aquí es concentra en estudiar la fenomenologia característica de l'escala mesoscòpica, és a dir, aquella en la que la dinàmica característica ve donada per l'activitat de milers o, fins i tot, milions de neurones. En aquesta escala l'activitat síncrona de grans poblacions neuronals dóna lloc a un fenomen col·lectiu pel qual es produeixen oscil·lacions del seu potencial mitjà. Aquestes oscil·lacions poden ser fàcilment enregistrades mitjançant aparells d'electroencefalograma (EEG) o enregistradors de Potencials de Camp Local (LFP). A més a més, les freqüències mitjanes d'aquestes oscil·lacions poden associar-se a estats mentals prototípics: així, l'enregistrament de senyals EEG d'una freqüència mitjana de 10 Hz a la zona occipital del crani s'ha associat a estats de concentració i meditació, mentre que l'enregistrament de senyals EEG d'uns 40 Hz s'ha relacionat amb estats de consciència i atenció.

Per tal d'entendre millor com les escales microscòpica i mesoscòpica del cervell interactuen, en el Capítol 5 mostrem com la comunicació entre dos columnes corticals (estructures mesoscòpiques) pot ser conduïda de forma eficient per una xarxa neuronal microscòpica. De fet, emprem la *sincronització* de les dues columnes corticals per comprovar que s'ha establert una comunicació efectiva entre les tres estructures neuronals. Els nostres resultats indiquen que hi ha règims dinàmics de la xarxa neuronal microscòpica que afavoreixen la correcta comunicació entre les columnes corticals: així, si la freqüència típica de LFP a la xarxa neuronal està al voltant dels 40 Hz la sincronització entre les columnes corticals és més robusta en comparació amb la situació en què la xarxa neuronal oscil·la a una menor freqüència ($\sim$ 10 Hz). Tanmateix, les característiques topològiques de la xarxa microscòpica també influeixen en la comunicació, essent una estructura de tipus món petit (*small-world*) la que millor afavoreix la sincronització

de les columnes corticals. Per últim, en aquest treball mostrem com la mediació exercida per la xarxa neuronal no pot ser substituïda per la mitjana de la seva activitat, és a dir, les propietats dinàmiques de la xarxa neuronal microscòpica són imprescindibles per a la correcta transmissió d'informació entre totes les estructures neuronals. Aquests resultats, doncs, donen una nova visió sobre els diferents rols que poden tenir les descripcions del cervell a diferents escales.

Una de les característiques més rellevants dels sistemes nerviosos és la presència de cèl·lules neuronals excitadores i inhibitòries. La seva tasca és oposada: les neurones excitadores afavoreixen l'activació elèctrica de les seves neurones veïnes, mentre que les neurones inhibitòries dificulten aquesta activació. A nivell microscòpic s'ha estudiat en detall com les xarxes neuronals estan influenciades pel balanç entre el nombre de neurones excitadores i inhibidores, així com de la força de les seves connexions. Així, l'activitat elèctrica oscil·latòria cerebral ve donada en gran mesura per la interacció entre excitació i inhibició. A més a més certes malalties i dolències mentals, tals com la depressió o l'esquizofrènia, estan associades a un balanç incorrecte entre excitació i inhibició. Malgrat haver estat un focus d'estudi en xarxes neuronals microscòpiques, pocs treballs han centrat l'atenció en saber quina és la dinàmica excitadora i inhibidora a escales més grans del cervell. En el Capítol 6 estudiem com grups de columnes corticals mostren patrons complexos d'excitació i inhibició segons quines siguin les seves característiques topològiques i la força dels seus acoblaments. D'aquesta manera les columnes corticals se *segreguen* entre aquelles dominades per l'excitació i aquelles dominades per la inhibició. A més a més, en aquest capítol estudiem com aquests patrons influeixen en les capacitats de sincronització de xarxes de columnes corticals, la qual està molt relacionada amb les complexes relacions que s'estableixen entre les senyals elèctriques o magnètiques enregistrades en diferents llocs del cervell.

La coordinació de l'activitat de milers o milions de neurones permet l'emergència del fenomen col·lectiu de les oscil·lacions neuronals. Tanmateix, s'ha comprovat que en molts altres sistemes naturals, com les xarxes genètiques, ecològiques o xarxes socials, l'activitat síncrona d'entitats dinàmiques dóna lloc a fenòmens emergents amb característiques completament diferenciades de les dels seus constituents. Es per això que en els darrers anys s'ha estudiat profusament quines són les bases per les quals emergeix la sincronització en sistemes tant variats. En el Capítol 7 estudiem un règim dinàmic, present en les columnes corticals estudiades en el Capítol 6, segons el qual patrons complexos de sincronització apareixen espontàniament en xarxes d'oscil·ladors caòtics. Mitjançant un tractament semi-analític, mostrem quines condicions s'han de donar en un conjunt de sistemes dinàmics acoblats per tal de mostrar heterogeneïtat en la sincronització, és a dir, *coexistència* de sincronitzacions dins d'una mateixa xarxa. D'aquesta manera relacionem els nostres resultats amb el fenomen de sincronització complexa en el cervell, que és un focus d'estudi avui en dia.

Finalment, en el Capítol 8 abordem una de les característiques més estudiades del cervell: la capacitat de *computar* i *processar informació*. La novetat aquí rau en l'ús que fem de la sincronització complexa a nivell mesoscòpic del cervell, per tal d'implementar elements bàsics de computació Booleana. D'aquesta manera, mostrem un possible escenari segons el qual la sincronització parcial de les oscil·lacions cerebrals estableix un codi neuronal en termes de sincronització/no sincronització (que anomenem estats 1/0, respectivament) i, d'aquesta manera, totes les funcions booleanes simples poden ésser implementades (AND, OR, XOR, etc).

Mostrem, també, com emprant xarxes mesoscòpiques extenses les capacitats de computació creixen proporcionalment. D'aquesta manera hipotetizem que funcions Booleanes complexes, com una memòria del tipus *flip-flop*, pot ésser construïda en termes d'estats de sincronització dinàmica d'oscil·lacions cerebrals.

En resum, aquesta Tesi té com a objectiu l'estudi de la dinàmica neuronal a diferents escales del cervell: primerament mostra quines característiques té la comunicació entre l'escala microscòpica i mesoscòpica del cervell, per després aprofundir en l'estudi de diferents característiques de la dinàmica de poblacions neuronals a la mesoescala cerebral . Els resultats que aquí es mostren donen una nova visió sobre el rol de l'excitació i la inhibició en xarxes corticals, caracteritzen la sincronització complexa d'oscil·ladors neuronals i revelen nous mecanismes de computació i de processament d'informació mitjançant la dinàmica oscil·latòria del cervell.

List of Figures

List of Tables

Contents

Part I

Introduction

Chapter 1

The human brain

"Mientras nuestro cerebro sea un arcano, el universo reflejo de su estructura también será un misterio."

Santiago Ramón y Cajal

The human brain is composed of a myriad of coupled neurons and glial cells that interact dynamically. It possesses a rich topological structure and exhibits complex dynamics, operating as a noisy, nonlinear, and highly dimensional system. Neuronal activity evolves at temporal scales ranging from a few milliseconds to tens of seconds, and emerges from neuronal assemblies that extend from micrometers to several centimeters. Due to a complex functional hierarchy between cell groups, the brain is able to store information for long periods of time, process multiple sensory inputs efficiently, and produce coherent output in the form of actions and thoughts.

Even though the brain has been studied for centuries, a full theoretical description of its normal and pathological functioning is still not available. Due partly to the lack of a full description of the anatomical connectivity, and partly to our incomplete knowledge of the interplay between different neural processes, the brain is still the great unknown organ. Its study is usually partitioned into different research sub-areas devoted to distinct brain structures (such as the thalamus, amygdala, hippocampus, etc), cortical functional areas (motor, visual, auditory cortex, etc.) or particular microscopic circuits, from the level of brain areas down to single-neuron responses. Moreover, studies of the global activity of the brain usually focus for convenience on specific cognitive or motor tasks, in order to compare them with a control state such as spontaneous activity at rest.

Lately, modern neuroscience has attempted to gather the biological basis of brain function with theoretical computing paradigms so as to unveil the mechanisms of its complex capabilities. However, there is still a long path towards the full comprehension of the brain features responsible for complex human traits. Thus, forthcoming research must bring together all known aspects of neuroscience - physiology, neuroanatomy and neural computation - in order to formulate an integrated theory of the brain and its behavior that eventually accounts for its prominent emergent dynamics.

Brief historical review: From the brain to the neuron and its dynamics

The study of the human brain has a long tradition in western culture, reaching back to the time of Egyptian mummifications. Although Egyptians did not consider the brain, but rather the heart, to be the locus of intelligence they became interested in the knowledge of its composition due to their practice of removing brain tissue when mummifying. Ancient Greek theories shifted the view towards a brain-based intelligence (Alcmaeon of Croton, 6th and 5th centuries BC, Hippocrates, 4th century BC). During the Egyptian Hellenistic period there were tremendous advances in the investigation of the anatomy and physiology of the brain and the rest of the nervous system's (Herophilus of Chalcedon, c.335/330-c.280/250 BC, Erasistratus of Ceos, c.304 - 250 BC), although, unfortunately, most of the work is now lost.

The most complete early view of brain function was formulated by Galen of Pergamon (AD 129 - c.200/c.216, Roman empire), who assumed that the brain and the nervous system worked like a gland (organ), and thus could be studied as such. He speculated about the processing of sensory information and announced an accurate theory of muscle control that took into account the already known anatomy of the nervous system. This view influenced the study of the brain in western neuroscience for more than a thousand years.

Physiological investigations of the nervous system profusely developed in the modern era (starting from the late 1700s) after the Italian physician and physicist Luigi Galvani (1737-1798) discovered that living excitable muscle and nerve cells produce electricity, showing that the electrical activity of one excited nerve cell affects the activity of adjacent cells in a predictable way (see Fig.1.1).

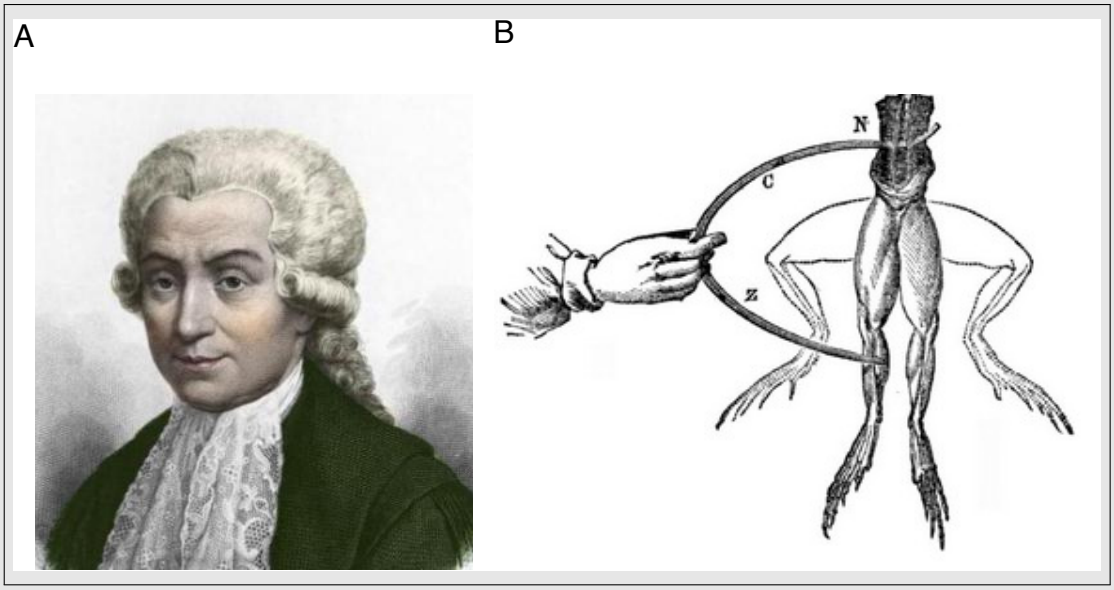

Figure 1.1: Galvani's experiments on animal electrical properties. (A) Portrait of the Italian physicist and physician Luigi Galvani (c.1770). (B) Cartoon depicting the famous Galvani experiment with dead frog's legs. In this case Galvani showed that a closed circuit between a bimetallic arch and the frog's legs produced muscular convulsions. Adapted from *Galvani* [2015].

The invention of the microscope, back in the eighteenth century, made possible to change

the view of the brain tissue from being a continuous fluid a discrete structure of cells. However, it was not until the very end of the nineteenth century when the first detailed descriptions of the cells composing the neural system, the neurons, were announced by both Camilo Golgi (1843-1926) and Santiago Ramón y Cajal (1852-1934) (see Fig.1.2A,B). Golgi developed a method for staining neurons with silver salts that allowed to observe in detail their entire structure under the microscope. Neurons clearly displayed cell bodies and two other major structures: branching *dendrites* (from Greek *dendron* or "*tree*") and a long cable-like *axon* (from Greek "*axis*"). Besides, Ramón y Cajal studied and described the morphology of individual cells, proposing that the structure of nervous tissues was a network of discrete cells. In this sense, he anticipated that the minimal structure for elementary signalling in the nervous system was the neuron and, thus, he was one of the first claimers of the *neuron doctrine* (see Fig.1.2C).

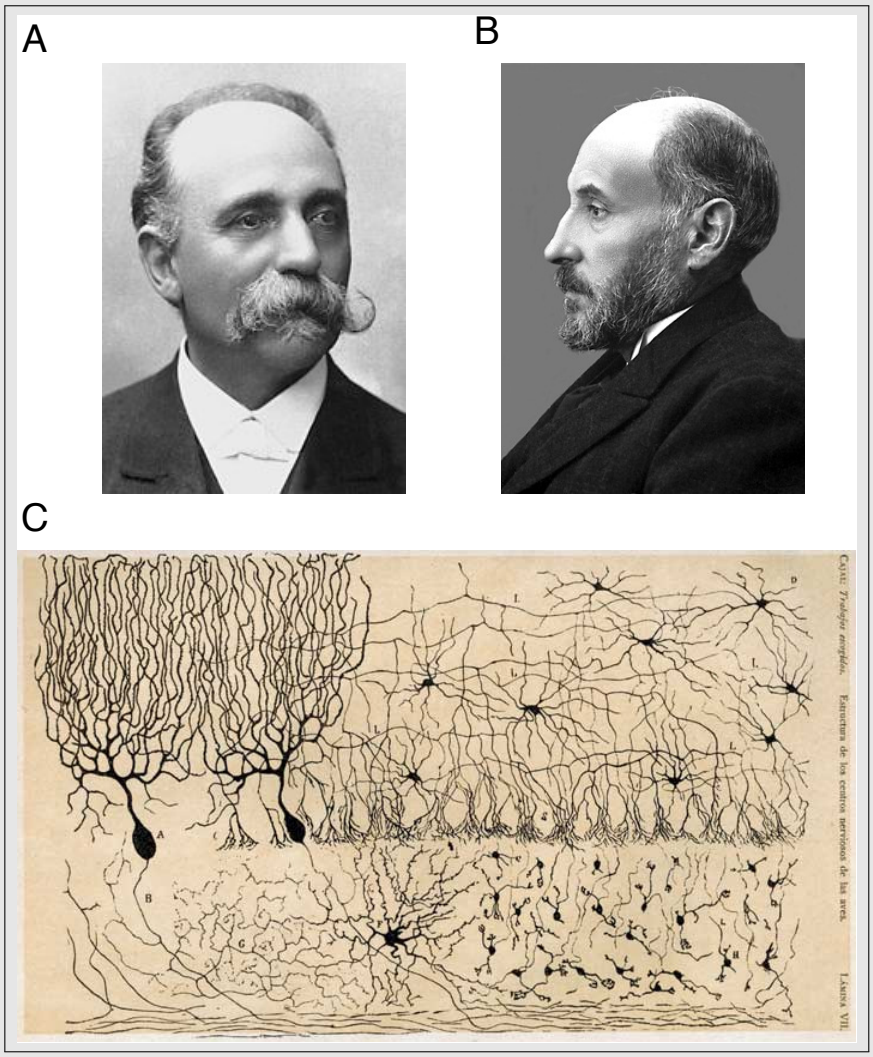

Figure 1.2: Camillo Golgi and Santiago Ramón y Cajal, fathers of the 'neuron doctrine'. (A) Portrait of Camillo Golgi. (B) Portrait of Santiago Ramón y Cajal. (C) Drawing by Ramón y Cajal depicting the structure of several cells that he observed with the help of a microscope. From *Nobel* [1967]; *Neomed* [2013]; *Sotelo* [2003].

The chemical basis of the communication between nerve cells was first described in the mid

XIXth century by Paul Ehrlich, in Germany, Claude Bernard, in France, and John Langley, in England, who demonstrated that drugs do not interact with neural cells arbitrarily but actually do it with selected neurons. It was later discovered that such drugs bind to specific receptors located in the surface membrane of neurons, affecting the overall dynamics of large ensembles of these cells. Besides, the chemical agents responsible for neuronal activation or deactivation were identified as the nowadays called *neurotransmitters*. A large collection of neurotransmitters have been discovered since these seminal studies. For example, *gamma-Aminobutyric acid* (GABA) was first synthesized in 1883, and in 1950 was found to play a role in the central nervous system, specifically by reducing brain excitability. Its counterpart, the *glutamic acid*, or *glutamate* in its ionized form, is the main responsible for neural activation. However, many other chemicals are involved in neural communication (*aspartate*, *dopamine*, *acetylcholine*, etc), endowing neural circuits with versatility in their dynamics.

One of the main goals of early neuroscience research, starting in the late 1800s, was to bring together biological and psychological concepts in the study of behavior. In this sense, many new ideas were proposed to gather biological evidence – with neuroanatomy, neurochemistry and neurophysics on its basis – and complex behavioral traits in a unique theory of brain and mind. One of the very first ideas, proposed by the german physician Franz Joseph Gall (1758-1828) postulated that particular regions of the cerebral cortex, the outermost part of the brain, controlled specific functions and so it was divided into several adjoined *organs*, each corresponding to a concrete mental faculty. He also stated that these areas, each one associated with a behavioral trait – generosity, religiosity, kindness, etc. – grew with use, creating a pattern of bumps and ridges easily indicating the most developed brain regions and so mapping anatomy and behavior. His method became known as *phrenology* (from Greek *phren*, mind, and *logos*, knowledge, see Fig.1.3A).

Gall's ideas were put in doubt when experimental evidence showed that lesions in specific brain sites did not affect specific behaviors. The french physiologist Pierre Flourens (1794-1867) showed that all brain regions, rather than specific ones, participated in every mental operation and, thus, any part of the cerebral hemisphere was involved in cognitive tasks. However, Gall's hypotheses were the basis for posterior advances in relating cognition and brain.

The french neurologist Pierre Paul Broca (1824-1880) was very much influenced by Gall's theories in the sense that functions could be localized in the brain. In the mid 1800s he extended Gall's thoughts by establishing a new experimental approach: the examination of damages to the brain produced by clinical lesions. To do so he studied cases of patients with *aphasia*, a language disorder in which subjects are capable of understanding what they are being told, but are unable to speak. Post-mortem analysis of such cases showed lesions in the posterior region of the frontal lobe, now called *Broca's area*, located in the left cerebral hemisphere.

Following up the work by Broca and others, the german neurologist and psychologist Karl Wernicke (1848-1905) developed a theory in which the most basic mental functions were distributed throughout the cerebral cortex. In particular, those related with simple perceptual and motor activities were localized in single areas of the cortex. In turn, he stated that more complex cognitive functions arise from interconnections between several functional sites. By gathering the principles functional localization with a connectionist framework, Wernicke anticipated that

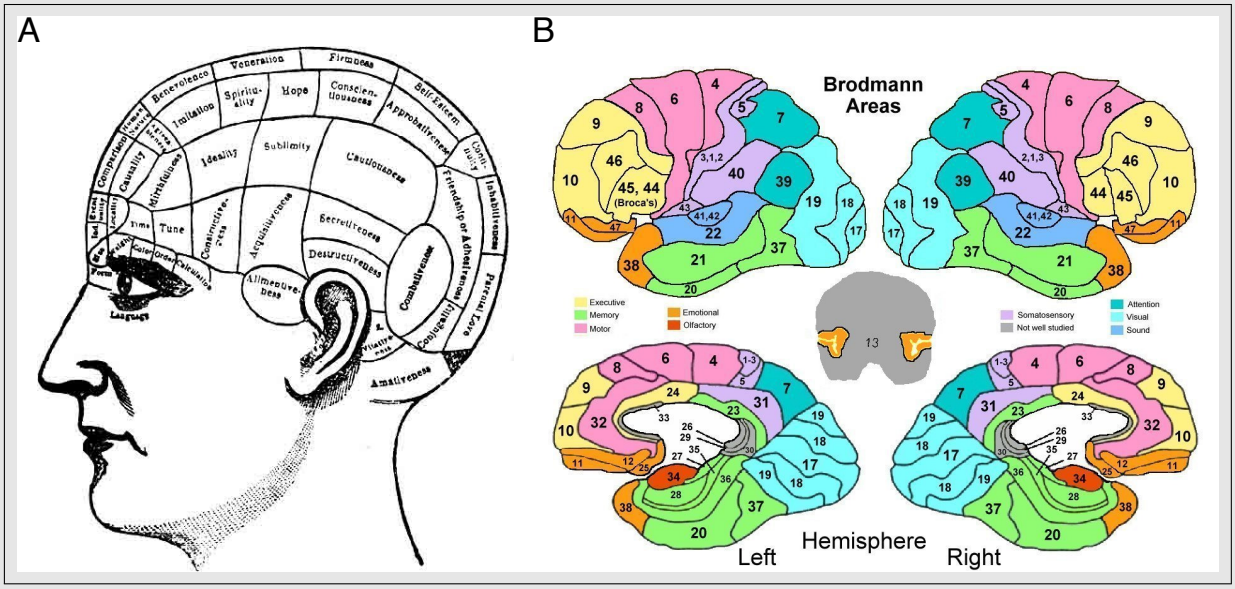

Figure 1.3: Functional parcellation of the human brain. (A) Cartoon depicting a phrenologist parcellation of the brain surface. Each division is related with a complex human feature. (B) Classification of brain areas under the Brodmann criterion. Each color indicates the main functional properties of these areas. From *Kandel* [2013]; *Kaiser* [2015]; *Brodmann* [1909]

different aspects of a single behavioral trait are processed in different regions of the brain, advancing the modern idea of *distributed processing*. Wernicke developed these ideas by focusing to a very precise cognitive task: language. He argued that language involves separate motor and sensory areas, located in different cortical regions. Thus, the complex task of speaking involves the recruitment of Broca's area, responsible for motor control of the tongue, vocal cords, etc, and a sensory area, responsible for word perception and located in the temporal lobe (now called Wernicke's area). Further research indicated the recruitment of a group of brain areas, collectively known as *association cortex*, which integrates auditory, visual and somatic stimuli into complex perceptions.

At the beginning of the XX^{th} century, the ideas of Karl Wernicke were taken as the basis for the classification of different functional areas of the cortex, deriving from variations in the structure of cells and their arrangement, using a method called *cytoarchitecture*. The german neurologist and anatomist Korbinian Brodmann (1868-1918) parcelled the human cortex into 52 anatomically and functionally distinct areas, which are widely used nowadays – with constant updating –. Several areas defined by Brodmann have been found to control very specific brain functions (e.g. the primary visual cortex, responsible for processing visual signals, matches with area 17; areas 41 and 42 encompass the primary auditory cortex; areas 1, 2 and 3 conform the primary somatosensory cortex, which receives stimuli from bodily sensation, see Fig.1.3B).

A great step forward in the study of the cerebral cortex and its structure came in the early XX^{th} century with the introduction of noninvasive recording techniques. Hans Berger (1873-1941) developed in 1924 a scalp electrical recording device which is still nowadays the most widespread method used in clinical and psychological laboratories, the *electroencephalogram* (EEG,

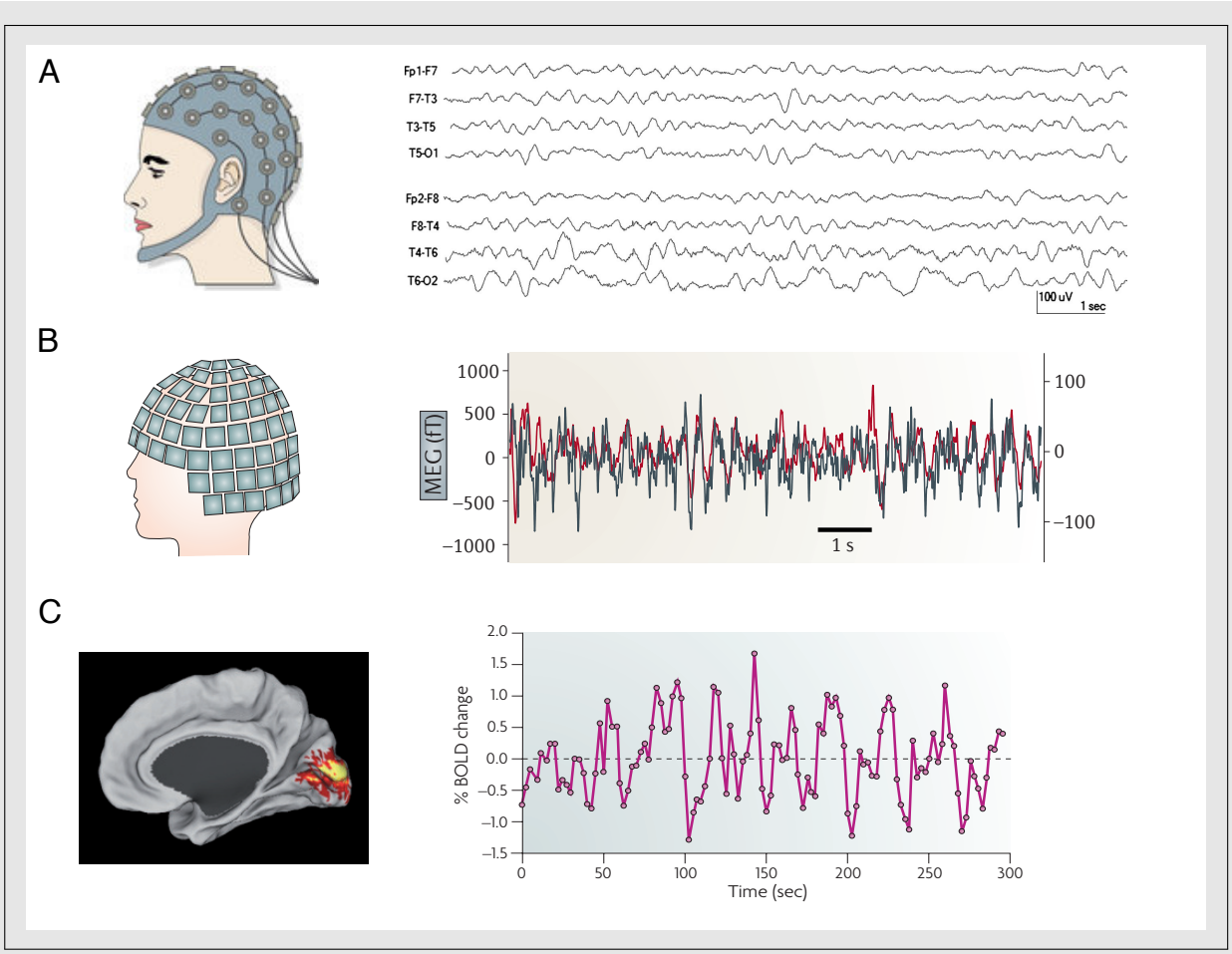

Figure 1.4: Non-invasive brain recording techniques. (A) Cartoon depicting an EEG recording helmet (left) and eight typical EEG time traces (right). (B) Cartoon depicting a MEG recording helmet (left) alongside with two typical MEG time traces (right). (C) Computer image of a functional magnetic resonance image (fMRI) based on Blood Oxygenation Level Dependent signal (BOLD, left) and a typical time trace (right). These signals display increases in oxygen levels in blood flowing through brain tissues. From *Britannica* [2014]; *EEG* [2014]; *Buzsáki et al.* [2012]

Fig.1.4A) [*Adrian and Matthews*, 1934]. This method entails an excellent temporal resolution, in the range of the millisecond, but a rather poor spatial resolution, of about a centimeter. Therefore, the activity reflected in EEG recordings results from the average behavior of large populations of neurons. From a theoretical point of view, the spatiotemporal integration problem of neuronal activity, arising from EEG-like activity, is similar to that of the statistical mechanics in physics because the details of the neuronal interactions are replaced by the average behavior, or *mean field*. In the late XX^{th} century a myriad of novel noninvasive techniques appeared, e.g. the magnetoencephalogram (MEG, 1.4B), functional Magnetic Resonance Imaging (fMRI, 1.4C) or Positron Emission Tomography (PET). Such techniques allow for the study of (healthy) subjects without the need of a surgical intervention, and thus allows for highly controlled experimental conditions. These advanced neuroimaging tools allow for a better spatial precision than the EEG

and, thus, a better characterization of precise brain region responses can be undertaken.

Nowadays a growing interaction between imaging and recording techniques has is enabling to propose new projects aim to understand to construct realistic whole brain simulations. One of such projects is the *Blue Brain Project*, which intends to understand brain dynamics by simulating the human cortex from a molecular level [*Markram et al.*, 2015]. The *BRAIN Initiative* (Brain Research through Advancing Innovative Neurotechnologies) is a counterpart project with the goal of providing a deeper understanding of brain dynamics through mapping the activity of neurons in mice or other animals, to later achieve a "functional connectome" that eventually may be applied to the study of the human brain.

1.1 General structure of the central nervous system

The central nervous system possesses seven main parts: the *spinal cord*, the *pons*, the *medulla oblongata*, the *cerebellum*, the *midbrain*, the *diencephalon* and the *cerebral hemispheres*. The latter are commonly grouped into three broader regions: the *hindbrain*, the *midbrain* and the *forebrain* (see Fig. 1.5A).

The **spinal cord** receives and processes sensory input coming from the skin, muscles and other bodily structures, and controls movement of the limbs and the trunk. It can be divided into cervical, thoracic, lumbar and sacral regions and extends into the *brain stem*, which comprises the medulla, the pons and the midbrain. Moreover, they convey information from the spinal cord to the brain and vice versa. The **pons** carries information about movement from the cerebral hemispheres to the cerebellum. It relays signals from the forebrain to the cerebellum, and it contains the *pneumotaxic center*, which regulates the change from inhalation to exhalation among other functions. The **medulla oblongata** connects higher levels of the brain to the spinal cord and includes centers responsible for vital autonomic functions, such as breathing, the control of heart rate, digestion or blood pressure. The **cerebellum** is a crucial structure involved in motor control and higher cognitive functions such as attention and language. It lies behind the pons and is connected to the brain stem by fiber tracts called *peduncles*. Besides, it conveys input from sensory systems of the spinal cord and other brain sites and later integrates this information to coordinate motor activity. It is composed by several types of neurons arranged in a regular manner, the most important being the Purkinje and granule cells.

The **midbrain** controls sensory and motor functions such as eye movement or visual and auditory reflexes. The **diencephalon** contains two main structures: the *thalamus*, which processes most of the information reaching the cerebral cortex from the rest of the central nervous system, and the *hypothalamus*, which is responsible for most of the autonomic, endocrine and visceral function. Finally, the **cerebral hemispheres** comprise four structures: the *cerebral cortex*, which is the wrinkled outermost layer responsible for most of the higher cognitive functions (Fig. 1.5B), the *basal ganglia* – involved in movement control –, the *hippocampus* – which is part of the limbic system and deals with physiological responses, memory and most prominently in the control of head direction and position in space – and the *amygdaloid nuclei* which also deal with endocrine and emotional responses.

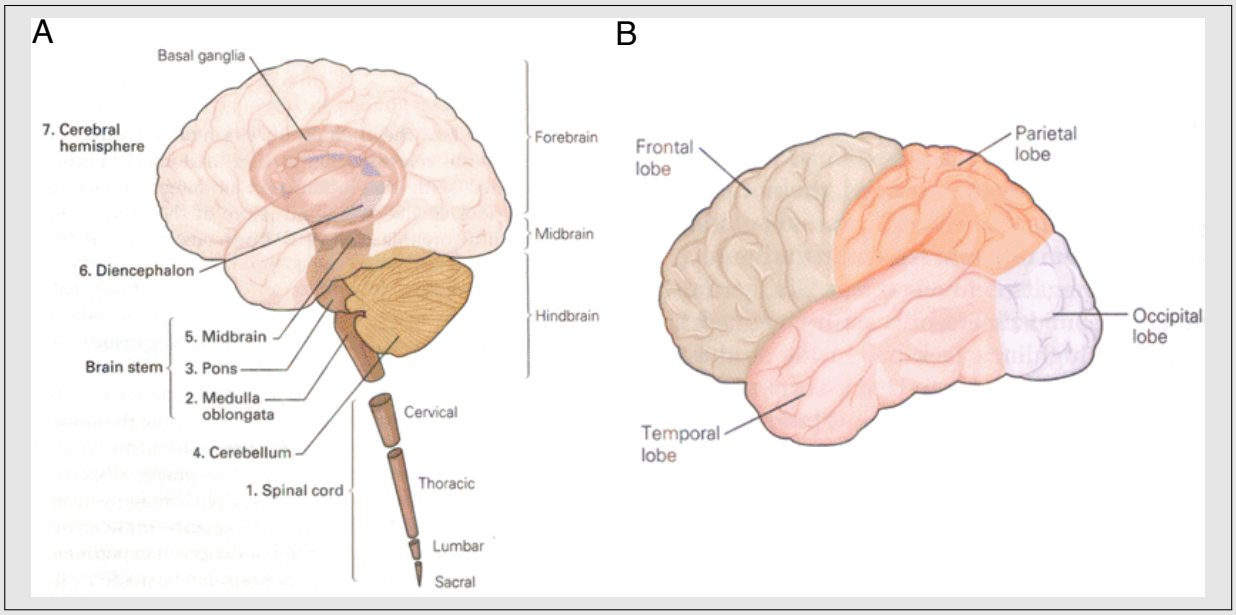

Figure 1.5: Structure of the brain and spinal cord. (A) Cartoon showing the structure of the central nervous system, comprising the brain and the medulla. (B) Division of the human brain into functional lobes, i.e. frontal, parietal, occipital and temporal. From *Kandel* [2013].

1.2 The cerebral cortex and cortical columns

The brain operations responsible for the human cognitive abilities take place primarily in the *cerebral cortex*, which is the outermost wrinkled structure of about 2.4mm in thickness that covers the two brain hemispheres. Each hemisphere is in turn subdivided into four anatomical distinct lobes: *frontal*, *parietal*, *temporal* and *occipital* (see Fig. 1.5B). There is clear evidence that these lobes have specialized functions, for instance , the occipital lobe is concerned with visual stimuli, the parietal lobe processes somatic sensation, the frontal lobe is involved with planning future actions and the control of movement and the temporal lobe is related with hearing and with aspects of learning, memory and emotions through its connections with deeper structures – amygdaloid nuclei and hippocampus –.

The structure of the cerebral cortex presents characteristic foldings. The current hypothesis tells that such foldings result from an evolutionary strategy for embedding more cells in a limited volume. Besides, the different folded parts of the cerebral cortex have distinct names: the crests are called *gyri*, while the deepest parts are called *sulci* or *fissures*. Moreover, the cortex has a particularity when processing information: each hemisphere is concerned with the stimuli conveyed by the contra-lateral side of the body, for instance sensory information coming through the spinal cord from the left hand is processed in the right hemisphere. However, although the hemispheres are similar in appearance, they are not completely symmetrical in structure and, thus, not equivalent in function. This fact has implications in the way humans process complex inputs and produce complex responses.

The lobes in the cortex can be ulteriorly parcelled into several small regions displaying cytoarchitecturally distinct patterns – related with the Brodmann areas mentioned above –,

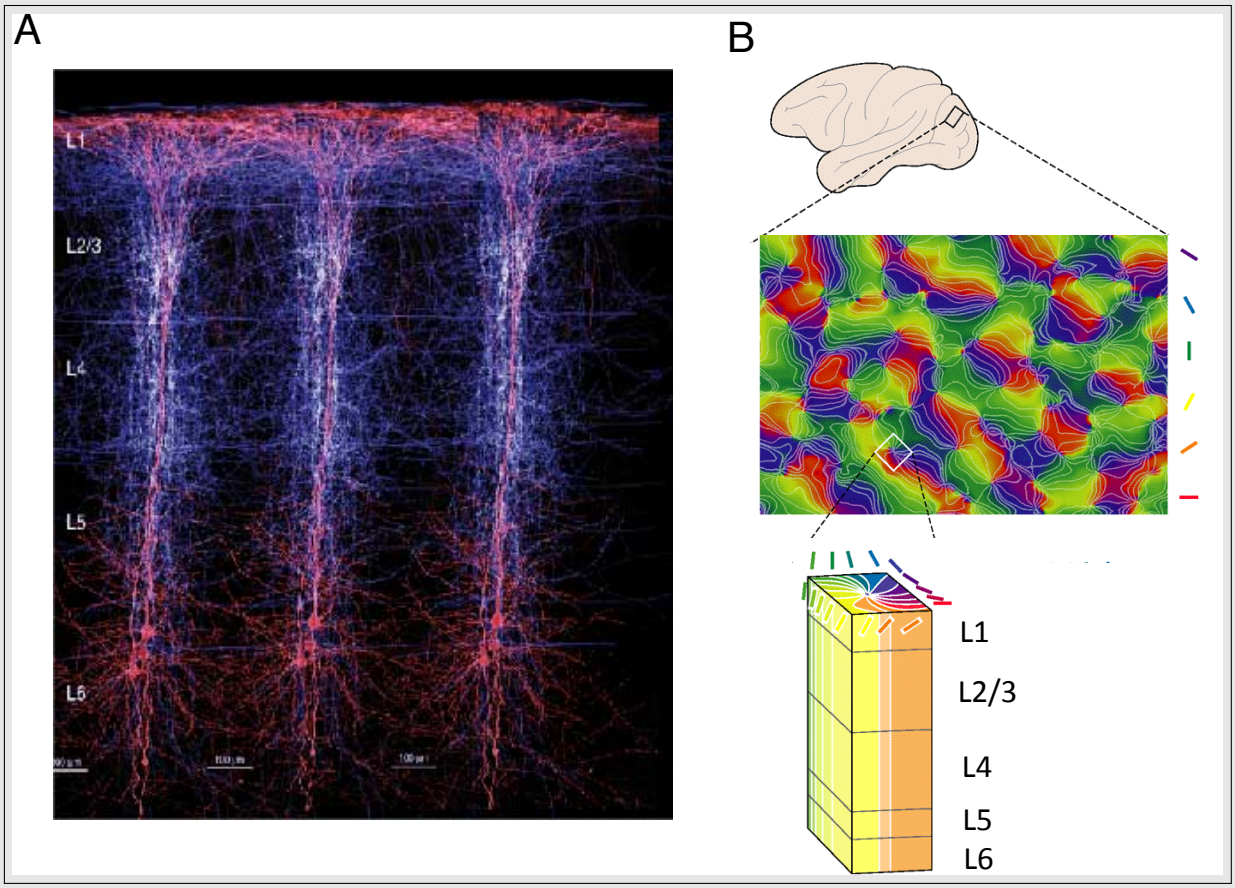

Figure 1.6: Structure of the brain cortex and cortical columns. (A) Schematic reconstruction of 3 neighboring cortical columns with highlighted layered organization. Each column displays cells bodies in deep layers 5 and 6 (pyramidal cells), whereas cell axons and dendrites arrange in a vertical manner reaching superficial layers 1, 2 and 3. Color coding represents cell bodies (reddish) and axons (whitish). (B) Representation of a macaque brain with a highlighted patch of the cortex showing the orientation preference -triggering a response in the corresponding receptive field- to visually presented bars (see color coding). A cortical macro column, which codes all orientation preferences, can be extracted from the visual cortex patch, as shown in the bottom image. From *Kandel* [2013].

which are in turn related with functional specificities. These small patches of the cortex also posses an anatomical substructure that extends into deeper layers: the **cortical column** (Fig. 1.6A). Cortical columns emerge as morphological structures composed by groups of neurons divided into layers that extend parallel to the cortex surface. Besides, and most importantly, they posses nearly identical *receptive fields* – i.e. a given type of stimulus triggers the firing of the whole set of neurons comprising a column, Fig. 1.6B –. Such feature allows to tessellate the cortex in terms of functional responses of groups of neurons within a cortical column.

The columnar structure of the cerebral cortex was initially described by Lorente de Nó (1902-1990) [*de No and Fulton*, 1938] as a morphological unit, usually referred to as "minicolumn", formed by several tens of neurons [*Buxhoeveden and Casanova*, 2002; *da Costa and Martin*, 2010]. The particular structure of cortical minicolumns was discovered by Vernon Mountcastle

(1918-2015) while recording from a cat somatosensory cortex [*Mountcastle*, 1957], who noted that all cells at a given vertical electrode penetration responded either to superficial or deep stimulation. It appeared that for a common receptive field location (e.g. the cat's foreleg), cells were segregated into domains representing different sensory modalities. By making multiple, closely spaced penetrations, Mountcastle concluded that individual minicolumns are no more than 500 mm wide. The existence of a strong interaction between several tens of minicolumns into a larger functional unit was initially recognized in the motor system, extended to the entire neocortex [*Mountcastle*, 1997] and referred to as "hypercolumn" in the visual cortex [*Hubel and Wiesel*, 1977] and "macro column" in general [*Rockland*, 2010]. The mesoscopic neuronal populations belonging to cortical macrocolumns composed of thousands of neurons exhibit coherent dynamical responses to sensory [*Petersen et al.*, 2003] and thalamic [*Swadlow et al.*, 2002] stimuli. Sensory stimulation has also been seen to lead to coherent oscillations between neighboring macrocolumns [*Eckhorn et al.*, 1988]. These observations indicate that brain dynamics can be studied (at least partly) at a scale in which averaged dynamical responses of large groups of neurons explain the observed dynamics, as we will show later.

1.3 Neurons and neuronal circuits

The brain contains a wide variety of neuronal (and glial) types of cells in terms of their morphology and physiology (see Fig. 1.7A), as well as dynamics (see Fig. 1.7B). In this sense, some neurons develop only a few dendrites, whereas other cells (e.g. Purkinje neurons) possess extensive dendritic trees, which makes the human cortex appear as a dense network of neurons, and enables the brain to function as the center for learning, reasoning and memory, among other features [*Gilbert*, 1985].

Neurons are the cells responsible for encoding, transmitting and integrating signals originating inside or outside the nervous system. Neuronal communication is mediated by changes in the so-called *membrane potential*, which is the electrical potential of the neurons at rest. Nerve cells connect to each other through synapses, which arbitrate the exchange of neurotransmitters. In turn, the action of these chemicals causes transient changes in the membrane potential of the downstream connected neuron, called *postsynaptic potentials*. Such potentials are generated by the flux of ions between intracellular and extracellular space, through ion channels present in the membrane, causing an integrative effect that translates into an impulse-like response (spike) whenever a threshold is reached. Spikes, or action potentials, are the units of information transmission at the interneuronal level. Information may be encoded either by the frequency of impulses (i.e. rate coding) or the their timing (i.e. temporal coding).

Learning and memory are associated with changes in the connectivity between neurons, paradigmatically defined as modulation of synaptic efficacy. However, network dynamics is also crucially determined by complex interactions between intrinsic neuron properties, and thus synaptic efficacy does not act as the sole agent for learning and memory. In particular, the strength of synaptic conductivity changes in real time depending on the neuron's activity, making neural circuits "*plastic*" [*Engel et al.*, 2001b]. Plasticity emerges in the form of long-term potentiation and depression of synapses, involving increased or decreased conductivity, which imply an overall increased or decreased activity over time. Such activity can be at the basis for

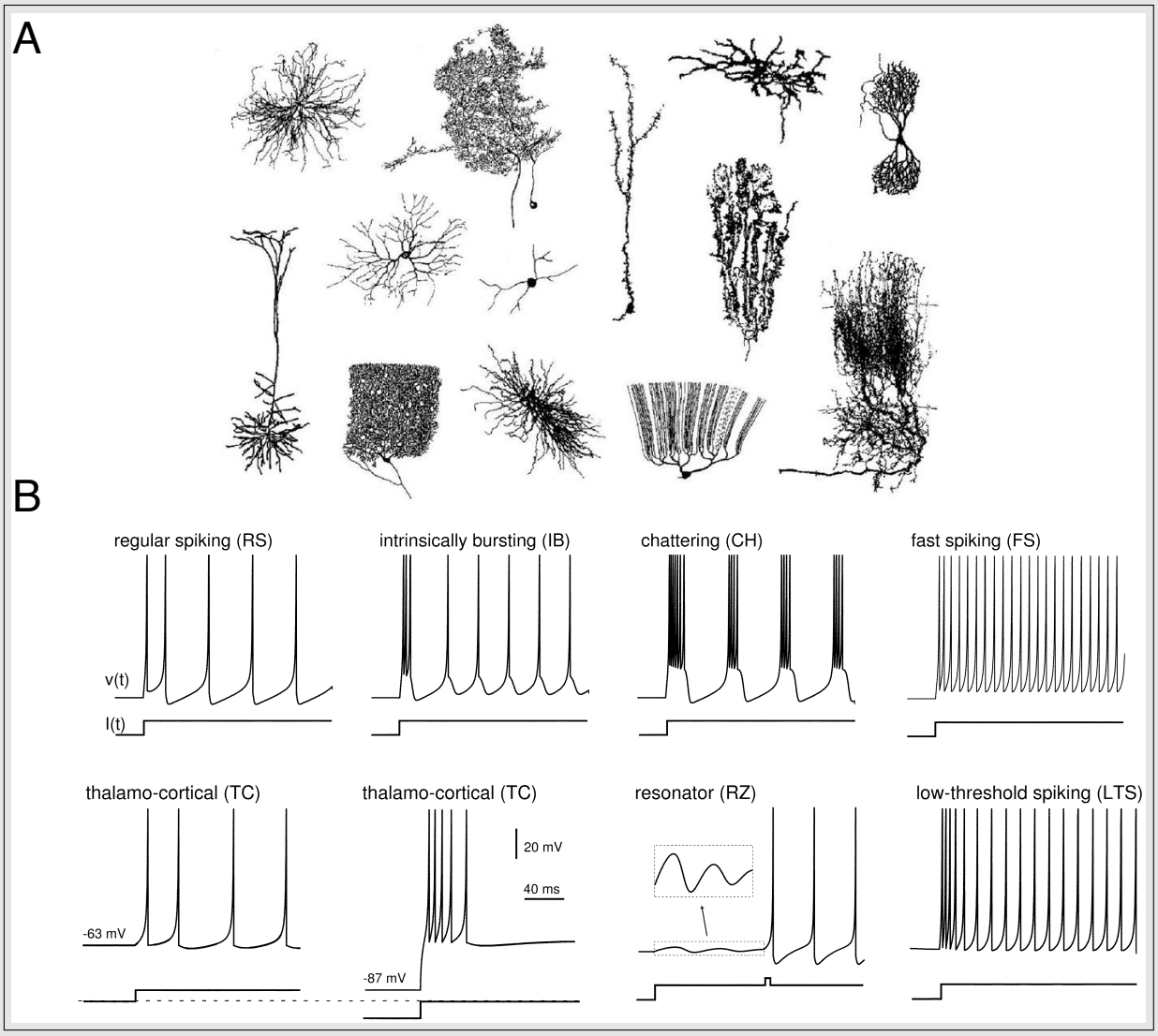

Figure 1.7: Neuronal morphology and dynamics. (A) Drawings of different neuronal types, showing the structural diversity of neural cells. (B) Neurons are excitable cells displaying a wide repertoire of dynamical behaviors in terms of their membrane potential. Depending on their intrinsic characteristics, neurons can fire regularly, or in bursts, or they can resonate while in their sub-threshold state. From *Rabinovich et al.* [2006]; *Izhikevich* [2004].

the implementation of several learning rules which may depend on spike timing, e.g. *Short-term Synaptic Plasticity* (STDP) [*Baudry et al.*, 2000], or rate, e.g. Rate-based Hebbian Learning. Finally, memory paradigms may also be implemented in large neuronal networks by means of synaptic plasticity combined with learning rules, such in the case of *working memory* or even *long-term memory*.

The anatomical mapping of the (human) brain is not yet well established. From the microscopic scale, neurons form intricate networks that can be tracked both *in vivo* and *in vitro* by calcium imaging [*Göbel and Helmchen*, 2007; *Orlandi et al.*, 2014]. In turn, these networks form populations that may be arranged under certain well defined anatomical structures, as in the

case of cortical columns. Besides, distant brain sites may also be connected structurally, forming the so-called *white matter*, as revealed by diffusion tensor imaging techniques [*Horn et al.*, 2014] (see Fig.1.8A).

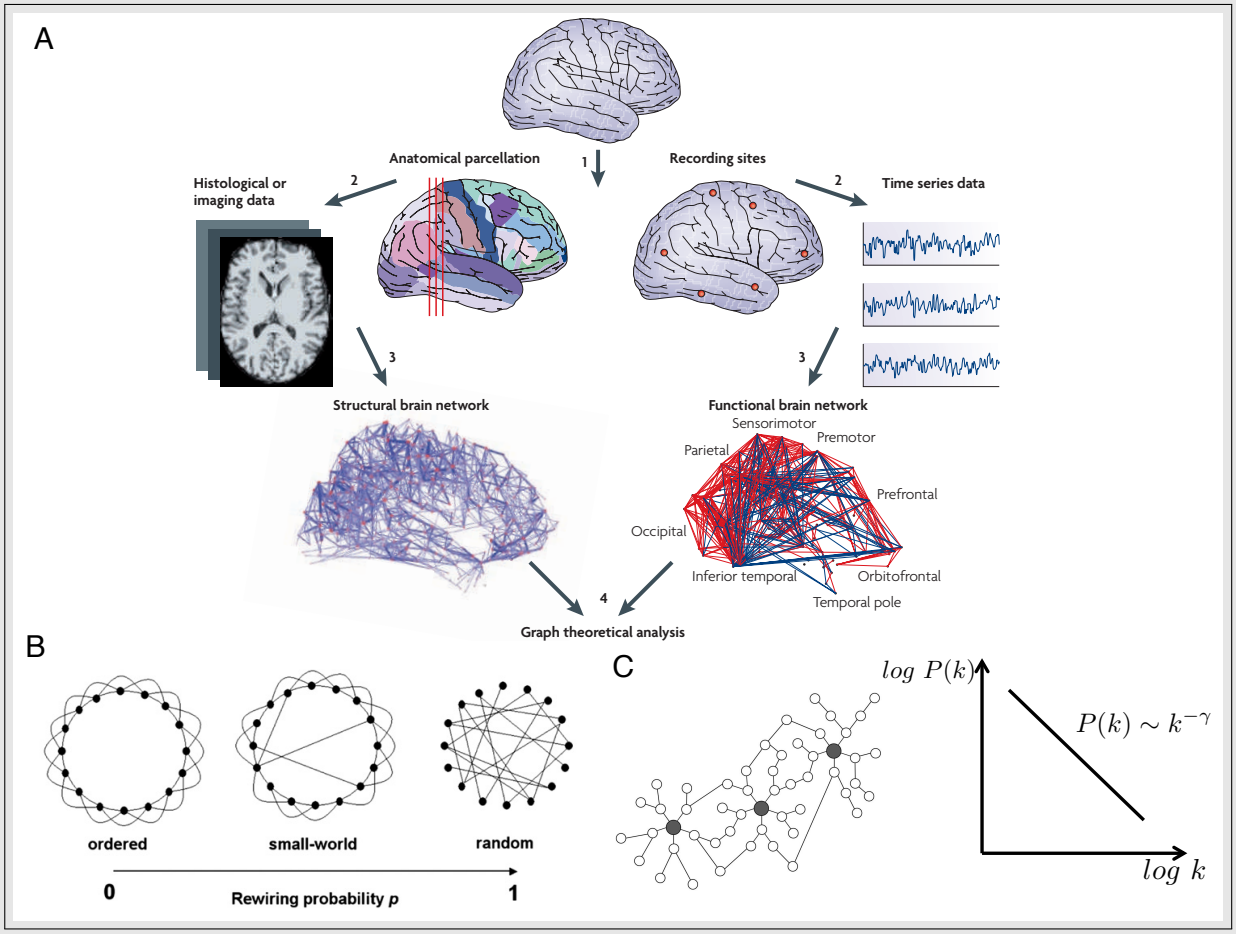

Figure 1.8: Graph theoretical analysis of brain networks. (A) Brain networks may be studied in terms of their structure (left) or functionality (right). From the structural point of view it is necessary to gather enough histological and anatomical data and combine it with imaging so as to construct precise structural networks to later analyze using graph theoretical tools. Functional networks are constructed after tracking correlations between different recordings (time series) extracted from specific brain sites. The emerging networks are later analyzed using graph theory. (B) Certain brain networks appear to possess small-world characteristics, which makes them lie in between ordered and random networks. (C) Scale-free networks have a hierarchy of highly connected nodes, with high degree (gray), and weakly connected nodes, with low degree (white), characterized by a power-law relationship between the connection probability and the number of links in the network (right side of the panel). From [*Bullmore and Sporns*, 2009; *Ponten et al.*, 2010].

From the dynamical point of view, the correlated activity of adjacent or distant neuronal groups allows to construct *functional connectivity maps*, based on the analysis of electrical signals [*Bullmore and Sporns*, 2009] emerging from their co-activation (see Fig. 1.8A). Moreover, information flow analysis of neuronal ensembles reveals the *effective connectivity* between brain

sites and its structure [*Zhou et al.*, 2006], as it relies in causality indicators upon stimulus onset.

Structural or functional connectivities may show precise topological features. For instance, at the microscopic scale it has been proven that neurons arranged in a *small-world* topology support self-sustained activity [*Roxin et al.*, 2004], whereas the scale of brain areas functional networks appear to display the same topology [*van den Heuvel et al.*, 2008]. **Small-world** networks were characterized in the seminal work by Watts and Strogatz [*Watts and Strogatz*, 1998] as arrangements of a majority of short-range connections with a certain probability of long projections onto far neighbors (see Fig.1.8B). Such feature shortens the *path length*, and thus allows shortcuts in information flow. However, when long projections are favored against short-range connections, small-world networks become **random** arrangements which still allow for an accurate signal propagation and logic gating [*Vogels and Abbott*, 2005] as well as synchronous firing [*Mehring et al.*, 2003].

Experimental evidence from functional Magnetic Resonance Imaging (fMRI) or EEG/MEG has also revealed a hierarchical organization of functional brain areas that can be described in terms of *scale-free* networks [*Eguíluz et al.*, 2005]. In **scale-free** networks the hierarchy is established in terms of the number of neighbors of each node, the *degree*, which follows a power-law distribution (see Fig. 1.8C). Thus, some nodes in such arrangements are much more connected that others, becoming essential in information routing across the network. Barabási and colleagues summarized the emergence of scale-free networks with a preferential attachment rule [*Barabási and Albert*, 1999]: any new node added to the network will tend to connect to those nodes with higher degree. Such networks appear to be resilient to random injuries, which may be a crucial feature in brain networks for preserving functionality upon structural degradation [*Pons et al.*, 2010; *Castellanos et al.*, 2011].

1.4 Excitation/Inhibition balance

Nerve impulses are processed by the neuronal networks of the central nervous system. In these networks, each neuron may be connected to several neighbors acting in two opposite ways: either exciting or inhibiting the cells downstream connected. This excitation and inhibition activity is produced by chemical synapses, so an excitatory synapse is the one in which a presynaptic action potential - produced in a presynaptic neuron -, increases the probability of occurrence of a postsynaptic action potential - in the postsynaptic neuron -, by means of an increase in the membrane potential or *depolarization*. On the other hand, in an inhibitory synapse such probability decreases, by means of a reduction of the membrane potential or *hyperpolarization*. The interplay between the excitatory and inhibitory inputs towards a neuron is at the basis of action potential generation. In a chemical synapse, the vesicular release of neurotransmitters from a presynaptic neuron onto the synaptic cleft and posterior uptake by the postsynaptic neuron receptors is responsible for either the *excitatory* or the *inhibitory postsynaptic potentials*. Potentials can also be generated by direct contact between cells through the so-called *gap junctions*. The postsynaptic response of neuronal cells is highly dependent on the temporal precision of the presynaptic potentials. Besides, the magnitude of the cellular response is quantified in terms of the changes in the conductance, depending on time and the magnitude of the depolarizing input (see Fig. 1.9A). The combined action of one excitatory and one inhibitory neuron is depicted

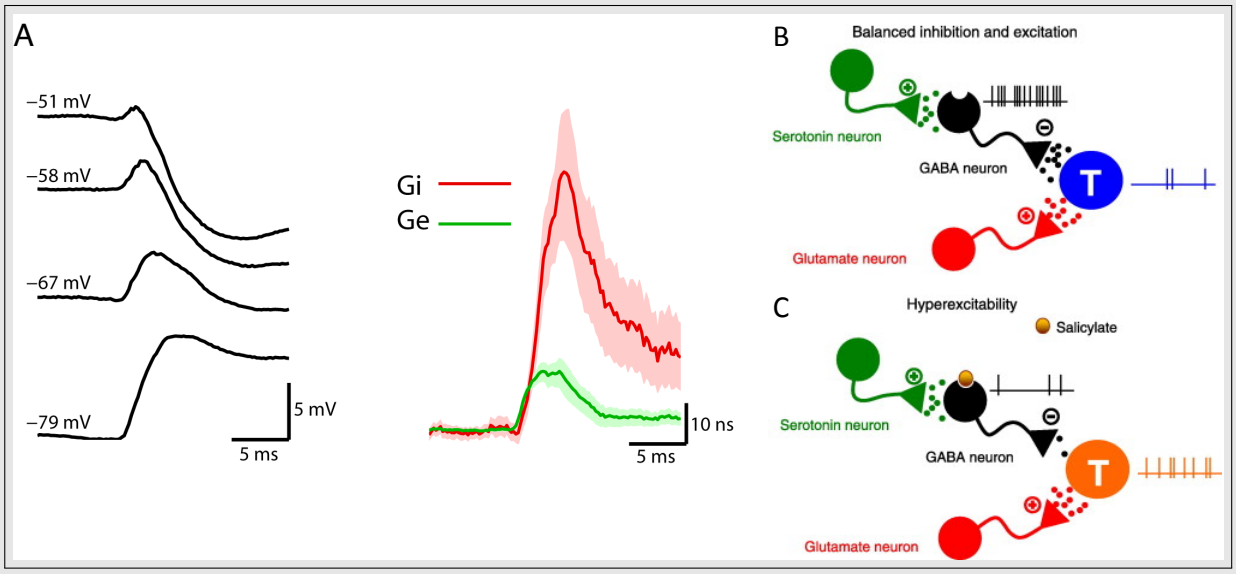

Figure 1.9: Excitation and inhibition in the brain. (A) Different excitatory or inhibitory currents provoke distinct impulse responses in the postsynaptic conductance. This can be summarized with the average response for excitatory neurons (G_e, green line) and inhibitory neurons (G_i, red line). These average impulse responses are taken as the integration core of excitatory and inhibitory neurons as well as the kernel for population dynamics input integration in mesoscopic systems [*Freeman*, 1975; *Jansen et al.*, 1993]. (B) The balance between excitation and inhibition can be sketched as follows: the combined action of one inhibitory GABAergic neuron (black) and one excitatory Glutamaergic neuron (red) onto a target neuron (blue) allows its correct spike response when the GABA neuron receives the excitatory influence of a serotoninergic neuron (green). (C) The action of a drug (salicylate) inhibiting the inhibitory GABAergic neuron entails the reduction of inhibition onto the target neuron and, consequently, an over excitatory influence that translates into an abnormal high firing behavior (orange). From *Okun and Lampl* [2009]; *Wang et al.* [2008]

in Fig. 1.9B and C, where changes in the balance between excitation and inhibition convey dramatic changes in the firing frequency of a target neuron.

One of the first proponents of the important role of excitation and inhibition in nerve tissue was sir Charles Scott Sherrington (1857-1952) who focused on the mechanisms by which excitatory and inhibitory processes interact to control the output of a pool of motoneurons [*Breathnach*, 2004]. He observed that reflex contractions in certain muscles, after decerebration, could be cut or enhanced by sensory stimulation, which he thought to be mediated by certain "inhibitory" and "excitatory" action, respectively. Excitation and inhibition seemed to act oppositely when applied to the same neuronal tissue, an observation that anticipated the discovery of synaptic excitation and inhibition and its chemical basis, revealed by 1936 Nobel prize recipients Otto Loewi (1873 - 1961) and Henry Dale (1875 - 1968). Besides, in 1922, T. Graham Brown (1882 - 1965) proved an asymmetry between the strength of excitation and inhibition in the flexion-reflex and extension-reflex experiments already conducted by Sherrington, producing diverse dynamical behavior when tuning the balance between excitation and inhibition. Indeed, the interaction between excitation and inhibition in the cerebral cortex is the responsible for emergent patterns

of activity [*Douglas et al.*, 1989]. Much effort has been devoted to understand the role played by the excitatory/inhibitory balance (understood as an equilibrium either among neurons within a network, or along time in a given neuron) to control the neuronal dynamics and to achieve regular and irregular synchronization at the cellular level [*Douglas et al.*, 1989; *van Vreeswijk and Sompolinsky*, 1996; *Hill and Villa*, 1997; *van Vreeswijk and Sompolinsky*, 1998; *Singer*, 1999; *Iglesias et al.*, 2005; *Morrison et al.*, 2007; *Roudi and Latham*, 2007].

The presynaptic irregularities generate extremely complex and non-trivial effects on postsynaptic neurons through inhibitory synapses even in the presence of constant inputs [*Segundo et al.*, 1976; *Kohn et al.*, 1981; *Segundo*, 2003]. Functionally, control in the excitation/inhibition balance is known to underlie a wide range of phenomena including sensory adaptation [*Higley and Contreras*, 2006; *Heiss et al.*, 2008], slow-wave sleep [*Haider et al.*, 2006], signal tuning [*Wu et al.*, 2006, 2008], motor control [*Berg et al.*, 2007], sound localization [*Magnusson et al.*, 2008], synchronization of brain waves [*Malagarriga et al.*, 2015b], and information processing [*Malagarriga et al.*, 2015a] among many other behaviors.

1.5 Neuronal oscillations and rhythms

Since the seminal discoveries by Hans Berger in the early XX^{th} century, numerous studies have reported the presence of oscillations in the brains of different mammalian species. These rhythms span from very slow oscillations with periods of minutes to very fast oscillations with frequencies of up to 600Hz. Following Berger's naming of his discovered brain waves, subsequent frequency bands were labeled by using Greek letters, with boundaries among them drawn rather arbitrarily. Thus, the frequency bands are named delta (δ - 0.4 to 4 Hz), theta (θ - 4 to 8 Hz), alpha (α - 8 to 12 Hz), beta (β - 12 to 30 Hz) and gamma (γ - >30 Hz) (see examples in Fig. 1.10A).

The relationship between the different rhythms can be unveiled by plotting the frequency bands in increasing order of frequency. In this way, a general principle emerges: discrete oscillation bands form a geometric progression of a linear frequency scale and a linear progression on a natural logarithmic scale (see Fig. 1.10B). Such classification allows to state that all frequencies ranging from 0.02 Hz to 600 Hz are continuously present in the brain. Each oscillatory cycle defines a temporal processing window, signalling the beginning and end of the encoded information. The period of the oscillation determines the temporal windows of processing, which comes often determined by the size of the neuronal pool involved. Thus, different frequencies favor different types of connections and different levels of computation. Fast oscillations, for instance, favor local integration whereas slow oscillations are related with the processing capability exhibited by distant neuronal groups in distinct structures for obtaining a global consensus. Even though the different oscillatory rhythms may have different synchronization properties [*Kopell et al.*, 2000], they have been explained as a result of the balance between excitatory and inhibitory neurons [*Börgers and Kopell*, 2003; *Börgers et al.*, 2005]. In turn, this synchronous firing may subserve complex coordinated patterns of spiking activity which may be transmitted in large neural networks with high temporal accuracy over long distances [*Abeles*, 1991; *Rodriguez et al.*, 1999; *Abeles et al.*, 2004; *Asai et al.*, 2008; *Asai and Villa*, 2012; *Barardi et al.*, 2014b]. Such collective dynamics throughout the different scales in the brain is likely to determine the functional role of normal and aberrant synchronization mechanisms during adaptive and cognitive processes

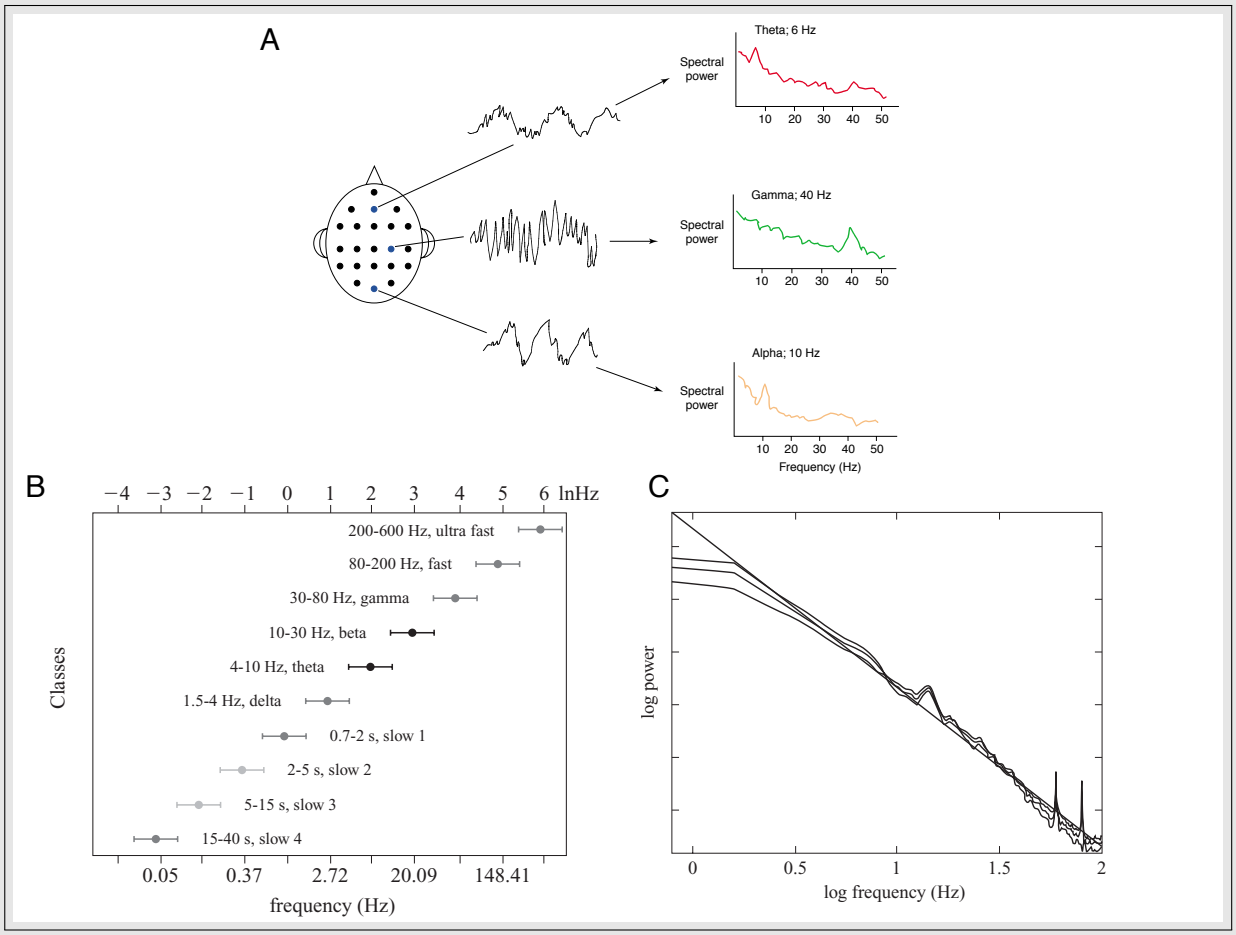

Figure 1.10: Complex oscillatory dynamics and rhythms of the brain. (A) Different brain sites display distinct rhythmic patterns when recorded intra or extra cranially. These rhythms can be classified depending or their frequency dominance (right power spectra). (B) Log scale representation of the frequency progression in the cerebral cortex, displaying a linear tendency. Each frequency "class" possesses a bandwidth that overlaps with the contiguous ones, making the progression smooth over the different time scales. Such overlapping is known as *cross-frequency coupling*. (C) EEG power spectrum from the right temporal lobe in an asleep human subject. The linear relationship between the log power and the log frequency is a sign for a complex noise, self-similarity and criticality. From *Ward* [2003]; *Buszáki* [2006]; *Freeman* [2005].

as well as brain diseases [*Del Prete et al.*, 2004; *Iglesias and Villa*, 2010; *Villa and Tetko*, 2010; *Pons et al.*, 2010].

One major question about the brain is how the microscopic laws of cell discharges and synaptic activity can lead to a complex system organized at multiple time scales. At the microscopic scale, small groups of neurons display fast oscillations of low power. On the other hand, slow oscillations involving large groups of neurons possess high power. In this sense, the power spectrum represents the relative dominance of the various constituent rhythms. Figure 1.10C shows a log-log plot of the logarithm of the power spectral density against the logarithm of EEG frequency. The straight line characterizing the logarithmic relationship between power and frequency is a hallmark for scale-free systems, which obey power laws. Thus, the frequency

power amplitude increases as frequency decreases, showing that EEG signals reflect the internal noise of the brain. However, this is not a random noise but rather a "colored" type of noise, determined by the exponent of the $1/f^{\alpha}$ relationship of (log) power and (log) frequency (f).

The scale invariant feature of EEG is the mathematical telltale sign of self-organization. If there were no relationships among the frequency bands, the power density would be constant over a finite frequency range and, thus, the spectrum would be flat ($1/f^0$). So power-frequency correlation must be explained in terms of "colored" noise, in which temporal (de)correlations at different time scales explain the observed stochastic dynamics. Overall, the $1/f^1$ behavior of EEG and magnetoencephalogram (MEG) seems to come from a balance between the underlying high entropy/information content dynamics (white noise) and the predictable low entropy/information content dynamics ("brown" noise, $1/f^2$).

It has been proposed that due to the scale-free nature of global synchronization of brain structures, its dynamics may lay in a state of "self-organized criticality" [*Chialvo*, 2004], which is a complex state at the border between predictable periodic behavior and unpredictable chaos. In this sense, the brain cortex displays state transitions which reflect fast and flexible responses to inputs [*Deco et al.*, 2008]. Such *metastable* states may be clearly an advantage for the cortex as it can rapidly react to small or weak perturbations. However, the reaction to different inputs depends on the actual state of the network as temporal correlations act over a finite temporal window of $1/f^1$, and so the out coming dynamics may look extremely different even in the presence of identical inputs. Besides, self-organized criticality theory also predicts the emergence of large synchronized events, called *avalanches* [*Petermann et al.*, 2009]. Even though neuronal networks are capable to generate avalanches in the form of highly synchronous activity in epilepsy, the normal dynamics of excitation and inhibition prevents such unexpected events.

Chapter 2

Modeling the brain

There is a long tradition of mathematical and computational approaches to neuroscience and cognition [*von Helmholtz and König*, 1896] in western science. Early mathematical theories of perception or current generation at the level of cell membrane were the basis of ulterior modern models such as the one proposed by Louis Lapicque (1866-1952) [*Brunel and van Rossum*, 2007], the *integrate-and-fire* neuron. He announced a model of polarization in nerve cells based on ionic current flow, as neurons are embedded in electrolytic media. He used a modification of Nernst's calculation of the membrane potential [*Junge*, 1981] using the different permeabilities of ions to account for a capacitor-like discharge. Lapicque's model became very popular, and it is still one of the most widely used models in computational neuroscience, setting a milestone in neuroscience modelling only surpassed by the model proposed by Alan Lloyd Hodgkin (1914-1998) and Andrew Fielding Huxley (1917-2012) [*Hodgkin and Huxley*, 1952].

Hodgkin and Huxley combined experiments on the giant squid axon with a robust mathematical description of the neuronal dynamics based on a system of non-linear differential equations representing the membrane lipid bilayer as a capacitance. Later they performed simulations in an early computer. Such gathering of theory and experiments, combined with extensive simulations, is at the core of modern computational neuroscience, which has developed several mathematical descriptions of neuronal dynamics [*FitzHugh*, 1955; *Morris and Lecar*, 1981; *Wilson and Cowan*, 1972].

The bridge between different descriptive theories can be built following two paths. *Bottom-up* approaches take into account what is known at lower levels (e.g., dynamics of ion channels) to describe phenomena occurring on higher levels (e.g., generation of action potentials). On the other hand, *top-down* approaches go from known cognitive functions of the brain (e.g. memory) towards a localization of the brain structures ruling it, and try to unveil how the lower level components may work to achieve such functions. The two approaches make use of both mathematical theory and computer simulations which, combined, provide a complete picture of the system behavior.

Bifurcation theory has also proven to be crucial in the study of the solutions of a set of differential equations representing neuronal dynamics in terms of their parameters [*Poincaré*, 1885; *Strogatz*, 1994]. Bifurcations appear as an abrupt change in the qualitative behavior of a system upon smooth changes in parameter values. They can be generally divided into two classes: *local* and *global* bifurcations. The former occur when there is a change in the stability of an

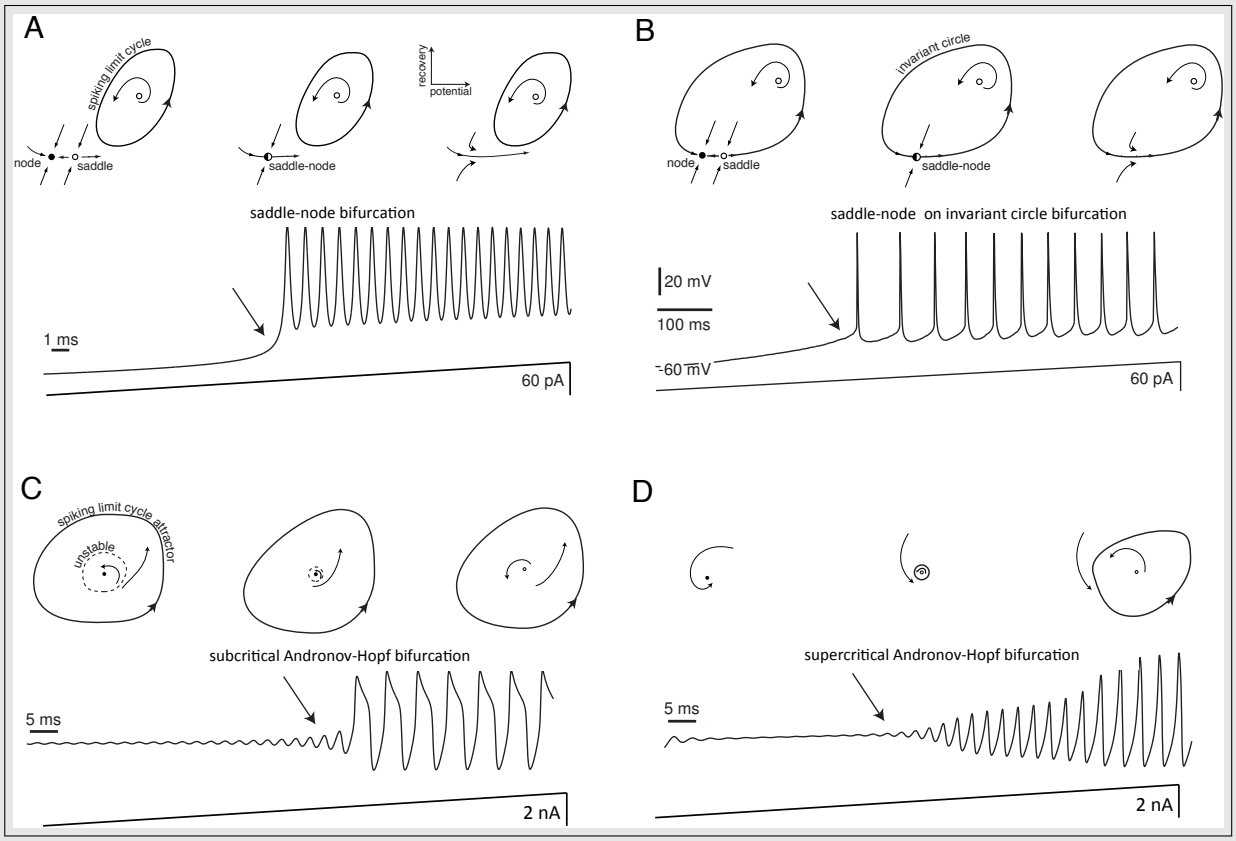

Figure 2.1: Transitions from silence to periodic behavior in terms of input strength in neural systems. (A) Saddle-node bifurcations are characterized by the merging between one stable point (black dot) with one unstable point (white dot) that eliminates the resting state in favor of the limit cycle attractor (circular line). This behavior is depicted in the transition from silence to periodic firing in a pyramidal neuron after increasing the input strength. (B) A variation on the saddle-node bifurcation appears when the two fixed points are already in the invariant circle, which becomes a limit cycle. This also gives rise to periodic firing. (C) In the subcritical Andronov-Hopf bifurcation a small unstable limit cycle collapses to a stable fixed point that becomes unstable and, thus, all trajectories close to the unstable fixed point converge to the large amplitude periodic orbit of the stable limit cycle. (D). In the supercritical Andronov-Hopf bifurcation a stable fixed point loses stability in favor of an initially small limit cycle attractor that enlarges as long as the input current increases. From *Izhikevich* [2007].

equilibrium point – *fixed point* –, induced by a 0-crossing of the real part of one of the equilibrium point's eigenvalues. The latter occur when other types of equilibria - e.g. *periodic orbits* - collide, transforming the global topology of trajectories in the phase space. Figure 2.1 shows examples of bifurcations that describe basic *excitable* dynamics of neurons or periodic behavior of neural populations. In the neural context, models of the brain should combine mathematical tractability and biological plausibility [*Spiegler et al.*, 2010]. The study of the behavior of a neural system in terms of its parameters allows to find a balance between both constraints, as well as characterize the neural dynamics for a broad range of parameter values. Thus, the transition from a quiescent to a spiking or oscillatory behavior may be governed by bifurcations such as *saddle-node* or subcritical and supercritical *Andronov-Hopf* bifurcations (see Fig. 2.1).

2.1 Levels of description in neuronal dynamics

The various aforementioned approaches to neural dynamics deal with different scales of description, from the macroscopic to the microscopic level (see Fig. 2.2A). Accordingly, different computational models have been developed to account for the activity at each scale. Single neurons, for instance, can be characterized by detailed biophysical models that consider ion-channel dynamics, as initially proposed by Hodgkin and Huxley [*Hodgkin and Huxley*, 1952; *Schwartz*, 1990; *Dayan and Abbott*, 2001], or by more abstract models of neural excitation such as the integrate-and-fire model [*Gerstner and Kistler*, 2002; *Brunel and van Rossum*, 2007] or the FitzHugh-Nagumo model [*Lindner et al.*, 2004; *Izhikevich*, 2007] (see Fig. 2.2B).

The basic idea governing neural control of behavior lays in the fact that specialized neurons transform environmental stimuli into a neural code. This encoded information travels along specific pathways to the brain or the central nervous system where it is combined with other information. However, it is nowadays almost impossible to apply a rigorous mathematical analysis of such encoding and processing at all levels of brain description. It is then necessary to construct models of the studied phenomena taking into account what is already known about the nervous system and use this information to limit the model.

The set of equations representing each neuron's membrane potential can be coupled in a way that mimics synaptic junctions. Thus, given a connectivity matrix, one can ideally build any neuronal network *in silico* from its individual constituents, and thereby move towards the mesoscopic level of neuronal assemblies. This allows the brain to be traditionally investigated in a reductionist way, using different simplified levels of description. This approach has been very fruitful in unveiling several mechanisms that lay at the basis of the observed neural tissue behavior, such as the emergence of oscillatory dynamics, rate-based coding or avalanche-like activity in epilepsy [*Kopell et al.*, 2000; *Fourcaud-Trocmé et al.*, 2003; *Goldbach et al.*, 2008; *De Sancristóbal et al.*, 2013].

Another set of models, named neural mass models [*Zetterberg et al.*, 1978; *Jansen and Rit*, 1995; *David and Friston*, 2003; *Grimbert and Faugeras*, 2006; *Spiegler et al.*, 2011a], avoid the single-neuron perspective and consider instead the averaged behaviour of the neuronal population. This mesoscopic description is more phenomenological than the single-neuron models, in the sense that it represents directly the collective behavior of the network, without singling out individual cells (see Fig. 2.2C). Moreover, single neurons operate at time scales faster than neural mass models. The former exhibit action potentials that last about 1 ms (see Fig. 2.2B), while the coordinated activity of a neuronal tissue, which emerges from the synchronization of multiple spikes, operates on time scales up to tens of seconds. Within a neuronal population all temporal scales work simultaneously, and the relative relevance of the different scales might change depending on the biological process. For instance, spike-timing precision is key to synaptic plasticity, and therefore to the formation of functional cell assemblies [*Ahissar et al.*, 1992; *Singer*, 1995]. On the other hand, the frequency of collective oscillations is relevant for the synchronization of distant areas, and thus for their effective interaction within specific information-processing tasks at a population level [*Fries*, 2005; *Sancristóbal et al.*, 2014].

While new theoretical studies have attempted to connect the microscopic (neuronal network) and mesoscopic (neural mass) descriptions of brain tissue, by directly applying mean-field

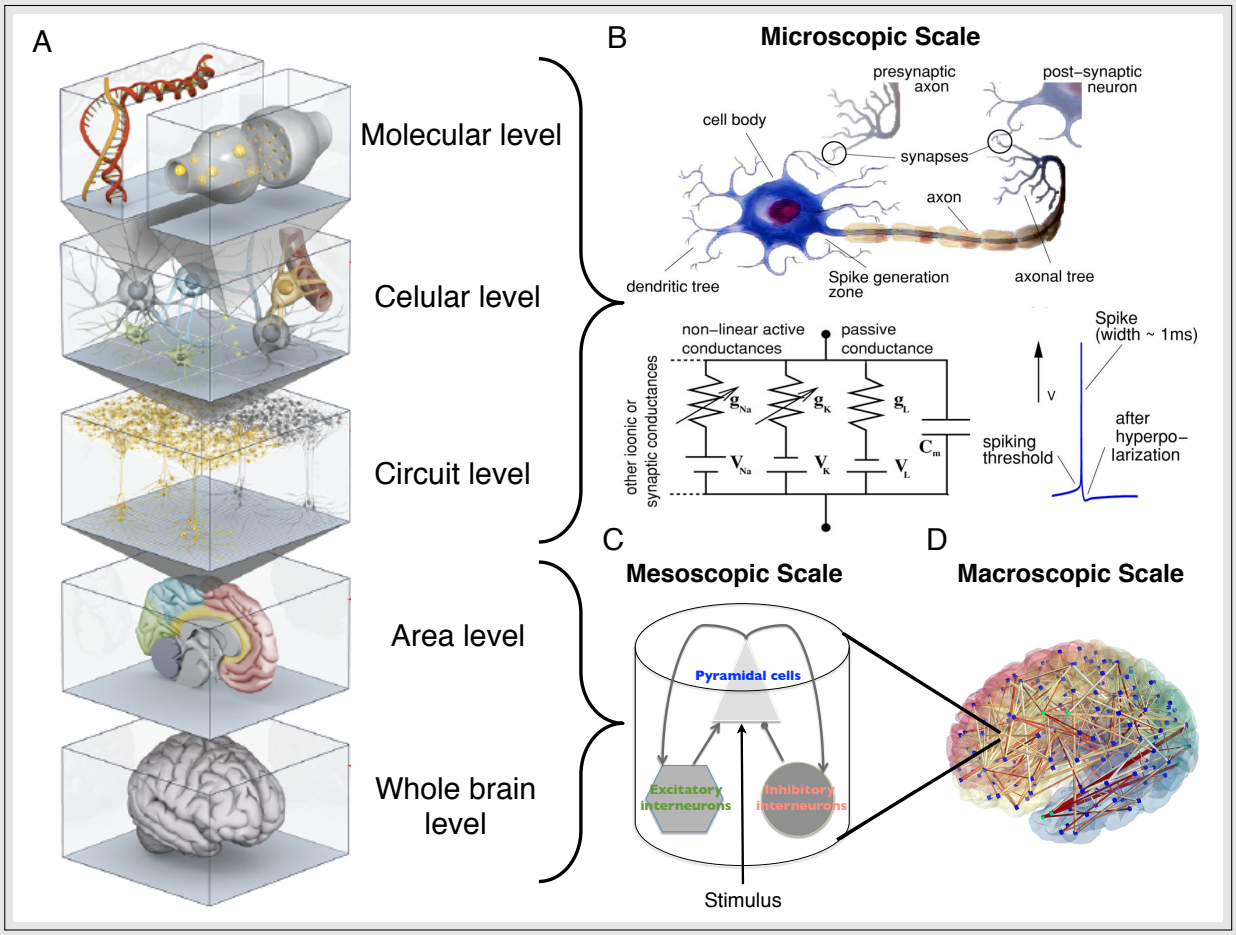

Figure 2.2: Scales in the structure of the human brain. (A) Brain dynamics can be described at many levels, starting from proteins and ions, continuing through the cell and neuronal circuit perspective to end up in an integrated whole-brain description. (B) Molecular, cellular and circuit approaches may be described in terms of the neurons and its microscopic scale features such as ionic channels or synaptic and electrical coupling (upper panel). Equivalent circuits (lower left panel) may be used to account for a neuron's activity, which translates into an all-or-none behavior (spikes, lower right panel). (C) The reduction of degrees of freedom leads to a mesoscopic point of view in which average values of large populations are described as neural masses characterized by mean field variables. (D) A whole brain description may be accomplished thanks to coupling several mesoscopic structures, or even starting from the most microscopic structure, as pretended in modern computational approaches to cerebral modeling. From *Christiansen* [2014]; *Rabinovich et al.* [2006]; *Connectome* [2015].

approaches to derive the latter from the former [*Faugeras et al.*, 2008; *Rodrigues et al.*, 2010], these strategies are fraught with limitations and hard-to-justify assumptions. Overall, a good indication that the level of the description was chosen wisely comes if the model can reproduce, with the same parameters, the main bifurcations observed in the experiments.

2.2 Microscopic approach

The biophysical and biochemical nature of neurons is really complex, requiring the use of phenomenological models to understand their dynamics. Neurons receive patterned synaptic inputs, perform computations and communicate among them by transforming these synaptic inputs into a sequence of output spikes that have almost identical waveforms. These almost identical spikes ensure that the information encoded relies on the inter-spike intervals rather than on the action potential itself, increasing the reproducibility in inter-neural communication.

Spikes crucially depend on the properties of voltage-gated ionic channels in neuron cell membranes. Detailed conductance based-models make use of several voltage-dependent channels (commonly sodium, potassium and calcium ions), the (inner and outer) concentration of such ions or a leakage current, usually of chloride ions. The probability of a channel to be opened depends non-linearly on the membrane potential and the state of the channel, which results in the generation of different spike patterns (high frequency bursts, for instance), encoding a variety of stimulus features. All this myriad of dynamical complex traits, coming from such detailed description of neurons, offers realistic biological features at the expense of computational tractability. It is then necessary to separate neuron models into classes depending on the general goal of the modeling. Reducing the degrees of freedom allows a better computational implementation. These simplified models may lose biological plausibility but provide good platforms to study neuronal dynamics with lower computational costs.

With this aim, theoretical neuroscientists have developed a wide set of models with very different levels of simplification. Among many others, some of the most frequently used neuronal models are (in chronological order):

Integrate-and-fire neuron model (1907)

The integrate-and-fire (IF) neuron is one of the simplest neuronal models [*Brunel and van Rossum*, 2007]. It was first introduced by Louis Lapicque. One of its multiple formulations go as follows (leaky integrate-and-fire model):

$$\frac{dv(t)}{dt} = \begin{cases} -\frac{v(t)}{\tau} + I_{ext} + I_{syn}(t), & 0 < v(t) < \theta \\ v(t^+) = 0, & v(t^-) = \theta, \end{cases} \tag{2.1}$$

$$\begin{aligned} I_{syn}(t) &= g \sum_{spikes} f(t - t_{spike}), \\ f(t) &= A[\exp(-t/\tau_1) - \exp(-t/\tau_2)], \end{aligned} \tag{2.2}$$

where $v(t)$ is the membrane potential, θ is the threshold for spike generation, I_{ext} is an external stimulus current, I_{syn} is the sum of the synaptic currents and τ_1 and τ_2 are time constants that characterize the synaptic currents and the overall dynamics. In this simple model a spike occurs whenever the threshold θ is reached by $v(t)$ (see sample of regular firing neuron in Fig.1.7B).

Hodgkin-Huxley model (1952)

The Hodgkin-Huxley model is one of the most detailed descriptions of neuronal dynamics and action potential generation [*Hodgkin and Huxley*, 1952]. It was described by Alan. L. Hodgkin

(1914-1998) and Andrew Huxley (1917-2012). In the Hodgkin-Huxley model the membrane acts as a capacitance (C_M), whereas voltage-gated ion channels are represented by voltage-dependent electrical conductances (g_n, $n = K, Na$) and a constant leakage conductance (g_L). The flow of ions is represented by voltage sources (V_i) and ionic pumps are characterized by current sources (I_p) (see the basic electrical circuit describing a neuron's membrane in Fig. 2.2B and the ionic generation of an action potential in Fig. A.2).

Different currents flowing through the membrane and the ionic channels are represented by:

$$I = C_M \frac{dV_M}{dt} + g_K(V_M - V_K) + g_{Na}(V_M - V_{Na}) + g_L(V_M - V_L), \tag{2.3}$$

where V_M is the membrane potential, V_K and V_{Na} are the potassium and sodium reversal potentials and V_L is the leak reversal potential. g_K and g_{Na} explicitly depend on voltage and time as follows:

$$\begin{aligned} g_K(t) &= \bar{g}_K n^4(t) \\ g_{Na}(t) &= \bar{g}_{Na} m^3(t) h(t), \end{aligned} \tag{2.4}$$

with n, m and h being dimensionless parameters related with the activation and inactivation of ionic channels. Thus:

$$\begin{aligned} \frac{dn}{dt} &= \alpha_n(V_M)(1-n) - \beta_n(V_M)n, \\ \frac{dm}{dt} &= \alpha_m(V_M)(1-m) - \beta_n(V_M)m, \\ \frac{dh}{dt} &= \alpha_h(V_M)(1-h) - \beta_h(V_M)h, \end{aligned} \tag{2.5}$$

where α_i and β_i are the opening and closing rate constants for each channel. Hodgkin and Huxley fitted the value of the rate constants to their voltage clamp measurements [*Hodgkin and Huxley*, 1952], deriving the following relationships:

$$\begin{aligned} \alpha_n(V_M) &= \frac{0.01(V_M - 10)}{\exp(\frac{V_M - 10}{10}) - 1}, \\ \alpha_m(V_M) &= \frac{0.1(V_M - 25)}{\exp(\frac{V_M - 25}{10}) - 1}, \\ \alpha_h(V_M) &= 0.07 \ \exp(\frac{V_M}{20}), \\ \beta_n(V_M) &= 0.125 \ \exp(\frac{V_M}{80}), \\ \beta_m(V_M) &= 4 \ \exp(\frac{V_M}{18}), \\ \beta_h(V_M) &= \frac{1}{\exp(\frac{V_M - 30}{10}) + 1}. \end{aligned} \tag{2.6}$$

Overall, the Hodgkin-Huxley model is one of the most detailed models for the generation of action potentials based on experimental fitting of parameters, but it entails a high computational cost when dealing with large populations of neurons.

FitzHugh-Nagumo model (1961)

The complexity of the Hodgkin-Huxley model, characterized by a set of differential equations for 4 state variables ($v(t), m(t), n(t)$ and $h(t)$), led to the development of simpler descriptions of neuronal dynamics. The analysis of the HH model allows to discover general behaviors and properties typical of nonlinear systems (limit cycles, bifurcations) that have been proven to be mappable to lower-dimensional descriptions.

One early approach was proposed by Richard FitzHugh (1922-2007) and later implemented in a circuit using tunnel diodes by Jin-Ichi Nagumo (1926-1999) and colleagues. FitzHugh first tried to reduce the HH model to a 2D representation for which phase plane analysis applied. He based his reduction in the fact that variables m, n and h presented different dynamical features, with n and h describing slower dynamics than m. Another further insight was the similitude between the V-nullcline and the shape of a cubic function, as well as the linear shape of the n-nullcline in the HH model. All these observations led to the dimensionless polynomial formulation of the model as:

$$\begin{aligned} \frac{dv}{dt} &= v - \frac{v^3}{3} - w + I_{ext}, \\ \tau w &= v + a - bw \end{aligned} \tag{2.7}$$

where v represents the fast variable (potential), w represents the slow variable (sodium gating variable), I_{ext} is an external current and a and b are constants that control the spiking behavior. This model can be seen as a generalization of the Van der Pol oscillator displaying excitable dynamics.

2.3 Mesoscopic approach

Realistic neuronal networks comprise a large number of neurons (e.g. a cortical macrocolumn has $\sim 10^8$ neurons with $\sim 10^4$ connections) whose description implies computationally expensive simulations. Thus, large brain circuits are frequently described as networks of nodes associated with neuronal assemblies, evolving in time at the mesoscopic scale, in such a way that their dynamics can be considered as that of limit-cycle oscillators subjected to (weak) forcing and coupling.

Mean-field models, formulated using concepts from statistical physics (e.g. law of large numbers, averaged population dynamics), are suited to data reflecting the behavior of a population of neurons – e.g. the electroencephalogram (EEG), the magnetoencephalogram (MEG) or the fMRI –. Among several simplifications, neural mass models summarize the description of the ensemble activity with a "single" number. In this sense, they describe neuronal dynamics in terms of the average values of neuronal states (average values), replacing the full ensemble activity with a "point mass" in phase space. Such approach may reveal inaccurate as variability in depolarization, for instance, may have a key role on the subsequent dynamics. However, the introduction of a sigmoid function relating the average postsynaptic depolarization to the average presynaptic firing rate implicitly encodes variability in the postsynaptic depolarization, as it nonlinearly relates the two expected values.

One of the very first mesoscopic approaches to model population dynamics was proposed by Hugh R. Wilson (1943-) and Jack D. Cowan (1933-) in 1972 [*Wilson and Cowan*, 1972] . They attempted to describe a cluster of neurons by averaging it to a distribution of potentials so as to remove the intrinsically noisy dynamics of individual neurons. Their results showed hysteresis phenomena and limit cycles able to explain the dependency between the frequency of oscillations and the stimulus intensity, found in a diversity of experimental conditions.

The first point-like mesoscopic model was published by Fernando Lopes da Silva (1935-) and colleagues in 1974 [*Lopes da Silva et al.*, 1974]. It described a linear two-ensemble model of the thalamus (excitatory relay cells coupled to interneurons) that was capable of generating 10 Hz frequency oscillations, lying in the alpha rhythm band. It was extended to a firing rate based description by Paul L. Nunez (1940-) [*Nunez*, 1974] the same year. A year after, in 1975, Walter J. Freeman III (1927-) coined the term *neural mass action* (later known as *neural mass model* or NMM) to account for an alternative to the already known ensemble density models, called *lumped parameter* models [*Freeman*, 1975]. According to Freeman, similar neurons could be lumped together and so NMMs could be described with only a set of parameters by means of the already known mean-field approximations. Thus, the ensemble state is the synchronous activity of similar neurons within a NMM. Later in 1978, L.H. Zetterberg, extending Lopes da Silva's work, described the cortical area as a basic element composed by three populations or neural masses: pyramidal cells, excitatory and inhibitory interneurons [*Zetterberg et al.*, 1978] that mutually interact by means of either positive of negative feedback loops (see Fig. 2.2C). Extrinsic inputs target pyramidal cells, although such restriction can be broadened to other subpopulations, as proposed by David and colleagues [*David and Friston*, 2003; *David et al.*, 2005]. An extension of the Zetterberg model was proposed by Jansen and Rit in 1993 [*Jansen et al.*, 1993], neglecting self-projection of pyramidal cells, to study visual evoked potentials and alpha rhythm in EEG (see detailed description in Appendix A.1.1). Posterior modifications have allowed to describe the emergence of faster rhythms in the gamma band [*David and Friston*, 2003; *Ursino et al.*, 2010; *Sotero*, 2015], or describe functional connectivity during motor tasks [*Zavaglia and Astolfi*, 2008], among other phenomena.

Generic formulation of a neural mass model

The derivation of the equations of a neural mass model, which takes into account the average voltage time evolution, is based on the solution of an inhomogeneous differential equation defined in the time domain:

$$L\mu_\nu(t) = S[\mu_\nu(t)], \tag{2.8}$$

with L being a linear differential operator, $\mu_\nu(t)$ the average membrane potential of the population and $S[\mu_\nu(t)]$ the input function of the population (ν). The impulse response of the population ν is the *Green's function* to be convoluted with $S[\mu_\nu(t)]$. The typical impulse response function for the postsynaptic depolarization, derived from experimental evidence (see G_e and G_i in Fig. 1.8A), is taken to be:

$$H(t) = A\gamma t e^{-\gamma t}, \tag{2.9}$$

with A being the height of the impulse response and γ the time rise of the voltage depending on the stimulus. Such function acts as the kernel of the convolution with the input function $S[\mu_\nu(t)]$, which in turn gives:

$$\mu_\nu(t) = \int_{-\infty}^{t} H(t')S[\mu_\nu(t')]dt'. \tag{2.10}$$

This convolution can be related with the differential form:

$$\left(\frac{1}{\gamma^2}\frac{\partial^2}{\partial t^2} + \frac{2}{\gamma}\frac{\partial}{\partial t} + 1\right)\mu_\nu(t) = A\gamma S[\mu_\nu(t)]. \tag{2.11}$$

The most popular formulation of neural mass models turns out to be a set of second order differential equations for the average postsynaptic voltage combined with a nonlinear gain represented by a sigmoid function. In general, these equations can be converted into first order differential equations as follows:

$$\begin{aligned} \dot{\mu}_\nu &= \mu_a, \\ \dot{\mu}_a &= A\gamma S(\mu_\nu) - 2\gamma\mu_a - \gamma^2\mu_\nu, \\ S(\mu_\nu) &= \frac{2\kappa}{1 + exp(-r\mu_\nu)} - \kappa, \end{aligned} \tag{2.12}$$

where μ_a is a current density, r is the gain of the sigmoid function and κ controls the average firing rate. This type of neural mass model, which we use in our work below (see Appendices A.1.1 and A.1.2), has been extensively used to model and simulate electrophysiological recordings, as well as a basis of a model for the generation of even-related potentials [*Jansen et al.*, 1993], event-related synchronization and desynchronization [*Suffczynski et al.*, 2001; *Zavaglia et al.*, 2006], visual or motor entrainment and chaos [*Spiegler et al.*, 2011a], cross-frequency coupling [*Jedynak et al.*, 2015], excitatory/inhibitory segregation [*Malagarriga et al.*, 2014, 2015b], and epileptic seizures [*Robinson et al.*, 2002].

2.4 Macroscopic approach

Recently, large-scale models of the brain have received special attention. Current large-scale implementations of neural mass models suggest that the simulation of neural dynamics in networks as large as the brain is feasible. However, there is no integrated neural theory that can serve as a guide to unveil the predictably emergent novel phenomena. Some researchers attempt to simulate of certain processes at a molecular level (e.g., the interaction of neurotransmitters with a synapse), and other processes at other scales (e.g., neurons at the level of biophysical models, neural networks at the level of large integrate-and-fire models and brain areas using mesoscopic approaches). However, the bridge between scales ensures the self-consistency of the model (see Fig. 2.2A).

So far, global brain activity has been modelled by dividing the brain into discrete volume elements, or voxels, and coupling them according to statistical correlations and structural information [*Sotero et al.*, 2007; *Pons et al.*, 2010; *Deco et al.*, 2013] (see Fig. 1.8A, 2.2D). Both the Human Brain Project and the Brain Activity Map project propose integrated views to bridge the gap between the behavior of single neurons and the functions of the full brain [*Alivisatos et al.*, 2012], but this quest is still in its infancy.

Chapter 3

Chaos, noise, synchronization and brain computation

The complexity of certain natural systems entails the emergence of highly irregular non-periodic dynamics, which can be defined as *chaos*. Indeed, a chaotic dynamical system is characterized by its sensitivity to its initial conditions or to small perturbations. Thus, two identical chaotic systems may evolve differentially after certain transient time if their initial conditions are different (see Fig. 3.1A right panel). The rate of divergence between two time evolutions is given by the *Lyapunov* exponents (real part of the *Floquet* exponents), which provide an indicator of the exponential separation of two trajectories in phase space (see Appendix B.1.1 for more details). In a neural context, recently, the observation of chaos in the analysis of experimental data has been reported in single neuron or ensemble recordings [*Celletti and Villa*, 1996; *Andrzejak et al.*, 2001] (see Fig.3.1B,C).

Chaotic signals have many of the traditional characteristics attributed to noise. However, chaos can be thought to be a sort of "deterministic irregularity" and thus, it possesses a structure in state space (see Fig. 3.1A left panel), whereas noise is an uncontrollable action in dynamical systems with no such structure. Besides, the information processing capacity may be enhanced by chaos (with the creation of information) but be damped by noise [*Rabinovich et al.*, 2006]. However, noise, even seen as a high-dimensional chaotic motion, may posses small basins of attraction where the system can be trapped. Thus, the boundaries of the basins can be dynamically lowered thanks to small perturbations so as the system can explore all possible attractor states and, thus, it would not miss any highly functional synchronized activity allowing the implementation of several important brain features (e.g. memory, plasticity, etc.).

The very first notion of *synchronization* between two dynamical variables comes from the observation of Greek naturalists of different phenomena that "*shared a common time*" (the Greek meaning of the word). The seminal works by Christian Huygens reported that two weakly coupled pendulum clocks adjusted their rhythms to finally end up in a dynamical situation in which both pendulums oscillated in agreement. Many other examples can be found in nature, such as the synchrony of organ pipes, described by Lord Rayleigh, or the synchronization of electronic generators, discovered by E.V. Appleton and B. Var der Pol in the 1920s. Consistently, phase-reduction theory has revealed synchronization to be among the most relevant features that

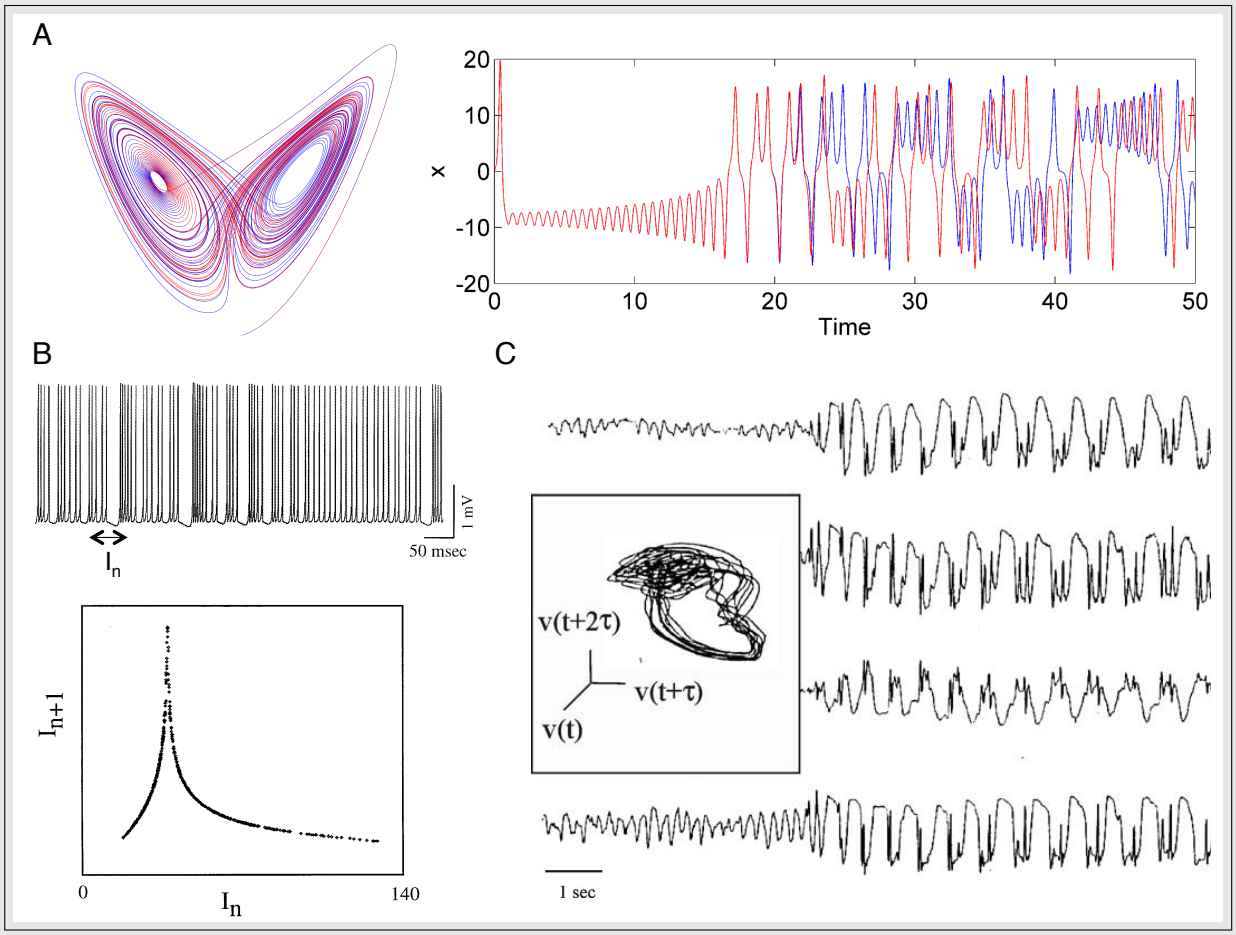

Figure 3.1: Complex dynamics and chaos in dynamical systems. (A) The Lorenz system displays strange attractor dynamics when represented in phase space (left panel). Such shape is a sign for chaotic dynamics, which is translated into an 'erratic' time evolution highly sensitive to the initial conditions (see the divergence between the blue and red lines in the right panel). (B) In a neural context, a sequence of spikes might seem completely stochastic and driven by noise at first sight but plotting successive inter-spike intervals (I_n vs I_{n+1}, upper panel) may indicate a strict relationship between them (lower panel). (C) EEG recordings can also display traces of determinism when plotted in a time embedded phase space ($v(t)$ vs $v(t+\tau)$ vs $v(t+2\tau)$). From *MacCabe* [2013]; *Faure and Korn* [2001]; *Korn and Faure* [2003].

determine the dynamical states of coupled oscillator systems [*Pikovsky et al.*, 2003; *Brown et al.*, 2004]. Furthermore, coupled oscillator theory has established the conditions that allow all the oscillators, or a subgroup of them, to operate in one of several synchronization regimes, including complete, lag, generalized, and phase synchronization (see an example in Fig.3.2A) [*Boccaletti et al.*, 2002; *Li and Chen*, 2004; *Malagarriga et al.*, 2016] (see Appendix B.1.3 for more details).

Recently, there has been an increasing interest towards the study of the synchronization of chaotic systems [*Pikovsky et al.*, 2003] and the emergence of non-trivial collective dynamics in such systems. The role of synchronization in coordinating and processing information at different spatiotemporal scales in the brain has been stressed very often [*Lachaux et al.*, 1999; *Buszáki*, 2006; *Stam and de Bruin*, 2004; *Malagarriga et al.*, 2015b]. For instance, synchronization-based

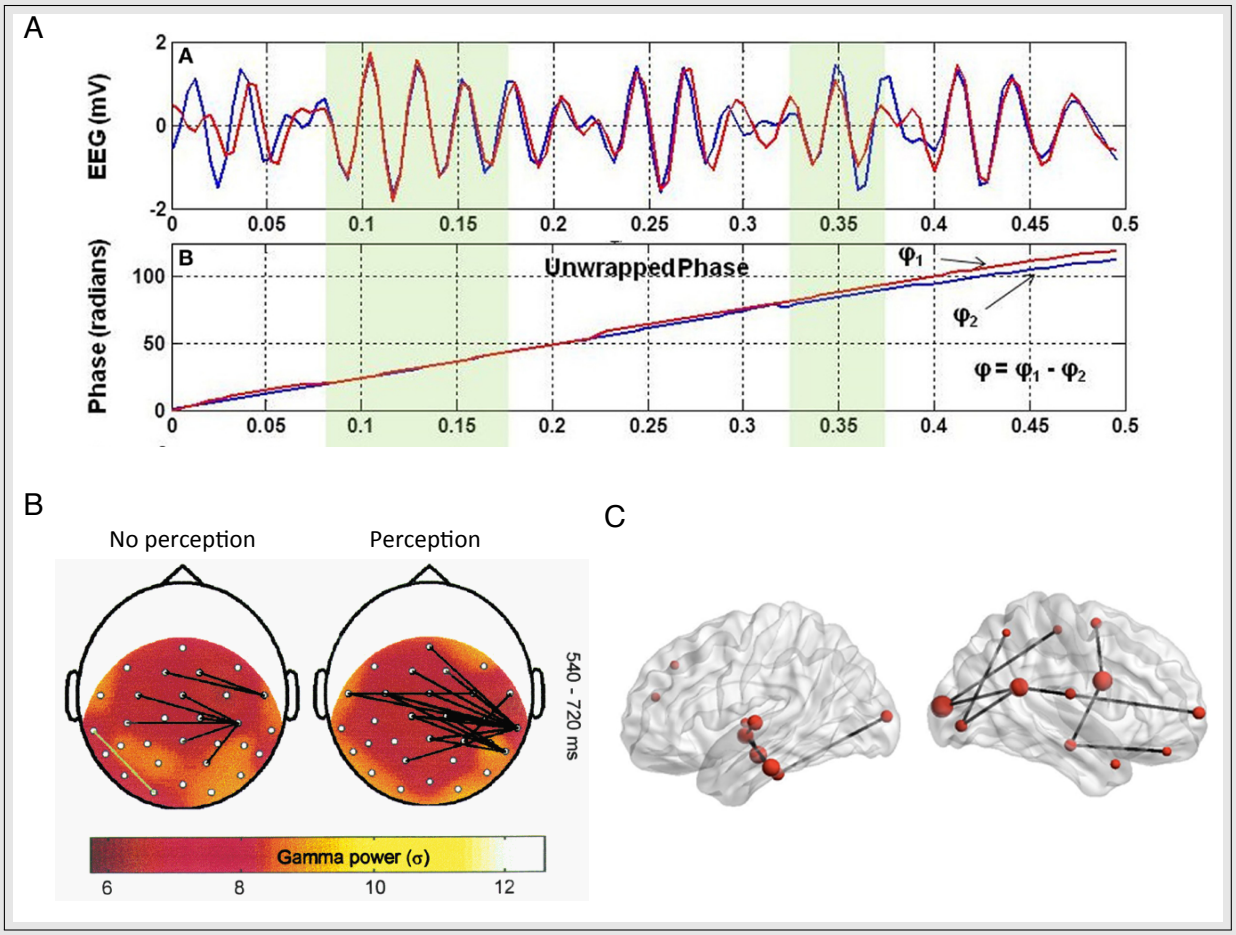

Figure 3.2: Synchronization of brain signals and construction of functional networks. (A) Phase synchronization of two EEG time series (top panel). The tracking of the two signals phases allows to see the linear relationship between them (lower panel). (B) Phase synchronization may be a sign for perception in a task displaying prominent gamma power. In this case, gamma activity is rather spatially homogeneous (see color coding) whereas phase synchrony (black lines) is markedly distinct between the perception and no perception stages. (C) Phase synchrony, among other types of synchronization, may be used for constructing *functional networks*, which are spatial representations of the dynamical dependence between brain sites. From *Ramon and Holmes* [2013]; *Rodriguez et al.* [1999]; *Doesburg et al.* [2013].

selectivity of visual responses has been studied in monkeys and cats [*Castelo-Branco et al.*, 2000; *Womelsdorf and Fries*, 2007] or even in humans [*Rodriguez et al.*, 1999]. Besides, synchronization participates in the odor perception [*Stopfer et al.*, 1997; *Laurent et al.*, 2001; *Blumhagen et al.*, 2011] and coherence of stimuli also affects the selective capability of oscillatory networks [*Börgers and Kopell*, 2008; *Börgers et al.*, 2008]. The processing and computation mechanisms based in all this diversity of synchronized elements has also been studied in detail [*Fries*, 2009; *Nikolić et al.*, 2013; *Womelsdorf et al.*, 2014; *Maris et al.*, 2013; *Engel et al.*, 2001a]. Thus, the interaction of different synchronized ensembles of neurons [*Womelsdorf et al.*, 2007; *Wulff et al.*, 2009] plays a role in tasks like learning item-context associations [*Tort et al.*, 2009], selective attention [*Womelsdorf and Fries*, 2007; *Fries et al.*, 2001, 2008; *Bosman et al.*, 2012] or even conscious perception (see

Fig. 3.2B) [*Melloni et al.*, 2007; *Levy et al.*, 2013]. At the larger spatial scale in the brain, synchronization participates in the control of task-switching [*Phillips et al.*, 2013] and is studied routinely in normal and abnormal EEG and MEG recordings [*Stam*, 2005] so as to extract functional and effective connectivities (see Fig. 1.8A and 3.2C). Besides, recent work shows that in networks of mesoscopic brain (chaotic) oscillators different forms of synchronization might coexist [*Malagarriga et al.*, 2015a,b].

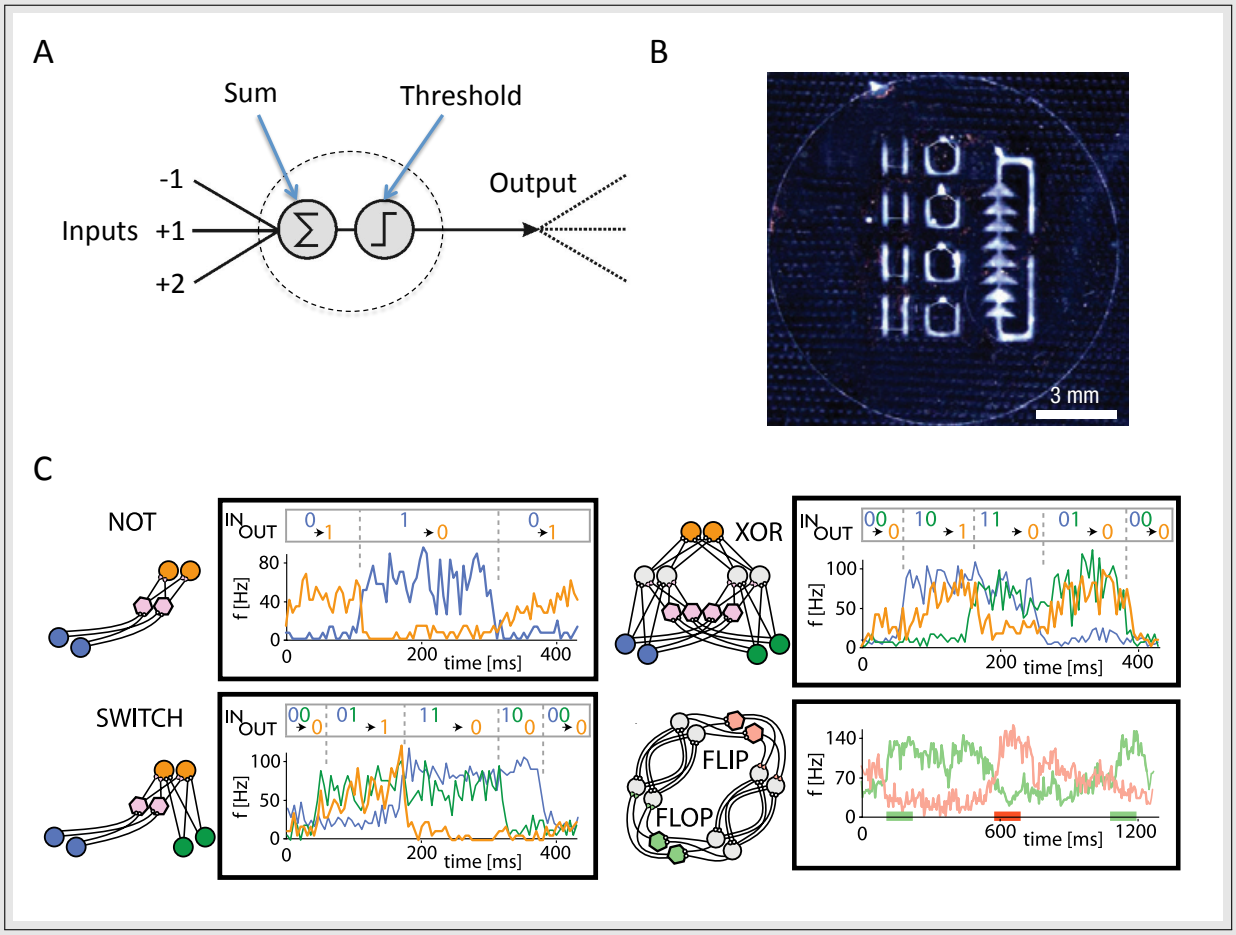

Figure 3.3: Models for Boolean logic computation in the brain. (A) McCulloch and Pitts model of a neuron. Several inputs impinge onto a cell, which sums all the contributions ($\sum$) and performs and applies a threshold so as to give an all-or-none output (e.g. a spike). (B) Neuronal patterned cultures have been used to implement logic calculus through logic gates. In this case the microscopic architecture mimics that of electronic devices (i.e. diodes). (C) From the theoretical point of view, small networks of coupled neurons have also been shown to display logic gating characteristics. These circuits may implement higher functions such as a flip-flop memory or full adders in terms of the changes in their firing frequency over time. From *Feinerman et al.* [2008]; *Vogels and Abbott* [2005].

This phenomenon enlarges the processing capacity of neural oscillators, and endows the corresponding networks with stability, flexibility and robustness against perturbations [*Zanette*, 2004]. Even though much progress in the understanding of these synchronization mechanisms has been gained during many years, it is not fully understood yet how these synchronization

relations are established with the participation of different scales simultaneously, or how they operate at the same time without interfering with each other [*Barardi et al.*, 2014a].

The information processing capacity of the brain operating under multiple scales has been described very often in terms of logic calculus. At the most microscopic level, the idea of logic calculus based on neuronal activities was embedded in the seminal work of McCulloch and Pitts (see Fig.3.3A) [*McCulloch and Pitts*, 1943]. Neuronal circuitry performing logic operations was physically implemented in cell cultures of *in vitro* models of selected brain areas (see Fig.3.3B) [*Wolf and Geisel*, 2008; *Feinerman et al.*, 2008]. This approach is mainly based on action potentials and on the connectivity within the network, rather than on a dynamical analysis of the ongoing activity. At the cellular level neurons have revealed that, in addition to behaving as a bistable system, they can be driven into a continuous oscillation by means of selected voltage-dependent inward currents controlled by intracellular calcium concentrations [*Contreras and Steriade*, 1995; *Hughes et al.*, 2002; *Crunelli et al.*, 2005]. Besides, from the microscopic point of view, neurons may coordinate their firing in response to incoming stimuli, opening the way to a neurocomputing paradigm characterized by different synchronized states where the neurons oscillate with equal frequencies and specific phase relationships [*Hoppensteadt and Izhikevich*, 2000; *Zanin et al.*, 2011]. By associating logical states to the dynamics of coupled oscillators, all usual Boolean operations can be implemented and a full computational model can be obtained (see Fig.3.3C) [*Xu et al.*, 2004; *Vogels and Abbott*, 2005].

Beyond the cellular level of neuronal oscillators, it was recently demonstrated that circuits of neurons embedded within a large-scale network of cortical cells were able to express logic functions that are dependent on complex spatiotemporal patterns [*Vardi et al.*, 2013; *Menon and Sinha*, 2014].

Chapter 4

Review and aim of the thesis

This Thesis is devoted to study of complex phenomena at the *mesoscopic* scale using different theoretical models. Mesoscopic dynamical systems are oftentimes derived from simplifications on the dynamics of its constituent microscopic structures. In a neural context, then, simplified descriptions of neuronal dynamics lead to average population behavior, usually oscillatory, characteristic of the mesoscale. Mesoscopic models allow for a significant reduction in computational costs summed to a good qualitative agreement with real population dynamics seen in, e.g. electroencephalographic (EEG) or magnetoencephalographic (MEG) recordings.

Although we have centered our research in the mesoscale, we have also studied the dynamics of descriptions of lower-scale brain structures, i.e. neurons, by means of microscopic *conductance-based* models. In this sense in Chapter 5 we explore the bi-directional interaction between microscopic and mesoscopic models to account for an effective interaction of scales in brain dynamics. The goal of the chapter is to provide evidence on the basic mechanisms responsible for the *cross-talk* between two levels of description in the brain, as well as bridging the gap between microscopic and mesoscopic scales in a more *phenomenological* way, i.e. using a proxy (synchronization of large brain structures) to asses that communication is established between microscopic and mesoscopic structures. We prove that the best fitted model for each scale consistently interacts with their counterparts in other scales, resulting in reduced computational costs. Therefore, these findings might reveal crucial if applied to whole-brain simulations.

We have also addressed another important issue in brain dynamics: the balance between excitation and inhibition (see Chapter 6). Our approach, however, is centered in the dynamical and topological aspects that allow certain groups of identical mesoscopic structures to behave as being dominated by excitation or inhibition when interacting in a weighted excitatory/inhibitory networks of cortical columns. Moreover, complex synchronization patterns also emerge in the form of *coexisting* synchronized dynamical evolutions, where different synchronizations - phase, lag, generalized - are present in our networks. Our findings, which seem to have an experimental counterpart [*Markounikau et al.*, 2010] show that complex patterns of excitatory and inhibitory dominated brain areas, as well as synchronized brain sites, emerge thanks to the combination of complex topology, excitatory and inhibitory couplings and resonant dynamics due to (complex) inputs.

Following the results presented in Chapter 6, where complex topologies led to complex

synchronization patterns, we identified the *coexistence of synchronizations* as being a phenomenon typically detectable in nonlinear systems embedded in complex arrangements. Such idea is explored in Chapter 7 by means of a simple nonlinear dynamical system –the Rössler equations –. Our results show that *coexistence* emerges in the route towards an all-synchronized network in an adjustable range of a control parameter – the coupling strength – that crucially depends on network topology and *weighting*. Networks with stable coexistence also possess another important trait, *consistence*, by which different initializations of the dynamics entail the same coexistence pattern, thus preserving the *functional relationship* between the nodes. In a neural context we show that the *consistence of coexistence* may be related with the stability of *functional networks* in the sense that functional networks with higher consistence are statistically more frequent and so functionally relevant. We have also related structural and functional networks, showing that highly consistent functional networks appear for well defined structural networks.

Finally, Chapter 8 makes use of the results in Chapter 7 and Chapter 6 to study the information processing capacity of a system of mesoscopic (neural) structures. We have explored the possible mechanisms by which synchronized oscillations may code for different oscillatory input patterns, as well as implementing networks of basic *logic gates* which lay at the basis of complex computation. To do so, we have extended the synchronization possibilities - by using the coexistence of synchronizations - so as to prove that several logic gates can be implemented by means of a 0/1 - not synchronized/synchronized states -. Our results show that extended mesoscopic structures - Jansen and Chua oscillator networks - are capable of performing distributed processing, as well as implementing, somehow, memory elements using complex logic functions to produce a *flip-flop* memory.

Part II

Results

Chapter 5

Scale interaction in brain dynamics

"You are nothing but a pack of neurons."

Francis Crick

The mammalian brain operates in multiple spatial scales simultaneously, ranging from the microscopic scale of single neurons through the mesoscopic scale of cortical columns, to the macroscopic scale of brain areas. These levels of description are associated with distinct temporal scales, ranging from milliseconds in the case of neurons to tens of seconds in the case of brain areas [*Buzsáki et al.*, 2012]. In this Chapter we examine theoretically how these spatial and temporal scales interact in the functioning brain, by considering the coupled dynamics of microscopic and mesoscopic neural structures. The two neural mass oscillators are taken to operate in a low-frequency regime with different peak frequencies (and distinct dynamical behaviour). The microscopic neuronal population, in turn, is described by a network of several thousand excitatory and inhibitory spiking neurons operating in a synchronous irregular regime, in which the individual neurons fire very sparsely but collectively give rise to a well-defined rhythm in the gamma range. We use the synchronization between the two neural mass models as a tool to probe the interaction between the mesoscopic scales of those neural populations and the microscopic scale of the mediating neuronal network. Our results show that this neuronal network, which operates at a fast temporal scale, is indeed sufficient to synchronize the two mesoscopic oscillators, which evolve dynamically at a slower scale. We also establish how this synchronization depends on the topological properties of the microscopic neuronal network, on its size and on its oscillation frequency.

5.1 Interaction between microscopic and mesoscopic neuronal populations

The effective interaction between neuronal ensembles described at different scales can be studied by coupling microscopic and mesoscopic models (Fig. 5.1). As mentioned in the Introduction, models of single neurons reproduce the time course of the electric currents crossing the neuronal membrane, and thus account for the individual action potentials and the postsynaptic response of each cell composing the network. In order to preserve the precision of the spiking times, these

models involve fast time scales. Networks built from spiking-neuron models can also provide measures of the population activity by averaging across neurons. Thus, patterns of collective activity can be observed in the synaptic current, evoked by the summation of multiple spikes on the target neurons. On the other hand, mesoscopic models are best exemplified by neural mass descriptions, which are derived phenomenologically from experimental studies, and characterize the average population activity by means of a mean field approximation. In particular, Neural Mass Models (NMs) describe the neuronal activity happening at slow time scales, such as the sum of synaptic potentials arising from the synchronized firing of thousands of neurons [*Jansen and Rit*, 1995].

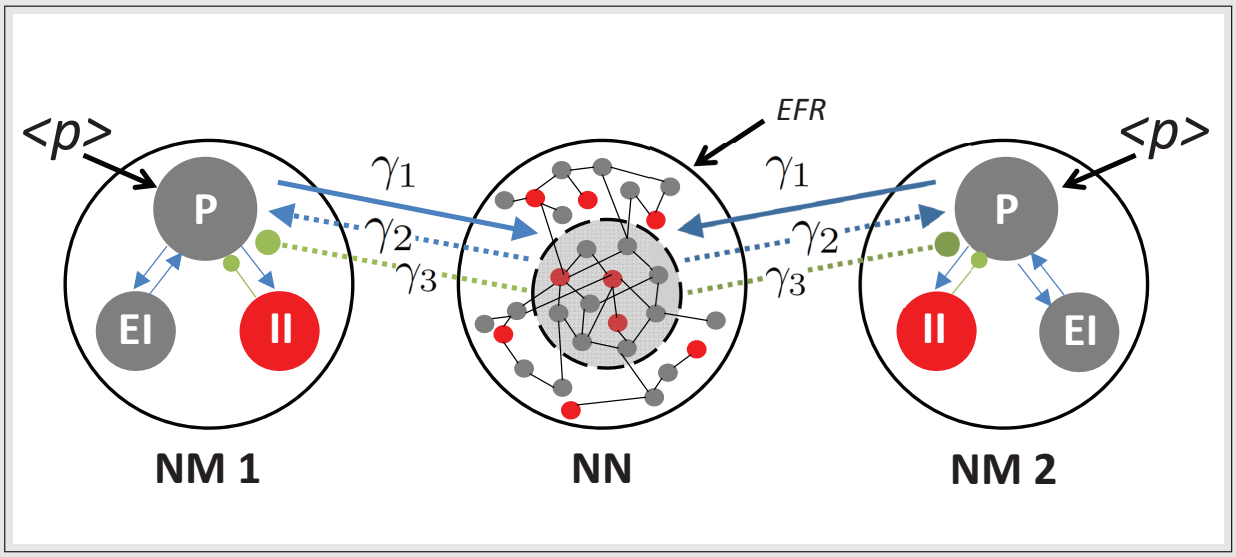

Figure 5.1: Diagram representing the coupling between the two distinct models. Two groups of neuronal populations, described by neural mass models (NMs), are coupled with a neuronal network (NN). The NMs represent the average dynamics of three coupled neural populations: pyramidal (P), excitatory interneurons (EI), and inhibitory interneurons (II). The NN consists of a set of 4000 excitatory and inhibitory interconnected neurons. Only a subset of neurons of the NN is coupled with the NMs. The coupling strength between the NMs and the NN is given by the three parameters, γ_1, γ_2 and γ_3. γ_1 quantifies the coupling from the pyramidal population of the NMs to the NN subpopulation. γ_2 and γ_3 represent the intensity of the excitatory and inhibitory couplings, respectively, from the NN subpopulation to the NMs' pyramidal population. $\langle p \rangle$ is the average excitatory input to the pyramidal population ($p_e(t)$ in Eq. A.6).

In order to analyze the evolution of the mesoscopic and microscopic models - described in detail in Appendices A.1.1 and A.2, respectively -, we consider two different dynamical variables corresponding to each of the two scales. The neural mass model activity is given by $y(t) = y_e(t) - y_i(t)$, where $y_e(t)$ is the excitatory postsynaptic potential (EPSP) and $y_i(t)$ is the inhibitory postsynaptic potential (IPSP) acting upon the pyramidal population (see Eqs. (A.6-A.8) in Appendix A.1.1, where $y_1(t)$ corresponds to $y_e(t)$ and $y_2(t)$ corresponds to $y_i(t)$). The neuronal network activity is quantified in terms of the local field potential (LFP) as defined in Eq. (A.25). Both types of models operate in an oscillatory regime. The neural mass model

is an intrinsic oscillator whose frequency can be varied by changing the parameters B and b (see Appendix A.1.1 and blue and green lines in Fig. 5.2A). On the other hand, the oscillations of the neuronal network are an emergent property of the system, reflecting the variability of the individual postsynaptic potentials (i.e. the microscopic events). Hence, its frequency is less defined (see red line in Fig. 5.2A and power spectra in Fig. 5.2C).

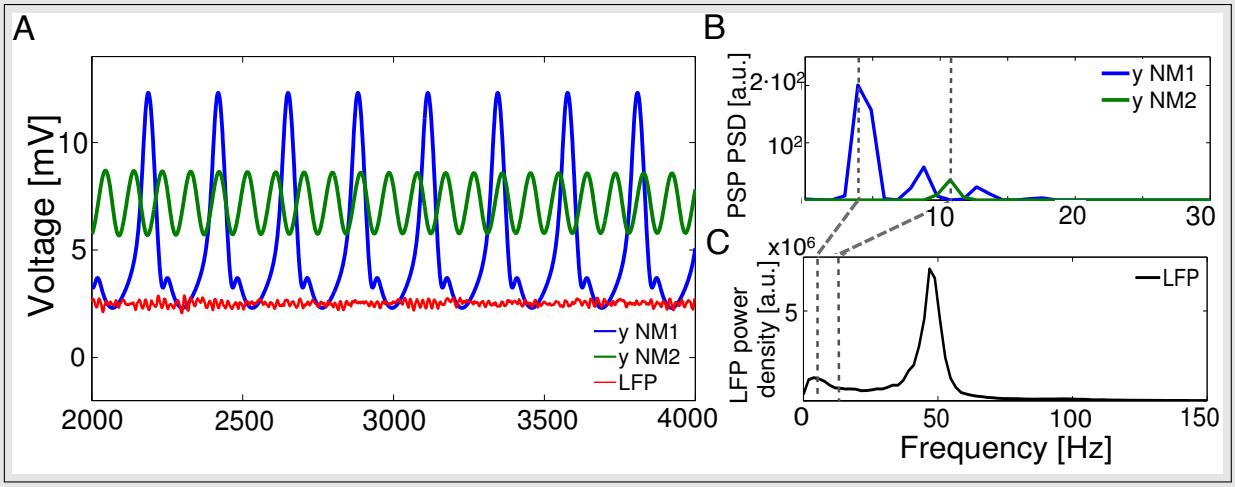

Figure 5.2: Collective dynamics of the uncoupled system. (A) Time traces of the net postsynaptic potential $y(t) = y_e(t) - y_i(t)$ of both neural masses working at different frequencies: at 4.5 Hz within the theta band (blue), and at 11 Hz within the alpha band (green). The local field potential, LFP, of the neural network (red) oscillates in the gamma range around 45 Hz. The three neural ensembles are uncoupled. (B) Power spectra of the net postsynaptic potential $y(t)$ of the neural masses in isolation. Primary peaks are tagged with vertical dashed lines at ∼4.5 Hz and ∼11 Hz. (C) Power spectrum of the LFP of the neuronal network in isolation.

Our aim here is to find fingerprints of an effective interaction of scales. To do so we have studied how the two neural mass models, one oscillating in the theta band and the other in the alpha band, synchronize their dynamics when the coupling is mediated by the neuronal network (Fig. 5.1). The interaction mechanism is bidirectional. This architecture was used by *Vicente et al.* [2008] and *Gollo et al.* [2010] to demonstrate the emergence of zero-lag synchronization mediated by dynamical relaying between neuronal network populations. In our case, the output of each NM is converted into a firing rate (see Eq. (A.21)) impinging on a subpopulation of 2000 neurons within the neuronal network. In turn, the firing rate of these selected neurons contributes to both the excitatory and inhibitory postsynaptic potential densities that act upon the pyramidal populations of the NMs. We also examine the effect of varying several properties of the subpopulation of neurons of the NN involved in the coupling (including its size), in order to explore the effect of the structural properties of that network on the scale interaction efficiency.

5.2 Effects of the inter-scale coupling

The effect of the coupling intensity k on the dynamics of the interacting populations is shown in Fig. 5.3. When the NMs are uncoupled to the NN, they oscillate in different dynamical regimes

that evolve at different frequencies, around 4.5 Hz and 11 Hz respectively. One NM oscillates in a spike-like fashion, while the other one oscillates more harmonically (Fig. 5.2A, compare the blue and green lines). The neuronal network, in turn, exhibits collective oscillations within the gamma range, around 45 Hz. The dynamical evolution for the coupled case, at $k = 1$, is shown in Fig. 5.3A. In this case, the dynamical regimes of the NMs are similar, and they become frequency locked.

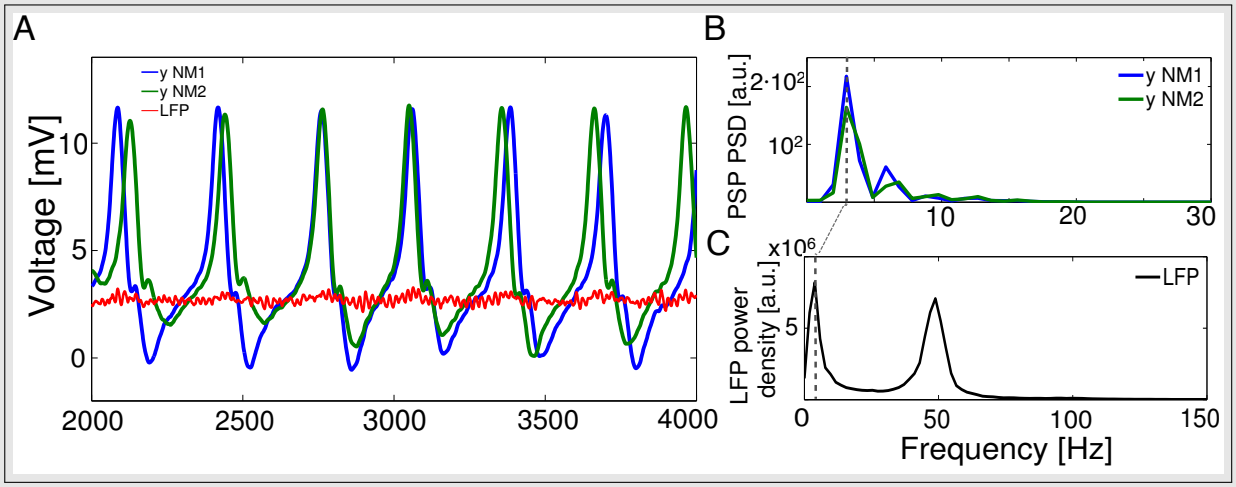

Figure 5.3: Collective dynamics of the coupled system. (A) (B) Power spectra of the net postsynaptic potential $y(t)$ of the neural masses when coupled ($k = 1$) through a subpopulation of 2000 neurons within the neural network. The common primary peak is tagged with a vertical dashed line at $\sim 4\ Hz$. (C) Power spectrum of the LFP when the subpopulation of the neuronal network is coupled ($k = 1$) to the neural mass models. Spectral densities are averaged over 20 trials.

We have further characterized the effect of the interaction through the power spectra of the time traces. As expected, the power spectra of the mass models in isolation (Fig. 5.2B) shows a clear peak at their natural frequencies (4.5 Hz and 11 Hz), while the LFP shows a strong peak around 45 Hz (Fig. 5.2C) that exceeds the non-zero contribution of the slower frequencies ∼4 Hz. We have seen that increasing coupling leads to a frequency locking regime between the neural masses, which is reflected in their spectral behaviour. For instance, at $k = 1$ the power spectra of the two NMs overlap, with a dominant peak around 4 Hz (Fig. 5.3B). The local gamma peak of the neuronal network is preserved (Fig. 5.3C), although the major change in amplitude occurs at slower rhythms, around the frequency of the NMs. This increase in the NN power at the delta band is due to the emergence of phase locking between this population and the outer NMs, as shown in Fig. 5.4A. This phase locking results in a sizable cross-correlation between the activities of the microscopic and mesoscopic populations for intermediate values of the size N of the NN subpopulation coupling the two NMs, as depicted in Fig. 5.4B (the difference between cross-correlations with NM1 and NM2 for small N is due to the different intrinsic dynamics of the two mesoscopic populations).

We have scanned k in order to track the transition to the frequency locked regime as coupling

increases. Fig. 5.4C shows the increase in the maximum cross covariance between the net postsynaptic potentials of the two neural mass models, averaged over 20 trials, when increasing k. When the NMs operate at different regimes they hardly synchronize but, for sufficiently high k, they increase their synchronization with increasing k. The averaged frequency mismatch decreases sharply at $k \approx 0.6$ (see Fig. 5.4D). According to these results, frequency locking for the two neural masses is achieved through a neuronal network that oscillates naturally at a much faster scale.

The effect of N, the size of the network, is studied in more detail below. The slower time scale of the NMs cannot follow the faster dynamics of the neural network and average out the gamma rhythm, resulting in a frequency shift towards the slower rhythm, which is also enhanced in the neuronal network.

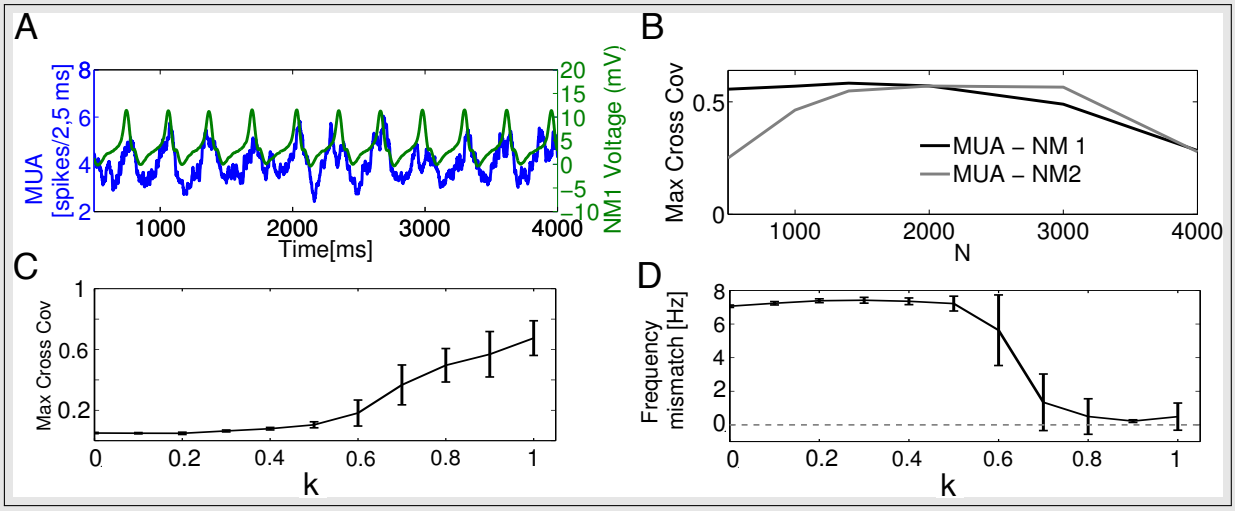

Figure 5.4: Correlation between NMs and NN activities for increasing NN size and coupling strength. (A) Time traces of the Multi-Unit Activity (MUA) signal of the neuronal network (blue, left axis) and the voltage of neural mass 1 (green, right axis). The MUA is calculated using a sliding window of length 50 ms. (B) Correlation between the MUA and voltage signals shown in panel E as a function of the number of neurons N from the central NN involved in the communication between the two NMs. (C) Averaged maximum cross covariance between the postsynaptic potential time traces of the neural masses for increasing inter-scale coupling strength k. (D) Frequency mismatch between the postsynaptic potential time traces of the neural masses for increasing coupling strength k.

Since the output of the neuronal network arises from the spiking activity of thousands of neurons, the interaction across models is mainly driven by the average dynamics of the population. Although the modelled LFP evolves in a faster time scale, neural mass models filter out rapid fluctuations. Therefore, the NMs mainly respond to changes of the mean input coming from the neuronal network modulated by k.

The input contribution into the NMs coming from the NN dynamics increases the average excitatory and inhibitory input signal into the pyramidal population (denoted by p_e and p_i, respectively, in Eqs. (A.23-A.24)). Since increasing the constant input to a NM can lead to

changes in the dynamical regime (and thus the frequency) of the oscillator, one could argue that the role of the neuronal network dynamics is unnecessary to mediate the synchronization transition observed. However, simulations in which the terms given in Eqs. (A.23 - A.24) are replaced by the temporal average of the coupling contributions indicate that the NMs are unable to synchronize their phases in these conditions (see Fig. 5.5B). This result shows that the NN dynamics is a key ingredient to achieve not only frequency locking but also phase locking between the two NMs.

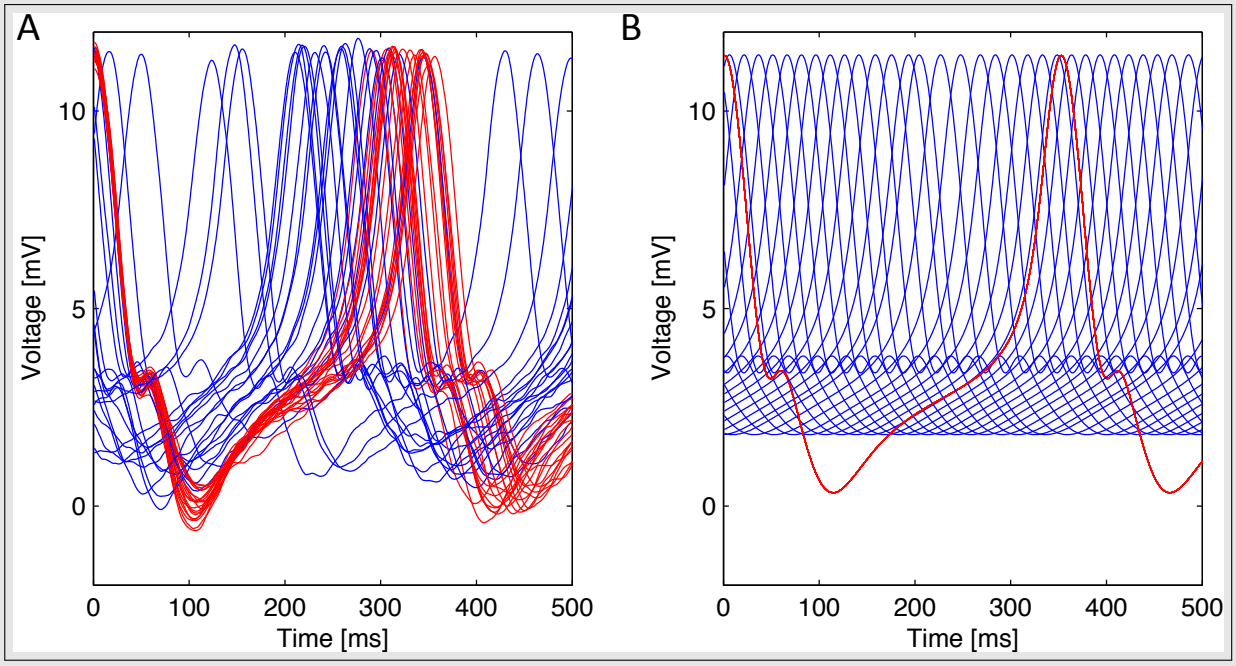

Figure 5.5: Coupling of NMs through dynamically evolving NN vs constant input. Phase consistence of different trials of PSPs of the NMs (the two colors correspond to the two NMs) when (A) the coupling is mediated by a variable MUA (coming from the NN) and (B) when MUA is replaced by its temporal average. In the latter case NMs are unable to synchronize their phases.

5.3 Effect of the topology of the microscopic neuronal population

In order to further study the role played out by the microscopic neural network in the synchronization dynamics we have also varied two main features of its architecture: its clustering (Figs. 5.6A,B) and the size of the area involved in the coupling, determined by the number of neurons projecting onto the NMs (Fig. 5.7). In graph theory, networks composed of nodes and edges can be characterized by their clustering coefficient, which quantifies the *connectedness* or local connectivity of the network (i.e. the probability that all nodes that are connected to a given node, are also connected between them). According to the Watts and Strogatz algorithm [*Watts and Strogatz*, 1998], a pure regular network can be turned into a small-world network, in which few edges separate any two nodes, by rewiring the connections. A rewiring

probability parameter, rp, determines the probability of replacing an existing edge by another one chosen randomly. Therefore, a rewiring probability equal to 0 implies a regular network whereas a rewiring probability equal to 1 implies a completely random network. By studying these parameters we are changing the dynamics of the NN and, therefore, its capacity to mediate the interaction between the two NMs.

Figures 5.6A,B outlines the dependence of the maximum cross covariance and the frequency mismatch between the two neural masses on the coupling strength k for different rp values. Note that the case $rp = 1$ corresponds to the results shown in Figs. 5.4C,D. Networks with higher clustering ($rp = 0.2$) are less efficient in synchronizing the oscillatory output of the neural masses. In this case, larger coupling strengths k are needed, with respect to a random network ($rp = 1$), to reach the frequency locking regime. Thus, the topology of the neural network affects the synchronization between the neural ensembles. Random networks have small path lengths at the expense of low clustering, and thus the average transmission time of the action potentials across the population is decreased. In this situation, synchronization arises for smaller coupling strengths. The result for a regular network, $rp = 0$ (which is not a realistic situation in the brain because the NN dynamics is lost), is also included in Figs. 5.6A,B.

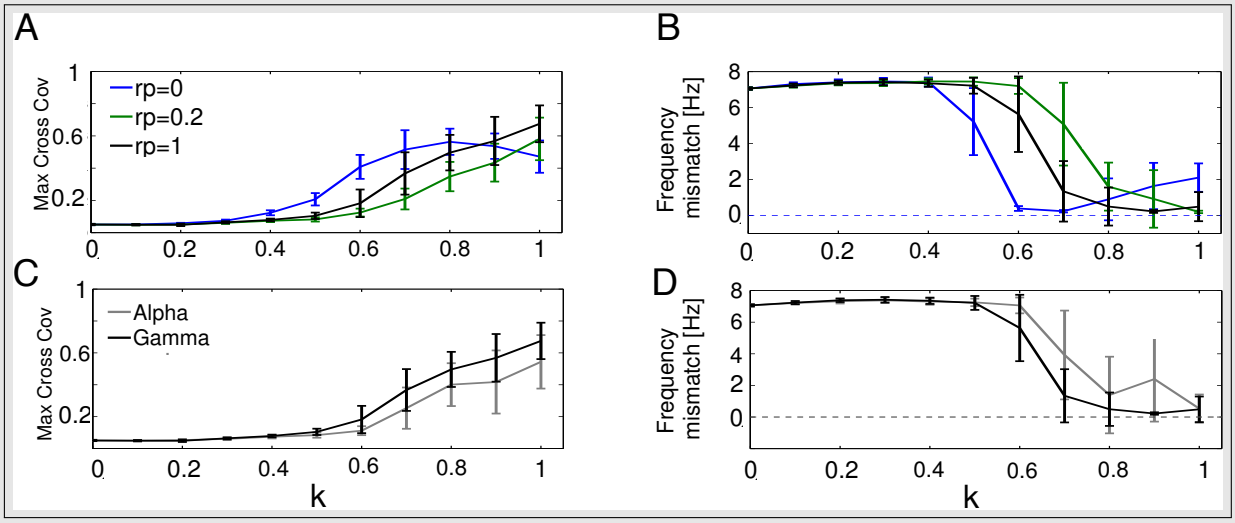

Figure 5.6: Influence of the topological and dynamical properties of the neuronal network on the interaction between the NMs. Maximum cross covariance (A) and frequency mismatch (B) between the NM average postsynaptic potentials for increasing rewiring probabilities rp of the neuronal network. Maximum cross covariance (C) and frequency mismatch (D) between the NM average postsynaptic potentials when the neuronal network works in the alpha regime, compared with the gamma case ($rp = 1$).

Besides topology, the intrinsic dynamics of the neuronal network also has an impact on the synchronization of neural masses. In our NN model we can slow down the frequency peak of the LFP by increasing the decay time constant τ_d of the inhibitory synapses (Eq. (A.19)), without altering the firing rate of the population. If the peak of the NN power spectrum is shifted towards the alpha band, closer to where the neural masses oscillate, the maximum cross

covariance is reduced and the frequency mismatch is increased for a given k value (Figs. 5.6C and 5.6D, respectively). Thus, even though the NN is operating closer in frequency to the NMs, and its individual neurons fire at the same rate as when the network operates in the gamma band (resulting in a similar MUA activity), the NMs are more difficult to synchronize. In the neural network, the action potentials are transiently synchronized and paced according to the time course of inhibition, leading to a recurrent behaviour that causes the global oscillatory dynamics. Faster rhythms, like gamma, correspond to a better precise timing of the firing, i.e. the action potentials of multiple neurons are tightly bounded in time, which seems to be key for the synchronization of the neural masses.

5.4 Effects of the size of the microscopic neuronal population

Finally, and as mentioned above, we have also studied how the synchronization of the NMs is affected by the size N of the subpopulation of neurons that mediate the coupling between them. In the results presented so far, this subpopulation was formed by $N = 2000$ neurons, randomly chosen from the whole population of 4000 neurons of the NN. We scanned N between 1 and 4000 neurons, the latter case corresponding to all neurons in the NN contributing to the firing rate impinging on the NMs and receiving their input. Figures 5.7A,B show the maximum cross covariance and the frequency mismatch for increasing coupling k at varying subpopulation sizes. The interaction between the NMs decreases as N decreases, and synchronization is only significant for $N > 1000$. N directly affects the strength of the coupling between the NN and the NMs, since this parameter determines the average MUA, i.e. the number of spikes elicited within the subpopulation. Hence, given a coupling strength k that enables an efficient interaction of the models, larger values of N lead to a lower frequency mismatch (Figs. 5.7C,D).

It is important to note that, although the size of the neural network is kept constant, increasing N boosts the coupling term, spreading the input from the neural mass across a larger population of neurons within the NN. Figure 5.7E shows the LFP power spectrum for increasing values of N for $k = 0.9$. Similarly to the transition from Fig. 5.2 (network in isolation) to Fig. 5.3 (coupled network with $k = 1$ for $N = 2000$), the major changes produced by the coupling occur at small frequencies, where the synchronization scale is centered, while the gamma rhythm interacts directly with the slower dynamics of the NMs. Decreasing N dramatically affects the dynamics of the coupling, which only takes into account the activity of this subpopulation. For sizes below $N \sim 1000$ the interaction is carried out by the low firing and highly noisy activity of small numbers of neurons, which are unable to synchronize large ensembles.

5.5 Conclusions

Our results do not imply that two neural mass oscillators can only synchronize through the mediation of a neuronal network. In fact if all three neuronal populations were described by NNs (or by NMs, for that matter) synchronization would also arise (see for instance Refs. [*Vicente et al.*, 2008; *Gollo et al.*, 2010] for the case of three coupled NNs leading to zero-lag synchronization). Neither do we claim that two brain oscillators can only synchronize through the mediation of a third one (see for instance *David and Friston* [2003] for an example of synchronization

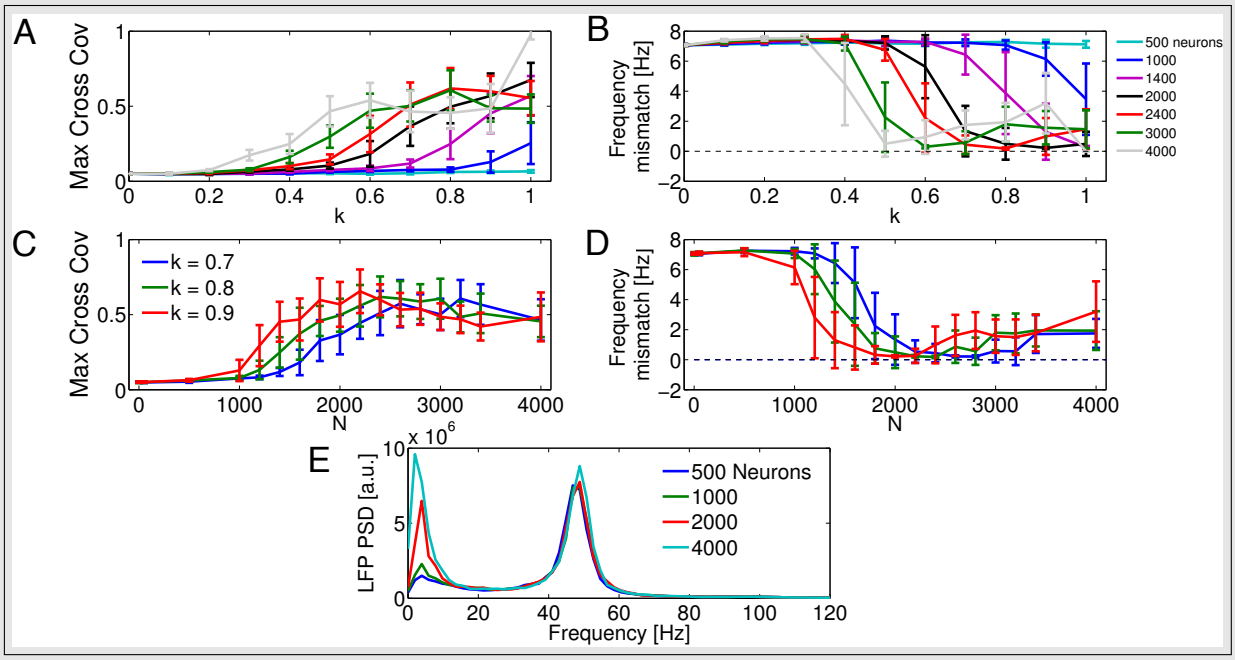

Figure 5.7: Effects of size of the microscopic neuronal population on the interaction between NMs. Maximum cross covariance (A) and frequency mismatch (B) between the NM average postsynaptic potentials as a function of coupling strength k, for various values of the size N of the subpopulation of the neuronal network that mediates the coupling. (C,D) Maximum cross covariance and frequency mismatch as a function of N for various values of the inter-scale coupling strength k. (E) Spectral power density of the LFP of the whole NN, when the NMs are connected with NN subpopulations of various sizes ($k = 0.9$). All results are averaged over 20 trials.

between two coupled NMs). What our study shows is that two mesoscopic brain oscillators can synchronize *even when* they are coupled only through a mediating population that is described by a microscopic model. In that sense, we use synchronization as a tool to probe the interaction between different spatial scales of neuronal populations. Previous efforts have been devoted to analyzing this interaction by performing a direct comparison of the behaviours of the microscopic and mesoscopic models. Faugeras et al., for instance, derived the equations of evolution of neural masses from the dynamics of a network of neurons described by a voltage-based model [*Faugeras et al.*, 2008], by performing an involved mean field analysis of the network, an approach that would be very challenging to apply to spiking neuron models. In order to perform such a multiscale mapping, *Rodrigues et al.* [2010] had to apply strong assumptions that included high correlation between the neurons in the microscopic populations and low-amplitude input currents. Here we have attempted to circumvent the complexity of those approaches by using a more phenomenological strategy, whose goal is to test whether microscopic and mesoscopic descriptions of neuronal populations communicate with one another by using synchronization as a proxy of effective communication.

Even when the neuronal network operates in a fast dynamical collective regime in the gamma range, a sufficiently large subpopulation of neurons within that network is able to mediate the

communication and subsequent synchronization between two neural masses that are described mesoscopically and operate at much lower frequencies. Frequency and phase locking arise even when the two neural masses operate at very different frequencies (in the theta and alpha bands) and with very different dynamical features (spike-like dynamics in one case and quasi-harmonic dynamics in the other). Structural clustering within the neuronal network diminishes the ability of the microscopic neuronal population to induce synchronization. The size of the subpopulation of neurons that directly coupled the two neural masses must also be large enough to allow the intrinsically irregular neurons to reach a sufficiently strong collective regime through which the two neural masses can communicate.

Two main features indicate the nontrivial contribution of the microscopic neuronal network in mediating the synchronization between the mesoscopic models. First, the two mesoscopic populations lock not only in frequency, but also in phase, when they interact with a dynamically evolving neuronal network. If the role of the network is played by an increased constant input to the neural masses equal to the average activity of the neuronal network, phase locking disappears. Second, if the neuronal network is made to operate in a slower collective regime (e.g. in the alpha band) the synchronization between the neural masses is decreased (while being still significant), even though the three oscillators are now closer in frequency.

The synchronization between the NMs is mediated by the locking between the NMs and the NN, which leads to an increase in the theta-band activity of the NN, as reflected in Fig. 5.3C. The fact that synchronization is maintained even when the NN is operating in the alpha band (Figs. 5.6C,D) indicates that the intrinsic NN dynamics does not interfere noticeably in the communication between the NM populations. Furthermore, the fact that synchronization improves slightly when the NN is operating in gamma (as shown also in Figs. 5.6C,D) shows that fast and slow scales interact only to a certain extent in order to drive the synchronization. We interpret this to be due to an increase in the precise timing of the firing that is associated with a faster neuronal rhythm. The results reported here point towards an alternative way to probe the interaction of scales in the brain, by using synchronization between neuronal populations as a way of testing the structural and functional conditions under which scale interaction occurs.

Chapter 6

Dynamics of excitation and inhibition at the mesoscale

"The role of inhibition in the working of the central nervous system has proved to be more and more extensive and more and more fundamental as experiment has advanced in examining it [...]. The whole quantitative grading of the operations of the spinal cord and brain appears to rest upon mutual interaction between the two central processes 'excitation' and 'inhibition', the one no less important than the other."

Sir Charles Scott Sherrington

Neurons in the brain are known to operate under a careful balance of excitation and inhibition, which maintains neural microcircuits within the proper operational range [*Dehghani et al.*, 2014]. Besides, excitatory and inhibitory couplings mediate in the interaction between microscopic and mesoscopic structures in the brain, as shown in the previous Chapter. However, how the balance between excitation and inhibition is played out at a pure mesoscopic level of neuronal populations is less clear. In order to address this question, in this Chapter we use a network of coupled neural mass models to study computationally the dynamics of networks of cortical columns operating in a partially synchronized (ir)regular regime. For the sake of simplicity, we first work with small motifs of 2 and 3 coupled elements, which already display complex excitatory and inhibitory patterns. We then consider larger topologies, focusing on a heterogeneous topology network, with a few of the nodes acting as connector hubs while the rest are relatively poorly connected. Our results show that in this type of mesoscopic network, excitation and inhibition spontaneously segregate, with some columns acting mainly in an excitatory manner while some others have predominantly an inhibitory effect on their neighbors. We characterize the conditions under which this segregation arises, and relate the character of the different columns with their topological role within the network. In particular, we show that the connector hubs are preferentially inhibitory, the more so the larger the column's connectivity. Besides, we show that the synchronization of the networks of cortical columns is extremely dependent on such excitation/inhibition patterns.

These results suggest a potential mesoscale organization of the excitation-inhibition balance in brain networks [*Kozyrev et al.*, 2014].

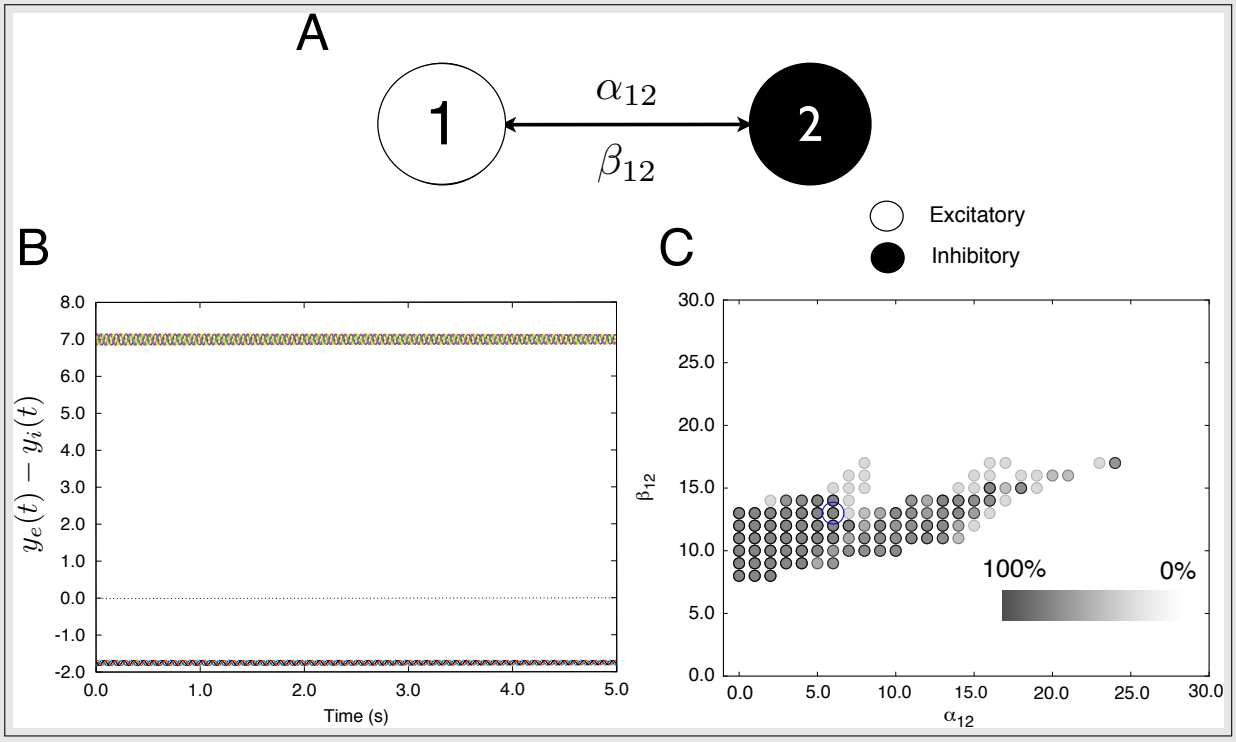

Figure 6.1: Excitation/Inhibition patterns in two coupled cortical columns. (A) Cartoon of two bidirectionally coupled cortical columns. (B) Time traces of the dynamical evolutions of the two nodes for 10 different sets of initial conditions. Segregation, in terms of $\langle y_e(t) - y_i(t) \rangle_t$, occurs. (C) Scatter plot of the occurrence of segregation in terms of the coupling constants α_{12} and β_{12} (see Eqs (A.6)-(A.8)). Gray circles indicate α_{12}, β_{12} values for which segregation occurs. Darker circles indicate higher occurrence of segregation for the 10 different sets of initial conditions. The blue circle indicates the case displayed in panel B.

6.1 Excitation/Inhibition patterns in a small system of coupled cortical columns

The interaction between excitatory and inhibitory populations of neurons in Eqs. (A.6, A.8) may give rise to oscillatory dynamics emerging at a mesoscopic time scale [*Jansen and Rit*, 1995]. Besides, the contacts between neural ensembles form loops that enhance the excitation or inhibition activity of these populations in a feedforward or in a feedback manner. Here, we study how different simple architectures allow a network of bidirectionally coupled cortical columns to *segregate*, i.e., to display different excitatory or inhibitory-dominated dynamics for the nodes which form the network. We focus on scenarios in which the interaction between the simple topology and the intrinsic dynamics results in the segregation of the columns.

First we consider a simple case (see Fig. 6.1A) where two identical columns are coupled bidirectionally. Each node representing a cortical column can be considered as inhibitory if the

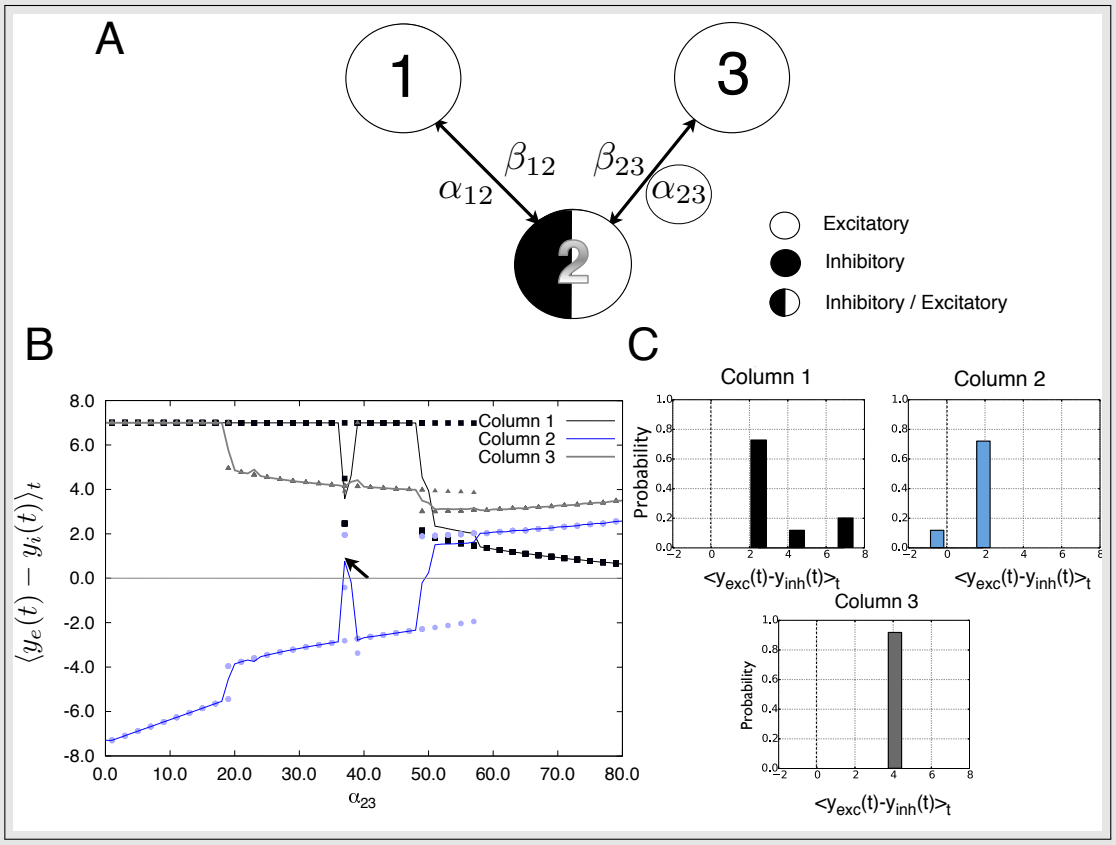

Figure 6.2: Excitation/Inhibition patterns in three coupled cortical columns (I). (A) Three bidirectionally coupled cortical columns forming a chain. (B) Variation of the coupling strength α_{23} while keeping all other coupling strengths fixed ($\alpha_{12} = 6.0$, $\beta_{12} = \beta_{23} = 13.0$). Points represent the values obtained for the different realizations and the continuous line the average of these values. The system shows complex excitatory-inibitory patterns in the region where α_{23} is approximately between 30.0 and 50.0. We can see that Column 1 remains excitatory through the different realizations, Column 2 switches from inhibitory to excitatory dynamics and Column 3 remains excitatory for all realizations. (C) Histogram of $\langle y_e(t) - y_i(t) \rangle_t$ for the three columns for the situation indicated with an arrow in panel B ($\alpha_{23} = 36.0$).

time averaged post-synaptic potential, resulting from the subtraction between the excitatory post-synaptic potential (EPSP, $y_e(t)$) and the inhibitory post-synaptic potential (IPSP, $y_i(t)$), is negative ($\langle y_e(t) - y_i(t) \rangle_t < 0$), or excitatory if the average post-synaptic potential is positive ($\langle y_e(t) - y_i(t) \rangle_t \geq 0$) ($\langle ... \rangle_t$ denotes temporal average, see Fig. 6.1B, see Appendix A.1.1). We have found the ranges for the excitatory coupling weight (α_{12}) and the inhibitory coupling weight (β_{12}) where the columns in Fig. 6.1A segregate into excitation and inhibition-dominated dynamics (see Fig. 6.1C).

Note that the bidirectional coupling sets a symmetry in the inter-column contacts that, nevertheless, allows an asymmetry in the settlement of $y_e(t) - y_i(t)$ for the two columns. In the different realizations of the dynamics the first (second) node may become excitatory (inhibitory) and in other realizations it may become inhibitory (excitatory). The excitatory/inhibitory character of the two nodes is dictated by the initial conditions of each column and the value of

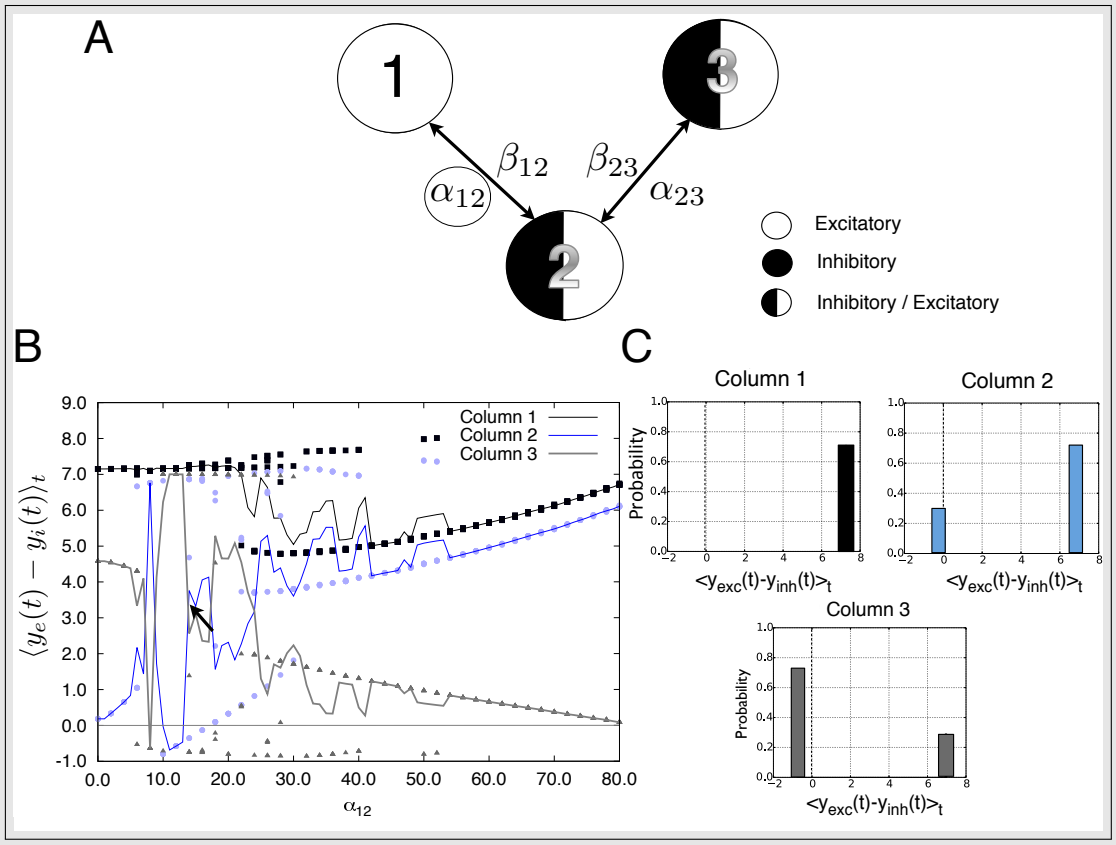

Figure 6.3: Excitation/Inhibition patterns in three coupled cortical columns (II). (A) Three bidirectionally coupled cortical columns forming a chain. (B) Variation of the coupling strength α_{12} while keeping all other coupling strength fixed ($\alpha_{23} = 12.0$, $\beta_{12} = 2.1, \beta_{23} = 21.5$). Points represent the values obtained for the different realizations and the continuous line the average of these values. The arrow indicates a situation in which Column 2 and Column 3 switch their characteristic excitatory/inhibitory behavior due to the influence of coupling strength α_{12}. The system is strongly multistable for α_{12} between 10.0 and 55.0. (C) Histogram of $\langle y_e(t) - y_i(t) \rangle_t$ for the three columns for the situation indicated with an arrow in panel B ($\alpha_{12} = 15.0$).

their coupling strength.

In Fig. 6.2 we have studied the dynamics of 3 columns coupled bidirectionally forming a chain. The central column is connected to other two, and so it is influenced by the coupling terms with them (see Fig. 6.2A). In this configuration we have set, on the one hand, α_{12} (the *excitatory coupling*) and β_{12} (the *inhibitory coupling*, see Eqs. (A.6, A.8)) to force the node 1 and the central node to segregate (as shown in Fig. 6.2) and, on the other hand, we have fixed the same inhibitory coupling strength on the other link and we have scanned the excitatory coupling α_{23} afterwards. The variation of α_{23} results in the identification of regions with monostable or multistable excitatory/inhibitory dynamics (see Fig. 6.2B).

Column 1 remains excitatory through this range of α_{23} but, in general, decreases when the parameter increases. $\langle y_e(t) - y_i(t) \rangle_t$ for Column 3 decreases in general but seems to start increasing for the highest values of α_{23}. Finally, the central column starts being inhibitory but becomes excitatory for $\alpha_{23} \approx 60$. So in this configuration, the excitatory unbalance between the

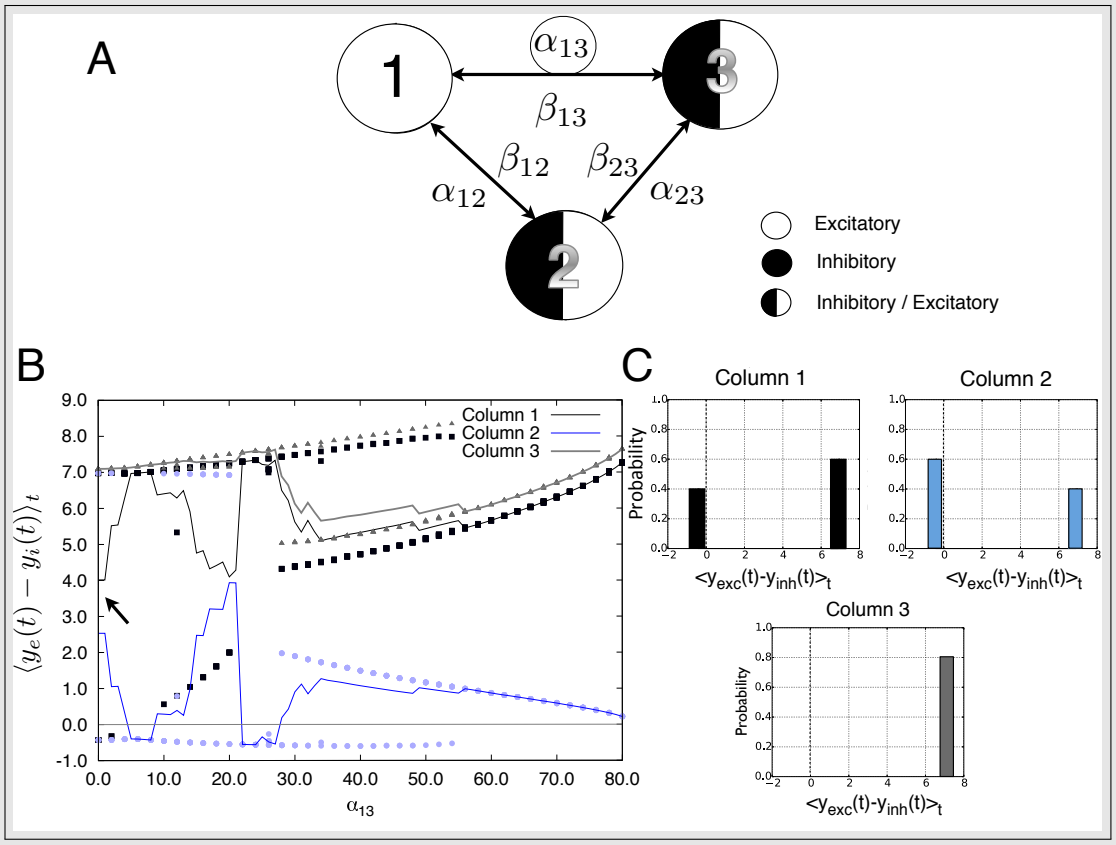

Figure 6.4: Excitation/Inhibition patterns in three coupled cortical columns (III). (A) Three bidirectionally coupled cortical columns forming a closed circuit. (B) Variation of the coupling strength α_{13} while keeping all other coupling strength fixed ($\alpha_{12} = \alpha_{23} = 1.0, \beta_{12} = 8.0, \beta_{13} = \beta_{23} = 1.0$). Points represent the values obtained for the 100 different realizations and the continuous line the average of these values. The arrow indicates a situation in which Column 2 and Column 3 switch their characteristic excitatory/inhibitory behavior due to the influence of coupling strength α_{13}. The system is strongly multistable for small values of α_{13} up to $\alpha_{13} \approx 50.0$. (C) Histogram of $\langle y_e(t) - y_i(t) \rangle_t$ for the three columns for the situation indicated with an arrow in panel B ($\alpha_{13} = 1.0$).

two branches fixes the (absence of) segregation of the central column. In particular, when α_{23} is small, the central node is inhibitory-dominated but as α_{23} increases the excitation becomes dominant in all nodes ($\langle y_e(t) - y_i(t) \rangle_t$ approaches common values for all nodes). One interesting result is the multistability observed for extended ranges of α_{23}. In Fig. 6.2C we have analyzed the case of multistable dynamics indicated by the arrow in Fig. 6.2B by computing the histograms of $\langle y_e(t) - y_i(t) \rangle_t$ for the different columns. As it can be seen some realizations in Column 2 are excitatory-dominated and others are inhibitory-dominated, whereas Columns 1 and 2 remain excitatory.

Still using the same topology, we have explored coupling values that allow multistable excitatory/inhibitory dynamics in two of the columns. Fig. 6.3B shows the behavior of $\langle y_e(t) - y_i(t) \rangle_t$ for each column and for increasing coupling strength α_{12}, keeping all other coupling strengths fixed (see caption in Fig. 6.3). In this case the inhibitory coupling strengths are not equal (i.e.

$\beta_{12} \neq \beta_{23}$), but, alongside with α_{12}, they force the Columns 2 and 3 to *segregate* and switch between excitation and inhibition (see dots indicating $\langle y_e(t) - y_i(t) \rangle_t$ values).
Like in Fig. 6.2, Column 1 remains excitatory but suffers from abrupt changes in $\langle y_e(t) - y_i(t) \rangle_t$ from very low α_{12} values up to $\alpha_{12} \approx 55.0$. Columns 2 and 3 can switch between excitatory or inhibitory dynamics between $\alpha_{12} \approx 5.0$ and $\alpha_{12} \approx 25.0$ (see blue circles and gray triangles in Fig. 6.3B). The histograms in Fig. 6.3C show the probability of Columns 2 and 3 to be either excitatory or inhibitory while Column 1 remains excitatory for the case indicated with an arrow in Fig. 6.3B. Again, there exist extended regions of multistability in terms of α_{12}.
Dynamical features displayed in Fig. 6.3 can also be found in Fig. 6.4 for closed circuit architecture and setting the coupling values to allow for segregated dynamics. The unbalance between inhibitory couplings in the circuit (see caption in Fig. 6.4) allows bistable dynamics to appear in Columns 1 and 2 for low values of coupling strengths (see Fig. 6.4B). The three columns suffer steep changes in $\langle y_e(t) - y_i(t) \rangle_t$ as α_{13} increases. Once more, there exist extended regions of multi-stability in terms of α_{13}. Finally, the multi-stable excitatory/inhibitory dynamics in Columns 1 and 2 for the case indicated with an arrow in Fig. 6.4B can be seen in the histograms of Fig. 6.4C, showing that this behavior is not exclusive of chain-like architectures.

6.2 Brain resonance and the balance between excitation and inhibition

Neurons in the brain may coordinate their spiking activity in the presence of external rhythmic stimuli. Such stimuli may be related with cognitive tasks, impaired brain performance or normal brain states. For instance, it has been shown that a periodic visual stimulation may entail an entrainment of the intrinsic alpha rhythm towards the stimulus frequency in the visual cortex. This stimulus may produce complex *chaotic* dynamical evolutions [*Spiegler et al.*, 2011a]. Besides, sine-graded stimuli in the auditory system is known to lead to synchronization patterns related with inter aural time differences, crucial for spatial localization of sounds [*Batra and Fitzpatrick*, 1997]. On top of this, it has also been shown that texture discrimination creates patterns of excitatory and inhibitory activity in large populations of neurons from the visual system [*Caelli*, 1980] and the barrel cortex [*Feldmeyer et al.*, 2013] upon whisker input. Such feature gives rise to competitive selection of active regions, also known as *winner-takes-all*, that determines the non-linearity and functional complexity of cortical networks. We here explore how complex dynamical evolutions emerge from the interaction between simple harmonic stimuli and the intrinsic oscillations of cortical columns. Besides, we study the conditions for which such complex time evolutions, in the form of oscillatory electric potentials, may synchronize given the constraints imposed by the topology and the strength of the excitatory and inhibitory couplings within the studied cortical columns networks.

6.2.1 Single column resonant dynamics

Chaotic dynamics appears in a cortical column when adding a periodic spike density, $\delta \sin(2\pi f t)$, to the constant excitatory external input, p_e (see Eq. (A.7)). The irregularity of this dynamics can be quantified by computing the Maximal Lyapunov Exponent (MLE) [*Spiegler et al.*, 2011b],

which computes the rate of exponential separation of two nearby trajectories in the phase space (see Appendix B.1.1), as shown in Figure 6.5A. That plot represents the MLE obtained for a periodically forced single cortical column when varying its driving amplitude δ and frequency f. A positive MLE corresponds to a chaotic dynamical evolution of the system. It is noticeable that many combinations of driving frequency and amplitude lead to chaos, and that a small domain characterized by negative MLE, with $f \sim 8.7\ Hz$ and scaled driving amplitude δ/C around $0.7\ Hz$, appears inside the chaotic domain. From now on we provide scaled values for input amplitudes and coupling strengths in order to compare the order of magnitude of these parameters with the global neural mass parameter C (see Table A.1). Calculating the MLE

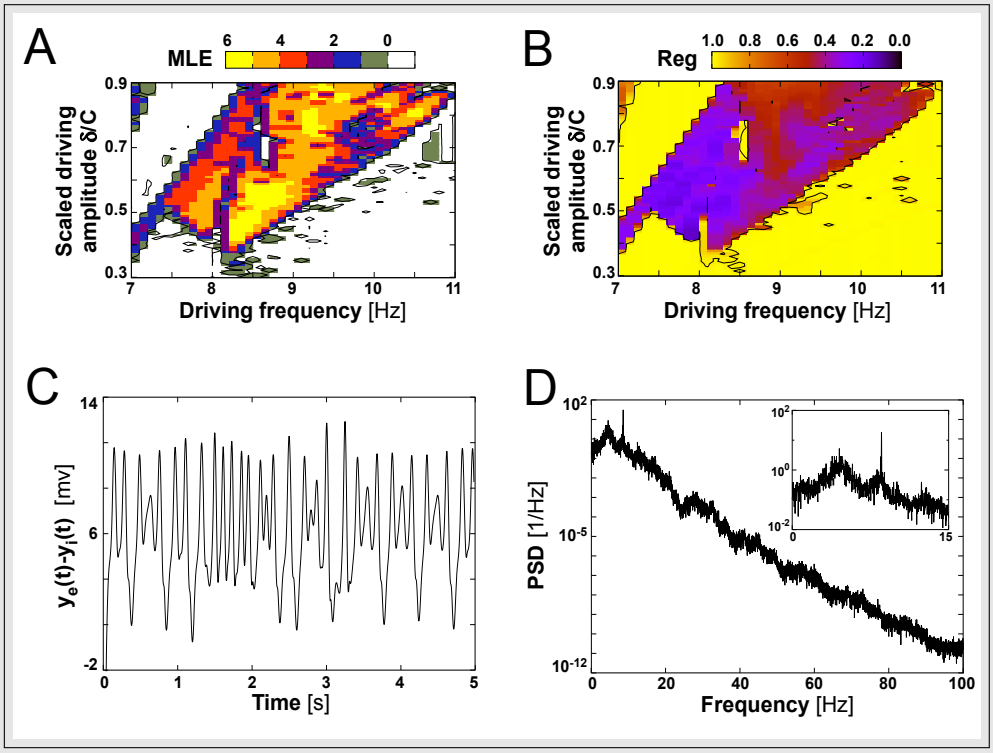

Figure 6.5: Chaotic behavior of an isolated, periodically driven cortical column. (A) Maximal Lyapunov Exponent (MLE) for different driving amplitudes and frequencies (see Appendix B.1.1). Parameter values are those given in Table A.1. (B) Regularity parameter obtained in the same conditions as in panel A (see Appendix B.1.1). (C) Example of a chaotic signal obtained for a driving frequency $f = 8.5\ Hz$ and scaled driving amplitude $\delta/C = 0.49\ Hz$. With these parameters MLE= 5.24 and $Reg = 0.37$. (D) Power spectrum of the signal shown in C. This complex spectrum shows a narrow peak at the driving frequency (see inset).

becomes costly in terms of computation when dealing with a large number of columns. Thus, we will use a different measure of the regularity of the dynamics, given by the parameter Reg, hereafter. This quantity is calculated using the second maximum of the autocorrelation function for $y_e(t) - y_i(t)$ signal, as defined in Eq. (B.4) of the Appendix B.1.1. Figure 6.5B shows the values taken by this parameter as a function of δ and f. The regions characterized by large positive (negative) values of the MLE in Figure 6.5A correspond to regions with low (high) value of Reg in Figure 6.5B. An example of chaotic evolution for driving frequency $f = 8.5\ Hz$ and scaled

driving amplitude $\delta/C = 0.49\ Hz$ is illustrated by the signal dynamics and its corresponding power spectrum density (PSD) in Figures 6.5C and D, respectively. These results show that the response of a node to a simple periodic driving may be very complex in both the time and frequency domains. The parameter *Reg* will be used hereafter to quantify the regularity of the signals that characterize the network dynamics.

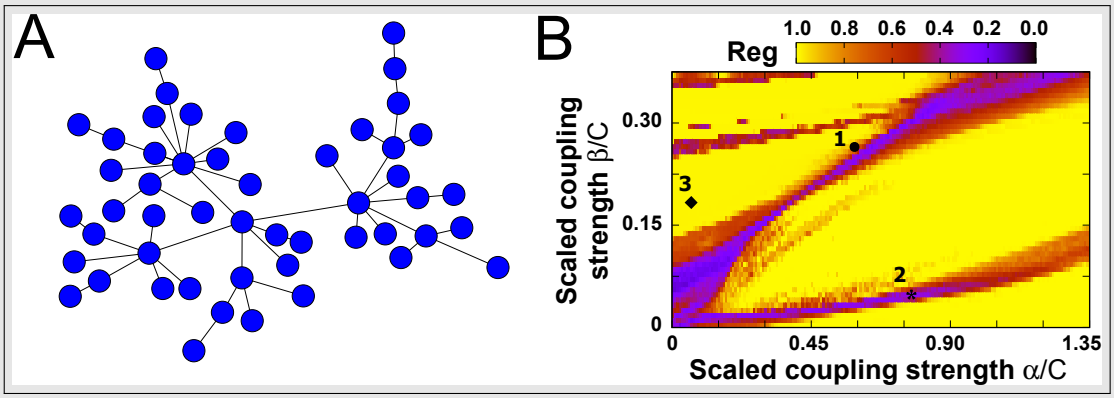

Figure 6.6: Regularity of the coupled system. (A) Topology of the network of cortical columns studied below. The network is constructed using the Barabási-Albert algorithm with $m_0 = 1$ initial nodes (see Appendix B.2.1 for details). (B) Regularity parameter averaged over 1 network of 50 coupled cortical columns (see panel (A)), for 20 different realizations of the initial conditions and for varying excitatory and inhibitory coupling intensities. Darker regions indicate less regular dynamics (chaotic), whereas lighter regions indicate more regular dynamics. Annotations in the plot indicate parameter values that will be studied later in Figures 6.7, 6.8A, 6.8C, 6.10A and 6.10B.

6.2.2 Network activity

Our study is centered in a 50-node network with inhomogeneous connectivity, represented in Figure 6.6A. The nodes' degree distribution in such network follows a power-law (a full characterization of the network and the coupling scheme is presented in the Appendix B.2.1). The network study was conducted using a fixed set of driving parameters, p_e, p_i, δ and f, which for isolated nodes produced irregular dynamical evolutions (see Table A.1 and Figure 6.5C). All nodes of the network are identical and receive the same external input. The input contribution resulting from the neighbors is weighted for each node in such a way that every node receives an input spike density within the same total bounded range (see Eqs. (A.9 - A.10) for more details).

The inter-columnar coupling intensities are determined by parameters α and β for the excitatory and inhibitory coupling, respectively (see Eqs. (A.6 - A.8)). We calculated the regularity averaged across the fifty nodes of a single network and over twenty different random realizations of the initial conditions. Figure 6.6B shows the map of the average regularity for the coupled nodes as a function of the two coupling intensities. This figure shows that certain regions of parameter space exhibit a low level of regularity. In particular, for a fixed value of the excitatory coupling α, the dynamics becomes irregular for both sufficiently large and sufficiently small values of the inhibitory coupling β. The distribution of these irregular regions, in terms of

α and β, depends on the other parameters of the system. For some α-β combinations (shown in more detail below) periodic, quasi-periodic and chaotic nodes coexist in a single network, even though all nodes receive the same driving. For other α-β combinations, the whole network exhibits either highly regular or highly irregular dynamics.

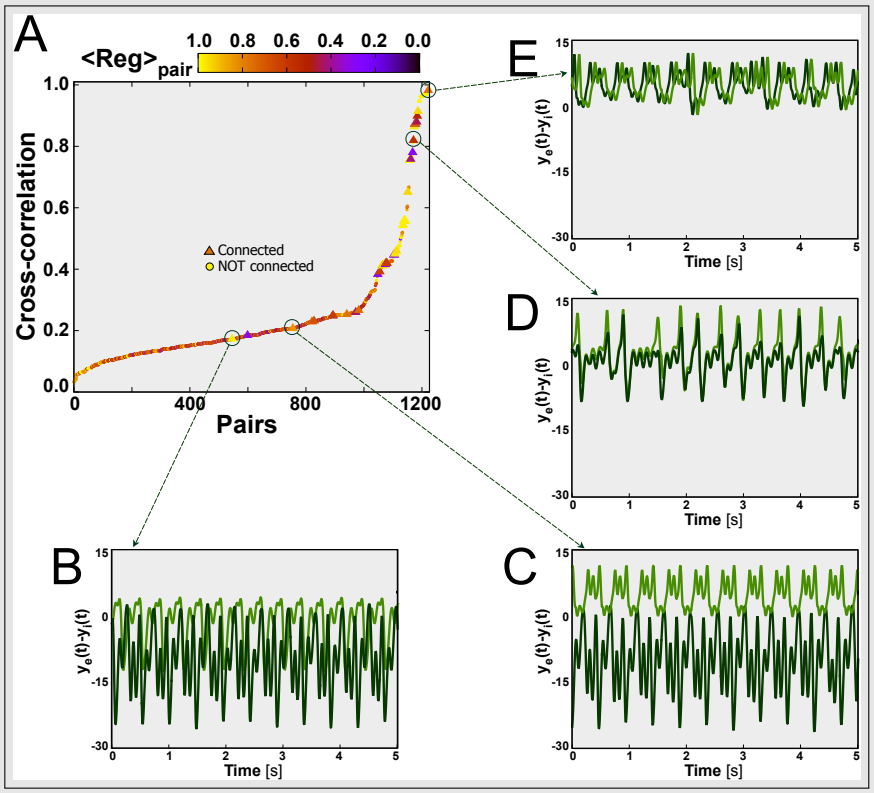

Figure 6.7: Node-pair correlation and dynamical clustering. (A) Maximal cross-correlation $C_{max}(\tau)$ (y axis) and average regularity (color coded) between pairs of cortical columns for scaled $\alpha/C = 0.56$ and $\beta/C = 0.26$ (point 1 in Figure 6.6B). Connected (not connected) pairs of nodes are shown as triangles (circles). The dynamical evolution of selected node pairs is shown in panels B-E. In (E) the two nodes are synchronized at zero lag, and one of the time traces has been shifted horizontally for clarity.

6.2.3 Correlation between pairs of cortical columns

The inter-columnar coupling intensities determine not only the regularity of the dynamics of the individual nodes, but also their synchronization capacity. In particular, for fixed α-β values, different degrees of synchronization appear between different pairs of nodes of the network. Figure 6.7A plots the maximal cross-correlation values, $C_{max}(\tau)$, for all pairs of nodes i, j, ordered for increasing correlation, for scaled $\alpha/C = 0.56$ and $\beta/C = 0.26$ (labeled as point 1 in Figure 6.6B). Directly connected pairs, represented by triangles in Figure 6.7A, have values of $C_{max}(\tau)$ in the range 0.2–1, and lie mostly above $C_{max}(\tau) = 0.4$, indicating that the activity of direct neighbors is highly correlated. For pairs of nodes that are not connected directly (shown as circles in Figure 6.7A) the cross correlation is spread across the entire range 0–1. In order to relate the amount of correlation between node pairs with the regularity of their dynamics,

Figure 6.7A shows in color coding the regularity parameter described above (averaged over the two nodes in the pair). For the set of parameters considered in Figure 6.7A, the network-averaged regularity is $Reg \approx 0.6$ (see point 1 in Figure 6.6B). In that case there are node pairs evolving in a regular way (lighter symbols, see e.g. Figures 6.7B,C) or in a more irregular manner (darker symbols, see e.g. Figures 6.7D,E), although there is no clear association between regularity and correlation level.

As described above, in the neural mass model used here the activity of each node is defined by the excitatory (EPSP) and inhibitory (IPSP) inputs to the pyramidal population ($y_e(t)$ and $y_i(t)$, respectively). Hence, each node (representing a cortical column) can be considered inhibitory-dominated if $\langle y_e(t) - y_i(t) \rangle_t < 0$, and excitatory-dominated if $\langle y_e(t) - y_i(t) \rangle \geq 0$, where $\langle \cdots \rangle_t$ denotes temporal average. Figure 6.7B shows the dynamics of the total post-synaptic potential signal $y(t) = y_e(t) - y_i(t)$ for a pair of directly connected nodes characterized by high regularity and low correlated activity. In this case, the activity of both nodes is dominantly inhibitory. In contrast, the pair of nodes illustrated in Figure 6.7C (which are also directly connected and have low correlation) have opposite activity, with one node being purely excitatory (light green curve), while the other is mainly inhibitory (dark green curve). The separation of the activities of the two nodes in two dominant exclusive types (one excitatory and one inhibitory) is an emergent feature that we have termed *segregation*, which was discussed in the previous section and will be analyzed in detail in the next one. Figure 6.7D shows an example of highly correlated activity and low regularity of two directly connected cortical columns which are excitatory. Finally, Figure 6.7E shows very highly correlated activity for a pair nodes that are not directly connected. In this case the correlation is so strong that the two nodes exhibit exactly the same dynamics, with zero-lag synchronization (one of the time traces as been slightly shifted horizontally so that the two series can be discerned). This unconnected pair is coupled indirectly through a third node, a feature that can give rise to generalized synchronization [*Zhou and Roy*, 2007; *Vicente et al.*, 2008].

6.2.4 Excitatory/inhibitory segregation

The results from Figure 6.7 show that coupled neural masses can exhibit a regime of partial synchronization in which the net activity of the nodes is segregated between mostly excitatory and mostly inhibitory activity (e.g. Figure 6.7C). We now consider the dependence of segregated dynamics with the inter-columnar coupling strengths α and β, for scaled $\alpha/C = 0.790$ and $\beta/C = 0.037$ (point 2 in Figure 6.6B). We run a set of 50 simulations, each one with a different network, constructed as described in the Appendix B, with the same topological parameters and different random seeds. For this α and β values, the activity $y = \langle y_e(t) - y_i(t) \rangle_t$ of all nodes is positive (Figure 6.8A). Note that now $\alpha \gg \beta$, which corresponds to the inter-columnar coupling being dominated by excitation. In the opposite case, when inter-columnar coupling is dominated by inhibition, (e.g. scaled $\alpha/C = 0.075$ and $\beta/C = 0.190$, point 3 in Figure 6.6B), the dynamics of the nodes is more regular and segregated, as illustrated by Figure 6.8C. In this case, a large fraction of the nodes maintain a dominantly excitatory activity, and approximately one fifth of the nodes exhibit inhibitory dynamics (Figure 6.8D). Visual inspection of Figure 6.8C seems to indicate that the connectivity hubs of the network are preferentially inhibitory. This observation

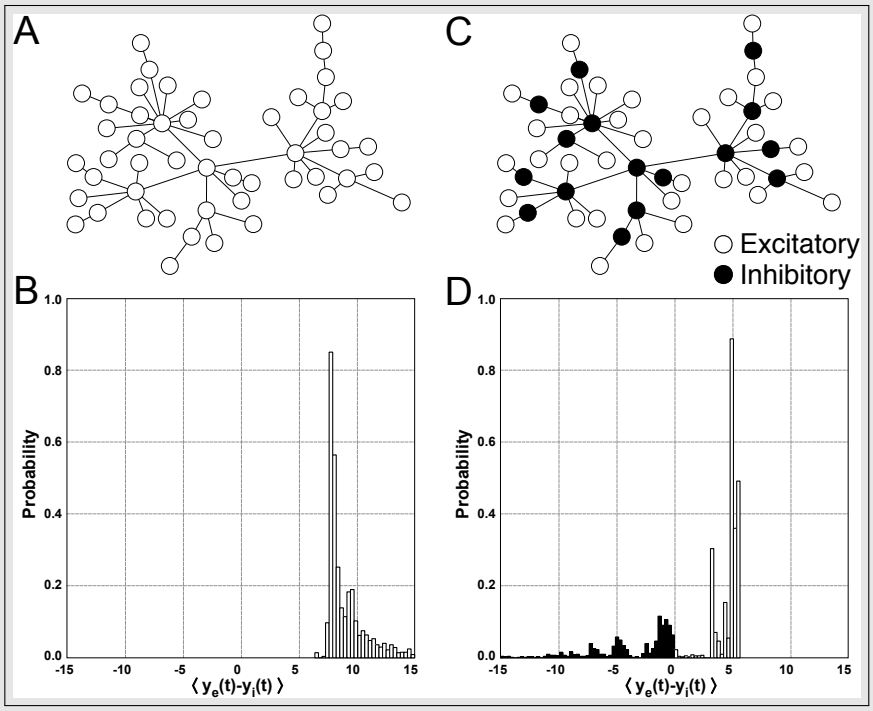

Figure 6.8: Excitatory/inhibitory segregation of cortical columns. (A) Example of a scale-free network with by all nodes exhibiting excitatory dynamics (empty circles). Here $\alpha/C = 0.790$ and $\beta/C = 0.037$ (see point 2 in Figure 6.6B). (B) Average distribution of the activity $\langle y_e(t) - y_i(t)\rangle_t$, obtained from the analysis of 50 different scale-free architectures using different random seeds for the same α and β parameters as in panel A. The extreme values in the tail of the distribution are not represented. (C) Example of a scale-free network with by some nodes exhibiting excitatory dynamics (empty circles) and some nodes exhibiting inhibitory dynamics (filled circles). Here $\alpha/C = 0.075$ and $\beta/C = 0.190$ (see point 3 in Figure 6.6B). (D) Average distribution of $\langle y_e(t) - y_i(t)\rangle_t$ corresponding to panel C.

will be quantitatively tested below.

In order to quantify the robustness of the segregation, we now compute the excitation/inhibition segregation index (EIS), as defined in the Appendix B.1.5, in terms of the parameter space defined by the coupling parameters α and β. This index compares the excitatory and inhibitory sides of the histogram distribution of $\langle y_e(t) - y_i(t)\rangle_t$ (as shown in plots B and D of Figure 6.8). A value $EIS = 0$ means that there is no separation between excitation and inhibition (all nodes are either purely excitatory or purely inhibitory), whereas large values of EIS mean that the number of nodes is evenly distributed in each side of the histogram, with a large difference of the $\langle y_e(t) - y_i(t)\rangle_t$ value between excitatory and inhibitory nodes. Figure 6.9 shows the distribution of EIS for the region of α-β parameter space studied so far. We observe that the dynamics is roughly separated in three domains. A domain characterized by no segregation, labeled as 'N' in the plot, corresponds to a dominantly excitatory input. An intermediate domain, labeled 'L', is characterized by a low level of segregation. Finally, if β is larger than α, a regime of high segregation, labeled 'S', arises. Note that the transitions between the three domains are rather sharp.

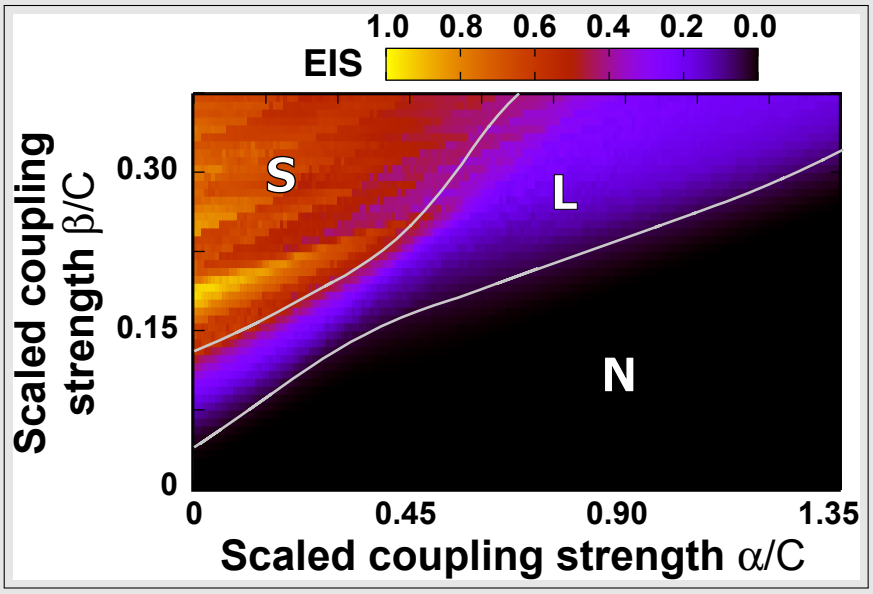

Figure 6.9: Excitatory/Inhibitory Segregation index (EIS). The EIS index quantifies the relative distribution of excitatory- and inhibitory-dominated dynamics. Three different domains exist, labeled by 'N' (no segregation), 'L' (low segregation) and 'S'(high segregation).

In order to determine the influence of the network characteristics on the dynamics of the nodes, we examined the relationship between the number of connections of each node (degree), its average activity $\langle y_e(t) - y_i(t) \rangle_t$, and its regularity. Figure 6.10 shows the results for the α-β combinations used in Figure 6.8. The first feature that is evident from those plots is that the average activity of the nodes is strongly correlated with their degree, both when the inter-columnar coupling is mainly excitatory (Figure 6.10A) and when it is mostly inhibitory (Figure 6.10B). This can be understood from the fact that a hub receives input from a large number of nodes, and if this input is mostly excitatory (as in Figure 6.10A) the resulting activity of the node will be strongly excitatory, more so than nodes with a small number of inputs. Conversely, if the coupling is mainly inhibitory (as in Figure 6.10B), the activity of the hubs will be dominantly inhibitory, while the poorly connected nodes will receive a weaker inhibitory input. In this case, however, and in contrast with the situation of Figure 6.10A, the weak inhibitory input received by the low-degree nodes will be counterbalanced by an external excitatory input (p_e as defined in the Appendix A.1.1), which acts upon all nodes of the network. For appropriate parameter values this external input dominates over the input coming from the neighboring nodes, resulting in an average activity that is predominantly excitatory for these low-degree nodes, while the highly connected nodes behave in an inhibitory manner. This leads to segregation between inhibitory and excitatory nodes, as described above and shown in Figures 6.8 and 6.9, with the inhibitory role taken over by the network hubs.

There is also an important difference in the distribution of regularity of the nodes, depending on the segregation exhibited by the network. In the absence of segregation (Figure 6.10A), the nodes of intermediate degree exhibit a broad range of regularity, from very irregular to very regular modes. In contrast, in the presence of segregation (Figure 6.10B) the intermediate-degree

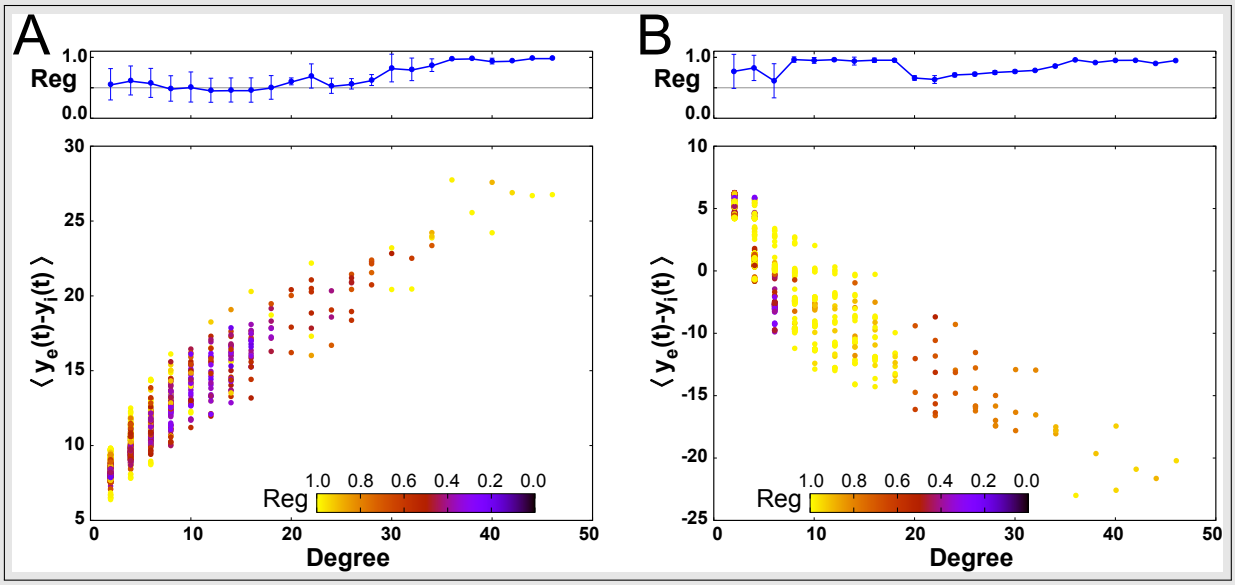

Figure 6.10: Degree organization of the excitation-inhibition segregation. (A) Average activity of all nodes of the networks as a function of their degree, corresponding to the cases analyzed in Fig. 6.8B. (B) Average activity of all nodes of the networks as a function of their degree, corresponding to the cases analyzed in Fig. 6.8D. Color coding denotes the regularity for each node in the networks, and upper panel shows the average regularity in the nodes' dynamics as well as its standard deviation. Both in panels A and B, color coding denotes the regularity of nodes in the networks, and upper panels show the average regularity in the nodes' dynamics as well as its standard deviation.

nodes display highly regular dynamics. This is due to the fact that in the latter case the dominant activity is inhibitory, and inhibition reduces irregularity and favors synchronization. A common feature of the networks, irrespective of the segregation level, is that low-degree nodes exhibit a large diversity of regularities. This happens because the regularity of the dynamics of a node will depend on the degree of the neighbors that are connected to it, and thus the low-degree nodes might be highly influenced by other low-degree nodes (given that the coupling is scaled by the inverse of the product of the degrees of the two connected nodes, see Appendix B) or weakly influenced by high-degree columns.

The extent of segregation in networks with other topological features is explored in Figs. 6.11 and 6.12. In Fig. 6.11 we study segregation in scale-free networks of higher clustering than the ones studied previously (see Figs. 6.6 to 6.10). The level of EIS is decreased substantially when the clustering is increased up to 0.4 (see Fig. 6.11A, see Appendix B for a definition of clustering), indicating a dependence of this effect on the heterogeneity of the network. However, for a clustering value of 0.7 EIS levels increase (see color bar in Fig. 6.11B), showing a complex dependence of segregation on the heterogeneity of scale-free networks. Moreover, segregated regimes display higher regularity, which can be related to the emergence of inhibitory columns in the network. In Fig. 6.12 we study other topologies ranging from ring to random arrangements. Figs. 6.12A,B show two ring networks whose nodes have a different number of neighbors. Remarkably, in this homogeneous networks segregation does no occur (see that the whole EIS landscape is 0).

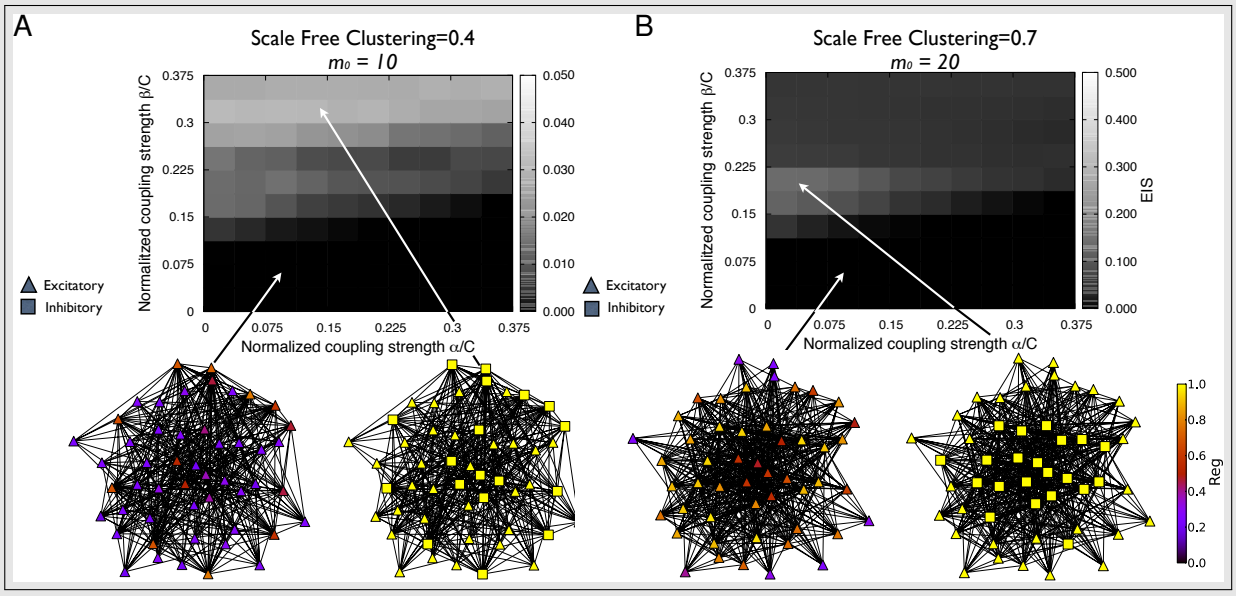

Figure 6.11: Segregation in scale-free networks. (A) EIS and examples of scale-free networks constructed using the Barabási-Albert algorithm with initial nodes $m_0 = 10$. The networks have a clustering of 0.4, which leads to a decrease in the level of segregation. Besides, low segregation allows low regularity whereas higher segregation induces higher regularity (see color coding). (B) For higher clustering EIS level increases (see color bar) which shows that there can be optimal levels of heterogeneity in scale-free networks depending on the clustering for segregation to occur. The regularity also depends on segregation, with low segregation networks displaying low regular signals and higher segregation networks displaying high regular signals.

Therefore, the transition between excitatory and inhibitory-dominated dynamics in the nodes (cortical columns) is abrupt. Such feature reinforces the hypothesis of a strong dependence of segregation on the heterogeneity of the network. Figs. 6.12C,D show two examples of small-world networks whose nodes have different number of neighbors. In such cases, segregation is present but decreases when the number of neighbors increases. Finally, Figs. 6.12E,F show two random networks whose nodes have different number of neighbors. In these cases, the dynamics of segregation is similar to that of small-world networks, i.e., the larger the number of neighbors the lesser the EIS values.

As a final remark, segregation is also present in other mesoscopic neural decriptions, showing the universality of the phenomenon. We studied the dynamics of two coupled Wilson-Cowan oscillators [*Wilson and Cowan*, 1972; *Campbell and Wang*, 1994] (see Fig. 6.7A), which showed different levels of segregation depending on the excitatory and the inhibitory coupling strengths K_{ij}^{exc}, K_{ij}^{inh} (see details of the model in Appendix A.1.1). This is shown in Fig. 6.11B in terms of $x(t) - y(t)$, which resembles the observable typically used in the Jansen and Rit model. Besides, segregation occurs when the excitatory and the inhibitory blocks of each oscillator receive a different level of external stimulus, that is, $p_1 \neq p_2$ as well as $q_1 \neq q_2$ (being $p_i \neq q_i$).

In Fig. 6.11C we show segregation in terms of K_{ij}^{exc}, K_{ij}^{inh}. For the case of Wilson-Cowan oscillators segregation might be excitatory or inhibitory-dominated, depending on which coupling term (K_{ij}^{exc} or K_{ij}^{inh}) is higher (as shown in Fig. 6.11C white regions).

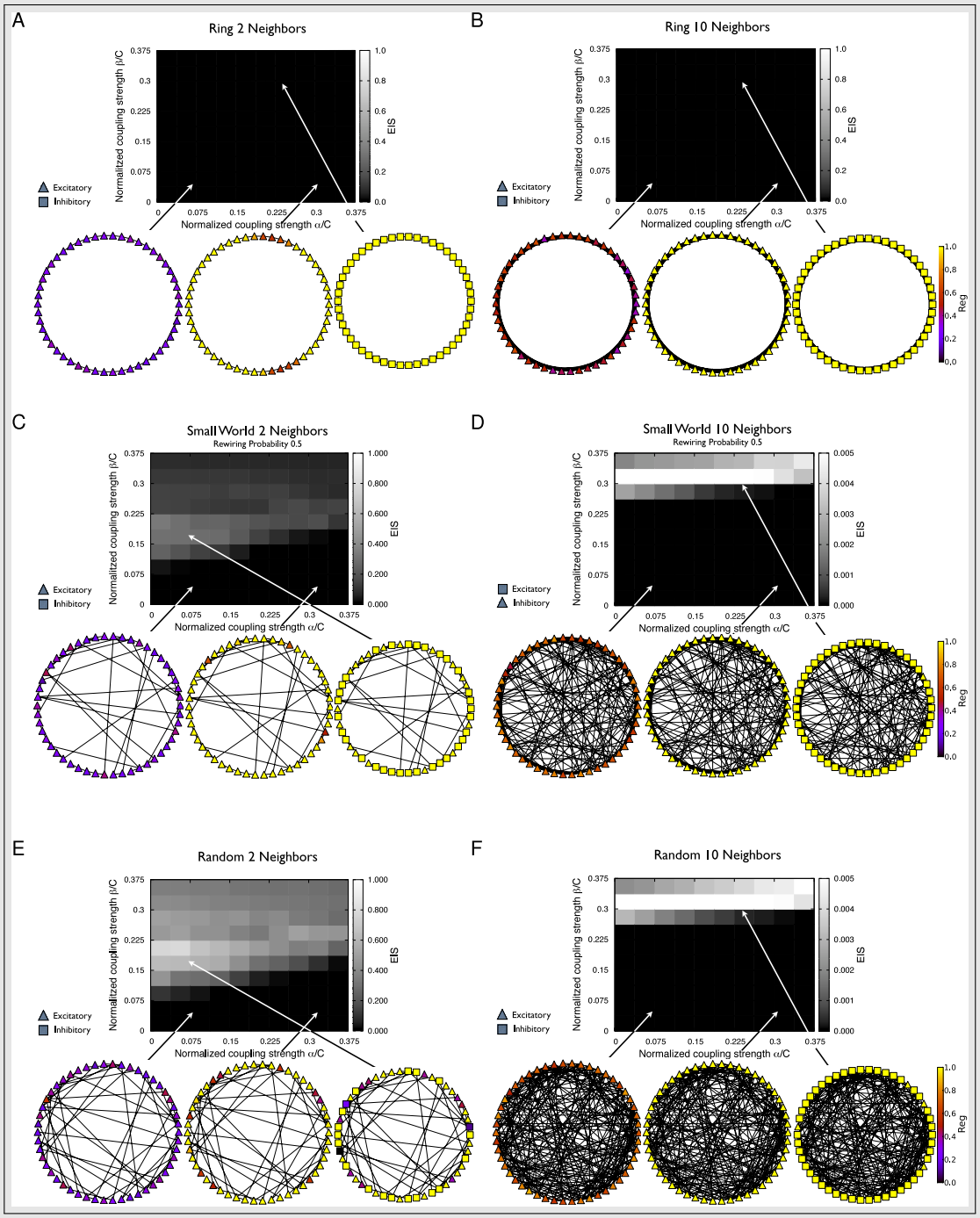

Figure 6.12: Segregation in ring, small-world and random networks. *EIS* levels and examples of networks in (A) ring topology with two neighbors and (B) ring topology with ten neighbors, in (C) small topology with two neighbors and (D) small-world topology with ten neighbors, in (E) random topology with two neighbors and (F) random topology with has ten neighbors.

We conclude that segregation may arise when some minimal ingredients are present: excitatory and inhibitory blocks exist and such blocks may couple through excitatory and inhibitory

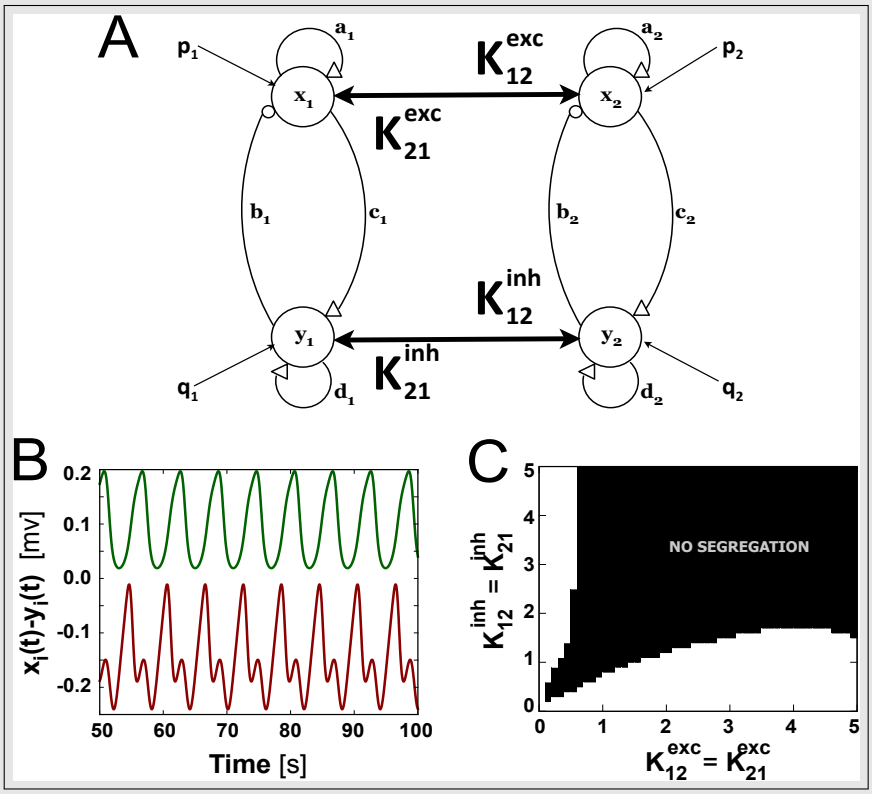

Figure 6.13: Segregation of two coupled Wilson-Cowan oscillators. (A) Coupling scheme between the two oscillators. (B) Time traces of the subtracted signal $x_i(t) - y_i(t)$ for the two segregated oscillators, in an excitatory-dominated coupling scheme ($K_{exc} = 1$, $K_{inh} = 0.1$). (C) Resulting segregation map for different excitatory and inhibitory coupling strengths.

connections. Then, segregation appears for the adequate range of coupling strengths.

6.3 Conclusions

Our computational analysis of small cortical columns shows that excitation and inhibition are distributed in a non-trivial manner at the mesoscopic level. This behavior requires the coupling of cortical columns via both excitatory and inhibitory connections. Our observations indicate that depending on the coupling architecture, each column may acquire a well-defined excitatory or inhibitory character, or the coexistence of excitation and inhibition in a network.

We make several assumptions. First, we consider that the cortical columns are subject to a periodic excitatory input that may have different origins. It may represent, for instance, the input activity from a nearby cortical column [*Huang et al.*, 2011], a sensory input reflecting periodic stimulation [*Spiegler et al.*, 2011b] or the afferent input from a sub-cortical structure (such as the thalamus) [*Gollo et al.*, 2010]. As a result of this periodic driving we may observe chaotic dynamics in single columns, in accordance with previous studies [*Spiegler et al.*, 2011b]. This irregular regime appears in broad regions of the parameter space defined by the frequency and amplitude of the input signal (Figure 6.5A,B).

A second assumption is the heterogeneous nature of the connectivity between coupled neuronal

populations. This implies that a small number of cortical columns are more strongly connected than the majority of the nodes in the neural mass network. Such heterogeneous connectivity profile is supported by experimental observations [*Zamora-Lopez et al.*, 2009; *Gong et al.*, 2009; *Modha and Singh*, 2010; *Guye et al.*, 2010; *Bullmore and Sporns*, 2009]. A third assumption is that the coupling between the cortical columns can be both excitatory and inhibitory. This assumption is reasonable if the network considered describes small brain areas communicating via short-range connections.

We choose a larger network of cortical columns that operates in the alpha band. Our analysis of the average regularity of the coupled nodes as a function of the inter-columnar excitatory and inhibitory coupling intensities reveals that the network includes nodes in different states (periodic, quasi-periodic, and chaotic). These results are also in agreement with the description of chaotic dynamics at a cellular level following periodic inhibitory inputs [*Segundo et al.*, 1991a,b]. The specific dynamics is controlled by the nature of the inter-columnar coupling, reflecting the dependence of the oscillations on the excitatory and inhibitory interactions at the mesoscopic scale. On this basis we can suggest that a sudden alteration of the inter-columnar coupling intensities (e.g. in an epileptic state) is associated with the modification of the regularity of the mesoscopic activity, and that with the capacity of information processing by the network.

One of the main features of the networks studied here is that even when the nodes are identical and receive a common driving input, their activity can be segregated in excitatory or inhibitory activity. This segregation results from the combined effect of the heterogeneous network connectivity, the specific excitatory-inhibitory couplings, and the external excitatory input to which all network nodes are subject. However, if no external input is fed into the columns segregation also emerges, though in lower levels, as shown in small motifs of connected cortical modules [*Malagarriga et al.*, 2014]. The same phenomenon appears in Wilson-Cowan oscillators [*Wilson and Cowan*, 1972] (see Fig. 6.7), so external stimuli makes the dynamics more complex, introducing chaotic-like time evolutions, and also enhances segregation.

At the microscopic level, segregation of excitatory and inhibitory behavior is well known [*Higley and Contreras*, 2006; *Haider et al.*, 2006; *Wu et al.*, 2006; *Heiss et al.*, 2008; *Berg et al.*, 2007; *Magnusson et al.*, 2008; *Yizhar et al.*, 2011]. Our study shows that mesoscopic segregation arises when inter-column couplings are predominantly inhibitory. As mentioned above, here we have focused on network architectures with inhomogeneous degree, which is one of the possible anatomical and functional based architectures in the brain [*Bullmore and Sporns*, 2009]. However, we thoroughly studied different network architectures ranging from regular rings to all-to-all topologies (see Fig. 6.12). We have also analyzed other scale-free arrangements (see Fig. 6.11). The emergence of excitatory-inhibitory segregation discussed here was typically found for complex topologies in contrast with regular topologies which do not exhibit segregated dynamics. Therefore, segregation is highly dependent on the topological features of the networks.

Driving inputs in a real brain are not as simple as the periodic input considered here. The irregular behavior observed here can be expected to have higher information content (e.g. in terms of Shannon/transfer entropy) than much simpler and regular signals. The normal functioning state of the brain, however, requires a certain degree of synchrony [*Varela et al.*, 2001]. A dysfunction in that synchrony leads often to aberrant behaviors and neurological

diseases [*Uhlhaas and Singer*, 2006, 2010]. For healthy working brains, it is therefore important to achieve a state in which coordinated irregular dynamics works to process information efficiently but non-trivially [*Skarda and Freeman*, 1987; *Freeman*, 1995]. In that way, the right amount of synchronization of the brain activity permits cooperative processing of information, thus increasing the computational power of the system [*Varela et al.*, 2001]. The results presented here suggest that organization of excitation and inhibition at the mesoscopic level might contribute to this cooperative information processing.

Chapter 7

Coexistence of synchronizations in complex weighted networks

"Sometimes you are in sync with the times, sometimes you are in advance, sometimes you are late."

Bernardo Bertolucci

In the previous Chapter we showed that the interaction between mesoscopic neural oscillators can give rise to complex patterns of synchronization when embedded in complex networks. We here want to deepen into the understanding of such phenomenon by thoroughly studying the conditions that allow groups of nonlinear oscillators, which display complex dynamics, to organize in clusters that exhibit different types of synchronization. We find that this diversity of synchronization patterns is promoted by increasing the heterogeneity in the distribution of coupling weights and/or asymmetries in small networks. We also analyze *consistency*, defined as the persistence of coexistent synchronization patterns regardless of the initial conditions. Our results show that complex weighted networks display richer consistency, suggesting why certain functional network topologies, for instance in the brain, are reconstructed more frequently when experimental data are analyzed.

7.1 Synchronization patterns in dynamical systems

Certain dynamical systems, which display oscillatory behavior in isolation, may display a wide repertoire of dynamical evolutions due to the coupling with their neighbors when embedded in networks of similar complex systems [*Pikovsky et al.*, 2003; *Uhlhaas and Singer*, 2006]. For instance, the interaction of rhythmic elements may entail an adjustment of their oscillatory dynamics to finally end up in a state of (dynamical) *agreement* or *synchronization* [*Strogatz*, 2003, 2000; *Glass*, 2001]. When coupling is strong, the oscillators in a network usually synchronize in a particular collective oscillatory behavior. However, this relationship may also be inhomogeneous, i.e., certain oscillators may synchronize whereas others may not [*Abrams and Strogatz*, 2004]. The specific patterns of synchronization, thus, may provide information about the underlying dynamics and the relationships established between the dynamical elements forming a network. Hence, a

better characterization of the system can be achieved, which shall be of crucial importance when the details of the contacts between the oscillators is not available.

Let's first consider two dynamical systems $\mathbf{x}$, $\mathbf{y}$ whose temporal evolutions are generally defined by $\dot{\mathbf{x}} = \mathbf{F}(\mathbf{x}(\mathbf{t}))$, $\dot{\mathbf{y}(\mathbf{t})} = \mathbf{G}(\mathbf{y})$ in isolation. Here we will consider a bidirectional coupling scheme, which introduces dissipation in the dynamics of the systems:

$$\begin{aligned} \dot{\mathbf{x}}(\mathbf{t}) &= \mathbf{F}(\mathbf{x}) + \hat{\mathbf{C}}(\mathbf{y}(\mathbf{t}) - \mathbf{x}(\mathbf{t})), \\ \dot{\mathbf{y}}(\mathbf{t}) &= \mathbf{G}(\mathbf{y}) + \hat{\mathbf{C}}(\mathbf{x}(\mathbf{t}) - \mathbf{y}(\mathbf{t})). \end{aligned} \tag{7.1}$$

$\mathbf{x}(\mathbf{t})$ and $\mathbf{y}(\mathbf{t})$ are the state vectors of the systems, $\mathbf{F}$ and $\mathbf{G}$ are their corresponding vector fields and $\hat{\mathbf{C}}$ is a nxn matrix that provides the coupling characteristics between the systems. When coupling is strong enough the synchronization relationships that can be established between these two prototypical dynamical systems, namely oscillators, can be categorized in four patterns [*Uchida et al.*, 2005; *Xiao-Wen and Zhi-Gang*, 2007]:

- Complete synchronization (CS) is observed when the coupled oscillators are identical or almost identical [*Boccaletti et al.*, 2002], and $\mathbf{x}(\mathbf{t}) = \mathbf{y}(\mathbf{t})$ for a sufficiently large coupling strength $\hat{\mathbf{C}}$.

- Phase synchronization (PS) appears if the functional relationship between the dynamics of two oscillators preserves a bounded phase difference [*Rosenblum et al.*, 1996], with their amplitudes being largely uncorrelated. This can be exemplified by the relationship $|n\phi_1 - m\phi_2| < const$, with $\phi_{1,2}$ being the phases of the two coupled oscillators.

- Generalized synchronization (GS) is observed if a complex functional relationship is established between the oscillators [*Abarbanel et al.*, 1996], e.g. $\dot{\mathbf{y}}(t) = H[\dot{\mathbf{x}}(t)]$, where $H[\dot{\mathbf{x}}(t)]$ can take any form other than identity. It can be thought to be a generalization of CS for non-identical oscillators.

- Lag synchronization (LS) appears when the coupling strength becomes larger, and if the amplitude correlation is high while at the same time there is a time shift in the dynamics of the oscillators [*Rosenblum et al.*, 1997], e.g $\mathbf{y}(t) = \mathbf{x}(t - \tau)$, with τ being a lag time.

There are several analysis techniques that can be used to assess the emergence of each of the mentioned synchronization motifs. Here we combine three of them: cross-correlation (CC) and Phase-Locking Value (PLV) (see Appendix B.1.3) and the Nearest-Neighbor Method (NNM) (see Appendix B.1.4). CC computes the lagged similarity between two signals, which provides a notion of the amplitude resemblance over time. Therefore it allows to state whether CS or LS are established between two timetraces. On the other hand, PLV makes use of the Hilbert transform of a signal so as to retrieve a phase ϕ and compute the time evolution of the difference in the phases of two oscillators, i.e. $\phi_1(t) - \phi_2(t)$ [*Lachaux et al.*, 1999]. Accordingly, combined with low CC it can assess the emergence of PS between two oscillators. Finally the NNM takes points in the phase space of one oscillator and determine its position in the phase space of the coupled oscillator [*Boccaletti et al.*, 2002]. It allows to visualize and exemplify each synchronization motif (see examples in Fig. 7.1A, lower panels).

With this set of analysis techniques, here we study the dynamics of networks of coupled Rössler oscillators (see model equations in A.5.2) [*Rössler*, 1976] arranged in complex weighted topologies – random (RN) [*Erdős and Rényi*, 1959], small-world (SW) [*Watts and Strogatz*, 1998] and scale-free (SF) [*Barabási and Albert*, 1999]. We show that several types of synchronization patterns may coexist depending on the topology and on the distribution of coupling strengths within the network. The novel finding of our study is the existence of regions in the parameter space where coexistence of synchronization patterns is stable. We relate the capacity of a network to display the same coexistence pattern regardless of the initial conditions with its *consistency*. We suggest that the retrieval of a network structure from its dynamics is very reliable when based on the consistency of coexistence patterns.

7.2 Coexistence of synchronizations

Two or more oscillators, which are part of a network, may synchronize in different ways (i.e., phase, generalized, lag or complete synchronization) forming heterogeneous synchronization patterns or giving rise to a coexistence of synchronizations. The coexistence of synchronizations in a network can be achieved if nodes can synchronize in different ways in terms of a parameter (e.g., coupling intensity, degree, clustering, etc.). Such scenario appears naturally in the route towards a fully synchronized network. Hence, the coexistence of synchronizations will be obtained often when the systems are not fully synchronized. Here we analyze the dependence of the distribution of different synchronization states with complex topologies by studying large Scale-Free (SF), Small-World (SW), and Random (RN) networks, where the tuning of topological properties allows to study the conditions for which coexistence occurs. We set the coupling weights to depend on the number of neighbors of each node as:

$$\alpha_{ij} = \frac{1}{\sqrt{\deg(v_i)\deg(v_j)}}, \tag{7.2}$$

for $i \neq j$, where $\deg(v_i)$, $\deg(v_j)$ are the degrees (number of coupled neighbors) of two dissipatively coupled nodes v_i, v_j, and we study regular and complex topologies of progressively larger networks.

Firstly, we set the dynamics of each node i to follow the Rössler equations (see Eqs. (A.32)). An isolated node with Rössler dynamics can display periodic, quasi-periodic or chaotic dynamics and each pair of nodes can display NS (no synchronization), PS, GS, LS or CS (see Fig. 7.1A, upper panels). The dynamics can also be characterized by means of the NNM in the return maps of the two oscillators: three groups of nearby points in one oscillator are tracked in the desired adjacent oscillator: if a functional relationship exists, i.e. in the PS, GS, LS or CS states, the tracked points are grouped according to the type of synchronization (see Fig. 7.1A, lower panels) [*Moskalenko et al.*, 2012].

Figure 7.1B,C and D show the distribution of synchronizations in three prototypical networks, namely, SF, SW and RN, alongside with their weight distributions (α) and the distribution of synchronizations within each network. All three networks are located in a region of the coupling parameter space which allows a complex distribution of synchronizations. In this sense, they show clusters of PS, LS and CS (SF), or PS, GS and LS (both SW and RN). However, such distribution is very sensitive to the coupling characteristics and the underlying topology. Therefore, we want

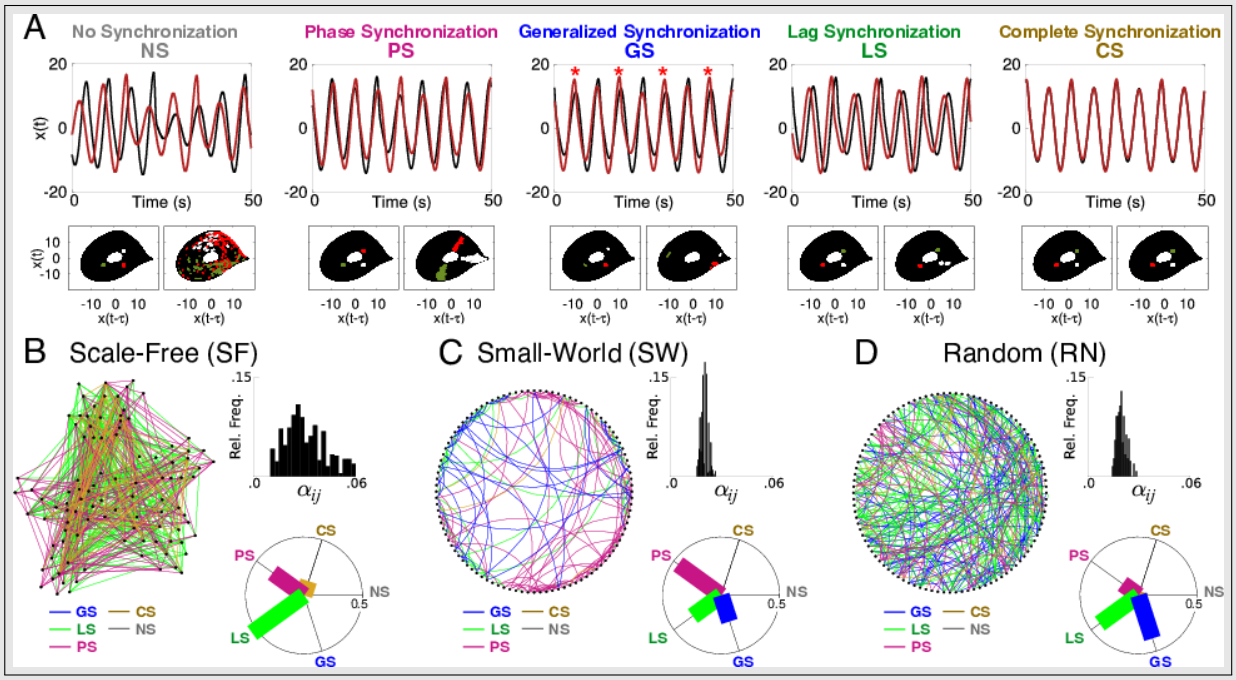

Figure 7.1: Heterogeneous synchronization patterns in complex weighted networks. (A) Examples of synchronization patterns (no synchronization NS, phase synchronization PS, generalized synchronization GS, lag synchronization LS and complete synchronization CS) displayed by dissipatively coupled Rössler oscillators using the nearest neighbor plot for each dynamical state [*Moskalenko et al.*, 2012]. τ is the delay time for maximal cross-correlation in LS and PS. Examples of (B) a scale-free (SF) network, (C) small-world (SW) network with low rewiring probability, and (D) random (RN) network of coupled Rössler oscillators displaying heterogeneous synchronization patterns. For each type of network the right panels show the distribution of the coupling strengths α_{ij} between pairs of nodes (upper panel) and the distribution of the synchronization patterns (polar histogram, lower panel). Each link is color-coded so as to show which synchronization pattern is displayed by each pair of oscillators within the network (NS, PS, GS, LS, see left bottom panel).

to better understand which are the conditions for the non trivial distribution of synchronizations to appear by analyzing the interaction of the nodes dynamics and the topological properties of the networks in which they are embedded. Hence, a question arises: *What are the conditions that are suitable for coexistent synchronization patterns in a network?*

7.3 Consistency of synchronizations

The heterogeneous synchronization motifs that emerge in complex networks are an excellent probe to detect functional connectivity between the oscillators in the network. Besides, the stability analysis of these motifs allows to identify synchronized states that show up recurrently even when initial conditions change and, thus, become an *invariant* feature of the dynamics of the network. Therefore in this section we study which are the conditions for which the same synchronization patterns persist in time for varying initial conditions.

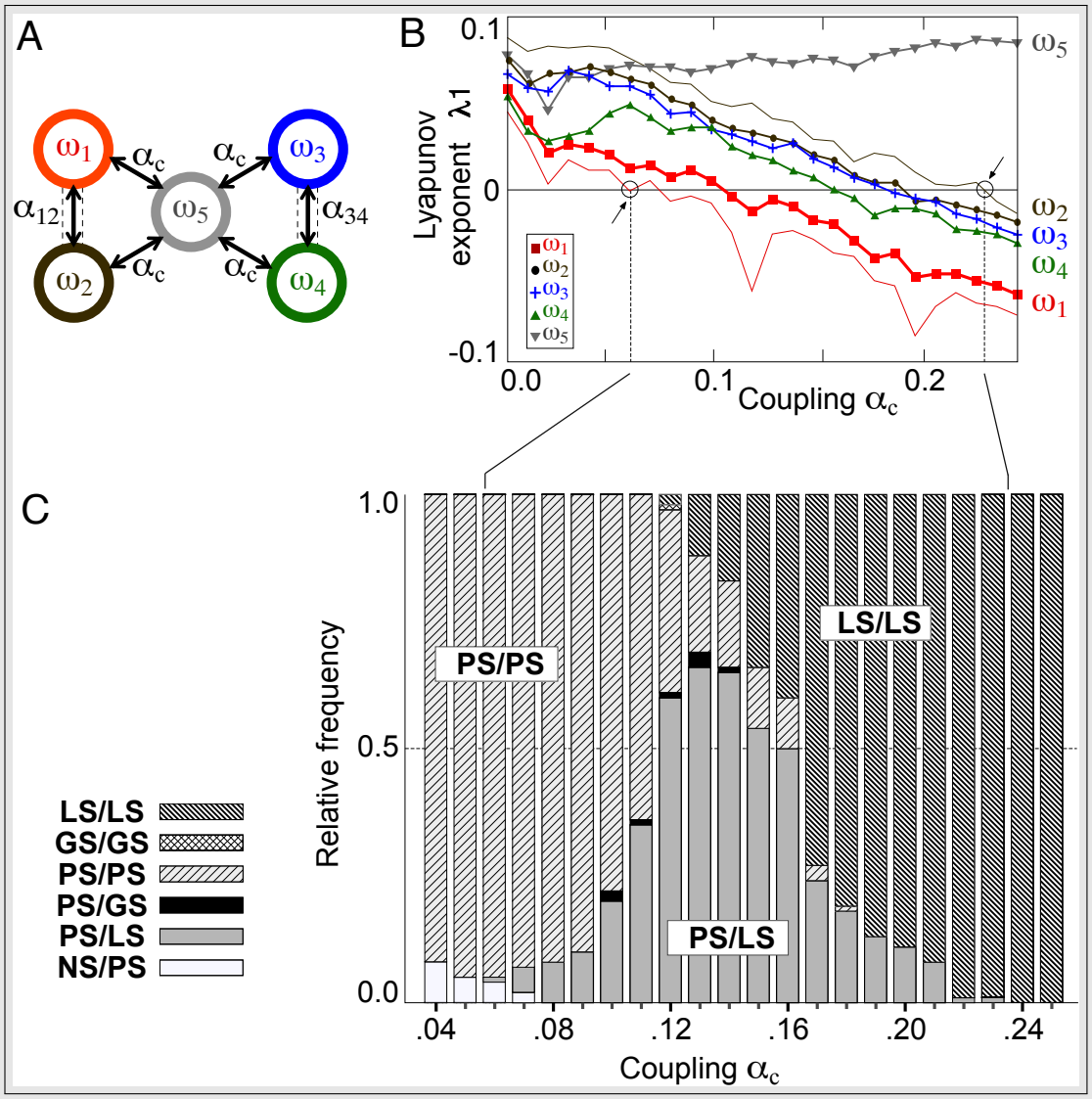

Figure 7.2: Dependence of the coexistence of synchronization patterns on the Lyapunov Exponents. (A) Simple weighted network formed by two pairs of peripheral nodes connected to a central node. The couplings between peripheral node pairs are $\alpha_{12} = 0.05$ and $\alpha_{34} = 0.03$. (B) For each node dynamics the curves show the mean value (computed over 100 runs with random initial conditions) of the maximum Lyapunov exponent ($\lambda 1$) as a function of the strength of coupling α_c of all nodes with the central node. The lowest thin curve corresponds to the lowest values of $\lambda 1$ for node ω_1 computed independently for each value of α_c. This curve crosses the zero line at $\alpha_c = 0.06$, as indicated by an arrow and a vertical dotted line. The uppermost thin curve corresponds to the largest values of $\lambda 1$ for node ω_2. This curve crosses the zero line at $\alpha_c = 0.23$, as indicated by an arrow and a vertical dotted line. (C) Histogram of the occurrences of the synchronized patterns for each peripheral node pair in the network (1-2 and 3-4). Notice that in the interval $\alpha_c \in [0.06, 0.23]$ several synchronization patterns may coexist for the same coupling α_c, depending only on the randomly chosen initial conditions. Notice that the heterogenous pattern PS/LS is the most frequently observed. Pattern PS/GS was rare and pattern GS/LS was never observed.

Our first example of coexistence of synchronization is studied in a very simple weighted network formed by two pairs of nodes connected bidirectionally with a fifth node (see Fig. 7.2A). Eqs. (A.32) describe the dynamics for these nodes. They only differ on the frequencies, ω_i, which are the following: $\omega_1 = 0.930$, $\omega_2 = 0.967$, $\omega_3 = 0.990$, $\omega_4 = 0.950$, $\omega_5 = 0.970$. After fixing two different initial synchronized states for the two couples of peripheral nodes we may change the nature of the synchronization coexistence within the network by increasing the bidirectional coupling α_c with the central node. Notice that we change the synchronization states without changing $\alpha_{1,2}$ and $\alpha_{3,4}$. Moreover, the cascade of coexistence of synchronized states in terms of α_c may be tracked numerically by considering in detail the evolution of the Conditional Lyapunov Exponents (LEs, $\lambda 1_{\omega_i}$) [*Boccaletti et al.*, 2002; *Moskalenko et al.*, 2012] when α_c changes (see Fig. 7.2B and Appendix B.1.1). LEs are a good indicator for the convergence or divergence of two infinitesimally separated trajectories of a dynamical system in the phase space. Here we will use LEs to estimate the rate of convergence or divergence of the trajectories of the synchronized elements starting from the trajectory defined by 1 coupled element (ω_1 in Figs. 7.2, 7.4).

Figure 7.2B shows that, in terms of α_c, three different regions may be defined for the 5 (realization-averaged) largest LEs $\lambda 1_{\omega_i}$.

- In the first region ($0 < \alpha_c < 0.06$) all the largest LEs are positive. The pair 1-2 is in PS ($\alpha_{1,2} = 0.05$), whereas 3-4 is NS ($\alpha_{3,4} = 0.03$). When increasing α_c in this region, peripheral nodes become PS with the central node until the first 0 crossing of $\lambda 1_{\omega_i}$ (light red line) defines the onset for GS for pair 1-2 and PS for 3-4 (vertical dashed line, first arrow, $\alpha_c = 0.07$).

- The second region ($0.07 < \alpha_c < 0.23$, in between dashed lines) sets a cascade of coexistence of synchronization regimes, i.e., successive 0 crossings of LEs determine the onset of GS and LS between the nodes: $\alpha_c = 0.14$ defines the onset of LS between oscillators 1-2 while 3-4 remain PS. $\alpha_c = 0.16$ marks the subsequent GS onset between oscillators 3-4 while maintaining oscillators 1-2 in LS.

- In the third region, after $\alpha_c = 0.23$, there is the onset of LS for the whole network.

Figure 7.2C shows the histogram of the occurrence of each pair of synchronized states between nodes 1 and 2 or 3 and 4, computed using CC and PLV (see Appendix B): in the coexisting region, there exists extended α_c values for which pairs 1-2 and 3-4 are, simultaneously, in two different synchronized regimes, e.g. 1-2 are in LS meanwhile nodes 3-4 are in PS. Therefore, two synchronized states can coexist in the network.

The relationship between the LEs exponents of this small network system and the statistical occurrence of synchronizations allows to show that the synchronization patterns obtained are stable and robust against perturbations. In order to prove so we have perturbed different nodes and tracked the evolution of the amplitude and phase differences. Figure 7.3A,B shows these time evolutions. In the coexistence regime, when the PS/LS situation is dominant ($\alpha_c = 0.13$), the stable synchronized dynamics forces the pair 1-2 (in LS) to return to its bounded amplitude difference when perturbing node ω_1, whereas phase differences suffer an abrupt change but do not increase for both pairs 1-2 and 3-4. Such characteristic proofs crucial for the system's stability.

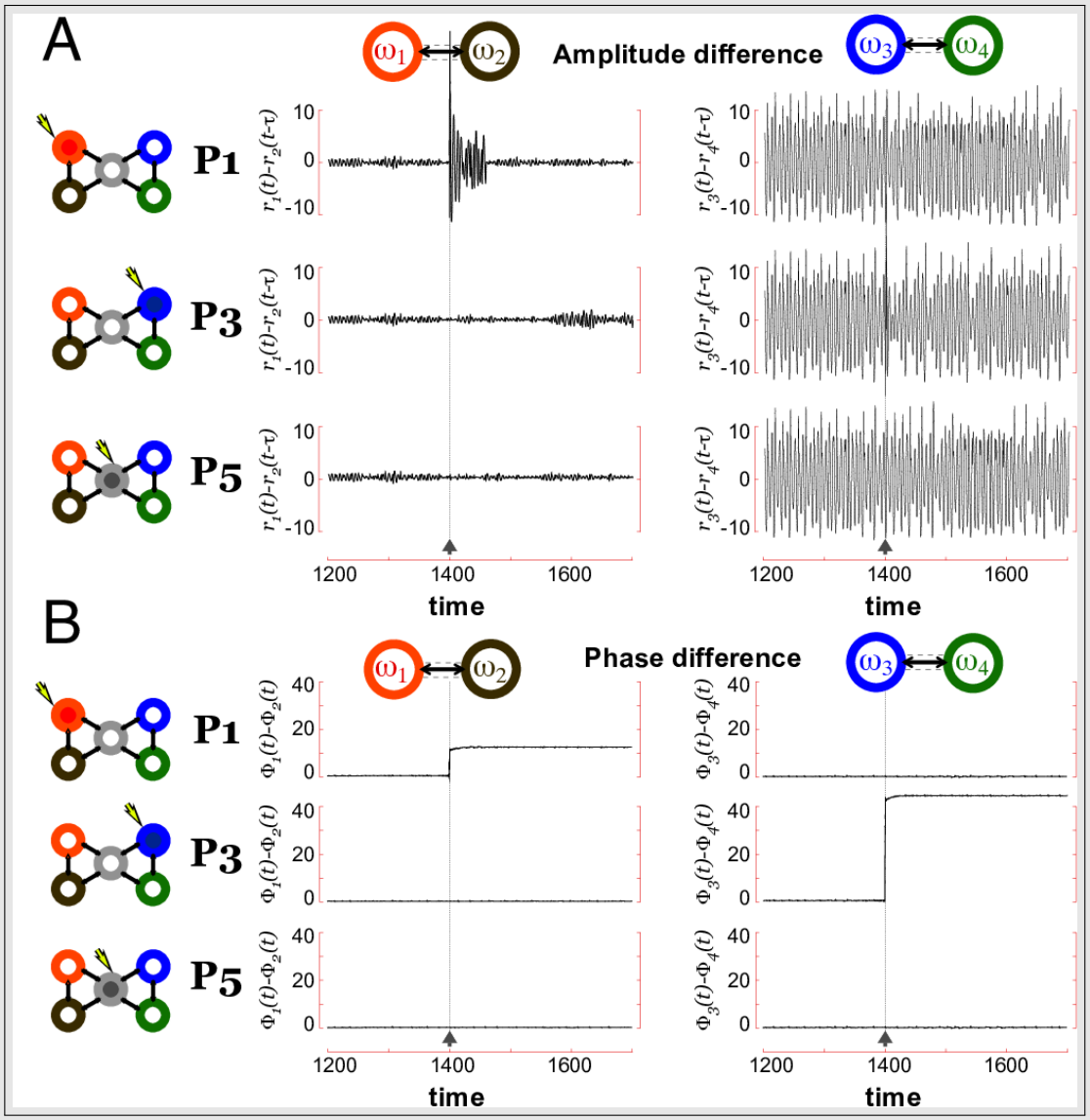

Figure 7.3: Robustness against perturbations. (A) We perform perturbations on node ω_1 (P1), node ω_3 (P3) and node ω_5 (P5) so as to track the amplitude difference of the two pairs of peripheral nodes. In this regard the amplitude difference is kept bounded for the two peripheral nodes, which are in LS (pair 1-2) and PS (pair 3-4), respectively ($\alpha_{1,2} = 0.05$, $\alpha_{3,4} = 0.03$, $\alpha_c = 0.13$). Notice the divergence in amplitude and phase evolution depending on the perturbation site, indicating that the system is globally connected and senses small perturbations. (B) The phase difference suffers a sudden increase but is also kept constant in time when perturbing the same nodes as in caption A.

Besides, perturbations in all sites of the network are sensed by all nodes, as it can be seen from the distinctive post-perturbation time evolutions of both amplitude and phase differences. This shows that pairs do not evolve as isolated entities.

The cascade of 0 crossings of the LEs in terms of α_c can be expanded or squeezed by increasing or decreasing the symmetries of the system. For a completely symmetrical system, i.e., equal

governing equations for all the nodes in a symmetric network, there are abrupt transitions to synchrony [*Leyva et al.*, 2012], without coexistence. Symmetry can be broken in a controlled way by means of a parameter governing the dynamics (e.g. oscillatory frequency), a parameter responsible for the topological characteristics of the network (e.g., clustering) or both features. In such scenarios different motifs of synchronized dynamics may show up, but they are restricted to a tiny region of the parameter space and, thus, appear to be spurious.

Now we study how symmetry, in terms of the heterogeneity of the coupling values α_{ij}, determines the coexistence region in the previous small network and its associated consistency. Figure 7.4A shows the motif studied previously, but with different coupling strengths between peripheral nodes; $\alpha_{1,2}$ is now one order of magnitude smaller than $\alpha_{3,4}$ (see caption of Fig. 7.4). Again, we have tracked the evolution of the LEs in this case for increasing α values.

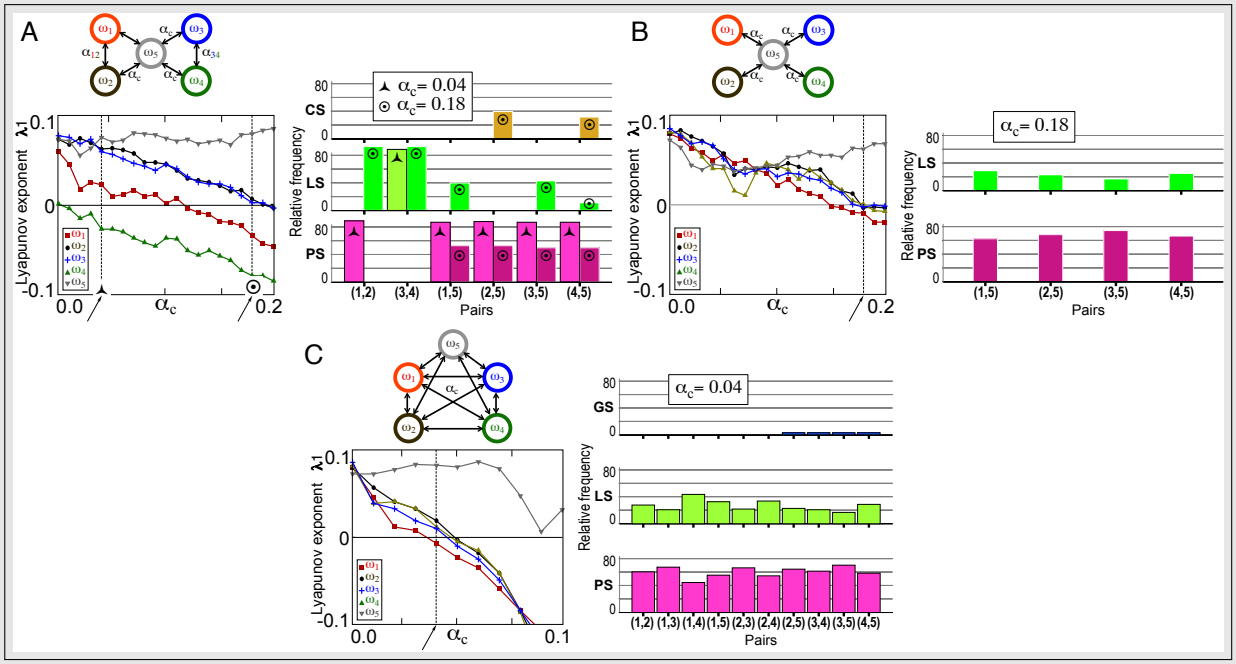

Figure 7.4: Consistency of the coexistence of synchronizations. (A) Same network of Fig. 7.2A with coupling $\alpha_{3,4} = 0.20$ for node pair (3,4). For each node dynamics the curves show the mean value of the maximum Lyapunov exponent ($\lambda 1$) as a function of coupling strength α_c (see Fig. 7.2B). The histogram shows the relative frequency of the synchronization patterns for selected values of α_c ($\alpha_c = 0.04$, $\alpha_c = 0.18$ indicated by the arrows). GS: general synchronization; CS: complete synchronization; LS: lag synchronization; PS: phase synchronization; NS: no synchronization (not shown in the histograms). (B) Homogeneous hub network with all couplings weighted by α_c. The maximum Lyapunov exponent curves for each node dynamics are similar and the interval of α_c for coexistence of synchronization patterns is small. The histogram shows the distribution of the synchronization patterns for $\alpha_c = 0.18$. (C) All-to-all network in which all couplings are weighted by α_c. The interval for coexistence of synchronization patterns is also small and occurs for smaller values of α_c. The histogram shows the distribution of the synchronization patterns for $\alpha_c = 0.04$.

Firstly, for $\alpha_c = 0$ nodes 1-2 are in PS meanwhile nodes 3-4 are in GS – i.e. a coexistence

situation –. As it can be seen in Fig. 7.4A, for different initial conditions 0 crossings of LEs appear along an extended α_c value region. In this case, the coexistence region spans from $\alpha_c = 0$ to $\alpha_c = 0.20$. The third panel in Fig. 7.4A shows a plot of the relative frequency of synchronizations found for each pair of nodes in the small motif for all the realizations of the initial conditions performed and for $\alpha_c = 0.04$ or $\alpha_c = 0.18$. Consistently, each pair of nodes lies in the same synchronization state for any of the imposed initial conditions for the value $\alpha_c = 0.04$, whereas for $\alpha_c = 0.18$ some pairs display two or more synchronization patterns (NS proportion not shown). Consequently, we define *consistency* as the capacity of a network to display the same coexistence pattern regardless of the initial conditions, as with $\alpha_c = 0.04$.

Figure 7.4B shows a non symmetric network, in terms of degree, with homogeneous coupling strengths α_c. Such relay configuration is less prone to synchronize for small coupling strengths and, therefore, larger α_c values are required to set synchronized states (see inset $\alpha_c = 0.18$). However, the coexistence region is also narrow and the LEs randomly cross the 0 value, which implies that the consistency will be low. This is shown in Fig. 7.4B lower right panel, in which the realizations of the initial conditions do not lead to the same synchronization dynamics.

Figure 7.4C shows an all-to-all small network in which all edges are weighted by the control parameter α_c. In this case the network topology is more symmetrical but the imposed distribution of natural frequencies of the oscillators ω_i allows for coexistence of synchronization – as it breaks the symmetry of the network –. Besides, the α_c range for which coexistence exists is narrower with respect to the previous studied motifs. This reduction of the area of coexistence has implications in the consistency of synchronizations: 0 crossings of LEs are randomly distributed in a tiny range of α_c and, so, coupled pairs in the network do not consistently lay in the same synchronized state for different initial conditions (see Fig. 7.4B right panel).

Overall, by gathering the results of the coexistence and the consistency phenomena, we show that network symmetries govern the synchronization dynamics emerging from a system of coupled dynamical units [*Nicosia et al.*, 2013]. In this regard, clusters of synchronizations dynamically emerge thanks to symmetry breaking (with respect to the topology, the system parameter values or both) and the statistics of the synchronization dynamics strongly depend on the type of symmetry breaking.

We now define synchronization clusters considering characteristic functional relationships between the coupled elements. Thus, by labeling each of the functional relationships (NS, PS, GS, LS, CS) one can have a better characterization of the global behavior of the system. Added to this, we have shown that there is a dependence of the statistics of coexistence on the underlying network. Therefore, when extracting *functional networks* from the statistics of synchronization,we will get the most *consistent* structural sub-network. The less consistent sub-networks, even though they can be coupled, may show up as disconnected functionally. We will use this feature to infer the characteristics of structural networks from reconstructed functional networks.

7.4 Construction of consistent networks

A fundamental question in network science is the relationship between network dynamics and network structure. In the past, studies of the synchronization patterns in networks of

oscillators were mainly aimed at describing the conditions associated with the emergence of specific synchronization patterns in all the nodes [*Chavez et al.*, 2005]. In the particular case of complex networks of coupled nonlinear oscillators, recent studies have provided evidence that it is possible to identify an appropriate interaction regime that allows to collect measured data to infer the underlying network structure based on time-series statistical similarity analysis [*Tirabassi et al.*, 2015] or connectivity stability analysis [*Lin et al.*, 2015]. In real-life systems, such as ecological networks [*Blasius et al.*, 1999], brain oscillations [*Robinson et al.*, 1998; *Hill and Villa*, 1997; *Cabessa and Villa*, 2014] or climate interactions [*Deza et al.*, 2015], various types of complex synchronized dynamics have been observed.

Functional networks can be constructed by establishing relationships between their (coupled) elements. One of the most prominent dynamical features which functionally relates two oscillators is synchronization, which may take the aforementioned forms (PS, GS, LS, CS) among others not studied in here. Thus, synchronization is a probe for assessing a (non) trivial relationship between two dynamical systems. Here we want to show how the statistics of coexistence may reveal a functional organization of synchronization within a network and, therefore, may help to construct functional networks.

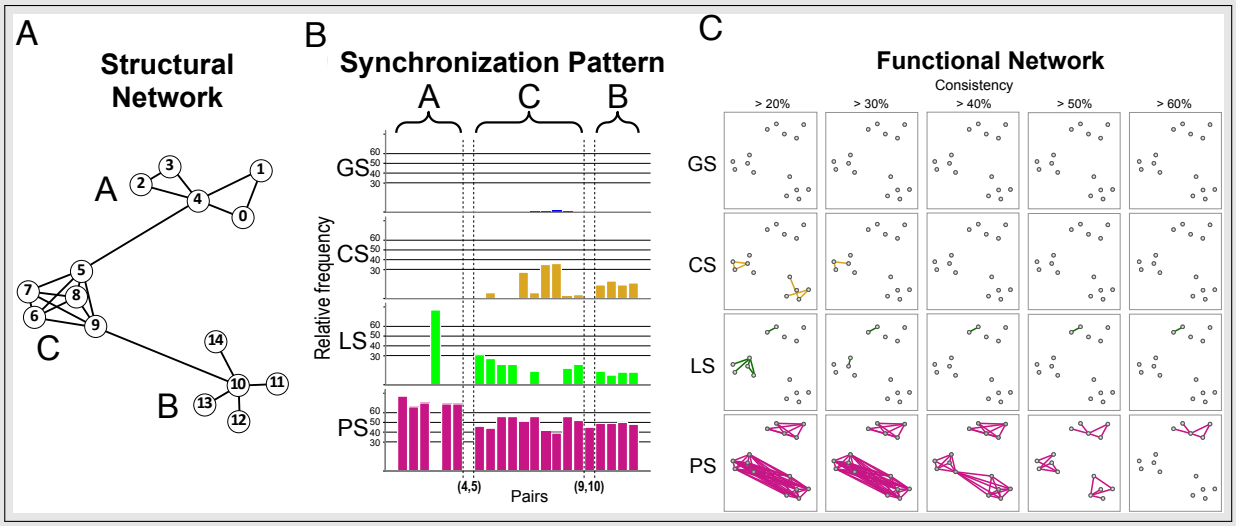

Figure 7.5: Construction of functional networks. (A) A structural network of modules is constructed by linking a module A, corresponding to a peripherally coupled network (Fig. 7.4A), with a module C, corresponding to an all-to-all network (Fig. 7.4C), by means of node pair (4,5) with coupling $\alpha_{4,5} = 0.03$ and by linking the module C with a module B, corresponding to an homogeneous hub network (Fig. 7.4B), by means of node pair (9,10) with coupling $\alpha_{9,10} = 0.04$. All other couplings are set equal to $\alpha_c = 0.04$. (B) Histogram of the relative frequency of the synchronization patterns for all intramodule and for the two intermodule node pairs. Notice that the consistency of synchronization patterns in modules B and C is different from the consistency observed in isolated networks with the same topology corresponding to modules B and C (see Fig. 7.4B,C). NS not shown in the histograms. (C) Functional networks can de determined on the basis of various threshold levels of consistency (between 20% and 60%) for each type of synchronization pattern.

Firstly, we take the motifs studied in Fig. 7.4 and construct a network by connecting these groups of nodes through their hubs (or most connected nodes). The resulting graph is shown in Fig. 7.5A, where each of the motifs is labeled as A, B or C. The intra-motif weights are the same as the selected in Fig. 7.4A, B, C, respectively, whereas the inter-hub links weights are shown in caption in Fig. 7.5. Figure 7.5B shows the statistics of synchronization occurrence in this network: cluster A shows a very robust consistency of its synchronizations whereas clusters B and C are much less consistent, i.e., they display a wide repertoire of different synchronization motifs depending on the initial conditions. However, as it can be noticed when comparing Fig. 7.4A,B,C and Fig. 7.5B consistency panels, the dynamics of synchronization is altered when the three motifs are embedded in a larger network. This fact is a signature for assessing that the dynamics of coexistence in the large network is not just the simple juxtaposition of the dynamics of its composite motifs. We now want to perform the task of constructing the functional networks arising from the synchronization patterns in this network. For such purpose we obviate the structural network and we make use of the statistical occurrence of each synchronization among pairs of nodes of the system. Indeed, thanks to the discrimination between each type of synchronization – as each one entails different types of functional relationships between nodes – we can better characterize the most salient synchronization motifs between the nodes. If we establish thresholds in the statistical occurrence for each pairwise synchronization, we can extract the links which, statistically, appear the most and so are more consistent. Thus, functional networks may be constructed by taking into account the consistency of each type of synchronization among pairs of nodes. Figure 7.5C shows the reconstruction of the motif-based network depending on different levels of consistency for each synchronization pattern. Each thresholded reconstruction takes into account links which show *the same* synchronization a number of times equal or larger than the consistency threshold. Accordingly, the reconstructed functional network coincides with the most consistent motif. This result may seem trivial as the conditions imposed in the network lead to the desired results. However, they apply to (larger) networks of coupled chaotic units.

We now take the SF prototypical network shown in Fig 7.1 and perform topological changes by taking clustering as a control parameter. Figure 7.6A shows the fraction of connected synchronized pairs in the SF networks whose consistency is above a certain threshold for increasing clustering. Noticeably, only low clustering networks have edges whose synchronization is consistent above a 50% of the realizations. Therefore, only low clustering SF networks are heterogeneous enough to hold consistent synchronized dynamics. Figure 7.6B shows an example of a very consistent realization-averaged SF network with clustering $C = 0.15$ and a consistency map displaying the statistics of synchronization for each pair of nodes in the network. According to the statistics, the realization-averaged colors in the network mostly coincide with pure synchronization colors. Fig. 7.6C shows a low consistency realization-averaged SF with clustering $C = 0.40$. The consistency map, performed for every pair of nodes in this network, shows no pattern compared to the case in panel B. Such patterns denote that the functional organization of these networks is robust in the first case, whereas for the network with larger clustering randomized functional relationships are established among pairs of (connected) nodes. We analyze how many of the reconstructed edges are true or false positives, i.e., we quantify the matching between the structural and the functional network. We perform the following calculation:

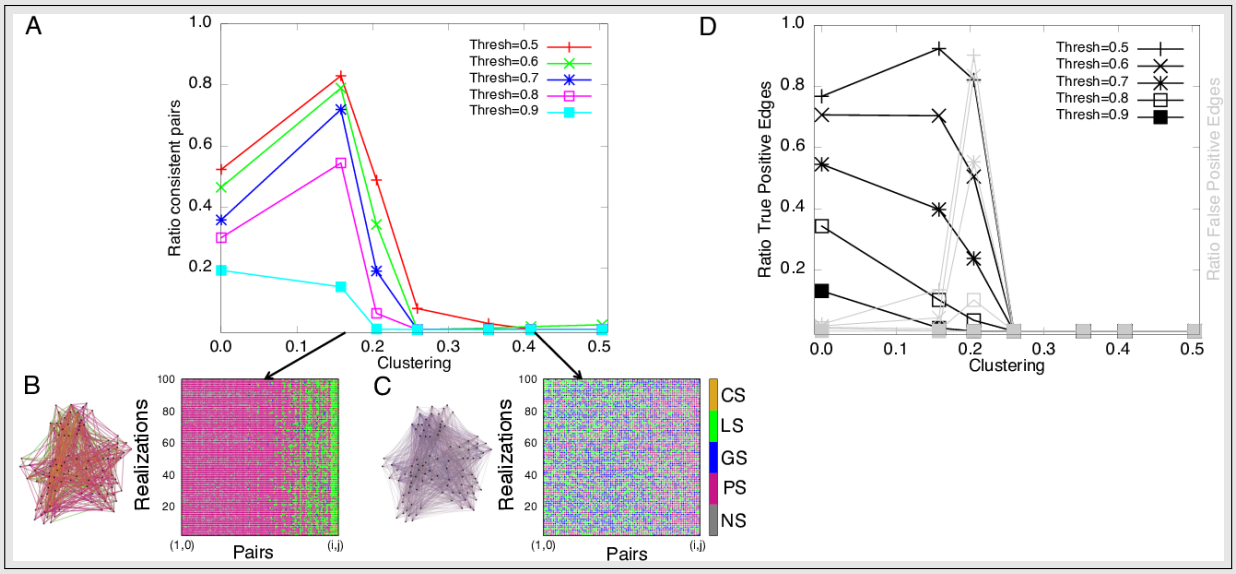

Figure 7.6: Relationship between structural and functional networks for increasing clustering. (A) Ratio of consistent pairs for increasing clustering and increasing consistency thresholds (*Thresh*). The ratio of consistent edges displays a maximum for low clustering values, showing the dependence of this feature on the symmetries of the networks. (B) Low clustering networks ($C = 0.15$) show consistent synchronization motifs, as shown in the synchronization-averaged network – which shows almost pure synchronization colors –, and in the realization vs. pair synchronization map – which displays patterns of synchronization –. (C) For larger clustering networks ($C = 0.40$), the synchronization-averaged networks show a single color and no patterns can be discerned in the realization vs pair synchronization map. (D) The combination of coexistence and its consistency allows to reconstruct functional networks that embed information of the underlying structural network. The ratio of true and false positive edges for the same networks as in panel A shows that low clustering structural networks can be reconstructed more reliably than higher clustering structural networks. In this regard, heterogeneous networks are more consistent in the synchronization dynamics and so may be easily found when extracting functional networks.

$$n_{true_+} = \frac{n_{correct}}{n_{totstruct}} \tag{7.3}$$

$$n_{false_+} = \frac{n_{incorrect}}{n_{all-to-all} - n_{totstruct}} \tag{7.4}$$

where $n_{totstruct}$ is the number of edges in the structural network, $n_{all-to-all}$ is the number of edges in an equivalent all-to-all network, $n_{correct}$ is the number of reconstructed edges that belong to the structural network, $n_{incorrect}$ is the number of reconstructed edges that do not belong to the structural network, n_{true_+} is the ratio of reconstructed edges that belong to the structural network and n_{false_+} is the ratio of reconstructed edges that do not belong to the structural network. In other words, n_{true_+} computes how many of the structural edges have been reconstructed, whereas n_{false_+} computes how many of the non-structural edges have been reconstructed. Note that the sum $n_{true_+} + n_{false_+}$ is not equal to 1 necessarily. In this sense, a reconstruction with high n_{true_+} and high n_{false_+} indicates that the reconstructed network is close to an all-to-all

network, i.e., all structural edges can be retrieved but the number of non structural edges is also high, implying a bad matching between structure and function. Figure 7.6B indicates that for clusterings below $C = 0.15$ the matching between structural and functional network is high for a consistency threshold of about 50%, whereas the reconstruction for higher clusterings provides either a high ratio of false positives (close to all-to-all functional network) or non-consistent networks. Interestingly, the system faces a transition point at a relatively low clustering value, $C \simeq 0.21$, which prevents the reconstruction of functional networks at higher clusterings. Indeed, as the heterogeneity in the structural network is progressively lost due to higher clustering, the system loses consistency in the synchronization motifs and so no robust functional relationships can be extracted.

The computation of true and false positives is not possible in many natural systems, e.g. the brain or signaling networks, where no exact knowledge of the anatomical structure is available. However, we raise the hypothesis that our results might unveil a potential relationship between the two if the statistics of coexistence are robust, i.e., the consistency of coexistence is high.

7.5 Conclusions

The coexistence of synchronizations can be regarded as a phenomenon in which a variety of complex functional relationships are established between the dynamical evolutions of some coupled elements. Here we have shown that such scenario emerges in the route towards an all-synchronized network, where trivial correlations are established among oscillators. Besides, the heterogeneity in the number of node contacts and coupling strengths allows for a broad distribution of synchronization motifs. Thus, weighted networks show much more coexistence than unweighted networks.

What is more, some networks can robustly display the same coexistence patterns regardless of the initial conditions imposed. Such feature allows to better characterize the stable functional relationships established in the network. Moreover, this feature is at the basis of functional network construction. We argue that our method allows a better construction in terms of the statistics of synchronization motifs because we consider different coexistent synchronization states to characterize the functional network. Besides, we have shown that the matching between structural and functional networks is high when applying a coexistence-based reconstruction.

The consistency of three prototypical networks shown in Fig. 7.1 is diverse: while SF networks with low clustering show high consistency, SW and RN networks do not display this feature because in SW or RN networks the number of node contacts fluctuates less. Moreover, if our conclusions are extrapolated to real networks, we would expect that the reconstruction of functional networks results in heterogeneous (non-symmetrical) networks because they are more consistent. More symmetric or homogeneous networks will appear as inconsistent if coupling is small: only when coupling is large enough to force global synchronization symmetrical networks will show up in the reconstructed functional networks.

On top of that, the consistency of the coexistence is a consequence of the heterogeneity of the network: the dynamical clusters consistently lay in the same synchronization manifold for any of the initial conditions imposed as the synchronized trajectories are always dominated by their most connected neighbor. This allows to construct robust functional networks that

have reminiscent characteristics of the structural network for increasing values of the thresholds imposed. Consistent dynamics eventually depends on the heterogeneity characteristics of the structural networks such that selected network topologies, for instance in brain dynamics, may have been retrieved much more often than others, as reported elsewhere [*Eguíluz et al.*, 2005; *Bullmore and Sporns*, 2009].

Chapter 8

Synchronization-based computation through networks of coupled oscillators

"No, I'm not interested in developing a powerful brain. All I'm after is just a mediocre brain, something like the President of the American Telephone and Telegraph Company."

Alan Turing

The mesoscopic activity of the brain is strongly dynamical and noisy, while at the same time exhibits remarkable computational capabilities. In previous chapters we have shown that networks of neural mass models, which represent the mesoscopic activity of cortical columns, display complex patterns of synchronization depending on the heterogeneity of the network. Besides, we have studied the conditions which make such synchronization patterns stable and robust. Therefore, in order to examine how complex dynamics may be involved in the computational capabilities of the brain, here we show that the patterns of synchronized oscillations displayed by networks of neural mass models may be used as substrates for generalized Boolean-like computations. Our results reveal that a neural mass network may process different combinations of dynamical inputs as *different* logical operations or combinations of them. This dynamical feature of the network allows it to process complex inputs in a very sophisticated manner. For instance, latency in the synchronization dynamics results in a hysteresis effect that may be related with memory, or also the presence of perturbations at different sites of the network alters the dynamics but keeps the synchronization state stable. In order to validate our hypotheses, these results are reproduced experimentally with electronic circuits of coupled Chua oscillators, showing the robustness of this kind of computation to the intrinsic noise and parameter mismatch of the coupled oscillators. We also show that the information-processing capabilities of coupled oscillations go beyond the simple juxtaposition of logic gates.

8.1 Small networks of neural mass oscillators

The oscillatory activity exhibited by different brain signals – e.g. LFP, EEG or MEG – results from the collective synchronization of the firings of large populations of neurons [*Iglesias et al.*,

2005]. Besides, the processing of different external inputs requires the recruitment of several brain areas in order to provide adequate responses to adaptive or cognitive processes [*Buzsáki and Draguhn*, 2004]. Therefore, at this large brain scale synchronization also plays an important role, for instance, in coordinating and processing information at different spatiotemporal scales [*Varela et al.*, 2001], in the selectivity in visual response [*Womelsdorf et al.*, 2006] or in the computation capabilities of oscillatory networks [*Engel et al.*, 2001a].

The idea of the implementation of logic calculus by the activity microscopic neural populations was first proposed by *McCulloch and Pitts* [1943]. In their work, the neural code was treated as a binary system, where firing is regarded as "1", whereas no firing is treated as "0". However, neurons may coordinate their firing in response to inputs and, therefore, their synchronized states may be also used as a substrate for a neurocomputing paradigm where their phase relationships determine their logic state [*Hoppensteadt and Izhikevich*, 2000]. Hence, the association of logical states to synchronized dynamics leads to the implementation of Boolean operations that may cover all logic computations.

Here we bring the notion of logic calculus to the level of synchronized neuronal oscillations. Specifically, we show that networks of coupled neural mass oscillators, which display complex heterogeneous synchronization patterns (see Chapters 6 and 7), may process inputs in a Boolean-like manner. However, far from suggesting that the processing capacity of the brain is the result of a more or less complex Boolean circuitry, we postulate that it results from its very complex collective dynamics in which synchronization may play a very relevant role [*Buzsáki and Draguhn*, 2004]. In this sense, more complex scenarios can be proposed: other types of non-Boolean logic, fuzzy logic, or even multiple-state logic.

As shown in Chapter 6 the (oscillatory) input received by two neural mass oscillators [*Jansen et al.*, 1993] within a network may determine their state of synchronization [*Malagarriga et al.*, 2015b] (see Fig. 8.1 and Eqs. A.6, A.7 and A.8). Thus, labeling arbitrarily the input signals as "1" - when they are present -and "0" - when they are not present - and the synchronization state of the two oscillators as "1" ("0") when the oscillators are (not) synchronized, we can interpret the dynamical response of these two nodes to their inputs in terms of binary logic gates. By changing the characteristics of the inputs and the excitatory/inhibitory coupling strengths between the two oscillators, α_{ij}/β_{ij}, several types of binary logic gates may be created.

Before studying large networks of coupled neural mass models we first study a simpler situation formed only by two bidirectionally coupled Jansen oscillators (See Figure 8.1 and Table 8.1). In this configuration, each oscillator (A_1 and A_2 from now on) receives an external oscillatory and stochastic input, i.e. Input A_1 (δ_{A_1}, f_{A_1}, ξ_{A_1}) and Input A_2 (δ_{A_2}, f_{A_2}, ξ_{A_2}), with δ_{A_i}, f_{A_i} and ξ_{A_i} being the amplitude, frequency and noise amplitude of the inputs that add to the other pulse density contributions (see Appendix A.1.1). The output signal of each oscillator is the difference between the Excitatory Postsynaptic Potential (EPSP) and the Inhibitory Postsynaptic Potential acting upon the pyramidal population ($y^i(t) = y^i_e(t) - y^i_i(t)$) (see triangles in Figure 8.1 and the Appendix A.1.1). The synchronization state of the output of the two elements that form the gate, y^i and y^j, determines the dynamical response of the pair to the input signal. Other characteristics of the response may also inform about the nature of the inputs received by the oscillators. For instance, it has been shown [*Spiegler et al.*, 2011a; *Huang et al.*, 2011] that the

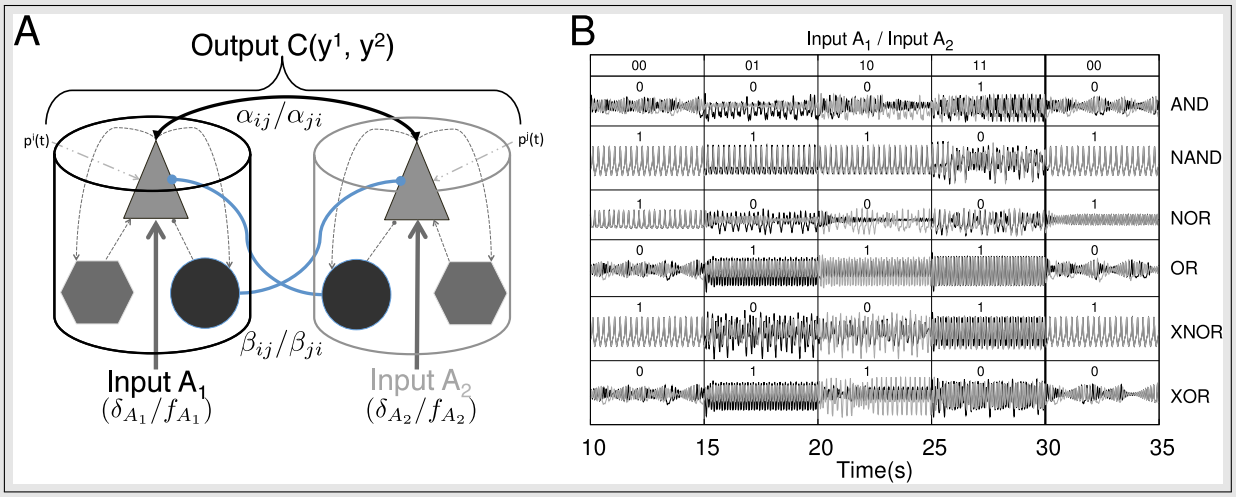

Figure 8.1: Implementation of binary logic gates formed by pairwise connected cortical columns. (A) Cartoon depicting two connected cortical columns i and j. Both columns are bidirectionally coupled through both excitatory-excitatory (black solid arrows) and inhibitory-excitatory (blue solid lines) contacts. The intensity of such connections is weighted by α_{ij}=α_{ji} and β_{ij}=β_{ji} coupling strengths, respectively. The pyramidal population within each cortical column additionally receives a constant background pulse density $\bar{p^i}$, an oscillatory input defined by an amplitude δ^i and a frequency f^i and a stochastic input contribution (see Eq. (A.6)). The characteristics of these inputs define states which feed this binary logic gate. The outcoming signals, $y^i = y^i_e - y^i_i$, of the two columns may ($C(y^1, y^2) \approx 1$) or may not ($C(y^1, y^2) \approx 0$) be correlated. The correlation value of the timetraces of the two nodes defines the output state of the gate for the given input stimulation (see Table 8.2). Intermediate values ($C(y^1, y^2) \approx 0.5$) are taken as "wrong" implementations of the gates. (B) Several binary logic gates can be obtained from the system shown in panel A if the appropriate combination of parameters and input protocols are selected (see Table 8.1). Correlated signals, in the form of PS, LS or CS, result in a "1" state of synchronization, however, not correlated signals are interpreted as a "0" state of synchronization. The time traces of the oscillators and the state resulting from their synchronization are shown for all the binary combinations of input protocols (00, 01, 10 and 11) for several logic gates (AND, NAND, NOR, OR, XNOR and XOR). The last column shows the return to the initial state. Y axis denotes the amplitude of the PSP ($y^i = y^i_e - y^i_i$).

driving of Jansen oscillators by a periodic input may result in chaotic, quasi-periodic or periodic dynamical evolutions. So, taken as a whole, both the synchronization state of two oscillators and their dynamical state (e.g. chaotic or oscillatory), inform about the characteristics of the input received by the gate. As mentioned above, we have assigned arbitrarily the "0" and "1" values to the absence of synchronization and its presence, respectively.

With all these ingredients we have constructed truth tables based on synchronized states as shown in Figure 8.1B. The time traces show the online implementation of AND, NAND, NOR, OR, XNOR and XOR gates that operate in different synchronization regimes. To obtain them, different input protocols and coupling strength relations between the two nodes are needed (see Table 8.1). However, a single pair of connected oscillators with fixed coupling strengths α_{ij}/β_{ij} may organize its response in different ways when the input characteristics (frequency,

Table 8.1: Coupling parameter values. Values of the coupling parameters and input stimulation protocols for inputs labeled as "1" in the implementation of the binary logic gates shown in Figure 8.1. Inputs labeled as "0" have $\delta_i = 0$.

	Logic gates					
Parameters	AND	NAND	NOR	OR	XNOR	XOR
$\alpha_{A_1A_2}$	2.0	27.0	5.0	2.0	27.0	2.0
$\beta_{A_1A_2}$	8.0	5.0	1.0	8.0	5.0	8.0
p_{A_1} (Hz)	250	150	155	250	155	250
p_{A_2} (Hz)	250	150	155	250	155	250
δ_{A_1} (Hz)	120	150	65	250	250	250
δ_{A_2} (Hz)	120	150	65	250	250	250
f_{A_1} (Hz)	10.8	8.5	8.5	8.5	8.5	9.5
f_{A_2} (Hz)	10.8	8.5	8.5	8.5	8.5	8.5
ξ_{A_1} (Hz)	0.0	0.0	1000	0.0	1000	0.0
ξ_{A_2} (Hz)	0.0	0.0	1000	0.0	1000	0.0

Table 8.2: Synchronization errors. Synchronization errors and phase synchronization indices for each logic gate implemented in Figure 8.1.

Inputs		AND			NAND			NOR			OR			XNOR			XOR		
A_1	A_2	γ	ϵ (mV)	Out	γ	ϵ (mV)	Out	γ	ϵ (mV)	Out	γ	ϵ (mV)	Out	γ	ϵ (mV)	Out	γ	ϵ (mV)	Out
0	0	0.3	0.5	0	0.98	0.001	1	0.99	0.001	1	0.31	0.75	0	0.99	0.001	1	0.19	0.5	0
0	1	0.2	0.7	0	0.97	0.003	1	0.25	0.64	0	0.98	0.42	1	0.23	0.54	0	0.95	0.3	1
1	0	0.1	0.602	0	0.98	0.001	1	0.27	0.73	0	0.97	0.45	1	0.14	0.75	0	0.98	0.45	1
1	1	0.91	0.002	1	0.5	0.3	0	0.63	0.47	0	0.98	0.05	1	0.91	0.2	1	0.24	0.41	0

amplitude, etc.) change (e.g. see AND, OR, XOR gates in Table 8.1). So the same brain circuit represented by a single pair of oscillators may behave as different logic gates depending of the inputs they receive. This ability to classify the response of the system in different ways depending of the inputs received results in a higher flexibility for the information processing capacity of the network [*Arenas et al.*, 2008]. The network is not a static circuit that computes passively the response to the inputs but a whole collection of circuits (based in the logic gates described here) that reconfigures itself depending of the input received. This type of complex networks of logic gates which reconfigure themselves dynamically to adapt its response to specific inputs has been found in other natural systems as the signaling networks in eukaryotic cells [*Domedel-Puig et al.*, 2011; *Rué et al.*, 2012]. As said above, we do not claim, however, that the brain is a circuit of Boolean gates but a highly complex dynamical system which processes information in a very sophisticated manner at the mesoscale.

Another trait of these logic gate implementations is related with the complex dynamical evolutions that the neural mass oscillators may show. For instance, for chaotic states, time evolutions depend strongly on the initial conditions. This feature introduces a very strong link between the dynamical evolution of one oscillator and its input. Resulting from this, we argue that our implementation may possess *reversible logic* characteristics [*Bennett*, 1973], as it allows

to recognize from the outcoming signals which of the two elements in the logic gate is receiving an input. The details of such paradigm are however out of the scope of this Thesis.

The extension of the previous results to a network of interacting cortical columns leads to spatially distributed computation. In this case, each node in the network receives inputs that determine their synchronization state with other network nodes, following one of the implemented logic gates shown in Figure 8.1B. In that way, different regions of the network may act as gates that process distributed inputs, enriching the processing capabilities of the network even further. In this Chapter, we present a first step towards analyzing these capabilities by considering only relatively simple network motifs. These motifs that behave as well established logic gates in isolation, change their behavior when operating within larger networks, producing complex or even unexpected dynamics, as shown in Figure 8.2. The whole network processes a whole set of its inputs following complex multidimensional logic rules. Figure 8.2A shows a network of five

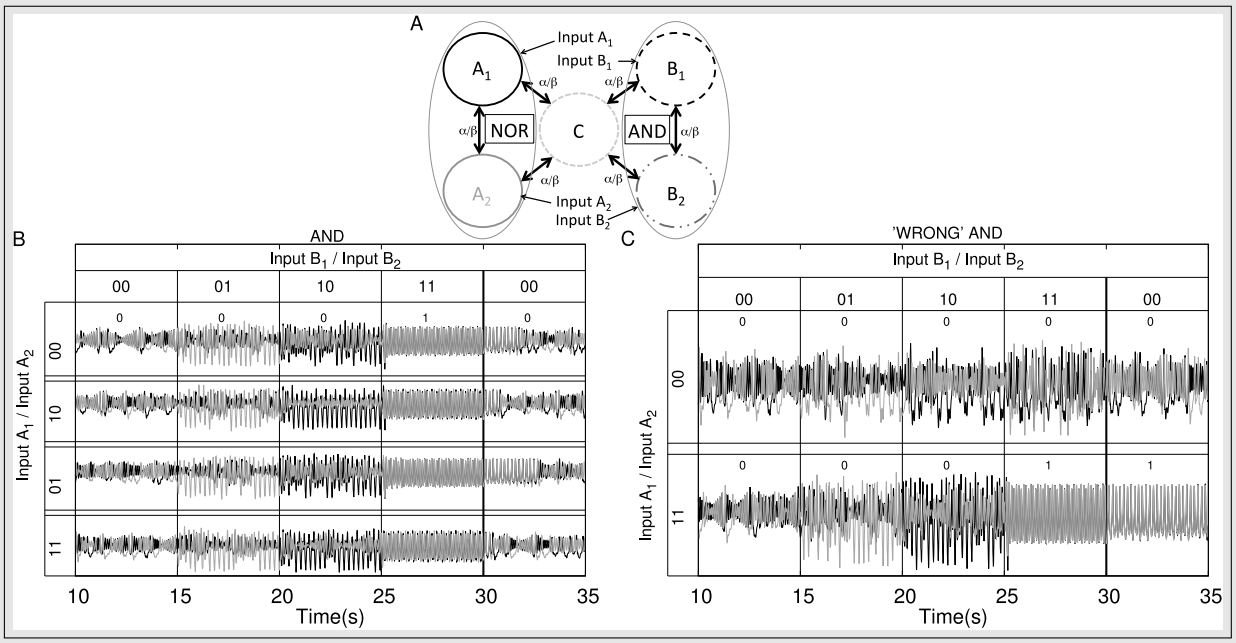

Figure 8.2: Implementation of two logic gates embedded in a network of coupled cortical units. (A) Cartoon depicting the network of coupled units. Nodes A_1 and A_2 implement a NOR gate while nodes B_1 and B_2 an AND gate. (B) Time traces of nodes B_1 and B_2 implementing an AND gate. Y axis shows the amplitude of the PSP ($y^i = y_e^i - y_i^i$). The implementation the AND gate in B_1 and B_2 is not altered by the state of synchronization of neighboring pairs, i.e. A_1 and A_2. However, the dynamics of B_1 and B_2 are indeed altered, as time traces are no longer the same for each of the four realizations. In fact, such changes in the dynamics may produce long transients before falling into the corresponding synchronized regime (see third pair of time traces between 30 and 35 seconds). The last column shows the return to the initial state of synchronization. (C) In some cases, when tuning the input, the dynamics of the oscillators no longer allows to implement the "*desired*" logic gates. For an A_1 and A_2 (constant) input configuration of 00, the implementation of an AND gate in nodes B_1 and B_2 "fails". Another type of "failure", observed in the second example of timetraces in panel C, is the impossibility to return to the initial state of (de)synchronization, shown in the last column. This results in a history-dependent logic gate.

interacting cortical columns that implement two logic gates: NOR (with CS synchronization) and AND (with PS synchronization). Each peripheral pair of columns evolves independently of the other, even though their dynamics are influenced by the behavior of the whole network. Figure 8.2B shows the truth table for the response of the AND gate (columns B_1 and B_2), while columns A_1 and A_2, which implement the NOR gate, receive different inputs. In this case it is worth mentioning that all four time traces for the AND implementation, which are symmetric realizations in terms of initial conditions, display distinctive dynamics depending on the A_1 and A_2 inputs. However, they do not lose the capacity of remaining synchronized/non-synchronized. Nevertheless, some realizations display states of long transient dynamics (see the "0" return state in all pairs of time traces) which are indeed not beneficial for fast brain computation. This long transient dynamics can be related with the ability to discern between the different input scenarios in terms of the different length of the transient dynamical evolutions. Such type of coding may be related with brain functions as proposed in *Rabinovich and Varona* [2011]. Moreover, the network implementation of logic gates is stable in terms of synchronization and arises from interdependent dynamics.

Despite being a robust dynamical feature, logic gate implementation strongly depends on the type of input and the coupling strength ranges between columns. In this regard, Figure 8.2C shows two situations in which there is a non-Boolean output configuration of an AND gate (here $\delta_{A_1} = \delta_{A_2} = 300$ Hz, while all other input characteristics are the same as those in Table 8.3). B_1 and B_2 both receive the standard oscillatory input protocol. In the first pair of time traces shown, the output displayed by nodes B_1 and B_2 does not show correlated dynamics (when B_1 and B_2 receive "1" inputs) as expected for an AND implementation. In turn, the second pair of time traces shows how, after displaying an AND output for the initial four pairs of input states, the subsequent return to the first output configuration is no longer possible. Such history dependent behavior entails the impossibility, for these conditions, of a forward implementation of the previous logic gate (AND) but results in the implementation of a state- (or history-) dependent one. These situations result only for specific input patterns. However, the response to other inputs may reproduce standard logic gates.

Table 8.3: Parameter values for NOR and AND gates. Values of the parameters used in the implementation of the NOR and AND logic gates appearing in Figure 8.2.

NOR and AND gates		
Parameters	NOR	AND
α_{ij}	5.0	2.0
β_{ij}	1.0	8.0
$\alpha_{iC} = \alpha_{jC}$	0.01	2.0
$\beta_{iC} = \beta_{jC}$	0.0	1.7
$p_i = p_j$ (Hz)	155	250
p_C (Hz)	250	
$\delta_i = \delta_j$ (Hz)	65	191
$f_i = f_j$ (Hz)	8.5	10.8
$\xi_i = \xi_j = \xi_C$ (Hz)	0.0	0.0

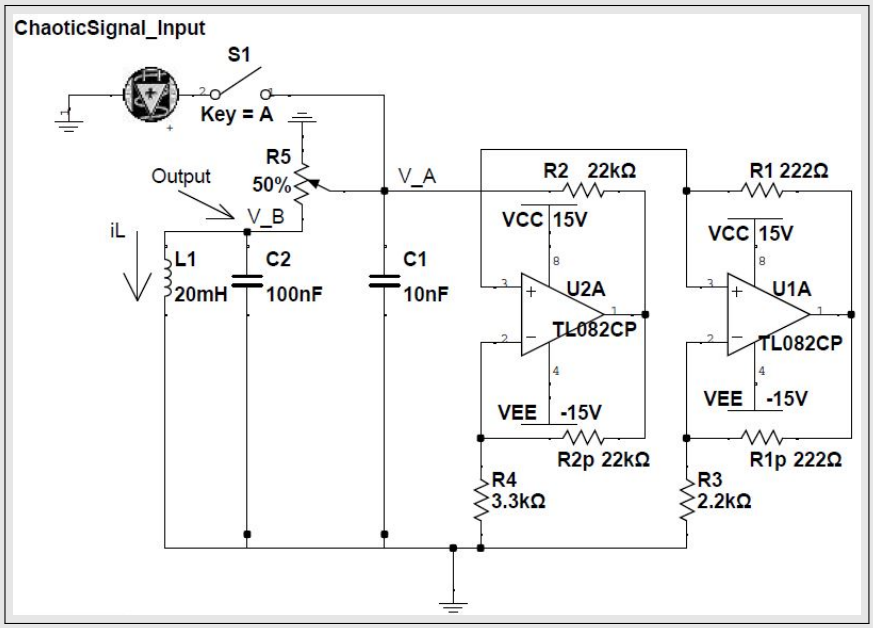

Figure 8.3: Electronic implementation of the Chua circuit. Two TL082 operational amplifiers are the core of the non-linear part of the circuit which follows the function given in Eq. (A.29). The input signal (0/1) is introduced through the capacitor C_1, while the output of the circuit is the voltage (v_B) of both C_2 and L_1.

These results can also be obtained experimentally by means of electronic circuits (see Fig. 8.3). We have used Chua oscillators [*Madan*, 1993] because they show several dynamic regimes, including chaos (see Appendix A.5.1).

The experimental implementation of small networks was conducted by the researchers in the lab of Prof. Javier Martin Buldú in the Rey Juan Carlos University. These experiments prove that the results considered in the previous section are robust against the parameter mismatch of electronic circuits and the intrinsic noise of real systems. Chaotic systems, such as Chua circuits, may display different kinds of synchronization that can be tuned through the coupling strength between the networked elements and the particular dynamics of input signals [*Arenas et al.*, 2008]. Even though the nature of the oscillators is different from those considered theoretically with neural mass models, these systems also have the ability to process information in a similar way. The experimental researchers designed and implemented experimentally several logic gates in the way described in Fig. 8.1B. Nevertheless, in what follows, we are going to focus on the description and integration of a XNOR and AND gates in a network, the former based on complete synchronization and the latter on phase synchronization. Figure 8.4A shows schematically the system integrating the outputs of a XNOR and AND gate. This circuit represents a network similar to that studied in Figure 8.2. It consists of an integrated circuit formed by five Chua oscillators, two of them implementing a XNOR gate (nodes A_1 and A_2), other two forming an AND gate (nodes B_1 and B_2) and the fifth Chua circuit (node C) integrating the output of both gates. The input of each dynamical unit can be either "1" (when a complex signal is injected into the node) and "0" (in the absence of an input signal). In order to assess the emergence of the synchronized time evolutions we have computed the synchronization errors of the two

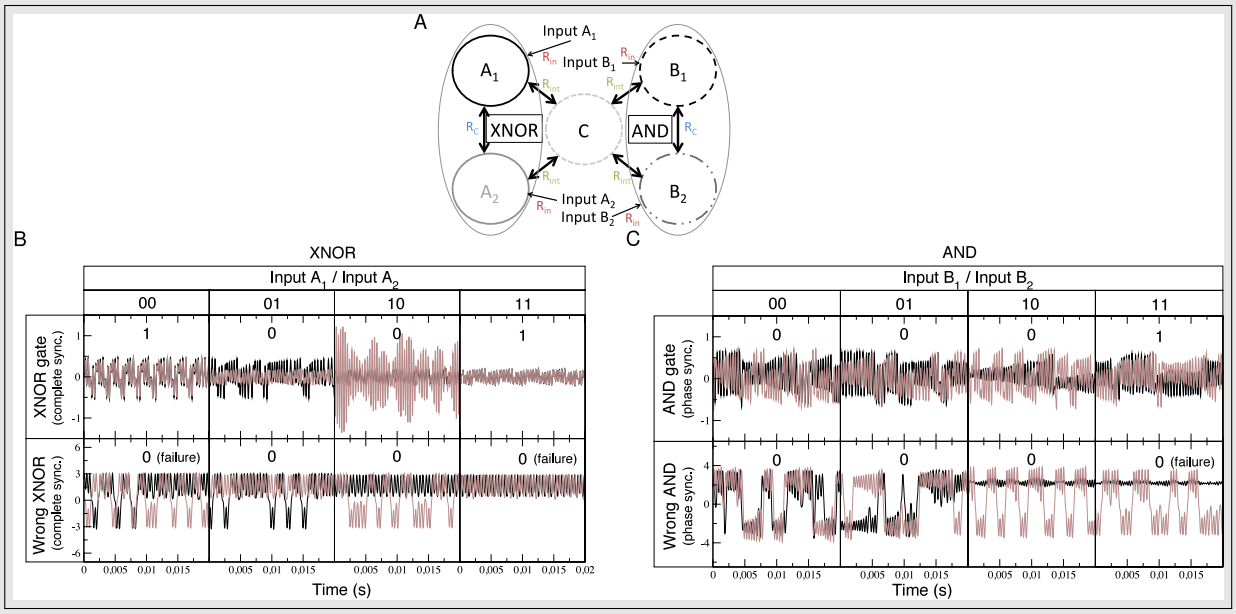

Figure 8.4: Experimental implementation of integrated logic gates. (A) Qualitative description of the experimental setup: Nodes A_1 and A_2 form a XNOR gate (in a CS regime) while nodes B_1 and B_2 implement an AND gate (in a PS regime). The output of the two sync-based gates is integrated through node C. (B) Time series of the Chua oscillators implementing the XNOR gate for low and high coupling with node C. The upper time trace, obtained for low values of the coupling with node C ($R_{int} = 100$ kΩ), shows the different outputs of the truth table of the XNOR gate (see Table 8.4). The bottom time trace, obtained for a higher coupling with node C ($R_{int} = 25$ kΩ), does not show a XNOR gate implementation. (C) Time series of the Chua oscillators implementing the AND gate for low and high coupling with node C. The upper time trace, obtained for low values of the coupling ($R_{int} = 100$ kΩ) with node C, corresponds to the different outputs of the truth table of the AND gate (see Table 8.4). In the bottom time trace, coupling with node C is increased ($R_{int} = 25$ kΩ), and the AND gate also begins to fail.

pairs of nodes that implement the logic gates (see Eq. (B.7)). Such errors allow us the determine a proper threshold to define each synchronized state, and thus each output state, in the truth tables of the logic gates. Time traces and the corresponding truth table for the XNOR gate are shown in Fig. 8.4B, while synchronization errors determining the gate's output are summarized in Table 8.4.

The AND gate is based on phase synchronization, and it is obtained by a fine tuning of the input and coupling resistances. In this case, we must reach a high phase synchronization but preventing complete synchronization, the latter leading to unavoidable (i.e., trivial) matching of the phases of the oscillators. To guarantee that we have phase, and not complete, synchronization we checked at the same time the synchronization error ϵ and the phase synchronization index γ (see Eq. (B.5)). A combination of a high ϵ and a high γ is the signature of phase synchronization between the two units forming the gate. Figure 8.4C shows the time series and the corresponding truth table for the AND gate. Table 8.4 summarizes the values of ϵ and γ that lead to a successful performance of both gates.

Table 8.4: Synchronization errors for experimental XNOR and AND gates. Synchronization errors and truth tables of the XNOR gate (with complete synchronization) and the AND gate (with phase synchronization) embedded in a network of coupled Chua oscillators. The thresholds to establish synchronized states are shown in Materials and Methods section.

Inputs		XNOR			AND		
A_1	A_2	γ	ϵ (V)	Out	γ	ϵ (V)	Out
0	0	0.991	0.085	1	0.734	0.357	0
0	1	0.750	0.641	0	0.760	0.294	0
1	0	0.885	0.449	0	0.692	0.285	0
1	1	0.994	0.039	1	0.920	0.288	1

Finally, it is worth mentioning that a tuning of the integrator resistances (see Table 8.4) allows the proper functioning of the ensemble of gates. When the integrator resistances are decreased (i.e. the coupling with the central node C is increased) to values close to $R_{int} \leq 25\text{k}\Omega$ the functioning of the gates is no longer possible due to their mutual interaction (see bottom panels of Fig. 8.4B and 8.4C). Such feature was also present in the case of the Jansen oscillators, in which increasing the coupling strength between the peripheral cortical columns and the central node led to an unstable implementation of logic gates.

8.2 Neural mass implementation of a Flip Flop circuit

Other extended systems able to perform more complex logical operations may be implemented by means of networks of coupled oscillators. We have constructed a Set Reset Flip Flop circuit, which is a circuit formed by two stable states and can be used to store a bit of information. In a flip-flop circuit the output depends on the present value of its input signals and on previous input states, therefore implementing *sequential logic* [*Vogels and Abbott*, 2005]. This system has two inputs (Set, S, and Reset, R) and two outputs C and $\bar{C}$, which follow the truth table shown alongside with the time traces in Fig. 8.5B. When neither S nor R receive an input the output states are $C = 0$ and $\bar{C} = 1$. This output state is preserved for the following input step, which is $S = 0$ and $R = 1$. Such feature keeps memory of the previous output state. The following step is $S = 1$ and $R = 0$ which "flips" the output states, being $C = 1$ and $\bar{C} = 0$. An undesired state is achieved when both S and R are 1, which leads to $C = 0$ and $\bar{C} = 0$ state. Figure 8.5A shows the network used to implement such memory: two inputs (S and R) feed two cortical columns A_1 and B_2 which in turn are connected bidirectionally with columns B_1 and A_2. These two couples of columns project unidirectionally, via intermediate cortical columns I_1 and I_2, onto B_1 and A_2, respectively. The state of synchronization of nodes A_1 and A_2 will give the output C, whereas the state of synchronization of nodes B_1 and B_2 gives $\bar{C}$. Figure 8.5B shows the online implementation of the flip-flop memory, with "flipped" output states and an undesired $C = \bar{C} = 0$ state in which none of the pairs A_1-A_2 or B_1-B_2 are synchronized. Note that transients affect the performance of the flip-flop implementation (see third pair of time traces below Fig. 8.5B) but such obstacle may be dependent on initial conditions. Moreover, as

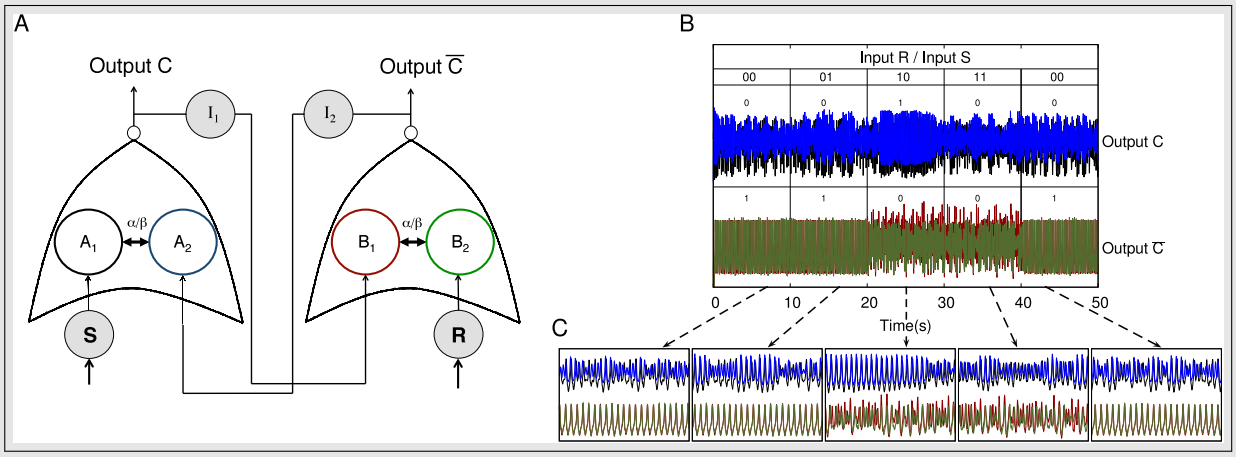

Figure 8.5: Implementation of a flip-flop memory. (A) Cartoon depicting the network of cortical columns that fulfill the flip-flop operational gate. S and R are cortical columns that receive oscillatory inputs, respectively. These columns excite upstream connected columns (A_1 and B_2) which are bidirectionally coupled to columns A_2 and B_1, accordingly. The latter receive inputs from two intermediate columns I_2 and I_1, respectively. In turn, these two columns receive the output from B_1 and B_2 (output $\bar{C}$) and A_1 and A_2 (output C), respectively. (B) Online implementation of a flip-flop. The state of synchronization is preserved when inputs $S = 0$ and $R = 0$ or $S = 1$ and $R = 0$, giving $C = 0$ and $\bar{C} = 1$, but "flips" when $S = 0$ and $R = 1$, giving $C = 1$ and $\bar{C} = 0$. A not desired situation is the one in which $C = 0$ and $\bar{C} = 0$, i.e., A_1 and A_2 or B_1 and B_2 are not synchronized. This happens when $S = 1$ and $R = 1$, which fulfills a flip-flop truth table. (C) Magnification of the time scale of the output signals for the sequence of five $S - R$ bit pairs of panel B. The full scale for each sub panel with a pair of signals is corresponding to 5 s.

in previous implementations, each output state is characterized by distinctive time evolutions, which, on top of memory storage, also give information about which terminal (S or R) receives the input.

8.3 Conclusions

In order to address how information can be processed, from the perspective of synchrony, at the mesoscopic scale we have analyzed theoretically networks of coupled neural mass oscillators describing cortical columns. These networks use synchronization as the essential ingredient to process the information arriving to/from each of their nodes. We have seen that by interpreting the inputs arriving to the columns of the network as “0” or “1” and defining the output of a binary operation in terms of the synchronized state of two columns also as “0” or “1”, several binary logic gates can be constructed. This dependence of the synchronization level of two columns on their stimulation has been observed experimentally, for instance, in the cat visual cortex [*Gray et al.*, 1989]. Interestingly, different binary logic gates constructed using the same physiological circuitry result only from changes in the input signals received by the oscillators (e.g. AND, OR and XOR gates in Fig. 8.1). This rich type of behavior shown by only two

Table 8.5: Parameter values for flip-flop. Values of the parameters used in the implementation of the flip-flop operational gate shown in Fig. 8.5.

Flip-flop operational gate			
Parameter	Value	Parameter	Values
α_{SA_1}	80.0	β_{SA1}	0.0
$\alpha_{A_1A_2}$	10.0	$\beta_{A_1A_2}$	5.0
α_{RB_2}	10.0	β_{RB_2}	0.0
$\alpha_{B_1B_2}$	9.0	$\beta_{B_1B_2}$	9.0
$\alpha_{I_1A_1}$	52.0	$\beta_{I_1A_1}$	9.0
$\alpha_{I_1A_2}$	52.0	$\beta_{I_1A_2}$	9.0
$\alpha_{I_2B_1}$	10.0	$\beta_{I_2B_1}$	2.0
$\alpha_{I_2B_2}$	10.0	$\beta_{I_2B_2}$	2.0
$\alpha_{A_2I_2}$	52.0	$\beta_{A_2I_2}$	0.0
$\alpha_{B_1I_1}$	10.0	$\beta_{B_1I_1}$	0.0

Parameter	Value
$p_i = p_j$ (Hz)	155
$p_S = p_R$ (Hz) $p_{I_1} = p_{I_2}$ (Hz)	57.8
p_{A_1} (Hz)	150
p_{A_2} (Hz)	150
p_{B_1} (Hz)	250
p_{B_2} (Hz)	250
δ_S (Hz)	220
δ_R (Hz)	200
$f_S = f_R$ (Hz)	8.5
ξ_{S,R,A_i,B_i,I_i} (Hz)	1000

coupled cortical columns may be very complex when many other columns are considered. In this sense, the ability to analyze input signals with very different characteristics (average density of spikes, amplitude and frequency of oscillations or noise level) is multiplied by the simple addition of this type of binary logic gates in a network. Nevertheless, this simplistic view may become even more sophisticated when putting the binary motifs together in a larger network. As shown in Fig. 8.2, simply by connecting two different logic gates through a hub may result in a system where the two gates operate in parallel independently of each other (Fig. 8.2A) or operate in a different way (Fig. 8.2B). In this case, outputs may depend on the input of both gates at the same time or on the history of the input states driving the nodes (see examples of both behaviors in Fig. 8.2B). This type of dynamics, in larger networks, makes selectivity of the states richer than just the repetition of simple binary logic gates in a network. In order to show the generality of this feature in other networks (and also its robustness in terms of the dynamical oscillators used to build the network) we have constructed several binary logic gates with electronic circuits – Chua circuits – operating in a chaotic regime. We have shown experimentally that a network built by coupling two of these gates through a hub (using the same simple motif as that studied with neural mass models) is able to process information as expected (see Fig. 8.4). Finally, we have shown theoretically that, by using a network of oscillators we can implement a Set Reset Flip Flop circuit [*Hahnloser et al.*, 2000], which is an example of another stimulus selector, in this case, that is able to store information.

In this work, we have considered only the simplest interpretation of input and output states (leading to Boolean logic). However, our results may be analyzed from a wider perspective,

for instance, if we explicitly consider the degree of synchronization of the different elements (resulting in fuzzy logic) or if we consider as possible output states as types of synchronization (phase, generalized, lag, complete, ...) between the different elements which form the network of oscillators. The fact that we consider only one of the different dynamical characteristics of the system, in our case its degree of synchronization, is a coarse simplification. The dynamical response of the network is not determined only by its degree of synchronization. For instance, the frequencies involved in the dynamics, or the degree of excitation/inhibition segregation, may also inform about the input stimulus characteristics. Further studies are required to analyze in more detail these complex scenarios.

Part III

Conclusions

Chapter 9

Conclusions

Neuronal networks and their dynamics are at the basis of the complex brain features such as memory, perception, consciousness or emotions. Altogether, all these features conform the so-called *mind*, the understanding of which is still eluding the scientific community [*Fuster*, 2003]. Different approaches to studying the brain deal with separate spatio-temporal scales, which ultimately result in a parcelled vision of the organ and, therefore, of its capabilities [*Zalesky et al.*, 2010]. Within all these parcellations, the study of the brain based on the analysis of its microscopic structures, namely neurons and glia, has been the main research since the seminal studies from Ramón y Cajal and Golgi [*Velayos-Jorge et al.*, 2003]. From the computational point of view, the work by Lapicque and later Hodgkin and Huxley provided a basis for the mathematical treatment of the dynamics emerging from the electrical activity of neurons [*Hodgkin and Huxley*, 1952]. In fact, modern neuroscience still stands on the grounds established from these mid-XXth century discoveries.

When analyzing brain activity at larger scales, population dynamics come into play: the activity of large ensembles of neurons display rhythmic dynamics which arise from the synchronized electrical activity of neural cells, as seen in electroencephalogram (EEG) or magnetoencephalogram (MEG) recordings [*Buzsáki and Draguhn*, 2004]. Therefore, its mathematical treatment requires tools coming from population dynamics, e.g. statistical methods or mean-field approaches [*Deco et al.*, 2008; *Faugeras et al.*, 2008]. From this perspective, the brain is described as a dynamical system in which characteristic complex phenomena arise: bifurcations leading to oscillations, noise-induced transitions and synchronization [*Horn et al.*, 1998].

In this Thesis we aimed to describe neural processes occurring at the mesoscopic scale, i.e. a scale where large populations of neurons exhibit (average) complex dynamics. Besides, since a collection of mesoscopic neuronal pools, e.g. cortical columns, is needed to characterize the dynamics of brain areas, the description which lies in between the microscopic and the macroscopic scale of brain dynamics better fits our descriptive needs. In the previous chapters we have shown that complex dynamics in the brain can explain well-known features such as the excitation-inhibition balance at the mesoscopic scale, or the heterogeneous synchronization between brain areas. We have also shown that synchronization may organize information flow in a network of mesoscopic dynamical units. Overall, the hypotheses posed in this Thesis may help to understand the potential neural mechanisms that may rule synchronization, computation and information processing at the mesoscopic scale of the brain.

9.1 Scales in brain dynamics

The goal of Chapter 5 is to provide theoretical evidence for a cross-talk between different scales in the brain. Nowadays, little is known about the impact of microscopic dynamics on other scales in the brain, as well as the impact of larger scale dynamics on individual neurons: Is the precise timing of neuronal discharges a feature that vanishes at the population level? Do mesoscopic oscillations have an impact on small populations of neurons?

We examined inter-scale interactions by using two distinct theoretical models of neuronal dynamics: on the one hand, we used a conductance-based neuronal description to account for the activity of a pool of neurons at the microscopic scale. Such type of model describes the action potential generation at the level of voltage-gated channel dynamics. On the other hand, we used a mesoscopic description of neuronal dynamics, which does not take into account neuronal spikes but rather the average population activity due to the synchronized time evolution of thousands of neurons. Previous works have addressed, from a theoretical point of view, the derivation of mesoscopic dynamics from the microscopic features of neurons [*Deco et al.*, 2008; *Faugeras et al.*, 2008]. From such approaches one can track the impact of small perturbations in neuronal discharges onto the overall brain dynamics [*Izhikevich and Edelman*, 2008], or derive mean field equations that characterize the dynamics of large ensembles of neurons [*Deco et al.*, 2008]. However, such works do not shed light on whether the different dynamical scales of the brain interact to produce emergent phenomena. Understanding the conditions under which the interaction of scales is relevant allows to determine the impact of each scale feature on its counterparts, and can result in a simplified scheme of interaction that can be useful for future research.

In Chapter 5 we have explored the use of synchronization as a proxy for assessing a detectable cross-talk between different description scales in the brain. Thanks to this, we investigated the features of each scale that were crucial for the cross-talk to be successful. In our paradigm, the communication between two neural mass models [*Jansen and Rit*, 1995] displaying distinct dynamical evolutions and characteristic frequencies was mediated by a neuronal pool in which neurons were described by conductance-based models. The three units displayed dynamics at low, medium and high frequencies – 4Hz and 10Hz the neural masses, and 40Hz the neuronal pool –, which in the absence of coupling do not display any frequency or phase relationships.

First we investigated which were the conditions that allow the frequency or phase locking of two neural mass nodes by coupling them to the neuronal pool (see Fig. 5.1). The neuronal pool is capable of mediating the communication between the two neural masses when a sufficiently large subpopulation of its neurons is involved. However, the synchronization is extremely sensitive to the topological features of the microscopic population. Indeed, increasing clustering impoverishes the neuronal pool capacity of mediating synchronization. Besides, frequency and phase locking, which can appear at the same time in the neural masses, are exclusively mediated by the neuronal pool. Strikingly, if we substituted the neuronal input into the neural masses by a constant parameter with the average value of the neuronal input, phase locking disappeared. Such feature indicates that phase differences are encoded in the irregular dynamics of neurons. Finally, if the neuronal pool works in a slower collective regime, e.g. the alpha band, the synchronization between the neural masses is decreased.

The main hypothesis of our work is that the two neural masses synchronize at the lower frequency band, close to theta rhythm, thanks to an increase in the low frequency activity of the neuronal network (see Fig. 5.3). Furthermore, the fast dynamics of the neuronal network do not seem to interfere with the neural mass dynamics, as displayed in the power spectra of the three nodes. This feature reveals that the neuronal network allows different frequency channels for communication between neural structures. We also show that the increase in the precise timing of the firings in a neuronal network working at the gamma range favors communication. Overall, we first report that the interaction of scales in brain dynamics is a feature that can be tested by means of synchronization, and we provide the conditions for this interaction to occur.

9.2 Dynamics of excitation and inhibition at the mesoscale

The study of the interaction between microscopic and mesoscopic dynamics shed light onto the cross-talk between scales. However such interaction was extremely depending on another crucial feature of brain dynamics: the balance between excitation and inhibition. In order to reproduce the cross-talk between our neural structures, we had to carefully tune the value of the excitatory and inhibitory couplings between the neurons inside the neuronal network and, at the same time, between the neuronal network and the neural mass models. Indeed, these results revealed a feature of great importance to establish a correct communication between the two neural masses. In order to deeper understand it, we focused on the study of the effect of excitation and inhibition in the synchronization characteristics of mesoscopic neural structures.

The importance of excitation and inhibition at the microscopic scale in the brain has been often stressed [*Deco et al.*, 2014]. However, its translation into large neuronal population dynamics has not been addressed in detail. In Chapter 6 we wanted to study the impact of excitatory and inhibitory couplings in the synchronization characteristics of coupled mesoscopic neural structures. Our first approach was to model the activity two cortical columns [*Jansen et al.*, 1993], which are well known mesoscopic structures, and to see whether their bidirectional coupling allowed for the emergence of excitation and inhibition patterns (see Fig. 6.1). By doing so, we model the well-known effect of *segregation*, or dynamical separation, between excitation and inhibition, which usually emerges in neuronal networks for different input discrimination paradigms [*Rinkus*, 2010], and we bring it to the cortical column level. The emergence of segregation in cortical columns permits to state that, at a population level, large ensembles of neurons behave as being excitatory-dominated, whereas others behave as being inhibitory-dominated. This fact has a deep impact in the overall dynamics in the brain [*Izhikevich and Edelman*, 2008], being crucial for a proper synchronization of distant brain areas which is at the basis of proper brain performance [*Knoblauch*, 2003].

Our model gives evidence for a topology-dependent segregation, which is also intimately bound to the coupling characteristics. By first studying small cortical column motifs, we found that there are regions in the coupling parameter space where segregation emerges spontaneously (Fig. 6.2), with columns within a network being excitatory and others being inhibitory. This segregation results from the emerging bistability in the model dynamics, in which the average output signal, defined as the subtraction between the average excitatory post-synaptic potential

(EPSP) and the average inhibitory post-synaptic potential (IPSP), may lay in the positive or negative range but, always, different from zero.

In Chapter 6 we also studied how the introduction of external inputs affected the dynamics of cortical columns in terms of segregation and synchronization. The interaction between oscillatory inputs and the intrinsic oscillatory dynamics of the columns gives rise to resonance phenomena and complex dynamical evolutions [*Spiegler et al.*, 2011b]. When embedded in large networks, the cortical columns display patterns of excitation and inhibition, as well as patterns of synchronization. The first have recently been traced in the visual cortex of cats [*Onat et al.*, 2011] whereas the latter are known to be characteristic of brain signals like EEG – which we model here – [*Müller and Anokhin*, 2012]. We have seen that the heterogeneity in cortical columns contacts allows a larger degree of segregation, with *scale-free* being networks the arrangements displaying the largest separation between excitatory and inhibitory dynamics. Moreover, the synchronization characteristics of the cortical columns also depend on the topology: the more heterogeneous the network is, the stronger coupling is required to be for the networks to synchronize completely. However, if inhibitory couplings dominate, hub nodes tend to be inhibitory and the irregularity in the signals is reduced, favoring network synchronization (see Figs. 6.7, 6.8). Such a feature can be thought to be a regulatory mechanism for synchronization.

Overall, we deepen on the understanding of the mesoscopic organization of excitation and inhibition and its impact on the synchronization dynamics of cortical columns. We hypothesize that the heterogeneity in the cortical columns networks allows for an optimal amount of synchronization within cortical networks: on the one hand because of the inherent difficulty to globally synchronize heterogeneous networks, and on the other hand thanks to the regulatory role played by inhibitory columns in favoring the overall synchronization when inhibitory couplings dominate. Therefore, a careful balance between excitation and inhibition is also crucial at the mesoscopic scale for proper brain synchronization and, arguably, proper brain performance.

9.3 Coexistence of synchronizations in complex weighted networks

Following up the results obtained when studying the synchronization characteristics of networks of cortical columns (see Fig. 6.7) we wanted to further reveal the conditions that allow several clusters of oscillators to display non-trivial synchronization patterns within a single network, which we termed *coexistence of synchronizations*. In Chapter 6, when studying cortical columns, we found regions of parameter space that allowed the emergence of several types of synchronization. Such feature resembles the synchronization patterns that can be found in EEG or MEG recordings [*Engel et al.*, 2001a] and, therefore, might be characteristic of brain dynamics. We asked ourselves whether this phenomenon can be found in arrangements of coupled oscillators, since no clear evidence has been found so far.

In Chapter 7 we made use of a simple dynamical system which displays complex dynamics, the Rössler oscillator [*Rössler*, 1976], and we studied the synchronization characteristics of networks of such oscillators. We found that complex synchronization clusters appearing in networks of coupled cortical columns also emerged in this system. Therefore, we undertook a careful analysis of the conditions for which the coexistence of synchronizations appears in these model networks One could argue that the phenomenon of *chimera states* is analogous to what we described as

coexistence of synchronizations. However, in the case of chimeras, the coupling scheme and the nature of the oscillators is different: non-local couplings are established between the oscillators which, in turn, must be identical for chimeras to appear [*Abrams and Strogatz*, 2004]. Besides, the spontaneous synchronization break is tracked by means of phase locking, which restricts the synchronization pattern to the phase locking between oscillator pairs. In the case of the coexistence of synchronizations the couplings can be local – we used diffusive couplings but other types of couplings can be also used – and the oscillators may not be identical. Within these conditions, not only phase locking but many functional relationships between the time evolutions of the oscillators can be established (see definitions in Chapter 7). In turn, we show that for well-defined coupling conditions the coexistence of synchronizations is stable. We do so by means of studying the evolution of the conditional Lyapunov exponents (LEs) in terms of a coupling parameter. The subsequent LE zero crossings were mapped to the calculation of the cross-correlation and the phase locking values between the dynamical evolutions of the oscillators, so as to establish the correspondence between each LE value and the emerging synchronization pattern. Finally, we showed that for coupling parameter values that allowed the LEs to expand between positive and negative values, the coexistence of synchronization was possible and delimited between the first and the last zero crossings of the maximal LEs of the system.

The most important feature that can be extracted from the coexistence of synchronizations and its stability is its *consistency*, that is, persistent coexistence patterns regardless of the initial conditions. Thanks to its consistency, the coexistence of synchronizations can be used to construct stable functional networks. The idea behind this is the fact that functional networks are established by taking into account the preservation of the same functional relationship between (oscillatory) signals. In the case of coexistence, we argue that the construction of functional networks is much more reliable because it is based in the preservation of heterogeneous synchronization patterns upon changes in the initial conditions. Such restrictive condition provides robustness to the constructed networks and allows a better characterization of its dynamics. Finally, we show that there is an intimate relationship between the underlying structural networks and the emerging consistency of the functional networks constructed with heterogeneous synchronization patterns. Remarkably that allows, in certain conditions, to retrieve structural networks from the reconstructed functional networks much more reliably than using single synchronization motifs, as done elsewhere [*Bullmore and Sporns*, 2009]. Finally, we show that certain functional network topologies may be retrieved much more often than others, specially complex arrangements such as scale-free or small-world, because the underlying structural networks do not allow consistent functional networks to appear statistically [*Eguíluz et al.*, 2005].

9.4 Synchronization-based computation through networks of coupled oscillators

It is usually accepted that the brain is capable of performing computation by integrating the input signals it receives from either sensory or non-sensory organs. At the microscopic scale

large neuronal networks are responsible for performing such computation, in the form of an all-or-none spike response. Such binary-like behavior was easily mapped to a Boolean-like computation paradigm, shifting the view of neuronal networks to large ensembles of coupled small Boolean devices [*McCulloch and Pitts*, 1943]. Successfully, many brain features have been explained by taking into account a binary approach to neuronal dynamics, with networks of integrate-and-fire neurons being able to store memory or implementing logic gates [*Vogels and Abbott*, 2005]. However, a question naturally arises: are the computational capabilities of the brain only restricted to microscopic scale neuronal networks?

At larger scales the precise timing of neuronal discharges is masked by the oscillatory dynamics emerging from the synchronization of the spikes of thousands of neurons. Therefore, it is plausible to think that some of the brain computational capabilities may not be particular to single neurons, and not even to small populations, but rather manifest in the activity of thousands or even millions of neurons. The idea of brain computation by means of brain oscillations has often been associated with phase coding and decoding [*Jensen*, 2004], phase precession [*Tort et al.*, 2009] or communication through coherence [*Fries*, 2005], which provides a framework in which both precise spiking and global oscillatory dynamics interact to integrate information. Besides, some works have also taken into consideration that synchronized spiking activity may also be a form of computation [*Zanin et al.*, 2011]. In Chapter 8 we gathered some of the theoretical evidence pointing towards a synchronization-based computation paradigm so as to export it to the level of brain oscillators.

The peculiarity of our approach is the use of the paradigms of synchronization coexistence, already described in Chapter 7, which allows us to posit that heterogeneous synchronized oscillations can implement Boolean functions and higher logical operations. In this sense, we show that a pair of coupled cortical columns – represented by neural mass models – can implement all known Boolean logic gates (see Fig. 8.1). Remarkably, we show that the states in the logic gates can be defined in a wide sense, that is: “0” if no synchronization arises or “1” if the oscillators are synchronized (see Fig. 7.1A). Therefore, logic gates are synchronization-dependent and define characteristic functional relationships between the coupled oscillators. Such feature allows to differentiate between the computation performed by an AND gate based in phase synchronization for instance, from an AND gate based in complete synchronization. Moreover, distributed computation can also be performed by networks of coupled neural masses via the coexistence of synchronizations.

Our theoretical hypotheses were tested using networks of electronic nonlinear oscillators, which were proven to be adequate to reproduce the expected results. Finally, as a proof of concept, we implemented a flip-flop memory by means of a network of neural masses. The synchronization characteristics of the output elements of the circuit undergo a hysteretic cycle that can store one bit of information and, therefore, be a potential memory-storage mechanism. Overall, our theoretical implementation allows to state that synchronized brain oscillations can be used to perform computation, store memory and, maybe, perform higher information processing features.

Chapter 10

Perspectives

The work presented in this Thesis covers topics spanning from classical neuroscience to the study of dynamical systems, altogether with the help of computational techniques. Such a broad spectrum of topics has helped me learning different theoretical paradigms, such as the stability analysis of dynamical systems or the implementation of Boolean logic. Besides, I have adquired expertise in different computational tools, mainly numerical integration and time series analysis techniques. On top of that, however, this Thesis has opened many research lines to be covered in the future.

Firstly, we have further pursued the development of a neural mass model that gathers some of the features found in Chapter 5, in line with the work by *Faugeras et al.* [2008]. We want to develop a neural mass model that embeds the capacity of a microscopic neural network to display several frequency components, at both alpha and gamma ranges. With that we pretend to emulate the effects found in microscopic neuronal networks when coupling mesoscopic and microscopic structures: the mediation of the phase and frequency locking between neural masses as well as the preservation of the intrinsic dynamics at the gamma range. Besides, it is known that cross-frequency coupling may be at the basis of learning or memory [*Tort et al.*, 2009], which has not been modeled at the mesoscopic scale. With all these elements we pretend to model complex brain features by means of a mesoscopic approach to brain dynamics.

Secondly, we obtained feedback from an experimental group aiming to obtain a theoretical description of a phenomenon related to excitation-inhibition segregation (Chapter 6). In their work they track the mesoscopic cortical activity by using voltage-sensitive dye imaging [*Markounikau et al.*, 2010]. Recently, they have found traces of enhanced excitability and inhibition in certain regions of the cortex upon the application of Transcranial Magnetic Stimulation (TMS) into cats [*Kozyrev et al.*, 2014], which resemble the predicted excitation-inhibition patterns found in [*Malagarriga et al.*, 2014, 2015b]. Therefore, we want to further study the mechanisms responsible for segregation at the level of cortical activity, caused by different types of stimulation protocols such as TMS or even electrical stimulation, and compare it to the experimental counterparts.

We also aim to further explore the implications of our work on the coexistence of synchronizations (Chapter 7). We hypothesize that this phenomenon may be ubiquitous in systems of coupled oscillators and, more importantly, may reveal topological features of coupled oscillatory

systems whose underlying structural network is not available. We argue that the consistency of the heterogeneous synchronization patterns allows to retrieve structure from function in a much more reliable way than with other techniques. Therefore, we have now started to analyze different data sets (EEG, climate time series) in terms of coexistence so as to proof the validity of our results and, ultimately, so as to obtain information about the functional and, hypothetically, structural networks that sustain these systems.

Finally, we plan to extend our work on computation using nonlinear oscillators (Chapter 8). Starting with the implementation of the complex logic function of a flip-flop memory we want to see whether such paradigm can be applied to well-known memory mechanisms present in the brain. We are also exploring the possibility to apply the obtained results into a robotic model that can make use of the synchronized oscillatory dynamics so as to integrate information and store it as a memory.

Part IV

Appendices

Appendix A

Models

A.1 Description of the neural mass models

A.1.1 Jansen and Rit Model

In Chapters 5, 6 and 8 the description of the mesoscopic neuronal ensemble forming a cortical column is based on a model proposed by Jansen and co-authors [*Jansen et al.*, 1993]. This model characterizes cortical dynamics by using a mean field approximation [*Grimbert and Faugeras*, 2006]. Jansen's model describes the average activity of three cortical populations; excitatory and inhibitory interneurons and pyramidal cells., which form a feedback circuit (see Fig. A.2B). The main pyramidal population excites both interneuronal populations in a feed-forward manner and the excitatory (inhibitory) interneurons feed back in an excitatory (inhibitory) manner into the pyramidal population. The dynamical evolution of these three populations is introduced considering two different transformations. Each population transforms the total average density of action potentials reaching their afferent synapses from different origins, $\sum^m p^m(t)$, into an average postsynaptic excitatory or inhibitory membrane potential $y_i(t)$. A linear convolution implements this transformation in terms of the kernel

$$h_e(t) = \begin{cases} Aate^{-at} & \text{if } t \geq 0 \\ 0 & \text{if } t < 0 \end{cases} \tag{A.1}$$

for the excitatory couplings and

$$h_i(t) = \begin{cases} Bbte^{-bt} & \text{if } t \geq 0 \\ 0 & \text{if } t < 0 \end{cases} \tag{A.2}$$

for the inhibitory couplings. A and B are related with the maximum height of the excitatory and inhibitory postsynaptic potentials (EPSP and IPSP, respectively), whereas a and b represent the inverse of the membrane time constants and the dendritic delays (see Table A.1).

The second dynamical transformation in the model is the conversion of the net average membrane potential into an average density of spikes. This conversion is done at the somas of the neurons that form the population, and is described mathematically by a sigmoid function

$$S(m(t)) = \frac{2e_0}{1 + e^{r(\nu_0 - m(t))}}. \tag{A.3}$$

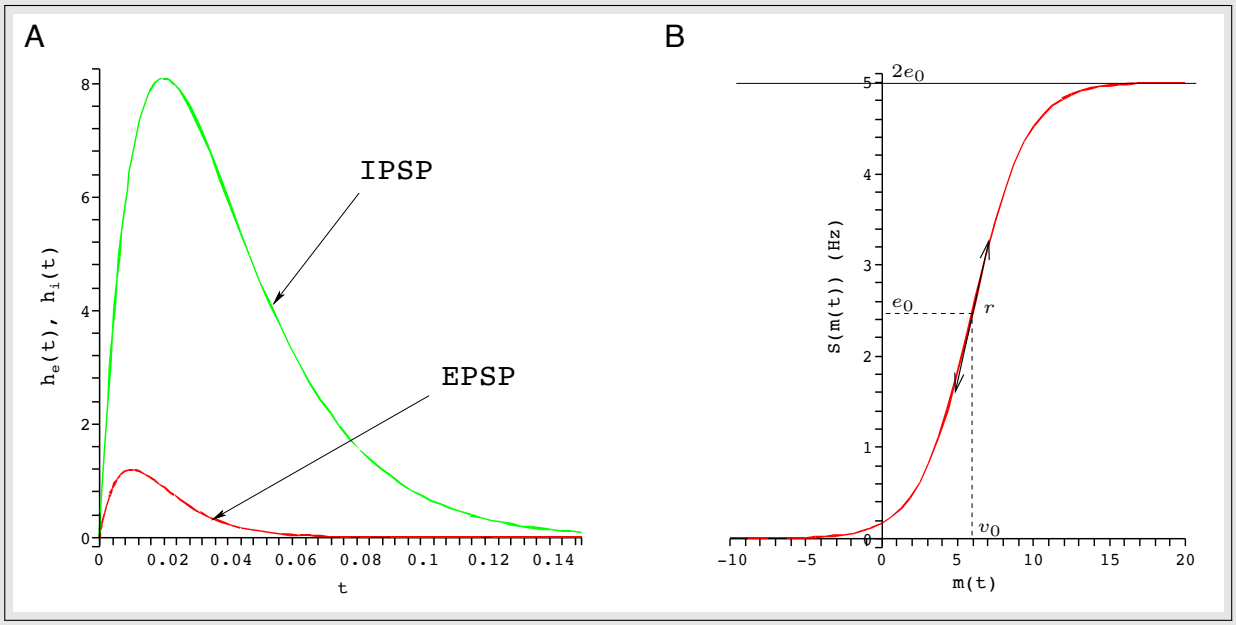

Figure A.1: Average postsynaptic potentials and average firing rate of Jansen and Rit model. (A) Shape of the transformation kernels A.1 (red) and A.2 (green). The inhibitory postsynaptic potential function (green) reflects the strong contribution of inhibitory cells onto pyramidal cells, compared to that of excitatory cells (red). (B) Sigmoid function $S(m(t))$ relating postsynaptic potentials to average firing rate. Adapted from *Jansen et al.* [1993]; *Grimbert and Faugeras* [2006].

The parameter values are depicted in Table A.1 and $m(t)$ corresponds to the net Postsynaptic Potential (PSP) input into the population being considered. The average density of action potentials produced by the presynaptic population acting upon the postsynaptic population, $p^m(t)$, turns out to be proportional to $S(m(t))$, where the proportionality constant weights the contact between the populations, and gives the range of efficiency of the synaptic interaction.

The transformation described by Equations (A.1) and (A.2) can be introduced using two differential operators:

$$L(y_i(t);a) = \frac{d^2y_i(t)}{dt^2} + 2a\frac{dy_i(t)}{dt} + a^2y_i(t) = Aa\left[\sum_m p^m(t)\right], \tag{A.4}$$

$$L(y_i(t);b) = \frac{d^2y_i(t)}{dt^2} + 2b\frac{dy_i(t)}{dt} + b^2y_i(t) = Bb\left[\sum_m p^m(t)\right], \tag{A.5}$$

for the excitatory and inhibitory integration of the average density of action potentials, respectively. Combining Eqs. (A.3-A.5), alongside with the topology described in Chapters 5, 6, 7, 8 and in Fig. A.2B, we obtain the complete model for a particular NMM i, representing a cortical column,

coupled to N_{neigh} neighbors in a network of N cortical columns:

$$\frac{d^2y_0^i}{dt^2} + 2a\frac{dy_0^i}{dt} + a^2y_0^i = AaS[y_1^i - y_2^i], \tag{A.6}$$

$$\frac{d^2y_1^i}{dt^2} + 2a\frac{dy_1^i}{dt} + a^2y_1^i = Aa\{C_2S[C_1y_0^i] + \sum_{j=1}^{N_{neigh}} \alpha_{ij}S[y_1^j - y_2^j] + \delta^i(t)sin(2\pi f^i t + \phi^i) + p_e^i(t) + \chi_i(t)\}, \tag{A.7}$$

$$\frac{d^2y_2^i}{dt^2} + 2b\frac{dy_2^i}{dt} + b^2y_2^i = Bb\{C_4S[C_2y_0^i] + p_i^i(t) + \sum_{j=1}^{N_{neigh}} \beta_{ij}S[C_3y_0^j]\}, \tag{A.8}$$

where y_0^i represents the PSP that feeds the interneurons populations, and y_1^i (y_2^i) represents the excitatory (y_e in the text) (inhibitory, y_i in the text) PSP that feeds the pyramidal population. The intensity of the excitatory (inhibitory) coupling of columns with their neighboring columns is given by α_{ij} (β_{ij}), where:

$$\alpha_{ij} = \frac{\alpha}{\sqrt{n_i n_j}}, \tag{A.9}$$

$$\beta_{ij} = \frac{\beta}{\sqrt{n_i n_j}}, \tag{A.10}$$

if not specified otherwise. Such weighting prevents the system integration to diverge, as couplings are bounded by the number of neighbors of the receiver node (n_i) and that of its neighbors (n_j). We intend to represent small cortical regions as no delays in the couplings are taken into account. Moreover, each column may receive a time dependent input composed of a constant input, $\bar{p^i}$, either excitatory or inhibitory, and a periodic external stimulus coming from other brain structures or the sensory system. We represent this periodic input as a sinusoidal driving, i.e. $\delta^i(t)sin(2\pi f^i t + \phi^i)$ (see Eq. (A.6)). Besides, each column may receive a random excitatory contribution onto the pyramidal cells, $\chi_i(t)$, which can be associated with a stochastic process occurring at a cellular level (see Eqs. (A.20, B.9)). The contribution of the column i to the EEG activity measured in the scalp is proportional to $y_1^i - y_2^i$. Thus we will analyze the activity of each cortical column considering the evolution of $y^i = y_1^i - y_2^i$ (represented by $y_e^i - y_i^i$ throughout the text).

In *Jansen et al.* [1993] the model produces alpha oscillations thanks to a supercritical Hopf bifurcation and epileptic-like waveforms thanks to a saddle-node bifurcation in terms of the external input $p_e(t)$ (see examples in Fig. 2.1). However, the model presented here has an extensive repertoire of dynamical states, being able to produce periodic, quasi-periodic or chaotic [*Spiegler et al.*, 2011a; *Malagarriga et al.*, 2015b; *Skarda and Freeman*, 1987] behavior. It also exhibits excitatory/inhibitory segregation [*Malagarriga et al.*, 2014, 2015b] depending on the choice of α_{ij} and β_{ij} values in the network. These coupling parameters also fix a whole set of synchronized regimes that may coexist in the network [*Malagarriga et al.*, 2016]. The intra-columnar connectivity constants values are defined in terms of C_i, with $i = 1, \ldots, 4$. We use the values given in Jansen et al. [*Jansen and Rit*, 1995].

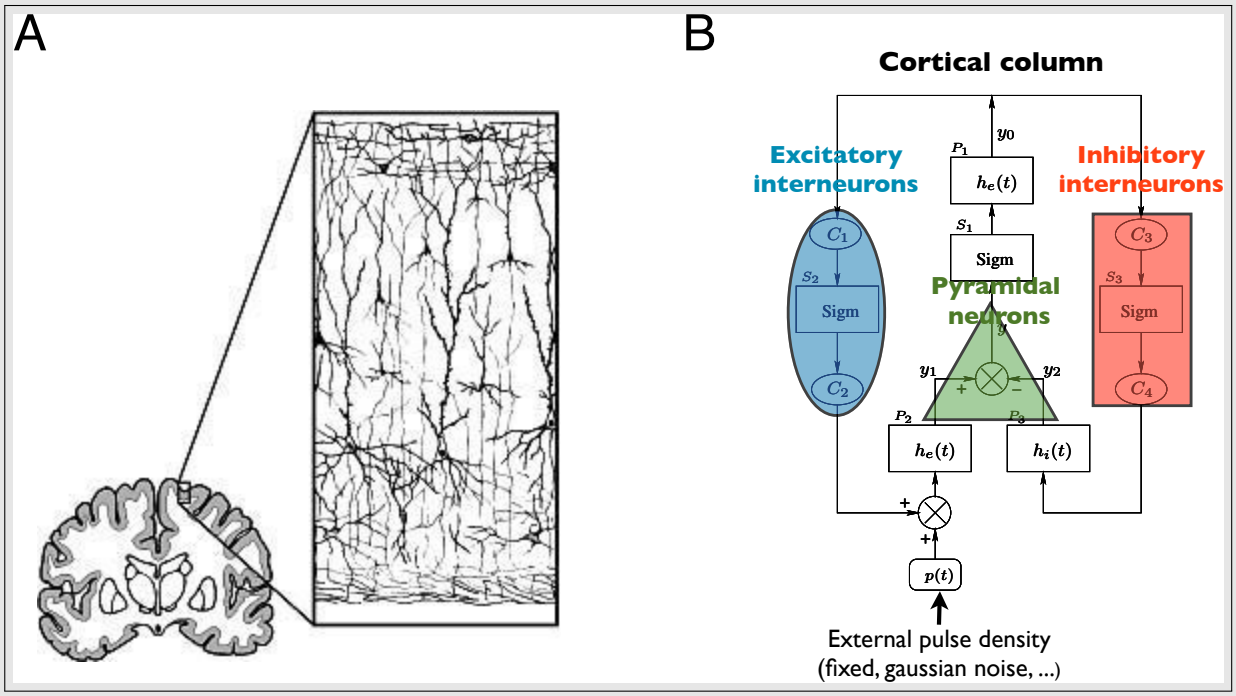

Figure A.2: Circuit describing a cortical column (Jansen and Rit model). (A) Cartoon depicting the location of a cortical column in the human cortex. (B) Jansen and Rit lumped parameter model circuit. Three interacting neural populations (excitatory/inhibitory interneurons and pyramidal cells) form a feedback loop and, therefore, create oscillations in their EPSP and IPSP. From *Faugeras et al.* [2008]

Table A.1: Jansen and Rit model parameters. All parameters have been adapted *Jansen and Rit* [1995] except for the sinusoidal input in Eq. (A.6).

Parameter	Value
Cortical PSP amplitude	$A = 3.25$ mV, $B = 22$ mV
Inverse of the dendritic conduction time	$a = 100$ Hz, $b = 50$ Hz
Intra-column coupling	$C = 133.5$ $C1 = C$, $C2 = 0.8\ C$ $C3 = 0.25\ C$, $C4 = 0.25\ C$
Maximum average action potential density	$e_0 = 2.5$ Hz
Steepness of the response function	$r = 0.56$ mV^{-1}
PSP for a 50% firing rate	$\nu_0 = 6.0$ mV

A.1.2 Wilson-Cowan Model

We have also used the Wilson-Cowan model [*Wilson and Cowan*, 1972] in Chapter 6 to show segregation dynamics. It is one of the first mean field models, which describes the activity of two pools of interacting neurons –excitatory and inhibitory– by averaging out individual responses.

The Wilson-Cowan model equations read as follows:

$$\dot{x} = -x + S(ax - by + p), \tag{A.11}$$

$$\dot{y} = -y + S(cx - dy + q), \tag{A.12}$$

$$S(v) = 1/(1 + exp(-v)), \tag{A.13}$$

with x (y) being the average activity of the excitatory (inhibitory) populations. a and d are the self excitation parameters for x and y units, and b and c are the couplings from the inhibitory (excitatory) unit y (x) to the excitatory (inhibitory) unit x (y), respectively (see Fig A.3 for more details). p and q represent external stimuli impinging upon each population. Each unit, x and y, can be interpreted as the average activity of the excitatory and the inhibitory neuronal populations, respectively. Moreover, $S(v)$ gives the proportion of excitatory (inhibitory) neurons receiving thresholded excitation per unit time. We chose as parameter values $a = 16$, $b = 12$, $c = 16$, $d = -2$ and varied the external inputs $p - q$ to find values that allowed segregation in the coupled scenario.

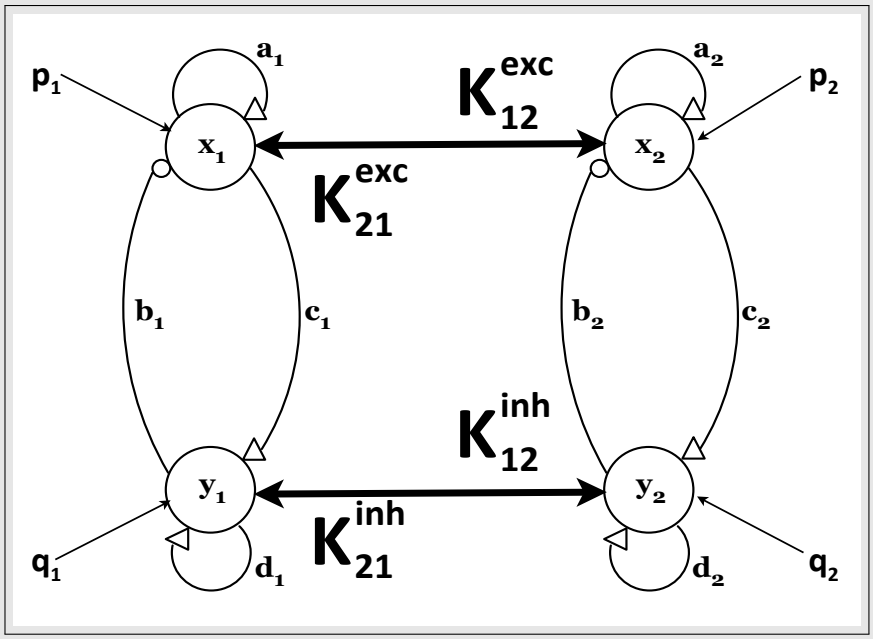

Figure A.3: Circuit describing the Wilson-Cowan model. Connectivity of the excitatory and inhibitory pools defining a Wilson-Cowan model. From *Campbell and Wang* [1994]

The coupling is performed as shown in Fig. A.3 . The equations for each oscillator read in this case:

$$\dot{x}_i = -x_i + S(ax_i - by_i + p_i) + K_{ij}^{exc}(x_j - x_i), \tag{A.14}$$

$$\dot{y}_i = -y_i + S(cx_i - dy_i + q_i) + K_{ij}^{inh}(y_j - y_i), \tag{A.15}$$

with $i, j = 1, 2$. We have explored which values of the coupling strengths K_{ij} (with $K_{ij} = K_{ji}$, either excitatory or inhibitory) allow the system to remain segregated for fixed values of external stimuli $p_1 = -3.5$, $q_2 = -6.5$, $p_2 = -1.0$ and $q_2 = -4.0$.

A.2 Description of the conductance-based neuronal model

In Chapter 5 we have worked with mesoscopic and microscopic models of neuronal activity. The generation of electrical activity in neurons can be explained in terms of an electrical circuit whose resistances and current sources can be related with transmembrane ionic channels and ionic pumps (see Fig. A.4). In *Hodgkin and Huxley* [1952] a complete model for action potential generation was presented. Here we used a simplified version of that model, a conductance-based model.

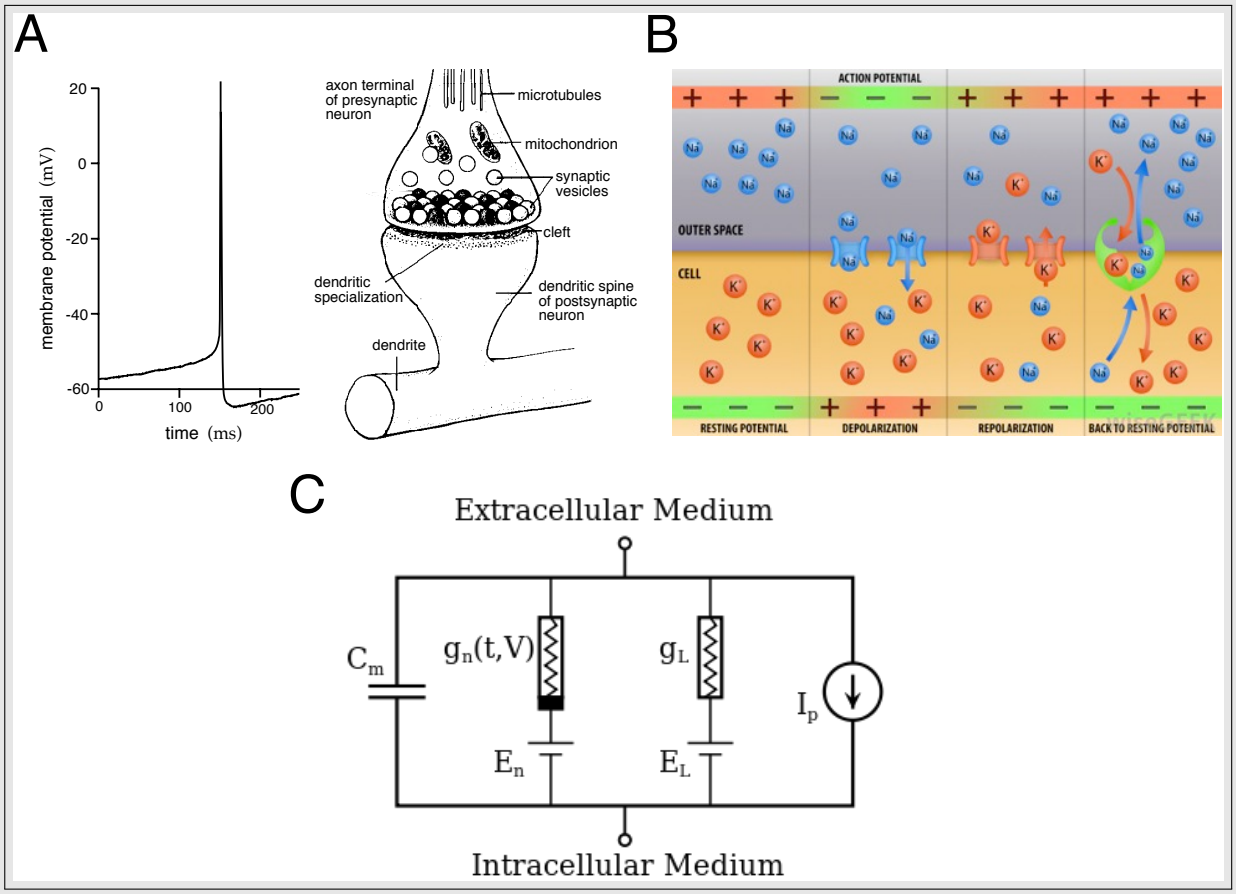

Figure A.4: Conductance-based model. (A) Recording of an action potential from a pyramidal cell and scheme of a synapse with organelles. When an action potential reaches a synapse, it releases neurotransmitters from the synaptic vesicles and a new action potential is generated in the downstream connected neuron. (B) Cartoon depicting transmembrane ionic fluxes involved in action potential generation. Four main stages can be drawn: membrane resting state, depolarization, repolarization and return to resting potential. (C) Electrical circuit summarizing the action potential generation. The membrane acts as a capacitor (C_m) and ionic pumps as current sources (E_n and E_L, respectively). Besides, ionic channels are resistances (g_n and g_L, respectively) and the action potential generates a current I_p.

The dynamics of the transmembrane potential of the soma of each neuron is described by the

following set of differential equations:

$$C_m \frac{dV}{dt} = -g_K n^4 (V - E_k) - g_{Na} m^3 h (V - E_{Na}) \\ -g_L (V - E_L) + I_{syn} + I_{ext}, \tag{A.16}$$

where g_K, g_{Na} and g_L are the maximum conductances for the potassium, sodium and the leak currents, respectively, and I_{syn} is the synaptic current coming from the neighboring neurons. The dynamics of the sodium and potassium channels is represented by the time-varying probabilities of a channel being in the open state:

$$\frac{dx}{dt} = \Phi \left[\alpha_x(V)(1 - x) - \beta_x(V) x \right], \qquad x = m, h, n \tag{A.17}$$

where x stands for the activation (m) and inactivation (h) of the sodium channels and the activation of the potassium channels (n). The rate functions α_x and β_x for each gating variable, as well as all the NN parameters used in Chapter 5 are given in *De Sancristóbal et al.* [2013].

The synaptic current I_{syn} is described using a conductance-based formalism:

$$I_{syn} = g_{syn}(t)(V(t) - E_{syn}), \tag{A.18}$$

where g_{syn} is the synaptic conductance and E_{syn} is the reversal potential of the synapse. For E_{syn} greater than the resting potential V_{rest} the synapse is excitatory (mediated by AMPA receptors), otherwise it is inhibitory (mediated by GABA receptors). We consider two temporal time constants, τ_d and τ_r (decay and rise synaptic time) for the dynamics of the synaptic conductance (alpha function, see Fig 1.9A)

$$g_{syn}(t) = \frac{\hat{g}_{syn}}{\tau_d - \tau_r} \left[\exp\left(-\frac{t - t_j}{\tau_d} \right) - \exp\left(-\frac{t - t_j}{\tau_r} \right) \right]. \tag{A.19}$$

We have chosen the maximal conductances $\hat{g}_{syn}$ such that the postsynaptic potential (PSP) amplitudes are within physiological ranges: the EPSP in the range from 0.42 mV to 0.83 mV and the IPSP in the range from 1.54 mV to 2.20 mV. In order to modify the activity time scale of the neuronal network we have changed τ_d for the GABAergic synapses, varying accordingly the inhibitory conductances $\hat{g}_{syn}$ in such a way that the maximum amplitude for $g_{syn}(t)$ is maintained.

All neurons receive an additional train of excitatory presynaptic potentials, coming from brain areas other than those explicitly modelled by the NMs, which contributes to the external current term I_{ext} in Eq. (A.16). Those spikes follow an heterogeneous Poisson process with a mean event rate, which varies following an Ornstein-Uhlenbeck process. The instantaneous rate $\lambda(t)$ of this external excitatory train of spikes is generated according to:

$$\frac{d\lambda}{dt} = -\lambda(t) + \sigma(t) \sqrt{\frac{2}{\tau}} \eta(t), \tag{A.20}$$

where $\sigma(t)$ is the standard deviation of the noisy process and is set to 0.6 spikes/s. The correlation time τ is set to 16 ms, leading to a $1/f$ power spectrum for the λ time series that is flat up to a cut-off frequency $f = 1/(2\pi\tau) = 9.9Hz$. The term $\eta(t)$ is a Gaussian white noise with mean 0 and standard deviation Σ.

This NN model is able to reproduce the well-known synchronous irregular regime [*Brunel*, 2000], in which recurrent activity leads collective oscillations at the population level while single neurons fire irregularly. The emergent rhythmicity is achieved by a balance between the excitatory and inhibitory synaptic currents and can be explained by periodic changes of the excitability in the network, i.e. periodic modulation of the distance to threshold. Despite the fact that excitatory neurons are dominant in the network, the stronger synaptic inhibitory conductances and the higher firing rate of the inhibitory neurons allows the system to reach a balance between excitation and inhibition. In order to obtain collective oscillations in the alpha (gamma) band, we set the decay synaptic time to be $\tau_d = 15\ ms$ ($5\ ms$).

A.3 Inter-scale coupling terms

In Chapter 5 the effect of the mass models upon the neural network also contributes to the I_{ext} term of the NN (see Eq. (A.16)), together with the external excitatory Poissonian train of spikes. Hence, each neuron of the NN receives a train of excitatory spikes whose mean firing rate, FR, is given by:

$$FR(t) = EFR(t) + k\gamma_1 S(y_1(t) - y_2(t)), \tag{A.21}$$

where $S(y_1(t) - y_2(t))$ translates the postsynaptic potential of the pyramidal population of the NM that affects that particular neuron (or both NMs if that is the case) into a spiking rate. γ_1 and k control the strength of this coupling. In Chapter 5 $\gamma_1 = 200$, while k will be a varying parameter. $EFR(t)$ corresponds to aforementioned Poissonian train of spikes:

$$EFR(t) = \langle EFR \rangle + \lambda_{OU}(t), \tag{A.22}$$

with $\langle EFR \rangle$ being the mean external firing rate and $\lambda_{OU}(t)$ an Ornstein-Uhlenbeck process (see Eq. (A.20)) representing the fluctuations around the mean. We have set $\langle EFR \rangle = 8.5\ KHz$. The neuronal network acts upon the neural mass models through $p_e^i(t)$ and $p_i^i(t)$ (see Eqs. (A.6, A.8)):

$$p_e^i(t) = \langle p \rangle + k\gamma_2 \overline{MUA}(t) \tag{A.23}$$

$$p_i^i(t) = k\gamma_3 \overline{MUA}(t), \tag{A.24}$$

where $\overline{MUA}(t)$ is the Multi-Unit Activity coming from the neural network, i.e. the sum of spikes over the subset of neurons coupled to the NMs, calculated within a sliding window of length 1 ms. $\langle p \rangle$ is a constant input coming from other areas of the brain distinct from those considered explicitly in our model ($\langle p \rangle = 160\ Hz$ for both neural masses in Chapter 5). γ_2, γ_3 and k are scaling factors that take into account the synaptic efficiency. Here, $\gamma_2 = 25$ and $\gamma_3 = 3$. Note that we assume that NN neurons affect only the pyramidal population in the neural mass. This is in accordance with previous models of two coupled neural masses [*Jansen and Rit*, 1995; *David and Friston*, 2003], which consider that only pyramidal cells receive excitatory input from the other column.

A.4 Local field potential

In Chapter 5, in order to quantify the activity of the neuronal network we have defined a collective measure, the local field potential (LFP), as the average of the absolute values of AMPA and

GABA synaptic currents acting upon a typical excitatory neuron [*Mazzoni et al.*, 2008]:

$$LFP = R_e \langle |I_{AMPA}| + |I_{GABA}| \rangle . \tag{A.25}$$

I_{AMPA} represents the external excitatory heterogeneous Poisson spike train and the recurrent excitatory synaptic current due to the network, I_{GABA} accounts for the recurrent inhibitory synaptic current and R_e represents the resistance of a typical electrode used for extracellular measurements. The symbol $\langle ... \rangle$ represents an average over all excitatory neurons.

A.5 Nonlinear oscillators

A.5.1 Description of the Chua oscillators

In Chapter 8 we tested experimentally whether coexisting synchronized states might be used for implementing Boolean logic gates. The first dynamical system in which we implemented logic gates was the Jansen and Rit model. The second dynamical system was the Chua oscillator. The feasibility and robustness of our theoretical results was proven experimentally by considering a network of Chua electronic oscillators [*Madan*, 1993] (see Fig. 8.3). These oscillators are described by the following equations [*Kennedy*, 1992; *Wagemakers et al.*, 2007]:

$$\frac{dv_A{}^i}{dt} = \frac{1}{C_1}\left(\frac{v_B{}^i - v_A{}^i}{R_5} - f(v_A{}^i) + \frac{v_A{}^i - s(t)}{R_{in}}\right), \tag{A.26}$$

$$\frac{dv_B{}^i}{dt} = \frac{1}{C_2}\left(\frac{v_B{}^i - v_A{}^i}{R_5} + i_L + \frac{v_B{}^i - v_B{}^j}{R_c}\right), \tag{A.27}$$

$$\frac{di_L{}^i}{dt} = -\frac{v_B{}^i}{L_1}, \tag{A.28}$$

where $v_A{}^i$ and $v_B{}^i$ are the voltages of the two capacitors (C_1 and C_2) and $i_L{}^i$ is the intensity through the coil of the circuit (L_1). $s(t)$ is an external oscillatory input signal that we may ("1") or may not ("0") activate, controlling the dynamical state at which the Chua operates. The strength of the input signal is proportional to the inverse of R_{in}. We tuned its value depending the type of logic gate we were considering. $f(v_A{}^i)$ is a piece-wise (nonlinear) function given by:

$$f(v_A{}^i) = G_1 v_A{}^i + \frac{1}{2}(G_1 - G_0)[\ |v_A{}^i + B_p| - |v_A{}^i| - B_p\ ], \tag{A.29}$$

with $B_p = 1.7$ V being the breaking point of the piece-wise function. The values of G_1 and G_2 are obtained from different resistances of the electronic circuit:

$$G_1 = \frac{-R_1}{R_1 + R_3} + \frac{1}{R_2}, \tag{A.30}$$

$$G_0 = \frac{-R_1}{R_1 + R_3} - \frac{R_2}{R_2 R_4}, \tag{A.31}$$

and the rest of the parameters are $V_{cc} = 15$ V, $V_{EE} = -15$ V, $R_1 = 222\ \Omega$, $R_2 = 22$ kΩ, $R_3 = 2.2$ kΩ, $R_4 = 3.3$ kΩ, $C_1 = 10$ nF, $C_2 = 100$ nF, $L_1 = 20$ mH and $R_5 = 1.38$ kΩ.

The coupling circuit between the different Chua circuits, represented as the last term in Eq. (A.27), consists on a voltage follower placed at the output of v_B^j combined with a coupling resistance R_c, whose value controls the amount of unidirectional coupling from v_B^j to v_B^i. The coupling from unit i to unit j is introduced in a similar way, thus leading to an effective bidirectional coupling.

A.5.2 Description of the Rössler oscillators

In Chapter 7 we used Rössler oscillators [*Rössler*, 1976] to study the coexistence of synchronizations in a dynamical system other than Jansen and Rit neural mass models. Rössler oscillators display a wide repertoire of behaviors and are suitable for an analytic or semi-analytic study of their stability. We chose this dynamical system because it is computationally affordable to compute the evolution of the Lyapunov exponents associated with synchronized trajectories in the phase space.

The equations describing Rössler oscillators are:

$$\begin{aligned} \dot{x}_i &= -\omega_i y_i - z_i + \sum_{j=1, j\neq i}^{N_{neigh}} \alpha_{ij}(x_j - x_i), \\ \dot{y}_i &= \omega_i x_i + a y_i, \\ \dot{z}_i &= p + z_i(x_i - c), \end{aligned} \tag{A.32}$$

where ω_i is the natural frequency of the node, which is normally distributed with average $< \omega >= 1$ and standard deviation $\sigma_\omega = 0.02$ for the networks studied in Chapter 7. Rössler dynamics can be periodic, quasi-periodic or chaotic. We choose $a = 0.15$, $p = 0.2$ and $c = 10$ to set the oscillators in a chaotic regime when the node is in isolation [*Boccaletti et al.*, 2002; *Moskalenko et al.*, 2012]. and therefore display complex time evolutions. Besides, Rössler oscillators in this regime are very sensitive to a change in initial conditions or perturbations, situations which we wanted to explore. Finally, α_{ij} accounts for the coupling intensities between two adjacent nodes, i and j. We set the coupling weights to depend on the number of neighbors of each node as:

$$\alpha_{ij} = \frac{1}{\sqrt{\deg(v_i)\deg(v_j)}}, \tag{A.33}$$

(if not specified otherwise) for $i \neq j$, where $\deg(v_i)$, $\deg(v_j)$ are the degrees (number of coupled neighbors) of two dissipatively coupled nodes v_i, v_j. We study regular and complex topologies of progressively larger networks.

Appendix B

Methods

B.1 Time series analysis

B.1.1 Lyapunov Exponents and Regularity

In Chapters 6 and 7 we characterize the regularity of the signals in terms of the autocorrelation function and the *Maximal Lyapunov Exponent* (MLE). Lyapunov exponents are a qualitative measure that characterize the stability and instability of the evolution of a dynamical system with respect to varying initial conditions. They give fundamental information about underlying properties of such systems associated with strange attractors. Briefly, if we assume that a dynamical system is described as $\dot{\mathbf{x}} = f(\mathbf{x})$ with $t > 0$ and initial conditions $\mathbf{x}(0) = \mathbf{x}_0 \in \mathbb{R}^n$, we can derive the variational equation of the system, if linearization is possible, which is:

$$\dot{Y} = J(\mathbf{x}(t))Y, \quad Y(0) = I_n, \tag{B.1}$$

where I_n is a nxn identity matrix and $J(\mathbf{x}) = \partial f(\mathbf{x})/\partial \mathbf{x}$ is the Jacobian matrix of f. We then consider the evolution of an infinitesimal parallelepiped in the phase space $[p_1(t), ..., p_n(t)]$, with axis $p_i(t) = Y(t)p_i(0)$ for $i = 1, ..., n$, where $[p_1(0), ..., p_n(0)]$ is an orthogonal basis of $\mathbb{R}^n$. The long-time sensitivity of the flow $\mathbf{x}(t)$ with respect to initial conditions $\mathbf{x_0}$ at the directions $p_i(t)$ is determined by the expansion rate of the length of the ith axis with respect to the orthogonal basis $p_i(0)$, and is given by:

$$\lambda_i = \lim_{t\to\infty} \frac{1}{t} ln \frac{||p_i(t)||}{||p_i(0)||} \quad i = 1, ..., n, \tag{B.2}$$

which corresponds to the Lyapunov spectrum $\{\lambda_i\}$.

In Chapter 7 we calculated the *conditional* Lyapunov exponents of the coupled oscillators in order to map their evolution in terms of the coupling strength to the emergence of heterogeneous synchronization patterns. Let's first suppose that we have two oscillators, $\mathbf{x}(t)$ and $\mathbf{u}(t)$ of dimensions N_x and N_u, respectively. For an unidirectional coupling scheme, in which $\mathbf{x}(t)$ drives $\mathbf{u}(t)$, we can consider the presence of a time-dependent functional relationship

$$\mathbf{u}(t) = \mathbf{F}[\mathbf{x}(t)]. \tag{B.3}$$

The dynamics of this coupled drive-response system is characterized by the Lyapunov exponent spectra $\lambda_1^x \geqslant \lambda_2^x \geqslant ... \geqslant \lambda_{N_x}^x$ and $\lambda_1^u \geqslant \lambda_2^u \geqslant ... \geqslant \lambda_{N_u}^u$, with the last being conditional Lyapunov

exponents. In this sense, the rate of convergence or divergence of the trajectory of oscillator $\mathbf{u}$ towards the trajectory defined by oscillator $\mathbf{x}$ is given by λ_1^u: if $\lambda_1^u > 0$ the trajectories diverge, whereas if $\lambda_1^u < 0$ they converge.

Since throughout this Thesis we consider a mutual coupling scheme, Eq. (B.3) no longer holds for all time t, but rather its implicit form $\mathbf{F}[\mathbf{x}(t), \mathbf{u}(t)] = 0$. However, locally (i.e. for $t^* - \delta < t < t^* + \delta$, with δ being infinitely small), the implicit-function theorem [*Jittorntrum*, 1978] allows to write $\mathbf{x}(t^*) = \hat{\mathbf{F}}[\mathbf{u}(t^*)]$ or $\mathbf{u}(t^{**}) = \tilde{\mathbf{F}}[\mathbf{x}(t^{**})]$, for other moments in time t. Therefore, without loss of generality, the spectrum of Lyapunov exponents can be computed in terms of the trajectory defined by one of the mutually coupled oscillators, either $\mathbf{u}$ or $\mathbf{x}$, as in the unidirectional coupling case. In Chapter 7 we consider the evolution of the flow of the trajectories of the coupled Rössler oscillators with respect to the trajectory defined by one of the oscillators in the networks. This calculation allows to estimate whether such trajectory is attractive, i.e. neighboring oscillators converge to it and therefore synchronize, or repulsive, i.e. neighboring oscillators diverge from it and desynchronize (in amplitude).

The Lyapunov spectrums in Chapters 6 and 7 were calculated using a Gram-Schmidt re-orthonormalization algorithm (or QR algorithm) by means of the Adams-Bashforth method [*Chen et al.*, 2006]. In Chapter 6 the integration of Jansen and Rit equations for MLE computation was performed with a time step of 1 ms and a total simulation time of 500 s, which was sufficient for the Lyapunov coefficients to converge. An initial time window of 100 s was omitted to avoid transients. We calculated the Lyapunov spectrum for 50 different initial conditions.

The degree of regularity of the NMM activity in Chapter 6 was calculated by taking the average of the second absolute maxima of the autocorrelation function (calculated with a Python package Numpy function [*van der Walt et al.*, 2011]) over all the nodes of the network:

$$Reg = \frac{1}{s}\frac{1}{N}\sum_{p=1}^{s}\sum_{q=1}^{N} h_{p,q}^{2nd}(\tau), \tag{B.4}$$

where s stands for the number of realizations for different initial conditions –50 in the case studied in Fig. 6.6B, 20 in the case studied in Fig. 6.8B and 10 for the subsequent regularity calculations–, N is the total number of cortical columns and $h_{p,q}^{2nd}(\tau)$ denotes the height of the second absolute peak of the autocorrelation function for each signal. This index provides us with a quantification of the periodicity of the signal.

B.1.2 Spectral analysis

The power spectral density (PSD) measurements in Chapters 5 and 6 were computed using Welch's average periodogram method. These calculations were performed using standard Python Numpy functions [*van der Walt et al.*, 2011].

B.1.3 Synchronization

We calculated the synchronization degree of pairs of oscillators ubiquitously in this Thesis. Each synchronized state is defined by a characteristic functional relationship between the dynamics of the interacting elements [*Boccaletti et al.*, 2002]. Phase synchronization (PS) entails a constant phase difference in time between the coupled oscillators, whereas amplitudes remain

uncorrelated [*Rosenblum et al.*, 1996]. Generalized synchronization (GS) is characterized by a complex functional relationship between the dynamics of the oscillators that can only be unveiled by the auxiliary system approach [*Abarbanel et al.*, 1996] or the nearest neighbor method [*Moskalenko et al.*, 2012]. In turn, lag synchronization (LS) implies a constant time shift between the signals of the two oscillators, with amplitudes being completely correlated, whereas in complete synchronization (CS) no time shift is present.

Accordingly, in Chapters 5, 6, 7 and 8 we computed in Jansen and Rit, Rössler and Chua oscillators the cross-correlation and a phase synchronization index between their output signals, $y^m(t)$, $x^m(t)$ and $v^m(t)$, respectively [*Lachaux et al.*, 1999]. The maximal cross-correlation for each pair of nodes, $C_{max}(\tau)$, was computed using the maximum value of the cross-correlation function provided by Python package Numpy [*van der Walt et al.*, 2011]. Cross-correlations allow us to distinguish between zero-lag (complete) synchronization (CS) and lag synchronization (LS), whereas the phase synchronization index and phase-locking value (PLV) provide evidence of phase synchronization (PS). The phase $\phi^m(t)$ of the output signal is obtained from the Hilbert transform of $y^m(t)$ [*Rosenblum et al.*, 1996]. The phase synchronization index γ (see Chapter 8) of two oscillators 1 and 2 is calculated from $\Delta\phi^{12}(t)=\phi^1(t) - \phi^2(t)$ as [*Mormann et al.*, 2000; *Quian Quiroga et al.*, 2002]:

$$\gamma \equiv |\langle e^{i\Delta\phi^{12}(t)}\rangle_t| = \sqrt{\langle \cos\Delta\phi^{12}(t)\rangle_t^2 + \langle \sin\Delta\phi^{12}(t)\rangle_t^2}. \tag{B.5}$$

and the phase locking value (PLV) in Chapter 7 [*Lachaux et al.*, 1999] is calculated as:

$$PLV_t = \frac{1}{N}|\sum_{n=1}^{N}\langle e^{i\Delta\phi^{12}(t,n)}\rangle_t|, \tag{B.6}$$

where N is the number of samples used. We used these two similar measurements because they fitted our computational demands in each of the mentioned Chapters. For the Chua circuits in Chapter 8, we evaluate the synchronization error as the average of the difference between the outputs of two systems (e.g., units A_1 and A_2 in Figure 8.4A):

$$\epsilon = \frac{1}{T}\sum_{t=1}^{T}|v_A^1(t) - v_A^2(t)|, \tag{B.7}$$

with T being the total number of time steps. We use a similar expression in terms of y^1 and y^2 for the neural mass oscillators. We consider two oscillators to have complete synchronization (or lag synchronization if there is a time shift of the signals) when the values of the synchronization error are lower than a certain threshold ϵ_{th} ($\epsilon_{th} = 0.10$V in the case of Chua oscillators, $\epsilon_{th} = 0.01$mV for Jansen oscillators). On the other hand, phase synchronization arises for high values of the phase synchronization index (with a threshold of $\gamma_{th} = 0.85$ for both cases) and, at the same time, high values of the synchronization error ($\epsilon > \epsilon_{th} = 0.10$ V, $\epsilon_{th} = 0.01$ mV, for the Chua and Jansen oscillators, respectively).

B.1.4 Nearest neighbor method

In Chapter 7 we used the Nearest Neighbor method to assess the presence of a functional relationship between the oscillators in a network. If such a function exists between the interacting

elements all close states in the phase subspace of a given system $\mathbf{x}(t)$ should have close images in the phase subspace of the coupled system $\mathbf{u}(t)$ (see examples in Fig. 7.1). Accordingly, in a bidirectional coupling scheme the inverse statement is true.

B.1.5 Excitatory-Inhibitory Segregation index

In Chapter 6 we computed the excitatory-inhibitory segregation (EIS) index as:

$$EIS = |CM_e A_e CM_i A_i|, \tag{B.8}$$

where CM_e (CM_i) stands for the position of the center of mass of the excitatory–positive (inhibitory–negative) part of the activity distribution (Fig. 6.8B,D), and A_e (A_i) is the corresponding area of the excitatory (inhibitory) distributions, respectively.

B.1.6 Numerical techniques

The integration of the model equations was performed using two methods. On the one hand we used Heun's method to integrate the Jansen and Rit, Rössler and Wilson-Cowan model equations [*García-Ojalvo and Sancho*, 1999]. On the other hand, Adams-Bashforth method was used for Lyapunov exponent calculation [*Chen et al.*, 2006]. Random number generation was implemented using standard GSL routines to set different initial conditions when performing the statistical analysis of data [*Galassi and et al.*, January 1, 2009]. Each simulation of the model had a time step of 1 ms and a total simulated time of $t = 50$ s. A period of 25 s was omitted to avoid transients.

We implement numerically the noise term $\chi_i(t)$ in Eq. (A.8) using [*Malagarriga et al.*, 2015a]:

$$\chi_i(t) = \sqrt{2\xi_i \Delta t}\eta(t), \tag{B.9}$$

where ξ_i is the noise amplitude and Δt is the integration time step, whereas $\eta(t)$ is a number resulting from a white noise Gaussian distribution with zero mean and variance equal to 1 [*García-Ojalvo and Sancho*, 1999].

B.2 Topology

B.2.1 Network construction

In Chapters 6 and 7 (see for example Figs. 6.6A 7.1B), scale-free networks were constructed using the Barabási-Albert algorithm [*Barabási and Albert*, 1999], which makes use of m_0 initial nodes connected randomly to which other nodes are added gradually. These new nodes are connected to $m \leq m_0$ existing nodes with a probability that increases with the number of links of the already connected nodes. This procedure gives rise to networks with heavily connected nodes, and therefore with a power-law distribution of degrees. In Figs. 6.8 and 6.10 we performed the analysis for 50 scale-free networks with $m_0 = 1$. In Fig. 6.6 we constructed 10 networks for each α and β pair.

The networks in Chapters 5, 6 and 7 (see for example Figs. 6.12, 7.1) were constructed using the Watts-Strogatz algorithm with rewiring probabilities (RPs) of 0, 0.5 and 1 [*Watts and*

Strogatz, 1998]. Each RP defines a different network: ring ($RP = 0$), small-world ($RP = 0.5$) and random ($RP = 1.0$). We constructed 10 networks for each RP in Chapter 6 and 100 networks for $RP = 0.5$ and $RP = 1.0$ in Chapter 7. In all cases every network was simulated using 10 sets of different initial conditions for the nodes and were constructed using the NetworkX Python package [*Hagberg et al.*, 2008].

B.2.2 Network analysis

In Chapter 7 we analyzed the topological characteristics of reconstructed networks of Rössler oscillators. We made use of functions embedded in the NetworkX Python package [*Hagberg et al.*, 2008] to calculate the *clustering coefficient*, which measures how groups of nodes in a network cluster together (see Fig. 7.6).

List of publications and research activities

List of publications

- A. Barardi, D. Malagarriga, B. Sancristobal, J. García-Ojalvo, and A. Pons, Probing scale interaction in brain dynamics through synchronization, *Philosophical Transactions of the Royal Society B: Biological Science*, pp. 369 (1653), 2014.

- D. Malagarriga, A. E. P. Villa, J. García-Ojalvo, and A. J. Pons. Excitation/inhibition patterns in a system of coupled cortical columns. In Artificial Neural Networks and Machine Learning - ICANN 2014, 651-658. Springer, 2014.

- D. Malagarriga, M. A. García-Vellisca, A. E. P. Villa, J. M. Buldú, J. García-Ojalvo, and A. J. Pons. Synchronization-based computation through networks of coupled oscillators. *Frontiers in computational neuroscience*, 9, 2015.

- D. Malagarriga, A. E. P. Villa, J. García-Ojalvo, and A. J. Pons. Mesoscopic segregation of excitation and inhibition in a brain network model. *PLoS Computational Biology*, 11(2): e1004007, 02 2015.

- D. Malagarriga, A. E. P. Villa, J. García-Ojalvo, and A. J. Pons. Consistency of heterogeneous synchronization patterns in complex weighted networks. *arXiv preprint*, arXiv:1601.05461, 2016.

- D. Malagarriga, A. J. Pons, and A. E. P. Villa. Complex spatiotemporal patterns transmitted through mesoscopic neural networks. *In preparation.*

Research stays

- Université de Lausanne (UNIL), Lausanne, Switzerland. September 2012 January, 2013 June, 2013 January, 2014 June, 2014 September, 2014 January, 2015 August, 2015.

Scientific events organization

- Organizing Committee Chair of the International Conference on Artificial Neural Networks, ICANN 2016, held in Universitat Politècnica de Catalunya, Barcelona, Spain, from Sept. 6 to Sept. 9, 2016.

Invited talks

- Agrupació astronòmica de Terrassa, Terrassa, Spain, 15th November 2013.

Conferences, workshops and seminars

- II Encuentro Ibersinc, University of Zaragoza, Zaragoza (Spain), from March 20th to 21st, 2012. Workshop.

- Centre de Recerca Matemàtica, Barcelona (Spain), from July 12th to 13th 2012. Dynamics of memory: what's the evidence?. Conference.

- Nonlinear Theory and its Applications (NOLTA), Palma de Mallorca (Spain), from Oct. 22nd to 26th, 2012. Conference.
  Talk: *Synchronizability and dynamics of coupled neural mass oscillators.*

- XXXIII Dynamics Days Europe, Universidad Politécnica de Madrid, Madrid (Spain), from June 3rd to 7th, 2013. Conference.
  Talk: *Spontaneous segregation of excitation and inhibition in a system of coupled cortical columns.*

- III Jornada Complexitat.cat, Institut d'Estudis Catalans, Barcelona (Spain), 19th June, 2014. Workshop.
  Poster presentation: *EEG correlates of cortical column synchronisation in mesoscopic brain dynamics.*

- XXIV International Conference on Artificial Neural Networks (ICANN), University of Hamburg, Hamburg (Germany) from Sept. 15th to 19th, 2014. Conference.
  Talk: *Excitation/inhibition patterns in a system of coupled cortical columns.*

- XI Neural Coding, INRIA Versailles, Versailles (France), from Oct. 7th to 10th, 2014. Workshop.
  Poster presentation: *Deterministic spatiotemporal activity processing by a neural mass model of a cortical column.*

- III Jornada d'Investigadors Predoctorals Interdiscriplinaria (JIPI), Universitat de Barcelona, Barcelona (Spain), Feb. 5th 2015. Conference.
  Talk: *Brain research in the mesoscopic scale.*

- Neural Coding, Computation and Dynamics (NCCD) , Bilbao (Spain), from Aug. 30th to Sept. 2nd, 2015. Workshop.
  Poster presentation: *Mesoscopic segregation of excitation and inhibition in a brain network model.*

- Net-works (Complex networks and their interdisciplinary applications), University of Granada, Granada (Spain), from Sept. 16th to 18th, 2015. Conference.
  Contribution: *Coexistence of synchronizations in complex weighted networks.*

Bibliography

H. Abarbanel, N. Rulkov, and M. Sushchik. Generalized synchronization of chaos: The auxiliary system approach. *Physical review. E, Statistical physics, plasmas, fluids, and related interdisciplinary topics*, 53(5):4528–4535, May 1996.

M. Abeles. *Corticonics: Neural Circuits of the Cerebral Cortex*. Cambridge University Press, first edition, 1991.

M. Abeles, G. Hayon, and D. Lehmann. Modeling compositionality by dynamic binding of synfire chains. *Journal of Computational Neuroscience*, 17:179–201, 2004.

D. Abrams and S. H. Strogatz. Chimera States for Coupled Oscillators. *Physical Review Letters*, 93(17):174102, oct 2004.

E. Adrian and B. Matthews. The Berger rhythm: potential changes from the occipital lobes in man. *Brain*, 57:355–385, 1934.

E. Ahissar, E. Vaadia, M. Ahissar, H. Bergman, A. Arieli, and M. Abeles. Dependence of cortical plasticity on correlated activity of single neurons and on behavioral context. *Science*, 257 (5075):1412–1415, 1992.

A. Alivisatos, M. Chun, G. Church, R. Greenspan, M. Roukes, and R. Yuste. The Brain Activity Map Project and the Challenge of Functional Connectomics. *Neuron*, 74(6):970–974, 2012.

R. Andrzejak, K. Lehnertz, F. Mormann, C. Rieke, P. David, and C. Elger. Indications of nonlinear deterministic and finite-dimensional structures in time series of brain electrical activity: Dependence on recording region and brain state. *Physical Review E*, 64(6):061907, nov 2001.

A. Arenas, A. Díaz-Guilera, J. Kurths, Y. Moreno, and C. Zhou. Synchronization in complex networks. *Physics Reports*, 469(3):93–153, 2008.

Y. Asai and A. E. P. Villa. Integration and transmission of distributed deterministic neural activity in feed-forward networks. *Brain Res*, 1434:17–33, Jan 2012.

Y. Asai, A. Guha, and A. E. P. Villa. Deterministic neural dynamics transmitted through neural networks. *Neural Netw*, 21(6):799–809, Aug 2008.

A.-L. Barabási and R. Albert. Emergence of scaling in random networks. *Science*, 286(5439): 509–512, 1999.

A. Barardi, D. Malagarriga, B. Sancristobal, J. García-Ojalvo, and A. J. Pons. Probing scale interaction in brain dynamics through synchronization. *Philosophical Transactions of the Royal Society B: Biological Sciences*, 369(1653), 2014a.

A. Barardi, B. Sancristóbal, and J. Garcia-Ojalvo. Phase-coherence transitions and communication in the gamma range between delay-coupled neuronal populations. *PLoS Computational Biology*, 10(7):e1003723, 07 2014b.

R. Batra and D. C. Fitzpatrick. Neurons sensitive to interaural temporal disparities in the medial part of the ventral nucleus of the lateral lemniscus. *Journal of Neurophysiology*, 78(1):511–515, 1997.

M. Baudry, J. L. Davis, and R. F. Thompson. *Advances in Synaptic Plasticity*, volume 1. MIT Press, first edition, 2000.

C. Bennett. Logical reversibility of computation. *IBM Journal of Research and Development*, 17 (6):525–532, Nov 1973.

R. W. Berg, A. Alaburda, and J. Hounsgaard. Balanced inhibition and excitation drive spike activity in spinal half-centers. *Science*, 315(5810):390–393, 2007.

B. Blasius, A. Huppert, and L. Stone. Complex dynamics and phase synchronization in spatially extended ecological systems. *Nature*, 399(6734):354–359, 1999.

F. Blumhagen, P. Zhu, J. Shum, Y. Schärer, E. Yaksi, K. Deisseroth, and R. Friedrich. Neuronal filtering of multiplexed odour representations. *Nature*, 479:493–498, 2011.

S. Boccaletti, J. Kurths, G. Osipov, D. Valladares, and C. Zhou. The synchronization of chaotic systems. *Physics Reports*, 366(1):1–101, 2002.

C. Börgers and N. Kopell. Synchronization in Networks of Excitatory and Inhibitory Neurons with Sparse, Random Connectivity. *Neural Computation*, 15:509–538, 2003.

C. Börgers and N. Kopell. Gamma Osillations and Stimulus Selection. *Neural Computation*, 20: 383–414, 2008.

C. Börgers, S. Epstein, and N. J. Kopell. Background gamma rhythmicity and attention in cortical local circuits: A computational study. *Proceedings of the National Academy of Sciences of the United States of America*, 102(19):7002–7007, 2005.

C. Börgers, S. Epstein, and N. J. Kopell. Gamma oscillations mediate stimulus competition and attentional selection in a cortical network model. *Proceedings of the National Academy of Sciences*, 105(46):18023–18028, 2008.

C. A. Bosman, J.-M. Schoffelen, N. Brunet, R. Oostenveld, A. M. Bastos, T. Womelsdorf, B. Rubehn, T. Stieglitz, P. D. Weerd, and P. Fries. Attentional stimulus selection through selective synchronization between monkey visual areas. *Neuron*, 75(5):875 – 888, 2012.

C. S. Breathnach. Charles Scott Sherrington's Integrative action: a centenary notice. *J. R. Soc. Med.*, 97(1):34–36, 2004.

E. Britannica. Electroencephalogram. `http://global.britannica.com/science/electroencephalography`, 2014. [Online; accessed 19-Oct-2015].

K. Brodmann. *Vergleichende Lokalisationslehre der Grosshirnrinde in ihren Prinzipien dargestellt auf Grund des Zellenbaues*. Barth, Leipzig, 1909.

E. Brown, J. Moehlis, and P. Holmes. On the phase reduction and response dynamics of neural oscillator populations. *Neural Comput*, 16(4):673–715, Apr 2004.

N. Brunel. Dynamics of sparsely connected networks of excitatory and inhibitory spiking neurons. *Journal of Computational Neuroscience*, 8(3):183–208, May 2000.

N. Brunel and M. van Rossum. Lapicque's 1907 paper: from frogs to integrate-and-fire. *Biological Cybernetics*, 97(5-6):337–339, 2007.

E. Bullmore and O. Sporns. Complex brain networks: graph theoretical analysis of structural and functional systems. *Nature Reviews Neuroscience*, 10(3):186–98, mar 2009.

G. Buszáki. *Rhythms of the Brain*. Oxford University Press, 2006.

D. P. Buxhoeveden and M. F. Casanova. The minicolumn hypothesis in neuroscience. *Brain*, 125(Pt 5):935–951, May 2002.

G. Buzsáki and A. Draguhn. Neuronal oscillations in cortical networks. *Science*, 304(5679): 1926–1929, 2004.

G. Buzsáki, C. a. Anastassiou, and C. Koch. The origin of extracellular fields and currents–EEG, ECoG, LFP and spikes. *Nature Reviews Neuroscience*, 13(6):407–20, June 2012.

J. Cabessa and A. Villa. An attractor-based complexity measurement for boolean recurrent neural networks. *PLoS ONE*, 9(4), 2014.

T. Caelli. Facilitative and inhibitory factors in visual texture discrimination. *Biological Cybernetics*, 39(1):21–26, 1980.

S. Campbell and D. Wang. Synchronization and desynchronization in locally coupled Wilson-Cowan oscillators. In *Neural Networks, 1994. IEEE World Congress on Computational Intelligence., 1994 IEEE International Conference on*, volume 2, pages 964–969 vol.2, Jun 1994.

N. P. Castellanos, I. Leyva, J. M. Buldú, R. Bajo, N. Paúl, P. Cuesta, V. E. Ordóñez, C. L. Pascua, S. Boccaletti, F. Maestú, and F. del Pozo. Principles of recovery from traumatic brain injury: reorganization of functional networks. *Neuroimage*, 55(3):1189–99, Apr 2011.

M. Castelo-Branco, R. Goebel, S. Neuenschwander, and W. Singer. Neural synchrony correlates with surface segregation rules. *Nature*, 405(6787):685–689, 2000.

A. Celletti and A. Villa. Low-dimensional chaotic attractors in the rat brain. *Biological Cybernetics*, 74(5):387–393, 1996.

M. Chavez, D.-U. Hwang, a. Amann, H. G. E. Hentschel, and S. Boccaletti. Synchronization is Enhanced in Weighted Complex Networks. *Physical Review Letters*, 94(21):218701, jun 2005.

Z.-M. Chen, K. Djidjeli, and W. Price. Computing lyapunov exponents based on the solution expression of the variational system. *Applied Mathematics and Computation*, 174(2):982 – 996, 2006.

D. R. Chialvo. Critical brain networks. *Physica A*, 340:756–765, 2004.

J. Christiansen. How Do You Visualize the Brain? . `http://blogs.scientificamerican.com/sa-visual/how-do-you-visualize-the-brain/`, 2014. [Online; accessed 19-Oct-2015].

Connectome. Brodmannn areas. `http://www.skiltopo.com/BA/myBrodmannsAreas2-802.jpg`, 2015. [Online; accessed 19-Oct-2015].

D. Contreras and M. Steriade. Cellular basis of EEG slow rhythms: a study of dynamic corticothalamic relationships. *The Journal of Neuroscience*, 15(1 Pt 2):604–622, Jan 1995.

V. Crunelli, T. I. Tóth, D. W. Cope, K. Blethyn, and S. W. Hughes. The 'window't-type calcium current in brain dynamics of different behavioural states. *The Journal of Physiology*, 562(1): 121–129, 2005.

N. M. da Costa and K. A. Martin. Whose cortical column would that be? *Frontiers in Neuroanatomy*, 4:16, 2010.

O. David and K. J. Friston. A neural mass model for MEG/EEG: coupling and neuronal dynamics. *Neuroimage*, 20(3):1743–1755, 2003.

O. David, L. Harrison, and K. J. Friston. Modelling event-related responses in the brain. *Neuroimage*, 25(3):756–70, Apr. 2005.

P. Dayan and L. F. Abbott. *Theoretical Neuroscience*, volume 1. MIT Press, first edition, 2001.

R. L. de No and J. F. Fulton. *Architectonics and structure of the cerebral cortex*. Oxford University Press, 1938.

B. De Sancristóbal, R. Vicente, J. M. Sancho, and J. Garcia-Ojalvo. Emergent bimodal firing patterns implement different encoding strategies during gamma-band oscillations. *Frontiers in Computational Neuroscience*, 7(18), 2013.

G. Deco, V. K. Jirsa, P. A. Robinson, M. Breakspear, and K. Friston. The dynamic brain: from spiking neurons to neural masses and cortical fields. *PLoS Computational Biology*, 4(8): e1000092, 2008.

G. Deco, V. K. Jirsa, and A. R. McIntosh. Resting brains never rest: computational insights into potential cognitive architectures. *Trends in Neurosci*, 36(5):268–274, 2013.

G. Deco, A. Ponce-Alvarez, P. Hagmann, G. L. Romani, D. Mantini, and M. Corbetta. How local excitation-inhibition ratio impacts the whole brain dynamics. *J. Neurosci.*, 34(23):7886–98, jun 2014.

N. Dehghani, A. Peyrache, B. Telenczuk, M. Le Van Quyen, E. Halgren, S. S. Cash, N. G. Hatsopoulos, and A. Destexhe. Multiscale Balance of Excitation and Inhibition in Single-Unit ensemble Recordings in Human and Monkey Neocortex. *ArXiv e-prints*, Oct. 2014.

V. Del Prete, L. Martignon, and A. E. Villa. Detection of syntonies between multiple spike trains using a coarse-grain binarization of spike count distributions. *Network*, 15(1):13–28, Feb 2004.

J. I. Deza, M. Barreiro, and C. Masoller. Assessing the direction of climate interactions by means of complex networks and information theoretic tools. *Chaos An Interdiscip. J. Nonlinear Sci.*, 25(3):033105, 2015.

S. M. Doesburg, J. Vidal, and M. J. Taylor. Reduced theta connectivity during set-shifting in children with autism. *Frontiers in Human Neuroscience*, 7(785), 2013.

N. Domedel-Puig, P. Rué, A. J. Pons, and J. García-Ojalvo. Information routing driven by background chatter in a signaling network. *PLoS Computational Biology*, 7(12):e1002297, 2011.

R. J. Douglas, K. A. Martin, and D. Whitteridge. A canonical microcircuit for neocortex. *Neural computation*, 1(4):480–488, 1989.

R. Eckhorn, R. Bauer, W. Jordan, M. Brosch, W. Kruse, M. Munk, and H. J. Reiboeck. Coherent Oscillations: A Mechanism of Feature Linking in the Visual Cortex? *Biological Cybernetics*, 60:121–130, 1988.

EEG. Cartoon of EEG device. `http://cartoondealer.com/illustrations/pg1/eeg.html`, 2014. [Online; accessed 19-Oct-2015].

V. M. Eguíluz, D. R. Chialvo, G. a. Cecchi, M. Baliki, and a. V. Apkarian. Scale-Free Brain Functional Networks. *Physical Review Letters*, 94(1):018102, jan 2005.

A. K. Engel, P. Fries, and W. Singer. Dynamic predictions: oscillations and synchrony in top–down processing. *Nature Reviews Neuroscience*, 2(10):704–716, 2001a.

D. Engel, I. Pahner, K. Schulze, C. Frahm, and H. Jarry. Plasticity of rat central inhibtiory synapses through gaba metabolism. *Journal of Physiology*, 535(2):473–482, 2001b.

P. Erdős and A. Rényi. On random graphs i. *Publicationes Mathematicae (Debrecen)*, 6:290–297, 1959.

O. D. Faugeras, J. D. Touboul, and B. Cessac. A constructive mean-field analysis of multi population neural networks with random synaptic weights and stochastic inputs. *Frontiers in Computational Neuroscience*, 3(1), 2008.

P. Faure and H. Korn. Is there chaos in the brain? I. Concepts of nonlinear dynamics and methods of investigation. *Comptes Rendus de l'Académie des Sciences III.*, 324(9):773–93, Sept. 2001.

O. Feinerman, A. Rotem, and E. Moses. Reliable neuronal logic devices from patterned hippocampal cultures. *Nature Physics*, 4(12):967–973, 2008.

D. Feldmeyer, M. Brecht, F. Helmchen, C. C. H. Petersen, J. F. Poulet, J. F. Staiger, H. J. Luhmann, and C. Schwarz. Barrel cortex function. *Progress in Neurobiology*, 103:3–27, 2013.

R. FitzHugh. Mathematical models of threshold phenomena in the nerve membrane. *The Bulleting of Mathematical Biophysics*, 17(4):257–278, 1955.

N. Fourcaud-Trocmé, D. Hansel, C. van Vreeswijk, and N. Brunel. How spike generation mechanisms determine the neuronal response to fluctuating inputs. *The Journal of Neuroscience*, 23(5):11628–40, 2003.

W. J. Freeman. *Mass action in the nervous system.* Academic Press, 1975.

W. J. Freeman. Chaos in the brain: Possible roles in biological intelligence. *International Journal of Intelligent Systems*, 10(1):71–88, 1995.

W. J. Freeman. A field-theoretic approach to understanding scale-free neocortical dynamics. *Biological Cybernetics*, 92(6):350–359, Jun 2005.

P. Fries. A mechanism for cognitive dynamics: neuronal communication through neuronal coherence. *Trends in cognitive sciences*, 9(10):474–480, 2005.

P. Fries. Neuronal gamma-band synchronization as a fundamental process in cortical computation. *Annual Review of Neuroscience*, 32(1):209–224, 2009. PMID: 19400723.

P. Fries, J. H. Reynolds, A. E. Rorie, and R. Desimone. Modulation of oscillatory neuronal synchronization by selective visual attention. *Science*, 291(5508):1560–1563, 2001.

P. Fries, T. Womelsdorf, R. Oostenveld, and R. Desimone. The effects of visual stimulation and selective visual attention on rhythmic neuronal synchronization in macaque area v4. *The Journal of Neuroscience*, 28(18):4823–4835, 2008.

J. Fuster. *Cortex and Mind: Unifying Cognition.* Oxford University Press, 2003.

M. Galassi and et al. Gnu scientific library reference manual (3rd ed.). January 1, 2009.

L. Galvani. Galvani Frog's legs electricity. `https://commons.wikimedia.org/wiki/File:Galvani-frogs-legs-electricity.jpg#filelinks`, 2015. [Online; accessed 19-Oct-2015].

J. García-Ojalvo and J. Sancho. *Noise in spatially extended systems.* Springer Verlag, 1999.

W. Gerstner and W. Kistler. *Spiking neuron models: Single neurons, populations, plasticity.* Cambridge Univ Press, 2002.

S. Gilbert. *Developmental biology.* Sinauer Associates, 1985.

L. Glass. Synchronization and rhythmic processes in physiology. *Nature*, 410(6825):277–284, 2001.

W. Göbel and F. Helmchen. In vivo calcium imaging of neural network function. *Physiology*, 22 (6):358–365, 2007.

M. Goldbach, M. Loh, G. Deco, and J. Garcia-Ojalvo. Neurodynamical amplification of perceptual signals via system-size resonance. *Physica D Nonlinear Phenomena*, 237(3):316–323, 2008.

L. L. Gollo, C. Mirasso, and A. E. Villa. Dynamic control for synchronization of separated cortical areas through thalamic relay. *Neuroimage*, 52(3):947–955, Sep 2010.

G. Gong, Y. He, L. Concha, C. Lebel, D. W. Gross, A. C. Evans, and C. Beaulieu. Mapping anatomical connectivity patterns of human cerebral cortex using in vivo diffusion tensor imaging tractography. *Cereb Cortex*, 19(3):524–36, Mar 2009.

C. M. Gray, P. Konig, A. K. Engel, and W. Singer. Oscillatory responses in cat visual cortex exhibit inter-columnar synchronization which reflect global stimulus properties. *Nature*, pages 334–337, 1989.

F. Grimbert and O. Faugeras. Bifurcation Analysis of Jansen's Neural Mass Model. *Neural Computation*, 18(2003):3052–3068, 2006.

M. Guye, G. Bettus, F. Bartolomei, and P. J. Cozzone. Graph theoretical analysis of structural and functional connectivity MRI in normal and pathological brain networks. *Magn Reson Mater Phy*, 23(5-6):409–21, Dec 2010.

A. A. Hagberg, D. A. Schult, and P. J. Swart. Exploring network structure, dynamics, and function using networkx. In G. Varoquaux, T. Vaught, and J. Millman, editors, *Proceedings of the 7th Python in Science Conference*, pages 11 – 15, Pasadena, CA USA, 2008.

R. H. R. Hahnloser, R. Sarpeshkar, M. A. Mahowald, R. J. Douglas, and H. S. Seung. Digital selection and analogue amplification coexist in a cortex-inspired silicon circuit. *Nature*, 405: 947–951, June 2000.

B. Haider, A. Duque, A. R. Hasenstaub, and D. A. McCormick. Neocortical network activity in vivo is generated through a dynamic balance of excitation and inhibition. *The Journal of Neuroscience*, 26(17):4535–45, Apr 2006.

J. E. Heiss, Y. Katz, E. Ganmor, and I. Lampl. Shift in the balance between excitation and inhibition during sensory adaptation of s1 neurons. *The Journal of Neuroscience*, 28(49): 13320–13330, 2008.

M. J. Higley and D. Contreras. Balanced excitation and inhibition determine spike timing during frequency adaptation. *The Journal of Neuroscience*, 26(2):448–457, 2006.

S. L. Hill and A. E. P. Villa. Dynamic transitions in global network activity influenced by the balance of excitation and inhibition. *Network: Computation in Neural Systems*, 8(2):165–184, 1997.

A. Hodgkin and A. Huxley. A quantitative description of membrane current and its application to conduction and excitation in nerve. *Bulletin of Mathematical Biology*, 52(1-2):25–71, 1952.

F. C. Hoppensteadt and E. M. Izhikevich. Synchronization of laser oscillators, associative memory, and optical neurocomputing. *Physical Review E*, 62(3):4010, 2000.

A. Horn, D. Ostwald, M. Reisert, and F. Blankenburg. The structural–functional connectome and the default mode network of the human brain. *Neuroimage*, 102:142–151, 2014.

D. Horn, N. Levy, and E. Ruppin. Memory maintenance via neuronal regulation. *Neural Computation*, 10(1):1–18, January 1998.

G. Huang, D. Zhang, J. Meng, and X. Zhu. Interactions between two neural populations: A mechanism of chaos and oscillation in neural mass model. *Neurocomputing*, 74(6):1026–1034, Feb. 2011.

D. H. Hubel and T. N. Wiesel. Functional architectureof macaque monkey visual cortex. *Proceedings of the Royal Society of London. Series B*, 198:1–59, 1977.

S. W. Hughes, D. W. Cope, K. L. Blethyn, and V. Crunelli. Cellular mechanisms of the slow (<1 hz) oscillation in thalamocortical neurons in vitro. *Neuron*, 33(6):947–958, 2002.

J. Iglesias and A. E. P. Villa. Recurrent spatiotemporal firing patterns in large spiking neural networks with ontogenetic and epigenetic processes. *Journal of Physiology - Paris*, 104(3-4): 137–146, May-Sep 2010.

J. Iglesias, J. Eriksson, F. Grize, M. Tomassini, and A. E. Villa. Dynamics of pruning in simulated large-scale spiking neural networks. *BioSystems*, 79(1):11–20, 2005.

E. Izhikevich. *Dynamical Systems in Neuroscience*. Computational neuroscience. MIT Press, 2007.

E. M. Izhikevich. Which model to use for cortical spiking neurons? *IEEE Trans. Neural Networks*, 15(5):1063–1070, 2004.

E. M. Izhikevich and G. M. Edelman. Large-scale model of mammalian thalamocortical systems. *Proceedings of the national academy of sciences*, 105(9):3593–3598, 2008.

B. H. Jansen and V. G. Rit. Electroencephalogram and visual evoked potential generation in a mathematical model of coupled cortical columns. *Biological Cybernetics*, 73(4):357–66, 1995.

B. H. Jansen, G. Zouridakis, and M. E. Brandt. A neurophysiologically-based mathematical model of flash visual evoked potentials. *Biological Cybernetics*, 68(3):275–283, 1993.

M. Jedynak, A. J. Pons, and J. Garcia-Ojalvo. Cross-frequency transfer in a stochastically driven mesoscopic neuronal model. *Frontiers in computational neuroscience*, 9, 2015.

O. Jensen. Computing with oscillations by phase encoding and decoding. In *Neural Networks, 2004. Proceedings. 2004 IEEE International Joint Conference on*, volume 1, pages –630, 2004.

K. Jittorntrum. An implicit function theorem. *Journal of Optimization Theory and Applications*, 25(4):575–577, 1978.

D. Junge. *Nerve and muscle excitation.* Sinauer Associates, 1981.

D. A. Kaiser. Brodmannn areas. `http://www.skiltopo.com/BA/myBrodmannsAreas2-802.jpg`, 2015. [Online; accessed 19-Oct-2015].

E. Kandel. *Principles of Neural Science, Fifth Edition.* Principles of Neural Science. McGraw-Hill Education, 2013.

M. P. Kennedy. Robust op amp realization of chua's circuit. *Frequenz*, 46:66–80, 1992.

A. Knoblauch. *Synchronization and pattern separation in spiking associative memories and visual cortical areas.* PhD thesis, Universität Ulm, 2003.

A. Kohn, A. F. da Rocha, and J. Segundo. Presynaptic irregularity and pacemaker inhibition. *Biological Cybernetics*, 41(1):5–18, 1981.

N. Kopell, G. B. Ermentrout, M. A. Whittington, and R. D. Traub. Gamma rhythms and beta rhythms have different synchronization properties. *Proceedings of the National Academy of Sciences*, 97(4):1867–1872, 2000.

H. Korn and P. Faure. Is there chaos in the brain? II. Experimental evidence and related models. *C. R. Biol.*, 326(9):787–840, Sept. 2003.

V. Kozyrev, U. T. Eysel, and D. Jancke. Voltage-sensitive dye imaging of transcranial magnetic stimulation-induced intracortical dynamics. *Proceedings of the National Academy of Sciences*, 111(37):13553–13558, 2014.

J.-P. Lachaux, E. Rodriguez, J. Martinerie, and F. J. Varela. Measuring phase synchrony in brain signals. *Human Brain Mapping*, 8(4):194–208, 1999.

G. Laurent, M. Stopfer, R. W. Friedrich, M. I. Rabinovich, A. Volkovskii, and H. D. Abarbanel. Odor encoding as an active, dynamical process: Experiments, computation, and theory. *Annual Review of Neuroscience*, 24(1):263–297, 2001. PMID: 11283312.

J. Levy, J. R. Vidal, R. Oostenveld, I. FitzPatrick, J.-F. Démonet, and P. Fries. Alpha-band suppression in the visual word form area as a functional bottleneck to consciousness. *NeuroImage*, 78(0):33 – 45, 2013.

I. Leyva, R. Sevilla-Escoboza, J. M. Buldú, I. Sendiña Nadal, J. Gómez-Gardeñes, A. Arenas, Y. Moreno, S. Gómez, R. Jaimes-Reátegui, and S. Boccaletti. Explosive first-order transition to synchrony in networked chaotic oscillators. *Physical Review Letters*, 108:168702, Apr 2012.

C. Li and G. Chen. Synchronization in general complex dynamical networks with coupling delays. *Physica A: Statistical Mechanics and its Applications*, 343:263–278, 2004.

W. Lin, Y. Wang, H. Ying, Y.-C. Lai, and X. Wang. Consistency between functional and structural networks of coupled nonlinear oscillators. *Physical Review E*, 92(1):012912, 2015.

B. Lindner, J. Garcia-Ojalvo, A. Neiman, and L. Schimansky-Geier. Effects of noise in excitable systems. *Physics Reports*, 392(6):321–424, 3 2004.

F. H. Lopes da Silva, A. Hoeks, H. Smits, and L. H. Zetterberg. Model of brain rhythmic activity. *Kybernetik*, 15(1):27–37, 1974.

G. MacCabe. Lorenz Attractor. `http://logicaltightrope.com/2013/08/29/edward-lorenzs-strange-attraction/`, 2013. [Online; accessed 19-Oct-2015].

R. Madan. *Chua's circuit: a paradigm for chaos*. World Scientific Publishing Company, 1993.

A. K. Magnusson, T. J. Park, M. Pecka, B. Grothe, and U. Koch. Retrograde gaba signaling adjusts sound localization by balancing excitation and inhibition in the brainstem. *Neuron*, 59 (1):125–137, 2008.

D. Malagarriga, A. E. P. Villa, J. García-Ojalvo, and A. J. Pons. Excitation/inhibition patterns in a system of coupled cortical columns. In *Artificial Neural Networks and Machine Learning–ICANN 2014*, pages 651–658. Springer, 2014.

D. Malagarriga, M. A. García-Vellisca, A. E. Villa, J. M. Buldú, J. García-Ojalvo, and A. J. Pons. Synchronization-based computation through networks of coupled oscillators. *Frontiers in computational neuroscience*, 9, 2015a.

D. Malagarriga, A. E. P. Villa, J. Garcia-Ojalvo, and A. J. Pons. Mesoscopic segregation of excitation and inhibition in a brain network model. *PLoS Computational Biology*, 11(2): e1004007, 02 2015b.

D. Malagarriga, A. E. Villa, J. García-Ojalvo, and A. J. Pons. Consistency of heterogeneous synchronization patterns in complex weighted networks. *arXiv preprint arXiv:1601.05461*, 2016.

E. Maris, T. Womelsdorf, R. Desimone, and P. Fries. Rhythmic neuronal synchronization in visual cortex entails spatial phase relation diversity that is modulated by stimulation and attention. *NeuroImage*, 74(0):99 – 116, 2013.

V. Markounikau, C. Igel, A. Grinvald, and D. Jancke. A dynamic neural field model of mesoscopic cortical activity captured with voltage-sensitive dye imaging. *PLoS Computational Biology*, 6 (9), 2010.

H. Markram, E. Muller, S. Ramaswamy, M. W. Reimann, M. Abdellah, C. A. Sanchez, A. Ailamaki, L. Alonso-Nanclares, N. Antille, S. Arsever, G. A. A. Kahou, T. K. Berger, A. Bilgili, N. Buncic, A. Chalimourda, G. Chindemi, J.-D. Courcol, F. Delalondre, V. Delattre, S. Druckmann, R. Dumusc, J. Dynes, S. Eilemann, E. Gal, M. E. Gevaert, J.-P. Ghobril, A. Gidon, J. W. Graham, A. Gupta, V. Haenel, E. Hay, T. Heinis, J. B. Hernando, M. Hines, L. Kanari, D. Keller, J. Kenyon, G. Khazen, Y. Kim, J. G. King, Z. Kisvarday, P. Kumbhar, S. Lasserre, J.-V. Le Bé, B. R. Magalhães, A. Merchán-Pérez, J. Meystre, B. R. Morrice, J. Muller, A. Muñoz Céspedes, S. Muralidhar, K. Muthurasa, D. Nachbaur, T. H. Newton, M. Nolte, A. Ovcharenko, J. Palacios, L. Pastor, R. Perin, R. Ranjan, I. Riachi, J.-R. Rodríguez, J. L. Riquelme, C. Rössert, K. Sfyrakis, Y. Shi, J. C. Shillcock, G. Silberberg, R. Silva, F. Tauheed, M. Telefont, M. Toledo-Rodriguez, T. Tränkler, W. Van Geit, J. V. Díaz, R. Walker, Y. Wang,

S. M. Zaninetta, J. DeFelipe, S. L. Hill, I. Segev, and F. Schürmann. Reconstruction and Simulation of Neocortical Microcircuitry. *Cell*, 163(2):456–492, 2015.

A. Mazzoni, S. Panzeri, N. K. Logothetis, and N. Brunel. Encoding of naturalistic stimuli by local field potential spectra in networks of excitatory and inhibitory neurons. *PLoS Computational Biology*, 4(12):e1000239–e1000239, 2008.

W. S. McCulloch and W. Pitts. A logical calculus of the ideas immanent in nervous activity. *The Bulleting of Mathematical Biophysics*, 5(4):115–133, 1943.

C. Mehring, U. Hehl, M. Kubo, M. Diesmann, and A. Aertsen. Activity dynamics and propagation of synchronous spiking in locally connected random networks. *Biol. Cybern.*, 88(5):395–408, 2003.

L. Melloni, C. Molina, M. Pena, D. Torres, W. Singer, and E. Rodriguez. Synchronization of neural activity across cortical areas correlates with conscious perception. *The Journal of Neuroscience*, 27(11):2858–2865, 2007.

S. Menon and S. Sinha. `defective´ logic: Using spatiotemporal patterns in coupled relaxation oscillator arrays for computation. In *Signal Processing and Communications (SPCOM), 2014 International Conference on*, pages 1–6. IEEE, July 2014.

D. S. Modha and R. Singh. Network architecture of the long-distance pathways in the macaque brain. *Proceedings of the National Academy of Sciences USA*, 107(30):13485–90, Jul 2010.

F. Mormann, K. Lehnertz, P. David, and C. E. Elger. Mean phase coherence as a measure for phase synchronization and its application to the {EEG} of epilepsy patients. *Physica D: Nonlinear Phenomena*, 144(3–4):358 – 369, 2000.

C. Morris and H. Lecar. Voltage oscillations in the barnacle giant muscle fiber. *Biophysics Journal*, 35(1):193–213, 1981.

A. Morrison, A. Aertsen, and M. Diesmann. Spike-timing-dependent plasticity in balanced random networks. *Neural Computation*, 19(6):1437–1467, 2007.

O. I. Moskalenko, A. A. Koronovskii, A. E. Hramov, and S. Boccaletti. Generalized synchronization in mutually coupled oscillators and complex networks. *Physical Review E*, 86:036216, Sep 2012.

V. B. Mountcastle. Modality and topographic properties of single neurons in cat's somatic sensory cortex. *Journal of Neurophysiology*, 20:408–434, July 1957.

V. B. Mountcastle. The columnar organization of the neocortex. *Brain*, 120:701–722, Apr 1997.

V. Müller and A. P. Anokhin. Neural synchrony during response production and inhibition. *PLoS ONE*, 7(6):1–11, 2012.

B. Neomed. Ramón y Cajal y el premio Nobel de Medicina. `http://blog.neomed.es/ramon-y-cajal-y-el-premio-nobel-de-medicina/#`, 2013. [Online; accessed 19-Oct-2015].

V. Nicosia, M. Valencia, M. Chavez, A. Díaz-Guilera, and V. Latora. Remote synchronization reveals network symmetries and functional modules. *Physical Review Letters*, 110:174102, Apr 2013.

D. Nikolić, P. Fries, and W. Singer. Gamma oscillations: precise temporal coordination without a metronome. *Trends in Cognitive Sciences*, 17(2):54 – 55, 2013.

M. Nobel. The Nobel Prize in Physiology or Medicine 1906. `http://www.nobelprize.org/nobel_prizes/medicine/laureates/1906/golgi-bio.html`, 1967. [Online; accessed 19-Oct-2015].

P. L. Nunez. The brain wave equation: a model for the eeg. *Mathematical Biosciences*, 21(3–4): 279 – 297, 1974.

M. Okun and I. Lampl. Balance of excitation and inhibition. *Scholarpedia*, 4(8):7467, 2009.

S. Onat, P. König, and D. Jancke. Natural scene evoked population dynamics across cat primary visual cortex captured with voltage-sensitive dye imaging. *Cerebral Cortex*, 21(11):2542–2554, 2011.

J. G. Orlandi, O. Stetter, J. Soriano, T. Geisel, and D. Battaglia. Transfer entropy reconstruction and labeling of neuronal connections from simulated calcium imaging. *PLoS ONE*, 9(6):e98842, 06 2014.

T. Petermann, T. C. Thiagarajan, M. A. Lebedev, M. A. L. Nicolelis, D. R. Chialvo, and D. Plenz. Spontaneous cortical activity in awake monkeys composed of neuronal avalanches. *Proceedings of the National Academy of Sciences U S A*, 106(37):15921–6, Sep 2009.

C. C. H. Petersen, A. Grinvald, and B. Sakmann. Spatiotemporal dynamics of sensory responses in layer 2/3 of rat barrel cortex measured in vivo by voltage-sensitive dye imaging combined with whole-cell voltage recordings and neuron reconstructions. *The Journal of Neuroscience*, 23(4):1298–309, Feb. 2003.

J. M. Phillips, M. Vinck, S. Everling, and T. Womelsdorf. A long-range fronto-parietal 5- to 10-hz network predicts "top-down" controlled guidance in a task-switch paradigm. *Cerebral Cortex*, 2013.

A. Pikovsky, M. Rosenblum, and J. Kurths. *Synchronization: a universal concept in nonlinear sciences*, volume 12. Cambridge university press, 2003.

H. Poincaré. Sur l'équilibre d'une masse fluide animée d'un mouvement de rotation. *Acta Mathematica*, 7(1):259–380, 1885.

A. J. Pons, J. L. Cantero, M. Atienza, and J. Garcia-Ojalvo. Relating structural and functional anomalous connectivity in the aging brain via neural mass modeling. *NeuroImage*, 52(3): 848–61, Sept. 2010.

S. C. Ponten, A. Daffertshofer, A. Hillebrand, and C. J. Stam. The relationship between structural and functional connectivity: graph theoretical analysis of an EEG neural mass model. *NeuroImage*, 52(3):985–94, Sept. 2010.

R. Quian Quiroga, A. Kraskov, T. Kreuz, and P. Grassberger. Performance of different synchronization measures in real data: A case study on electroencephalographic signals. *Physical Review E*, 65:041903, Mar 2002.

M. Rabinovich, P. Varona, A. Selverston, and H. Abarbanel. Dynamical principles in neuroscience. *Reviews in Modern Physics*, 78(4):1213–1265, Nov. 2006.

M. I. Rabinovich and P. Varona. Robust transient dynamics and brain functions. *Frontiers in Computational Neuroscience*, 5(June):24, jan 2011.

C. Ramon and M. D. Holmes. Stochastic behavior of phase synchronization index and cross-frequency couplings in epileptogenic zones during interictal periods measured with scalp deeg. *Frontiers in Neurology*, 4(57), 2013.

G. J. Rinkus. A cortical sparse distributed coding model linking mini- and macrocolumn-scale functionality. *Frontiers in Neuroanatomy*, 4:17, 2010.

P. A. Robinson, J. J. Wright, and C. J. Rennie. Synchronous oscillations in the cerebral cortex. *Physical Review E*, 57:4578–4588, Apr 1998.

P. A. Robinson, C. J. Rennie, and D. L. Rowe. Dynamics of large-scale brain activity in normal arousal states and epileptic seizures. *Physical Review E*, 65:1–9, 2002.

K. S. Rockland. Five points on columns. *Frontiers in Neuroanatomy*, 4:22, 2010.

S. Rodrigues, A. V. Chizhov, F. Marten, and J. R. Terry. Mappings between a macroscopic neural-mass model and a reduced conductance-based model. *Biological Cybernetics*, 102(5): 361–71, May 2010.

E. Rodriguez, N. George, J. Lachaux, J. Martinerie, B. Renault, and F. Varela. Perception's shadow: long-distance synchronization of human brain activity. *Nature*, 397:430–433, 1999.

M. G. Rosenblum, A. S. Pikovsky, and J. Kurths. Phase synchronization of chaotic oscillators. *Physical Review Letters*, 76:1804–1807, Mar 1996.

M. G. Rosenblum, A. S. Pikovsky, and J. Kurths. From phase to lag synchronization in coupled chaotic oscillators. *Physical Review Letters*, 78:4193–4196, Jun 1997.

Y. Roudi and P. E. Latham. A balanced memory network. *PLoS Computational Biology*, 3(9): e141, 09 2007.

A. Roxin, H. Riecke, and S. Solla. Self-Sustained Activity in a Small-World Network of Excitable Neurons. *Physical Review Letters*, 92(19):198101, May 2004.

P. Rué, N. Domedel-Puig, J. Garcia-Ojalvo, and A. J. Pons. Integration of cellular signals in chattering environments. *Progress in biophysics and molecular biology*, 110(1):106–112, 2012.

O. Rössler. An equation for continuous chaos. *Physics Letters A*, 57(5):397 – 398, 1976.

B. Sancristóbal, R. Vicente, and J. Garcia-Ojalvo. Role of frequency mismatch in neuronal communication through coherence. *Journal of Computational Neuroscience*, 37(2):193–208, 2014.

E. L. Schwartz. Methods in neuronal modelling. from synapses to networks. *Trends in Neurosciences*, 13(10):436 – 437, 1990.

J. Segundo, E. Altshuler, M. Stiber, and A. Garfinkel. Periodic inhibition of living pacemaker neurons (I): locked, intermittent, messy, and hopping behaviors. *International Journal of Bifurcation and Chaos*, 1:549–581, 1991a.

J. P. Segundo. Nonlinear dynamics of point process systems and data. *International Journal of Bifurcation and Chaos*, 13(08):2035–2116, 2003.

J. P. Segundo, B. F. Tolkunov, and G. E. Wolfe. Relation between trains of action potentials across an inhibitory synapse. Influence of presynaptic irregularity. *Biological Cybernetics*, 24 (3):169–179, Nov 1976.

J. P. Segundo, E. Altshuler, M. Stiber, and A. Garfinkel. Periodic inhibition of living pacemaker neurons (II): Influences of driver rates and transients and of nondriven postsynaptic rates. *International journal of Bifurcation and Chaos*, 1:873–890, 1991b.

W. Singer. Development and Plasticity of Cortical Processing Architectures. *Science*, 270: 758–764, Nov. 1995.

W. Singer. Neuronal synchrony: a versatile code for the definition of relations. *Neuron*, 24:49–65, 1999.

C. A. Skarda and W. J. Freeman. How brains make chaos in order to make sense of the world. *Behavioral and brain sciences*, 10(02):161–173, 1987.

C. Sotelo. Viewing the brain through the master hand of Ramon y Cajal. `http://www.nature.com/nrn/journal/v4/n1/fig_tab/nrn1010_F2.html#close`, 2003. [Online; accessed 19-Oct-2015].

R. C. Sotero. Generation of phase-amplitude coupling of neurophysiological signals in a neural mass model of a cortical column. *bioRxiv*, page 023291, 2015.

R. C. Sotero, N. J. Trujillo-Barreto, Y. Iturria-Medina, F. Carbonell, and J. C. Jimenez. Realistically coupled neural mass models can generate EEG rhythms. *Neural Computation*, 19 (2):478–512, 2007.

A. Spiegler, S. J. Kiebel, F. M. Atay, and T. R. Knösche. Bifurcation analysis of neural mass models: Impact of extrinsic inputs and dendritic time constants. *Neuroimage*, 52(3):1041–58, sep 2010.

A. Spiegler, T. R. Knösche, J. Haueisen, and F. M. Atay. Complex behavior in a modified Jansen and Rit neural mass model. *BMC Neuroscience*, 12(Suppl 1):P5, 2011a.

A. Spiegler, T. R. Knösche, K. Schwab, J. Haueisen, and F. M. Atay. Modeling brain resonance phenomena using a neural mass model. *PLoS computational biology*, 7(12):e1002298, Dec. 2011b.

C. Stam. Nonlinear dynamical analysis of eeg and meg: Review of an emerging field. *Clinical Neurophysiology*, 116(10):2266 – 2301, 2005.

C. J. Stam and E. A. de Bruin. Scale-free dynamics of global functional connectivity in the human brain. *Human Brain Mapping*, 22(2):97–109, 2004.

M. Stopfer, S. Bhagavan, B. Smith, and G. Laurent. Impaired odour discrimination on desynchronization of odour-encoding neural assemblies. *Nature*, pages 70–74, 1997.

S. H. Strogatz. *Nonlinear Dynamics and Chaos: With Applications to Physics, Biology, Chemistry, and Engineering*. Advanced book program. Westview Press, 1994.

S. H. Strogatz. From kuramoto to crawford: exploring the onset of synchronization in populations of coupled oscillators. *Physica D: Nonlinear Phenomena*, 143(1–4):1 – 20, 2000.

S. H. Strogatz. *Sync: The Emerging Science of Spontaneous Order*. Hachette Books, 2003.

P. Suffczynski, S. Kalitzin, G. Pfurtscheller, and F. H. L. Da Silva. Computational model of thalamo-cortical networks: dynamical control of alpha rhythms in relation to focal attention. *Int. J. Psychophysiol.*, 43(1):25–40, 2001.

H. a. Swadlow, A. G. Gusev, and T. Bezdudnaya. Activation of a cortical column by a thalamocortical impulse. *The Journal of Neuroscience*, 22(17):7766–73, Sept. 2002.

G. Tirabassi, R. Sevilla-Escoboza, J. M. Buldú, and C. Masoller. Inferring the connectivity of coupled oscillators from time-series statistical similarity analysis. *Scientific reports*, 5:10829, 2015.

A. B. L. Tort, R. W. Komorowski, J. R. Manns, N. J. Kopell, and H. Eichenbaum. Theta–gamma coupling increases during the learning of item–context associations. *Proceedings of the National Academy of Sciences*, 106(49):20942–20947, 2009.

A. Uchida, F. Rogister, J. García-Ojalvo, and R. Roy. Synchronization and communication with chaotic laser systems. volume 48 of *Progress in Optics*, pages 203 – 341. Elsevier, 2005.

P. J. Uhlhaas and W. Singer. Neural synchrony in brain disorders: relevance for cognitive dysfunctions and pathophysiology. *Neuron*, 52(1):155–168, 2006.

P. J. Uhlhaas and W. Singer. Abnormal neural oscillations and synchrony in schizophrenia. *Nature Reviews Neuroscience*, 11(2):100–113, 2010.

M. Ursino, F. Cona, and M. Zavaglia. The generation of rhythms within a cortical region: analysis of a neural mass model. *Neuroimage*, 52(3):1080–94, Oct. 2010.

M. P. van den Heuvel, C. J. Stam, M. Boersma, and H. E. Hulshoff Pol. Small-world and scale-free organization of voxel-based resting-state functional connectivity in the human brain. *Neuroimage*, 43(3):528–39, Nov. 2008.

S. van der Walt, S. C. Colbert, and G. Varoquaux. The numpy array: A structure for efficient numerical computation. *Computing in Science & Engineering*, 13(undefined):22–30, 2011.

C. van Vreeswijk and H. Sompolinsky. Chaos in neuronal networks with balanced excitatory and inhibitory activity. *Science*, 274(5293):1724–1726, Dec 1996.

C. van Vreeswijk and H. Sompolinsky. Chaotic balanced state in a model of cortical circuits. *Neural Comput*, 10(6):1321–1371, Aug 1998.

R. Vardi, S. Guberman, A. Goldental, and I. Kanter. An experimental evidence-based computational paradigm for new logic-gates in neuronal activity. *EPL (Europhysics Letters)*, 103(6): 66001, 2013.

F. Varela, J.-P. Lachaux, E. Rodriguez, and J. Martinerie. The brainweb: phase synchronization and large-scale integration. *Nature Reviews Neuroscience*, 2(4):229–239, 2001.

J. L. Velayos-Jorge, J. J. Hernandez-Roca, and F. J. Moleres-Echevarria. The neurobiology of sleep: Cajal and present-day neuroscience. *Rev Neurol*, 37(5):494–498, 2003.

R. Vicente, L. L. Gollo, C. R. Mirasso, I. Fischer, and G. Pipa. Dynamical relaying can yield zero time lag neuronal synchrony despite long conduction delays. *Proceedings of the National Academy of Sciences*, 105(44):17157–17162, 2008.

A. E. P. Villa and I. V. Tetko. Cross-frequency coupling in mesiotemporal eeg recordings of epileptic patients. *Journal of Physiology - Paris*, 104(3-4):197–202, May-Sep 2010.

T. P. Vogels and L. F. Abbott. Signal propagation and logic gating in networks of integrate-and-fire neurons. *The Journal of neuroscience*, 25(46):10786–95, nov 2005.

H. von Helmholtz and A. König. *Handbuch der physiologischen Optik*. 1896.

A. Wagemakers, J. M. Buldú, and M. A. F. Sanjuán. Isochronous synchronization in mutually coupled chaotic circuits. *Chaos: An Interdisciplinary Journal of Nonlinear Science*, 17(2): 023128, 2007.

H.-T. Wang, B. Luo, Y.-N. Huang, K.-Q. Zhou, and L. Chen. Sodium salicylate suppresses serotonin-induced enhancement of {GABAergic} spontaneous inhibitory postsynaptic currents in rat inferior colliculus in vitro. *Hearing Research*, 236(1–2):42 – 51, 2008.

L. M. Ward. Synchronous neural oscillations and cognitive processes. *Trends in Cognitive Sciences*, 7(12):553 – 559, 2003.

D. J. Watts and S. H. Strogatz. Collective dynamics of'small-world'networks. *Nature*, 393(6684): 409–10, 1998.

H. R. Wilson and J. D. Cowan. Excitatory and inhibitory interactions in localized populations of model neurons. *Biophysical Journal*, 12:1–24, 1972.

F. Wolf and T. Geisel. Neurophysics: logic gates come to life. *Nature Physics*, 4(12):905–906, 2008.

T. Womelsdorf and P. Fries. The role of neuronal synchronization in selective attention. *Current Opinion in Neurobiology*, 17(2):154 – 160, 2007. Cognitive neuroscience.

T. Womelsdorf, P. Fries, P. P. Mitra, and R. Desimone. Gamma-band synchronization in visual cortex predicts speed of change detection. *Nature*, 439(7077):733–736, 2006.

T. Womelsdorf, J.-M. Schoffelen, R. Oostenveld, W. Singer, R. Desimone, A. K. Engel, and P. Fries. Modulation of neuronal interactions through neuronal synchronization. *Science*, 316 (5831):1609–1612, 2007.

T. Womelsdorf, T. A. Valiante, N. T. Sahin, K. J. Miller, and P. Tiesinga. Dynamic circuit motifs underlying rhythmic gain control, gating and integration. *Nature neuroscience*, 17(8): 1031–1039, 2014.

G. K. Wu, P. Li, H. W. Tao, and L. I. Zhang. Nonmonotonic synaptic excitation and imbalanced inhibition underlying cortical intensity tuning. *Neuron*, 52(4):705–715, 2006.

G. K. Wu, R. Arbuckle, B.-h. Liu, H. W. Tao, and L. I. Zhang. Lateral sharpening of cortical frequency tuning by approximately balanced inhibition. *Neuron*, 58(1):132–143, 2008.

P. Wulff, A. A. Ponomarenko, M. Bartos, T. M. Korotkova, E. C. Fuchs, F. Bähner, M. Both, A. B. L. Tort, N. J. Kopell, W. Wisden, and H. Monyer. Hippocampal theta rhythm and its coupling with gamma oscillations require fast inhibition onto parvalbumin-positive interneurons. *Proceedings of the National Academy of Sciences*, 106(9):3561–3566, 2009.

L. Xiao-Wen and Z. Zhi-Gang. Phase Synchronization of Coupled Rossler Oscillators: Amplitude Effect. *Commun. Theor. Phys.*, 47(2):265–269, feb 2007.

D. Xu, J. C. Principe, and J. G. Harris. Logic computation using coupled neural oscillators. In *Circuits and Systems, 2004. ISCAS'04. Proceedings of the 2004 International Symposium on*, volume 5, pages V788–V791. IEEE, 2004.

O. Yizhar, L. E. Fenno, M. Prigge, F. Schneider, T. J. Davidson, D. J. O'Shea, V. S. Sohal, I. Goshen, J. Finkelstein, J. T. Paz, K. Stehfest, R. Fudim, C. Ramakrishnan, J. R. Huguenard, P. Hegemann, and K. Deisseroth. Neocortical excitation/inhibition balance in information processing and social dysfunction. *Nature*, 477(7363):171–8, Sep 2011.

A. Zalesky, A. Fornito, I. H. Harding, L. Cocchi, M. Yücel, C. Pantelis, and E. T. Bullmore. Whole-brain anatomical networks: does the choice of nodes matter? *Neuroimage*, 50(3):970–83, Apr 2010.

G. Zamora-Lopez, C. Zhou, and J. Kurths. Graph analysis of cortical networks reveals complex anatomical communication substrate. *Chaos*, 19(1):015117, 03 2009.

D. H. Zanette. Propagation of small perturbations in synchronized oscillator networks. *EPL (Europhysics Letters)*, 68(3):356, 2004.

M. Zanin, F. Del Pozo, and S. Boccaletti. Computation emerges from adaptive synchronization of networking neurons. *PLoS ONE*, 6(11):e26467, 11 2011.

M. Zavaglia and L. Astolfi. A model of rhythm generation and functional connectivity during a simple motor task: preliminary validation with real scalp EEG data. *International Journal of Bioelectromagnetism*, 10(1):68–75, 2008.

M. Zavaglia, L. Astolfi, F. Babiloni, and M. Ursino. A neural mass model for the simulation of cortical activity estimated from high resolution EEG during cognitive or motor tasks. *Journal of Neuroscience Methods*, 157(2):317–329, 2006.

L. Zetterberg, L. Kristiansson, and K. Mossberg. Performance of a model for a local neuron population. *Biological Cybernetics*, 31(1):15–26, 1978.

B. B. Zhou and R. Roy. Isochronal synchrony and bidirectional communication with delay-coupled nonlinear oscillators. *Physical Review E*, 75:026205, Feb 2007.

C. Zhou, L. Zemanová, G. Zamora, C. C. Hilgetag, and J. Kurths. Hierarchical organization unveiled by functional connectivity in complex brain networks. *Physical review letters*, 97(23): 238103, 2006.